INTERNATIONAL DOCTORAL SCHOOL OF THE USC

Sanaz
Sabzehei

PhD Thesis

UNFOLD TO REFOLD: TRACKING THE INITIAL STEPS OF PrP^{C} UNFOLDING IN THE CONTEXT OF PrP^{Sc} PROPAGATION

Santiago de Compostela, 2026

Doctoral Programme in Molecular Medicine

ESCOLA DE DOUTORAMENTO
INTERNACIONAL DA USC

DOCTORAL THESIS

UNFOLD TO REFOLD: TRACKING THE INITIAL STEPS OF PRP^{C} UNFOLDING IN THE CONTEXT OF PRP^{SC} PROPAGATION

Author

Sanaz Sabzehei

Supervisor/s: Jesús Rodríguez Requena

Tutor: JUAN BAUTISTA ZALVIDE TORRENTE

PHD PROGRAMME IN MOLECULAR MEDICINE

SANTIAGO DE COMPOSTELA - 2026

Conflict of interests

There is a potential conflict of interests when a researcher has financial/personal interest or opinion that might affect his/her objectivity or influence his/her acts in an inappropriate manner. lt is understood that the existence of such conflict does not imply that his/her acts are unethical, however, it may still give rise to situations where his/her objectivity or scientific judgement as author could be influenced. Therefore, the author of a doctoral thesis should inform regarding any real, potential or apparent conflict of interest related to the thesis.
Possible source of conflicts of interests are:

- Having obtained or having the possibility to obtain financial benefits from the investigation disclosed in the thesis. This includes ownership/inventorship of a patent (pending or granted) or having stock options/shares of a company with interests in the outcome of said investigation.
- Receiving funding (current or past) during the course of the thesis by an entity that may potentially obtain financial benefit from the results. This includes the funding of the investigation (total or partial) by a company with potential interest in the outcome, or being employed, granted or paid (e.g. expert advice or counselling) by a company with said interests.
- Personal involvement, such as direct family member working at a company with potential financial interests.

The declaration of conflict of interests will be made by including a sentence in the Thesis detailing possible conflicts of interest or their non existence. **This will be located after the cover of the doctoral thesis**

- The doctoral candidate declares no conflicts of interest related to his/her thesis

A presente tese de doutoramento contou coas seguintes fontes de financiamiento: Agencia Estatal de Investigación (AEI), coa participación de fondos EU FEDER (Grant number: PID2020-117465GB-I00), JPND-Instituto Carlos III (Grant number AC23_2/00049).

--

La presente tesis de doctorado contó con las seguientes fuentes de financiación: Agencia Estatal de Investigación (AEI), con la participación de fondos EU FEDER (Grant number: PID2020-117465GB-I00), JPND-Instituto Carlos III (Grant number AC23_2/00049).

--

This thesis has received funding from: Spanish National Research Agency (AEI), with participation of EU FEDER funds (Grant number: PID2020-117465GB-I00), JPND-Instituto Carlos III (Grant number AC23_2/00049)

"In the order of the universe, the disorder of my heart finds its place."

— Hafez

Acknowledgement

I would like to express my deepest gratitude to everyone who stood beside me throughout this journey. To my family, whose endless encouragement and quiet strength carried me through the most challenging moments. Even when they missed me deeply, they pretended to be fine just to keep me motivated. Their love and support were the main source of strength that sustained me.
Coming to a country that wasn't mine four years ago, speaking a language I once cried trying to learn, was not an easy path. I still remember leaving my mother at the airport with a hug that had to last for years. There were nights when I was alone, disappointed, and stressed. I called home at 3 a.m. just to hear a familiar voice while my own country was under the sound of bombing. There were nights I wanted to quit and go back, but every time, I heard my family's dreams louder than my fear.

So, I stayed and studied when I was broken. I smiled when I wanted to cry while I kept going. To my sister, the most valuable person in my life, who supported me unconditionally despite facing her own struggles. She was always there to listen to my worries, especially the difficulties I experienced as a foreigner, and her presence gave me the courage to keep going when I felt weakest.

My heartfelt appreciation goes to my supervisor, Jesús, and Manolo who has helped me so much that he has virtually acted as a co-supervisor. Having them in my life has truly been a blessing. Jesús supported me in countless ways, and by providing opportunities and essential resources, he played a significant role in my academic growth. He encouraged me to participate in oral presentations, attend conferences, and choose projects I was passionate about. He stood by me through every challenge I faced as an International Student and never allowed me to face them alone. I cannot be more grateful for everything he has done for me.

I am equally thankful to Manolo Martin-Pastor, who became not only a supervisor but also one of my best friends. His kindness, patience, and willingness to guide me whenever I needed help made a profound difference in my journey. I cannot fully express how much these two incredible mentors have meant to me; they were both my scientific and spiritual guides, teaching me lessons about humanity as much as about science.

I would also like to express my sincere gratitude to Víctor. His guidance, support, and clear direction, as well as his meticulous attention to detail helped me tremendously throughout this work.

I would also like to thank my colleagues Sonia, Nuria, Alex, Iria, and Raúl and to my friends, Sara and Eva in platelet Lab for their support, companionship, and kindness during this time.
To all of you, thank you for shaping this chapter of my life. I will carry your support and everything I learned from you into every step of my future.

Abstract

The structural elucidation of PrP^{Sc}, the infectious and misfolded conformer of the cellular prion protein (PrP^{C}), was long anticipated to provide definitive insight into the enigmatic process of prion propagation. It was widely assumed that determining the atomic arrangement of PrP^{Sc} would directly unveil how PrP^{C} converts into its pathogenic counterpart. Contrary to these expectations, PrP^{Sc} revealed itself as a relatively "simple" amyloid structure composed of repeating β-sheet motifs devoid of unique features beyond what is typically found in other amyloid fibrils. This finding suggested that PrP^{Sc} primarily serves as a passive structural template that stabilizes partially unfolded states of incoming PrP^{C} monomers by sequestering them into a fibrillar conformation. This revelation redirected the focus of this research toward the conformational dynamics and intrinsic properties of PrP^{C} itself, especially its role as an active participant in its own conversion.

It is possible to visualize a templated refolding mechanism wherein the unfolded N-terminal tail of PrP^{C} (residues ~90–120) initially binds to exposed β-strands on the surface of PrP^{Sc}, driven by hydrogen bonding interactions. This anchoring event is relatively straightforward due to the intrinsically disordered nature of the ~90–120 region in PrP^{C}. However, the conversion of the remaining globular folded domain (FD; residues ~121–231), which comprises three α-helices and two short β-strands, presents a greater structural challenge. It was hypothesized herein that the rigid and β-sheet-dominated surface of PrP^{Sc} is poorly suited to interact with intact α-helical elements, implying that partial unfolding of the FD is a prerequisite for successful templating. This would reframe PrP^{C} not as a passive conformational recipient but as an actively unfolding molecule, responding dynamically to the templating landscape presented by PrP^{Sc}.

To explore this hypothesis, a comprehensive study was conducted on the thermal unfolding of recombinant bank vole PrP^{C} ($BVPrP^{C}$, residues 90–231), a widely used model due to its high compatibility with cross-species prion transmission. Using variable-temperature solution nuclear magnetic resonance (VT-NMR), residue-specific conformational changes were tracked under increasing thermal stress, with the goal of identifying early unfolding events that might mimic those involved in the PrP^{Sc} templated conversion pathway.

The NMR data obtained here revealed that the initial destabilization occurs within the β1–β2 hairpin and its flanking loops, as well as in the N-terminal stretch of helix α1. These regions exhibited significant chemical shift perturbations (CSPs) that deviated from expected temperature-dependent linear trends, indicating early conformational flexibility or partial unfolding. In contrast, other secondary structural elements, particularly helix α2, showed a greater degree of thermal resilience, maintaining spectral visibility and linear behavior across a broad temperature range. These observations were reinforced by complementary analyses

including Temperature Coefficients for amide protons, NOE distances and the solvent water accessibility studied by CLEANEX-PM. Backbone ^{15}N amide relaxation measurements showed that there is a substantially higher mobility for the disordered ~90-120 N-terminus than for the rest of the structure, for the following six residues, ~V121-G126 segment, there is a gradual decrease in mobility which is followed by large amplitude conformational fluctuations for residue G131 in β1, another proof of the conformational instability of β1. The backbone ^{15}N_CEST spectra indicated that these structural changes result in an altered but stable protein conformation, with no dynamic excursion to other intermediate forms.

Molecular dynamics (MD) simulations conducted at elevated temperatures (>80°C) supported the experimental data, identified the separation of two major FD subdomains: the β1–α1–β2 unit and the α2–α3 helical core. This "flattening" of the FD facilitates spatial rearrangement, potentially allowing the polypeptide to adopt an extended, β-sheet-compatible structure required for propagation. Notably, such domain separation was observed in some but not all simulations of bank vole PrP^C, suggesting that it is a rare event.

Experimentally, one of the most intriguing findings emerged at temperatures exceeding ~50°C. At this threshold, $BVPrP^C$ underwent a non-reversible conformational transition, resulting in the formation of a stable oligomeric species. Diffusion-ordered NMR spectroscopy (DOSY) and Size Exclusion Chromatography (SEC) confirmed the presence of a multimeric assembly composed of 8-12 monomers. These oligomers exhibited dramatically reduced signal intensities in solution-state NMR spectra, indicative of high molecular packing and conformational rigidity. Interestingly, upon cooling, the oligomeric state persisted, suggesting that this assembly represents a kinetically trapped, stable intermediate that may be highly relevant to early stages of PrP^{Sc} fiber formation.

Although most residues within these oligomers became invisible to solution NMR due to line broadening from reduced mobility, residual HSQC signals suggested that specific segments particularly within helix α2 retain significant conformational stability. This segment may be part of a "folded core" that remains intact until the very last stages of conversion.

Taken together, the results obtained herein support a model of prion propagation wherein PrP^C is not a passive substrate awaiting transformation but an active participant that undergoes strategic partial unfolding to align and couple with the PrP^{Sc} template. The identification of discrete early unfolding events particularly within labile β-hairpin motifs and helix α1 provide new mechanistic insights into how PrP^C transitions toward the pathogenic conformation. These findings not only deepen our understanding of prion biology but also open new avenues for the development of therapeutic interventions aimed at stabilizing the native fold of PrP^C or disrupting key unfolding steps.

Looking forward, the aim is to integrate these experimental observations with advanced computational modeling approaches to construct a complete atomistic model of the PrP^{Sc} propagation pathway.

In summary, the thermally induced unfolding of $BVPrP^{C}$ has provided a powerful experimental window into the early conformational events underlying prion propagation. By pinpointing structurally labile regions and identifying conversion-relevant intermediates, the study carried out advances the foundational understanding of prion biology and sets the stage for rational intervention strategies against transmissible spongiform encephalopathies.

Resumen

La reciente elucidación estructural de PrP^{Sc}, la conformación infecciosa y con plegamiento anómalo de la proteína priónica celular (PrP^{C}), hacía pensar que sería la clave definitiva para comprender todo el proceso de propagación de los priones. Se asumía ampliamente que la disposición atómica de PrP^{Sc} revelaría directamente cómo PrP^{C} se convierte en su contraparte patogénica. Contrariamente a estas expectativas, la PrP^{Sc} ha resultado tener una estructura amiloide relativamente "simple", compuesta por motivos repetitivos de láminas β, sin características distintivas más allá de las observadas comúnmente en otras fibras amiloides. Este hallazgo sugiere que PrP^{Sc} actúa principalmente como un molde o plantilla estructural pasiva que estabiliza los estados parcialmente desplegados de los monómeros de PrP^{C} entrantes, incorporándolos a la conformación fibrilar. Esta constatación desplazó el enfoque de esta investigación hacia el estudio de la dinámica conformacional y las propiedades intrínsecas de PrP^{C}, desde el punto de vista de que juega un papel activo en su propia conversión.

Se puede visualizar un mecanismo de replegamiento guiado por este molde o plantilla en el que la cola N-terminal desplegada de PrP^{C} (residuos ~90–120) se une inicialmente a láminas β expuestas en la superficie de PrP^{Sc}, mediante interacciones de enlaces de hidrógeno. Este anclaje es relativamente simple debido a la naturaleza intrínsecamente desordenada de la región ~90–120 de PrP^{C}. Sin embargo, la conversión del dominio globular plegado restante (FD; residuos ~121–231), que contiene tres hélices α y dos láminas β cortas, representa un desafío estructural mayor. La hipótesis inicial es que la superficie rígida y dominada por láminas β de PrP^{Sc} no se adapta bien a convertir elementos α-helicoidales intactos, lo que implica que un desplegamiento parcial del FD es un requisito previo para la conversión. Esto resignifica a la PrP^{C} no como un receptor pasivo, sino como una molécula que se despliega activamente, actuando dinámicamente frente al paisaje de la plantilla de PrP^{Sc}.

Para explorar esta hipótesis, en este trabajo se ha realizado un estudio integral del desdoblamiento térmico de PrP^{C} recombinante de topillo rojo ($BVPrP^{C}$, residuos 90–231), un modelo ampliamente utilizado por su alta compatibilidad con la transmisión priónica entre especies. Utilizando espectroscopía de resonancia magnética nuclear (NMR) en solución a temperatura variable (VT-NMR), se han rastreado cambios conformacionales específicos de cada residuo bajo estrés térmico creciente, con el objetivo de identificar eventos tempranos de desplegamiento que puedan imitar los involucrados en la conversión guiada por una plantilla de PrP^{Sc}.

Los datos de RMN obtenidos revelan que la desestabilización inicial ocurre en la región β1–β2 y sus lazos ("coils") adyacentes, así como en el tramo N-terminal de la hélice α1. Estas regiones mostraron perturbaciones significativas en los desplazamientos químicos (CSPs) que se desviaron de la tendencia lineal esperada para un cambio de temperatura, indicando flexibilidad conformacional temprana o desplegamiento parcial. En contraste, otros elementos estructurales

secundarios, en particular la hélice α2, mostraron mayor resistencia térmica, manteniendo sus características espectrales y un comportamiento lineal a lo largo de un amplio rango de temperaturas. Estos resultados fueron corroborados con análisis complementarios que incluyeron coeficientes de temperatura de protones amida, distancias NOE y estudios de la accesibilidad del agua del disolvente mediante CLEANEX-PM. Las medidas de relajación de ^{15}N demostraron una mayor movilidad de la región desordenada N-terminal ~90-120 que, para el resto de la estructura, para los seis residuos que siguen a continuación, segmento ~V121-G126, se produce una reducción paulatina de la movilidad, a lo que sigue el residuo G131 en β1 con fluctuaciones conformacionales de gran amplitud, otra prueba más de la inestabilidad conformacional de β1. Los espectros ^{15}N_CEST indicaron que estos cambios estructurales dan lugar a una conformación alterada pero aún estable de la proteína, sin que se detectaran cambios dinámicos hacia otras conformaciones intermedias.

Las simulaciones de dinámica molecular (MD) realizadas a temperaturas elevadas (>80 °C) respaldan estos datos experimentales. Se identificó la separación de dos subdominios principales del FD: el bloque β1–α1–β2 y el bloque α2–α3. Este "aplanamiento" del FD facilita una reorganización espacial, permitiendo potencialmente que el polipéptido adopte una estructura extendida compatible con láminas β, necesaria para la propagación. Es notable que dicha separación de dominios se observó, en algunas, pero no todas, las simulaciones de BVPrP^{C}, lo que sugiere que es un suceso raro.

Experimentalmente, uno de los hallazgos más intrigantes surgió a temperaturas superiores a ~50 °C. En este umbral, BVPrP^{C} sufre una transición conformacional no reversible, dando lugar a la formación de una especie oligomérica estable. La espectroscopía de difusión por RMN (DOSY) y la cromatografía de exclusión molecular (SEC) confirmaron la presencia de un ensamblaje multimérico compuesto por 8-12 monómeros. Estos oligómeros mostraron una marcada reducción en la intensidad de señales en los espectros de RMN en solución, indicativa de un empaquetamiento molecular denso y rigidez conformacional. Curiosamente, al enfriar, el estado oligomérico persistió, lo que sugiere que este ensamblaje representa un intermediario estable atrapado cinéticamente, potencialmente relevante en las etapas iniciales de la formación de fibras de PrP^{Sc}.

Aunque la mayoría de los residuos del interior de estos oligómeros se volvieron invisibles a la RMN en solución debido al ensanchamiento de líneas por movilidad reducida, las señales residuales del espectro HSQC sugieren que segmentos específicos, particularmente dentro de la hélice α2, retienen estabilidad conformacional significativa. Este segmento podría constituir un “núcleo de plegamiento” que permanece intacto hasta las últimas etapas de la conversión.
En conjunto, nuestros datos respaldan un modelo de propagación priónica en el que PrP^{C} no es un sustrato pasivo en espera de transformación, sino un participante activo que experimenta un desplegamiento parcial estratégico para alinearse y acoplarse a la plantilla de PrP^{Sc}. La identificación de eventos tempranos de desplegamiento, particularmente en motivos lábiles como el par β1/ β2 y la hélice α1, proporciona nuevos conocimientos mecanísticos sobre cómo

PrP^C progresa hacia la conformación patogénica. Estos hallazgos no solo profundizan en la comprensión de la biología de los priones, sino que también abren nuevas vías para el desarrollo de intervenciones terapéuticas dirigidas a estabilizar el pliegue nativo de PrP^C o interrumpir pasos clave del desplegamiento.

De cara al futuro, el objetivo sería integrar estas observaciones experimentales con enfoques avanzados de modelado computacional para construir un modelo atomístico completo de la vía de propagación de PrP^{Sc}. Dicho modelo ayudaría a esclarecer la secuencia de reorganizaciones conformacionales durante la conversión.

En resumen, el desplegamiento inducido térmicamente de $BVPrP^C$ ha proporcionado una poderosa ventana experimental hacia los eventos conformacionales tempranos que subyacen en la propagación priónica. Al identificar regiones estructuralmente lábiles e intermediarios relevantes para la conversión, este estudio avanza en la comprensión fundamental de la biología de los priones y sienta las bases para estrategias racionales de intervención contra las encefalopatías espongiformes transmisibles.

Resumo

O despregamento térmico da proteína priónica celular recombinante da rubia corta, Myodes glareolus, bank vole en inglés, (BVPrP^{C,} residuos 90-231) revela un panorama exhaustivo e integrado dos eventos conformacionais iniciais que permiten a súa conversión asistida pola forma patóxena PrP^{Sc} na propagación priónica. A estrutura atómica da PrP^{Sc}, composta por monómeros apilados en disposición de láminas β paralelas en rexistro (PIRIBS), actúa como un molde pasivo que captura segmentos parcialmente despregados da PrP^{C} entrante.

O dominio N-terminal intrinsecamente desordenado (residuos ~90-120) da PrP^{C} ancorase facilmente á superficie do molde de PrP^{Sc} mediante enlaces de hidróxeno coas cadeas β expostas, pero o dominio globular pregado ("folded domain", FD, residuos ~121-231), que comprende tres hélices α, dúas láminas β curtas e bucles de conexión ben definidos, require un despregamento parcial previo para acoplarse á topoloxía estendida e inerte da superficie PrP^{Sc}, comparable a un "leito de Procusto" que demanda unha reorganización precisa dos subdominios β1-α1-β2 e α2-α3, conectados por unha bisagra flexible ao redor dos residuos ~164-168. Este proceso converte a PrP^{C} nun participante activo que debe sufrir cambios conformacionais temperáns para alinear o seu esqueleto polipeptídico coa estrutura fibrilar da PrP^{Sc}, evitando así a enerxía prohibitiva dunha conversión directa de elementos α-helicoidais intactos á configuración β estendida. A análise integrada de múltiples técnicas experimentais e computacionais descrita nesta tese mostra que o despregamento non é un proceso aleatorio nin global inmediato, senón unha secuencia ordenada de eventos onde rexións específicas do FD inician a desestabilización, facilitando unha reorganización progresiva en cremalleira.

A análise do comportamento térmico global mediante dicroísmo circular (CD) no ultravioleta distante mostra que o despregamento da BVPrP^{C} segue un modelo sigmoide de Boltzmann de dous estados, sen intermediarios detectables, cunha temperatura de fusión (Tm) de 63°C, que foi monitorizada pola redución do mínimo asociado á hélice α a 222 nm. Este modelo indica que a transición principal ocorre de forma cooperativa, pero a análise a nivel de residuo, realizada mediante Resonancia Magnética Nuclear (RMN) revela que certos segmentos do FD comezan a perder estrutura moito antes de alcanzar a Tm global. Ata 45°C, os cambios estruturais son completamente reversibles, con recuperación da estructura orixinal ao arrefriar a proteína a 25°C, o que indica que ésta mantén a súa capacidade de repregarse á conformación nativa tras estrés térmico moderado e que os movementos observados nesta fase representan flutuacións dinámicas transitorias que non comprometen a integridade global do pregamento. Non obstante, a partir de aproximadamente 50°C prodúcese unha transición irreversible que leva á formación dunha especie oligomérica estable, soluble e multimérica, composta por 8-12 monómeros, confirmada pola ausencia de precipitación mesmo tras centrifugación a 16 000 g durante 15 minutos. Ao arrefriar mostras aquecidas ata 75°C, o espectro CD mostra unha redución do 50 % na intensidade global e un desprazamento cara a un perfil rico en láminas β,

consistente coa estabilización dun estado oligomérico que representa un intermediario cineticamente atrapado.

Este limiar de irreversibilidade a ~50°C marca o punto no que o despregamento parcial do FD se converte nunha reorganización que non permite o retorno á estrutura nativa, suxerindo que eventos conformacionais temperáns por baixo deste umbral poden mimetizar os pasos iniciais da vía de propagación asistida por PrP^{Sc} antes de entrar nunha ruta de mispregamento espontáneo. A solubilidade persistente dos oligómeros, sen formación de agregados insolubles visibles, indica que estes estados representan unha fase pre-fibrilar ordenada onde os monómeros se asocian de forma específica, posiblemente a través de interfaces expostas polo despregamento parcial.

A RMN en solución a temperatura variable (VT-NMR) proporciona unha resolución residuo-específica destes procesos, permitindo mapear con precisión cada cambio conformacional ao longo da secuencia. Os espectros HN-HSQC rexistrados de 15 a 75°C mostran que, ata 45°C, os sinais manteñen intensidades fortes, anchuras estreitas e desprazamentos químicos ben dispersos, con cambios graduais consistentes coa dependencia lineal coa temperatura dos protóns de amida. Estes cambios lineais reflicten principalmente o aumento da taxa de intercambio dos protóns de amida co solvente e pequenas vibracións libracionais sen perda significativa de estrutura secundaria. A partir de 50°C, prodúcense ensanchamentos significativos, diminucións de intensidade e desaparicións de picos, câmbios que se fan máis pronunciados co aumento da temperatura ata 70°C, cando só permanecen visibles un subconxunto de sinais. Ao arrefriar as mostras, as que foron aquecidas ata 45°C recuperanse os espectros orixinais de 25°C, confirmando a reversibilidade e a natureza transitoria dos movementos nesta fase. En contraste, as mostras aquecidas por riba de 50°C exhiben alteracións persistentes, cunha desaparición da maioría dos sinais do dominio pregado FD debido ao empaquetamento denso e á rixidez no oligómero. No espectro post-70°C (arrefriado a 25°C), os sinais residuais corresponden principalmente a residuos da cola N-terminal ~90-121 e segmento C-terminal ~227-231, caracterizados por alta mobilidade, pero tamén a algúns picos correspondentes a resíduos do FD con desprazamentos inalterados. Isto indica que hai segmentos que conservan movementos independentes parcialmente desprendidos do núcleo oligomérico. Tamén hai un número moi pequeno de novos sinais, que suxiren conformacións locais alteradas pero estables. Esta combinación única de sinais apunta a que o oligómero posúe un núcleo ríxido onde a maioría dos residuos do FD perden visibilidade por mobilidade restrinxida, mentres que rexións periféricas, especialmente en certas partes da hélice α2, conservan flexibilidade suficiente para producir sinais nítidos.

A espectroscopía de difusión ordenada (DOSY) corrobora a formación oligomérica de forma cuantitativa: o coeficiente de difusión propio baixa de $0,96 \pm 0,04 \times 10^{-10}$ m²/s na mostra fresca (correspondente a unha masa molecular estimada de 15 ± 2 kDa, en concordancia co monómero de 17,02 kDa) a $0,63 \times 10^{-10}$ m²/s na mostra post-70°C, excluíndo unha simple transición a

monómero despregado e confirmando a agregación en especies de maior tamaño hidrodinámico. Unha análise mediante cromatografía de exclusión molecular (SEC) complementa estes datos, mostrando un único pico monomérico en mostras post-50°C, pero picos adicionais de elución máis temperá (correspondentes a especies maiores) en mostras post-60°C e post-70°C, co oligómero persistente ao arrefriar e reducindo drasticamente as intensidades de sinais en espectros de RMN en solución debido á mobilidade restrinxida e ao aumento do tempo de correlación rotacional. A persistencia do estado oligomérico ao arrefriar indica que se trata dun mínimo cinético estable, cunha enerxía de activación para a disociación alta, e que este estado pode representar un análogo experimental dos intermediarios pre-fibrilares que se forman durante a propagación natural asistida por PrP^{Sc}, na que a asociación de monómeros parcialmente despregados com segmentos da superfície de moldeado da PrP^{Sc} estabilizaría a estrutura estendida.

Dentro do rango reversible 15-45°C, a análise de parámetros de relaxación ^{15}N (NOE heteronuclear e ratios R_2/R_1) revela unha fronteira non abrupta entre o dominio desordenado ~90-120 e o FD. O segmento ~90-120 exhibe valores de ^{15}N NOE negativos en toda a súa extensión, indicativos de alta mobilidade interna en escala de picosegundos a nanosegundos, con movementos rápidos e descoordinados típicos de cadeas intrinsecamente desordenadas, agás un tramo ~Q98-N108 con valores positivos que suxire a presenza de estrutura secundaria transitoria local, posiblemente pequenas hélices ou voltas que se forman e disipan dinamicamente. O dominio pregado ~127-231 mostra valores de NOE positivos consistentes cunha estrutura máis ríxida, pero a transición ~V121-G126 presenta un gradiente de mobilidade intermedia pronunciado, com valores ^{15}N NOE que pasan progresivamente de negativos a positivos e ratios R_2/R_1 que aumentan desde valores inferiores a 5 (dominados por movementos internos rápidos) ata o rango 10-20 (típico de dominios globulares pregados). Este gradiente indica que a fronteira entre a cola desordenada e o FD non é unha transición abrupta senón gradual, onde a rigidez aumenta de forma progresiva desde o extremo N-terminal ao extremo C-terminal do segmento ~V121-G126. Por outra banda, o residuo G131 en β1 destaca por un valor R_2/R_1 anormalmente alto a 25°C sen un NOE concordante, indicando unha combinación paradoxal de movementos rápidos e intercambio conformacional intermedio na escala de microsegundos a milisegundos, mentres que a 45°C G131, V161 e Y163 (en β2) exhiben as ratios máis elevadas de toda a secuencia, confirmando flutuacións de gran amplitude e a inestabilidade inherente da lámina β1 como punto de ruptura preferencial. A secuencia ~G127-W146, que inclúe β1 e bucles adxacentes, mostra mobilidade elevada a pesar de NOE positivos característicos dun dominio pregado, o que se explica pola presenza de enlaces de hidróxeno intramoleculares débiles e unha propensión elevada a pequenos movementos de apertura e peche que preparan o terreo para o despregamento inicial.

Os coeficientes de temperatura (Tc) dos protóns de amida, que reflicten directamente a estabilidade dos enlaces de hidróxeno (valores entre 0 e -4,6 ppb/K indican protección do solvente ou enlaces estables, mentres que valores < -4,6 ppb/K sinalan exposición ao solvente

ou desorde dinámica), corroboran e amplían esta imaxe con detalle, residuo por residuo. A maioría dos residuos no segmento ~90-120 presentan valores de Tc marcadamente negativos, por debaixo de -4,6 ppb/K, consistentes coa súa natureza intrinsecamente desordenada e alta exposición ao solvente, agás o tramo ~H96-P102 que mostra valores menos negativos ou mesmo próximos ao limiar, suxerindo a formación de estrutura transitoria local que protexe temporalmente algúns protóns amida (vide supra). Unha secuencia continua ~A113-E146, que abarca o resto da cola desordenado, a transición ~V121-G126, a lámina β1, o bucle β1-α1 e a porción N-terminal da hélice α1, mostra Tc fortemente negativos ao longo de toda a súa extensión, indicando unha propensión uniforme ao despregamento parcial dentro do que se consideraba o dominio pregado. Esta rexión representa o punto de partida máis probable para o despregamento temperán do FD, con enlaces de hidróxeno suficientemente débiles como para permitir movementos térmicos que, en contacto coa superficie PrP^{Sc}, poderían amplificarse en reorganizacións estendidas. O resto da hélice α1 e o bucle de conexión a β2 exhiben Tc > -4,6 ppb/K, sinalando unha maior estabilidade e protección dos protóns de amida, o que suxire que esta parte da estrutura actúa como un ancoraxe temporal durante as fases iniciais. As láminas β2 e o bucle denominado "ríxido" (que liga β2 a α2 e ao mesmo tempo os dous subdominios clam-like β1-α1-β2 e α2-α3) presentan unha mestura complexa de valores altos e baixos, reflectindo unha complexidade estructural na que certas posicións manteñen enlaces estables mentres outras permiten flexibilidade. As hélices α2 e α3 mostran un patrón claro de rigidez central ao redor do enlace disulfuro que as conecta, con Tc menos negativos nesta zona, e maior flexibilidade nos extremos N- e C-terminais de cada hélice, con valores que se volven máis negativos, indicando que estes extremos son puntos de vulnerabilidade que facilitan o desenrolamento progresivo. O bucle G195-T199 entre α2 e α3 tem valores de Tc moi negativos ao longo de toda a súa lonxitude, suxerindo un alto grao de desorde pronunciada que actúa como bisagra. Algúns residuos específicos como H96 (na cola desordenada), I139 (bucle β1-α1), E146 (N-terminal de α1), I182 (medio α2) e V215 (en α3) mostran Tc > 0, un fenómeno raro que indica cambios conformacionais inducidos pola temperatura onde o desprazamento químico se move en dirección oposta á esperada, posiblemente debido a rupturas locais de enlaces ou exposicións temporais que preparan conformacións alternativas.

A análise da non linealidade dos desprazamentos químicos combinados (CCSD) dos protóns de amida HN e ^{15}N identifica con gran sensibilidade os residuos que exploran conformacións alternativas de alta enerxía en intercambio rápido dentro da escala de tempo da RMN. A maioría dos residuos do FD mostran unha dependencia lineal do CCSD coa temperatura, indicativa de estabilidade conformacional na que os movementos son pequenos e non exploran estados alternativos de forma significativa, pero desviacións significativas e non lineares ocorren en clusters ben definidos: en β1 (M129, L130, G131), en β2 (Y163, R164), no C-terminal de α2 (T193, K194, G195) e no N-terminal de α3 (D202, V203), así como no bucle α2-α3. Estas desviacións indican que estas rexións son especialmente dinámicas, explorando estados de maior enerxía que poden corresponder a aperturas parciais ou rotacións de cadeas laterais que facilitan o despregamento. Outros residuos como H140 (bucle β1-α1), N159 (bucle α1-β2),

C179 e I184 (medio α2), V210 e M213 (medio α3) e Y226 (C-terminal de α3) tamén mostran non linealidade clara, mentres que V121, V122 e L125 no tramo de transición presentan comportamentos modestamente non lineares que, aínda que menos pronunciados, son notables polo seu agrupamento na fronteira entre a cola desordenada e o FD. Na cola desordenada, só K101 mostra non linealidade significativa, consistente coa dominancia de interaccións co solvente en rexións altamente móbiles que normalmente producen relacións lineais, pero que aquí revela un punto local de comportamento anómalo posiblemente ligado á estrutura transitoria observada com outras técnicas (vide supra).

Os cambios en NOE de longa distancia entre 25 e 45°C, medidos en espectros ^{15}N- e ^{13}C-editados, medidos a concentración máis alta de proteína para compensar a menor sensibilidade do experimento, revelan movementos modestos pero altamente informativos nas distancias inter-protónicas (0,2-0,5 Å na maioría dos 20 pares analizados), compatibles cos movementos globais pequenos e totalmente reversibles observados nos espectros HSQC. Acurtamentos notables inclúen as distancias entre M129 e Y163, e entre G131 e V161, que apoian mobilidade interna dentro do ensamblaxe β1/β2 e suxiren que esta rexión experimenta flutuacións que poden ser capturadas pola superficie PrP^{Sc} para iniciar a propagación en cremallera. Aumentos como o de 0,7 Å entre W145 (en α1) e o protón HD de R148 suxiren un desenrolamento parcial reversible de α1, mentres que o aumento entre Y149 e o protón HE de M205 (na interface α1-α3) indica un amago de separación dos subdominios β1-α1-β2 e α2-α3, aínda que non completada nesta fase. Movementos na bisagra P165-N171 explican acurtamentos como o entre V166 e o protón HD de Y225, e o acurtamento entre M154 e Y157 suxire un desprazamento lateral de α1 lonxe do bucle α1-β2 por rotación ao redor da súa bisagra. O acurtamento entre Q160 e o protón HE de M213, aparentemente inconsistente coa separación de subdominios, reconcíliase por unha combinación de torsión e separación parcial de α1 do bucle α1-β2, o que permite unha reorganización sen perda total de contacto. No conxunto, estes datos apuntan a tensións dinámicas no ensamblaxe β1/β2 e nas interfaces entre subdominios e entre α1 e o resto do FD, sen separación completa neste rango de temperaturas pero preparando o terreo para ela en fases posteriores.

Ademais dos experimentos baseados en seguimento mediante RMN, realizáronse estudos de dinâmica molecular (MD). As simulacións de MD a temperaturas elevadas (>80°C) apoian e estenden os datos experimentais, identificando de forma consistente a separación dos dous subdominios principais do FD: a unidade β1-α1-β2 e o núcleo helicoidal α2-α3. Este aplanamento progresivo do dominio facilita a reorganización espacial do polipeptido cara a unha estrutura estendida compatible con láminas β para a propagación, permitindo que os segmentos se aliñen coa superficie templante da PrP^{Sc}. A separación obsérvase en algunhas pero non todas as simulacións, indicando que se trata dun evento raro pero posible que pode ocorrer mais tarde das fluctuacións observadas experimentalmente.

A integración de todos estes datos experimentais e computacionais emerxe unha liña temporal coherente e detallada dos eventos temperáns de despregamento: a desestabilización inicial prodúcese no motivo β1-β2 e os bucles flanqueantes, así como no tramo N-terminal da hélice α1 (rexión ~113-146 con Tc negativos, CCSD non lineares e alta mobilidade en G131). O segmento ~121-140, contiguo á cola desordenada, é o máis propenso a despregarse primeiro, permitindo que o polipeptido sexa capturado pola rexión equisecuencial da superfície da PrPSc, passando da conformación despregada á conformación estendida β. En contraste, a hélice α2 mostra maior resiliencia térmica, mantendo visibilidade espectral e comportamento lineal nun rango amplo, o que suxire que forma parte dun núcleo pregado que permanece intacto ata as últimas fases da conversión. A formación de oligómeros a >50 °C, con sinais residuais principalmente en α2, reforza a idea de que este segmento actúa como un elemento de estabilidade ata o final do proceso. As flutuacións conformacionais no bucle α2-α3 e extremos das hélices α2/α3 facilitan a separación dos subdominios, permitindo que o FD se reorganice espacialmente para acoplarse á superficie PrP^{Sc}.

Este modelo integrado refuta calquera visión da PrP^{C} como substrato pasivo e destaca o seu papel activo e dinámico na propagación priónica: o despregamento parcial estratéxico do FD, especialmente nos motivos lábeis β-hairpin e hélice α1, permite o aliñamento e acoplamento á plantilla PrP^{Sc}. A análise detallada dos coeficientes de temperatura e a non linealidade dos CCSD non só confirma a inestabilidade da rexión β1-β2 senón que tamén revela como o bucle α2-α3 actúa como un punto de flexibilidade clave que facilita a separación dos subdominios "clam-like". Cada residuo con Tc < -4,6 ppb/K na secuencia ~A113-E146 representa un sitio potencial de iniciación do despregamento, onde os enlaces de hidróxeno débiles permiten movementos térmicos que. Do mesmo xeito, os residuos con CCSD non lineares en β1 e β2 indican que estas láminas curtas son puntos de ruptura preferenciais, onde a exploración de conformacións alternativas de alta enerxía prepara o camiño para a transición de β a despregada. A resiliencia de α2, observada tanto en relaxación ^{15}N como en sinais residuais dos oligómeros, suxire que esta hélice actúa como un ancoraxe temporal que mantén un núcleo estrutural ata que o resto do FD se reorganice completamente. Ademais, os movementos detectados polos NOE de longa distancia, como o acurtamento entre G131 e V161, reforzan a idea de que o ensamblaxe β1-β2 experimenta flutuacións que poden ser capturadas pola PrP^{Sc} para iniciar a propagación en cremallera.

Estos resultados non só ilustran a natureza activa da PrP^{C} na súa propia conversión senón que tamén proporciona obxectivos moleculares precisos para o deseño de terapias que modulen a estabilidade destes rexións lábeis, potencialmente detendo a propagación priónica en etapas moi temperáns. A través desta análise exhaustiva, o despregamento da $BVPrP^{C}$ emerxe como unha ferramenta experimental inestimable para desentrañar os misterios da bioloxía priónica e avanzar cara a intervencións clínicas efectivas contra as encefalopatías esponxiformes.

Ademais, a consistencia entre as diferentes técnicas –relaxación ^{15}N, Tc, CCSD, NOE e MD– reforza a robustez dos achados, onde cada método contribúe a unha imaxe multidimensional: a relaxación ^{15}N capta movementos en escalas temporais curtas e medias, os Tc revelan a forza dos enlaces de hidróxeno, os CCSD detectan exploracións conformacionais, os NOE miden distancias específicas e as simulacións MD proporcionan visións dinámicas a maior escala. Esta integración permite construír un mapa completo da propensión ao despregamento ao longo da secuencia, identificando non só as rexións máis lábeis senón tamén aquelas que manteñen estabilidade ata o final, como segmentos de α2. A propensión ao despregamento na rexión ~121-146, contigua á cola desordenada, é especialmente relevante porque permite que o anclaxe inicial do N-terminal se estenda progresivamente ao FD sen requirir unha ruptura global enerxeticamente custosa. En última instancia, estes resultados establecen as bases para comprender como a PrP^{C}, a través de despregamento parcial estratéxico, se converte nunha molécula activa que responde dinamicamente á plantilla PrP^{Sc}, abrindo novas perspectivas para o desenvolvemento de compostos que estabilicen especificamente as rexións vulnerables ou que bloqueen a formación dos oligómeros intermedios, contribuíndo así de forma significativa ao avance na loita contra as enfermidades priónicas.

A identificación de rexións estruturalmente lábeis e intermediarios de conversión relevantes non só avanza na comprensión fundamental da bioloxía dos prións senón que abre vías para o desenvolvemento de intervencións terapéuticas dirixidas a estabilizar o pregamento nativo da PrP^{C} ou interromper os pasos clave de despregamento. A integración destes achados experimentais con modelos computacionais avanzados permitirá construír un modelo atomístico completo da vía de propagación da PrP^{Sc}, esclarecendo a secuencia temporal precisa de eventos conformacionais e establecendo as bases para estratexias racionais contra as encefalopatías esponxiformes transmisibles. En resumo, o estudo do despregamento inducido térmicamente da $BVPrP^{C}$ proporciona unha xanela experimental poderosa sobre os eventos temperáns subxacentes á propagación priónica, destacando a necesidade de despregamento parcial como requisito indispensable para a refoldación guiada pola PrP^{Sc} e enfatizando o papel dinámico da propia PrP^{C} no proceso propagativo. Estes resultados profundizan na mecánica molecular da conversión priónica e establecen un marco conceptual sólido para investigacións futuras sobre a estabilización conformacional e o deseño de inhibidores que bloqueen os pasos iniciais de despregamento, contribuíndo así á loita contra as enfermidades priónicas en humanos e animais.

List of Abbreviations

°C	Celsius degree
Å	Angstroms
%	Percentage
2D	Two-Dimensional
3D	Three-Dimensional
µg	Microgram
µL	Microliter
µM	Micromolar
λex	Wavelength of excitation
λem	Wavelength of emission
2K56	PDB code (Protein Data Bank identifier for a structure)
K	Kelvin
263K	Hamster-adapted prion strain
4RβS	4-rung-β-solenoid
4-mer	Tetramer (a complex of four monomer units)
^{13}C-glucose	Carbon-13-labelled glucose
^{13}C edited TOCSY-HSQC	^{13}C-edited Total Correlation Spectroscopy – HSQC
^{15}N_CEST	^{15}N Chemical Exchange Saturation Transfer
^{15}N_R_1	^{15}N Longitudinal Relaxation Rate (Spin-lattice relaxation)
^{15}N_R_2	^{15}N Transverse Relaxation Rate (Spin-spin relaxation)
^{15}N_NOE HSQC	^{15}N Heteronuclear NOE (Nuclear Overhauser Effect) HSQC Experiment
^{15}N-NH_4Cl	Ammonium Chloride enriched with Nitrogen-15
^{16}R-PrP	Prion Protein mutant or variant with 16-residue
α2	Alpha helix 2
β1, β2	Beta strands 1 and 2

A

Aβ	Amyloid- β
aRML	GPI-anchorless RML prion strain
ATM	Atomic force microscopy

B

BSE	Bovine spongiform encephalopathy
BV	Bank vole
BVPrP	Bank vole prion protein
BMRB	Biological Magnetic Resonance Data Bank
BSE	Bovine Spongiform Encephalopathy

C

C1	C-terminal fragment of PrP^C generated by α-cleavage
C2	C-terminal fragment of PrP^C generated by β-cleavage
cAMP	Cyclic adenosine monophosphate
$CaCl_2$	Calcium Chloride
CB	Conversion buffer
C-BSE	Classical bovine spongiform encephalopathy
CCPN	Collaborative Computing Project for NMR
CD	Circular dichroism
CJD	Creutzfeldt-Jakob disease
CNS	Central nervous system
CSPs	Chemical Shift Perturbations
CSIs	Chemical Shift Indexes
CLEANEX-PM	Clean Chemical Exchange – Phase-Modulated
Cryo-EM	Cryo-electron microscopy
CCSD	Combined Chemical Shift Deviation
CWD	Chronic wasting disease

D

Da	Dalton
DARR	Dipolar assisted rotational resonance
DOSY	Diffusion-Ordered NMR Spectroscopy
DE3	T7 RNA polymerase-expressing E. coli strain
DNase	Deoxyribonuclease
DSS	4,4-Dimethyl-4-silapentane-1-sulfonic acid

E

E. coli	Escherichia coli

EDTA	Ethylenediaminetetraacetic Acid (metal chelator)
EM	Electron microscopy

F

FarUV	Far-ultraviolet (Far-UV circular dichroism spectra)
FDA	Food and drug administration
FD	Folded domain
FFI	Fatal familial insomnia
FSE	Feline Spongiform Encephalopathy
FTIR	Fourier-transform infrared spectroscopy

G

Gdn	Guanidine
GPI	Glycosylphosphatidylinositol
GSS	Gerstmann-Sträussler-Scheinker syndrome

H

H	Hours
H-BSE	H-type atypical bovine spongiform encephalopathy
HC	Hydrophobic core
HR	Hydrophobic region
HSQC	Heteronuclear Single Quantum Coherence
HisTrap FF Crude	Nickel-affinity chromatography column for His-tagged proteins
Hu	Human

I

i.c.	Intracerebral
iCJD	Iatrogenic Creutzfeldt-Jakob disease
IPTG	Isopropyl β-d-1-thiogalactopyranoside

K

kDa	Kilo Dalton
kHz	Kilohertz
kV	Kilovolt
k_{ex}	Kinetic exchange rate

L

L	Liter

LB	Luria Bertoni, bacteria growth medium
L-BSE	L-type atypical bovine spongiform encephalopathy

M

M	Molar
MHz	Megahertz (frequency unit for NMR spectrometers)
mg	Milligram
min	Minutes
MD	Molecular Dynamics
mL	Milliliter
mM	Millimolar
Mo	Mouse
MoPrP	Mouse Prion Protein
MQ	Milli-Q water
MS	Mass spectrometry
ms	Milliseconds
MSE	Mink spongiform encephalopathy
MW	Molecular weight

N

NMR	Nuclear Magnetic Resonance
Ns	Nanoseconds
NPT ensemble	Constant Number, Pressure, and Temperature Ensemble
NOESY	Nuclear Overhauser Effect Spectroscopy

O

OD	Optical density
OD600	Optical Density at 600 nm (used to measure cell density)
on	Overnight
OPR	Open reading frame
OR	Octarepeats

P

PBS	Phosphate-buffered saline
PIRIBS	Parallel-in-register-intermolecular-β-sheets
PK	Proteinase K
PMSF	Phenylmethylsulfonyl Fluoride (protease inhibitor)
ppm	Parts per million

PRNP	Prion protein gene
PrP	Prion protein
PrPd	Disease-associated Prion Protein
PrP^{C}	Cellular prion protein
PrPres	PK-resistant PrP
PrP^{Sc}	Scrapie prion protein

R

RCT	Rotational Correlation Time
recPrP	Recombinant prion protein
Rex	Exchange Contribution to Relaxation (chemical exchange term in NMR)
RML	Rocky Mountain Laboratory prion strain
RNAi	Ribonucleic acid interference
RMSD	Root-Mean-Square Deviation
rpm	Revolutions per minute
RT	Room temperature
RT-QuIC	Real-time quaking-induced conversion

S

s	Seconds
sCJD	Sporadic Creutzfeldt-Jakob disease
SD	Standard deviation
SDS-PAGE	Sulfate Sodium Dodecyl Polyacrylamide Gel Electrophoresis
SEM	Standard error of the mean
SEC	Size Exclusion Chromatography
sFI	Sporadic fatal insomnia
ssNMR	Solid-state nuclear magnetic resonance

T

TBS-T	Tris buffer saline - tween
TEM	Transmission electron microscopy
Tg	Transgenic
TgVole	Transgenic mice bearing bank vole PrP sequence
ThT	Thioflavin-T

TC	Temperature Coefficients
Tris-HCl	Tris(hydroxymethyl)aminomethane Hydrochloride buffer
TSE	Transmissible spongiform encephalopathy
TSEs	Transmissible Spongiform Encephalopathies

V

VCJD	Variant Creutzfeldt-Jakob disease
VT-NMR	Variable-Temperature Nuclear Magnetic Resonance
VT-HSQC	Variable-Temperature Heteronuclear Single Quantum Coherence
VCJD	Variant Creutzfeldt–Jakob Disease

W

WT	Wild type
W/V	Weight/Volume concentration ratio

Table of natural L-Amino acids

Amino acid	Three-letter abbreviation	One-letter abbreviation	Amino acid	Three-letter abbreviation	One-letter abbreviation
Alanine	Ala	A	Leucine	Leu	L
Arginine	Arg	R	Lysine	Lys	K
Asparagine	Asn	N	Methionine	Met	M
Aspartic acid	Asp	D	Phenylalanine	Phe	F
Cysteine	Cys	C	Proline	Pro	P
Glutamic acid	Glu	E	Serine	Ser	S
Glutamine	Gln	Q	Threonine	Thr	T
Glycine	Gly	G	Tryptophan	Trp	W
Histidine	His	H	Tyrosine	Tyr	Y
Isoleucine	Ile	I	Valine	Val	V

Overview of methodology

Technique	Description	Information obtained
CD Spectroscopy	Sensitive to the global secondary structure	Determines the % of secondary structure elements
$^{1}H–^{15}N$ HSQC NMR	Detect amide proton and nitrogen resonances. Residue-level unfolding	Detects localized destabilization
CCSD Coefficient	Temperature study followed by $^{1}H–^{15}N$ HSQC. Thermally induced conformational changes at residue level	Residues with abnormal thermal profile explore alternative conformations
Tc	Temperature study followed by $^{1}H–^{15}N$ HSQC. Thermally induced changes in hydrogen bonding or water accessibility at residue level.	Detects more/less hydrogen bonding or residues hindered more/less from the solvent
CLEANEX-PM $^{1}H–^{15}N$	Detect amide proton and nitrogen resonances. Solvent-exposed residues	Detects more/less solvent exposed residues not involved in hydrogen bonding or hindered from the solvent
^{15}N-R_1, $^{15}N\_R_2$, ^{15}N_NOE relaxation	Residues experiencing conformational fluctuations at a fast rate (ps to ns). Vibrational motions and chain rotations	Detects structurally more/less disordered residues
^{1}H-^{1}H- NOE	The peak-intensity in this type of experiment can be related with the interproton distance	Structural determination of a protein in solution
Chemical Shift Index (CSI)	The NMR chemical shift or frequency of specific backbone atoms (nuclei) in a protein can be correlated with the residue's secondary structure.	Protein secondary structure at the residue level
^{15}N-CEST-HSQC	Residues experiencing conformational fluctuations at an intermediate rate (ms): domain reorientation	Identifies residues that adopt alternative conformations with large-scale amplitude changes
DOSY	Provides self-diffusion coefficient related with the size and mass of protein species	Measures the protein aggregation state
TEM	Aggregate morphology	Confirms final aggregate species
SEC	Size of protein species	Measures the protein aggregation state
Molecular Dynamics (MD)	Theoretical simulation of the changes in the molecular structure as a function of time with a full atom coordinates description	Exploration of the protein's conformational landscape at a specific temperature, focusing on its tendency for unfolding and aggregation.

Index

LIST OF TABLES

LIST OF FIGURES

Note: All figures presented in this thesis were prepared by the author unless otherwise stated in the corresponding figure legends; referenced materials are reproduced under free licenses.

1. INTRODUCTION

1. INTRODUCTION TO PRIONS

Prions represent a separate category of biological agents that are defined as proteinaceous infectious particles, which reproduce by inducing misfolding of the normal host proteins, without nucleic acids (1). This concept, which apparently invalidated the central dogma of molecular biology, was initially established when infectious activity was found to persist even after treatments that destroy nucleic acids, meaning protein alone was able to transmit biological information (1) Unlike viruses, bacteria, fungi, or parasites, prions lack DNA and RNA and rather employ a self-templating mechanism of conformational change to transmit their infectious state (2). Given that prions have also the potential to function as heritable, epigenetic determinants in fungi and yeast, prion nomenclature has been broadened outside of mammalian systems to encompass similar protein-mediated inheritance phenomena (3).

Therefore, prions are now more appropriately characterized as biological principles demonstrating how the structure of a protein alone may encode and transmit biological information, not just as etiologic agents for disease (3,4). In addition, the prion phenomenon's diversity and complexity are evidenced by finding that one polypeptide sequence may give rise to multiple self-sustaining conformations, or "prion strains" (5). These discoveries remind us once again that prions represent a new biology paradigm that suggests proteins not only can serve as informational carriers in a manner previously determined only by nucleic acids (1,4).

In mammals, prion diseases result in transmissible spongiform encephalopathies (TSEs), which are progressive and fatal neurodegenerative disorders. Both humans and animals are susceptible to these deadly, progressive, and currently incurable disorders. These include chronic wasting disease (CWD) in cervids, bovine spongiform encephalopathy (BSE, also known as "mad cow disease"), sheep scrapie, and human Creutzfeldt-Jakob disease (CJD) (6,7) . Originally believed to be caused by a virus, Stanley Prusiner coined the term "prion" to describe an infectious protein (8). The formation of a pathogenic and misfolded state (PrP^{Sc}) from the naturally folded and cellular prion protein (PrP^{C}) is primarily caused by species diversity and conformational changes in prion pathogenesis (6,8).

PrP^{C} consists of two domains, one, ~23-120 is disordered, while the other, ~121-231 is folded. The folded domain (FD), whose structure was resolved in 1996 by Riek et al. using solution NMR(9) is made up by three α helices and two short β-strands (*vide infra*). With two facultative N-linked glycans and attached to the cell membrane by glycosylphosphatidylinositol (GPI), PrP^{C} is a membrane-associated protein (10,11) . The misfolded isoform (PrP^{Sc}), on the other hand, is rich in β-sheet secondary structures, partially resistant to proteinase K, and insoluble in detergents. PrP^{Sc} can serve as a template thanks to its atypical shape, which promotes the

conversion of PrP^{C} into more PrP^{Sc}. PrP^{Sc} builds up and becomes more pathogenic as this self-propagating mechanism develops (12,13).

During the conversion of PrP^{C} to PrP^{Sc}, the normal fold of the protein gets disrupted. Namely, the α-helical regions to turn into β-sheet-rich structures (6,14) . We now understand that this self-propagating process is a key part of prion diseases and other neurodegenerative conditions that show "prion-like" spreading of misfolded protein aggregates, like Parkinson's and Alzheimer's diseases (15).

For decades, the study of infectious PrP^{Sc} was limited by its insolubility and variability. This made it difficult to use direct or high-resolution (16). In turn, this hampered an understanding of prion propagation.

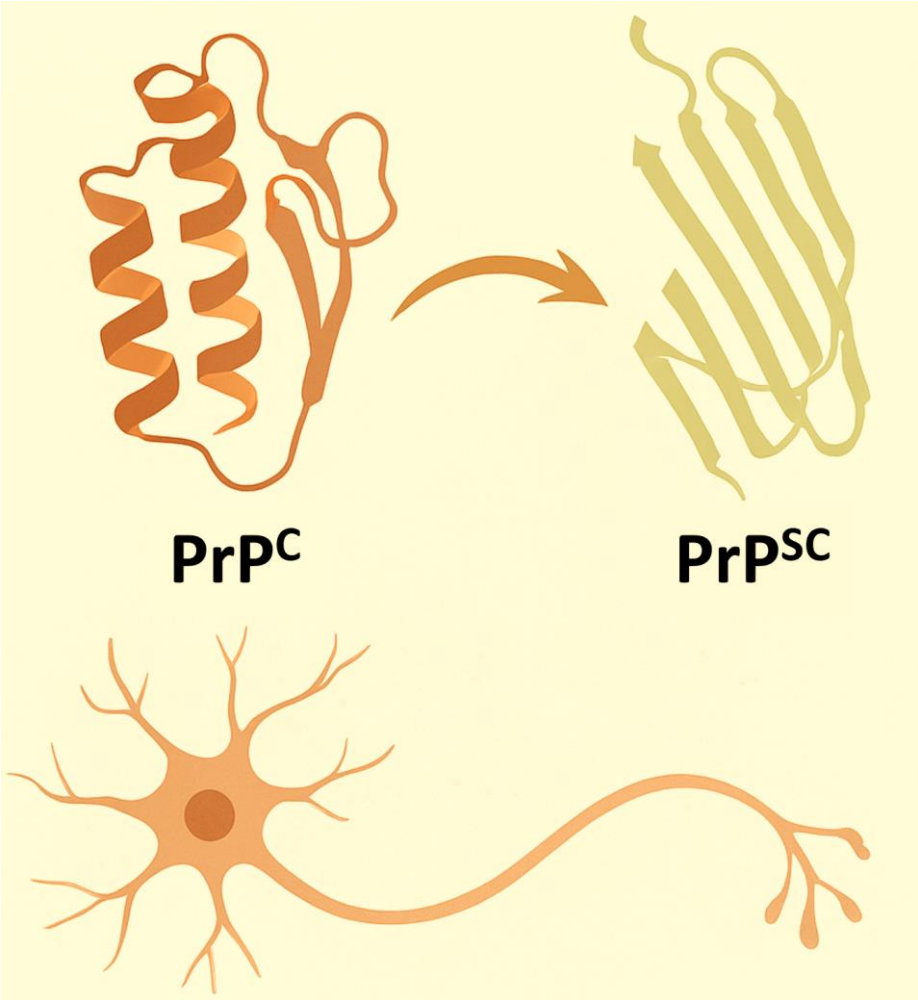

Figure 1 Schematic of the initial stage of misfold conversion of PrP^{C} to PrP^{Sc} in neurodegenerative diseases.

1.1 PRION DISEASES

Neuroscience, public health, and veterinary medicine focus on prions because of their unique way of spreading, ability to infect various species, and potential to cause death (17,18) . The molecular mechanism behind prion disease involves PrP^{Sc}. This conformer causes normal PrP^{C} to change into the same abnormal shape. Without nucleic acids, this process multiplies the amount of infectious agent (19–21). The existence of different prion strains complicates the situation. These strains of PrP^{Sc} vary in their incubation times, patterns of brain damage, and the species they infect, even though they have similar amino acid sequences (22–24).

Significant challenges in diagnosis, treatment, and biosafety are that prions are resistant to standard detergents and decontamination techniques and the absence of an immune response to prion infections (25,26). Several different prion diseases occur in humans. Each has its own pathological, and clinical features. Creutzfeldt-Jakob disease (CJD) is the most common form and affects about one to two people per million each year. Several unique prion diseases in humans displays their own discrete pathological, clinical, and genetic features. They may show up as iatrogenic, genetic, sporadic, or infectious forms (27,28). While genetic CJD is caused by mutations in the PRNP gene, sporadic CJD arises spontaneously and considers for the vast majority of cases (29,30).

Human-derived growth hormone preparations, dura mater grafts, or contaminated surgical instruments have all resulted in iatrogenic transmission (31,32). Another iatrogenic prion disease is variant CJD caused by blood transfusions from patients who had undiagnosed vCJD at the time of donation, of which there have been four reported cases of probable transfusion-associated vCJD identified in the UK surveillance system (33).

However, most cases of vCJD are associated with eating food containing the BSE agent during the BSE epizootic of the 1980s and 1990s, with over 230 cases reported worldwide since the disease was first recognized. Variant CJD affects younger patients more prevalently, with a median age of onset of approximately 28 years compared with classic CJD (34).

Prior to developing dementia and neurological decline, these patients exhibit severe mental illnesses and sensory symptoms (18,28). One of the other human prion diseases, which is considered a rare autosomal dominant disorder, is Gerstmann-Sträussler-Scheinker syndrome (GSS), which causes of this rare autosomal dominant disorder that contains PRNP mutations can be characterized by advanced cerebellar ataxia, dementia, and aggregation of amyloid plaque (29,30,35). Fatal familial insomnia (FFI) represents a D178N mutation in PRNP, associated with methionine at codon 129. It is marked by severe sleep issues, problems with the autonomic nervous system, and rapid neurodegeneration focused in the thalamus (29,36,37).

Moreover, variably protease-sensitive prionopathy (VPSPr) was recognized as an uncommon form of sporadic prion disease in humans, characterized by distinct biochemical patterns, such

as the partial sensitivity of the abnormal prion protein PrP^{Sc} to protease digestion, abnormal accumulation patterns of the prion proteins, and relatively slow progression rates compared to those in classical sporadic CJD. The known phenotypic and molecular variability of the prion diseases in humans is further increased by the existence of the new condition, which mainly occurs in the elderly population (29,38,39).

Kuru, which used to only affect the Fore people of Papua New Guinea in the 1950´s to 1980´s spread through ritualistic cannibalism. It provided essential evidence of the contagious nature of prions (40,41). Kuru is still important for prion research, even though it is essentially gone now.

Many non-human mammals can also get prion diseases, which can be bad for farming, the environment, and public health. Scrapie, which was first found over 250 years ago, affects sheep and goats. The primary symptoms are intense itching, behavioral alterations, impaired coordination, and weight reduction (42,43).

The appearance of bovine spongiform encephalopathy (BSE), also called mad cow disease, was in the United Kingdom in the 1980s, and transmission to humans as vCJD, already mentioned, counts as a significant public health tension (17,22). Another prion disease is contagious in deer, elk, and moose is Chronic wasting disease (CWD) which can spread easily and persist in the environment (44,45). Infected animals recognized with the symptoms of neurological problems, act strangely, and slowly lose weight, and the outbreaks of CWD over North America and Europe has raised concerns about its zoonotic potential (46–48).

Another type of prion disease which can be transmitted through infected food is Transmissible mink encephalopathy (TME) and additional animal prion infection, Feline spongiform encephalopathy (FSE) can be transmitted through contact with the BSE agent. The risk of prion diseases spreading to humans confirms the importance of observing and prevention endeavors .The BSE crisis demonstrated that prions can move between species and cause serious illnesses in humans (22,28,49). Although chronic wasting disease (CWD) has not been reported to be spread to humans, experiments showing infection in nonhuman primates raise serious concerns about potential future cases (47,48)
The zoonotic potential of prion diseases highlights the need for continuous monitoring and prevention strategies. The BSE crisis showed how prions can cross species barriers and cause severe human disease (22,28,49).

1.2 Structural Characteristics and Models of PrP^{C} and PrP^{Sc}

As mentioned, two distinct isoforms exist for the prion protein: the “cellular” isoform of the prion protein (PrP^{C}) and the misfolded “scrapie” conformer (PrP^{Sc}) (50,51). Although sharing the same amino acid sequence, they feature extreme differences in secondary, tertiary, and

quaternary structures, which make them different with respect to solubility, protease resistance, and aggregation (52,53) . PrP^C is a GPI-anchored glycoprotein expressed on neuronal membranes and many other cell types. It has an N-terminal disordered region and a C-terminal globular domain (FD), as shown in (**Fig. 2**).

The PrP^C protein consists of an N-terminal intrinsically disordered domain (residues ~23–120 in human PrP), which includes regions important for metal binding and cellular signaling, and a C-terminal globular folded domain (FD). The FD contains three α-helices and two short β-strands connected by loops and coils, forming a stable tertiary structure. While the residue numbers refer to human PrP, the FD architecture is highly conserved across mammalian species, including mouse, hamster, cattle, and cervids, allowing generalization of these structural features. The flexible N-terminal domain and structured FD together provide a scaffold for membrane anchoring, solubility, and protease sensitivity, and serve as the template for conversion into PrP^{Sc} (51,53–55).

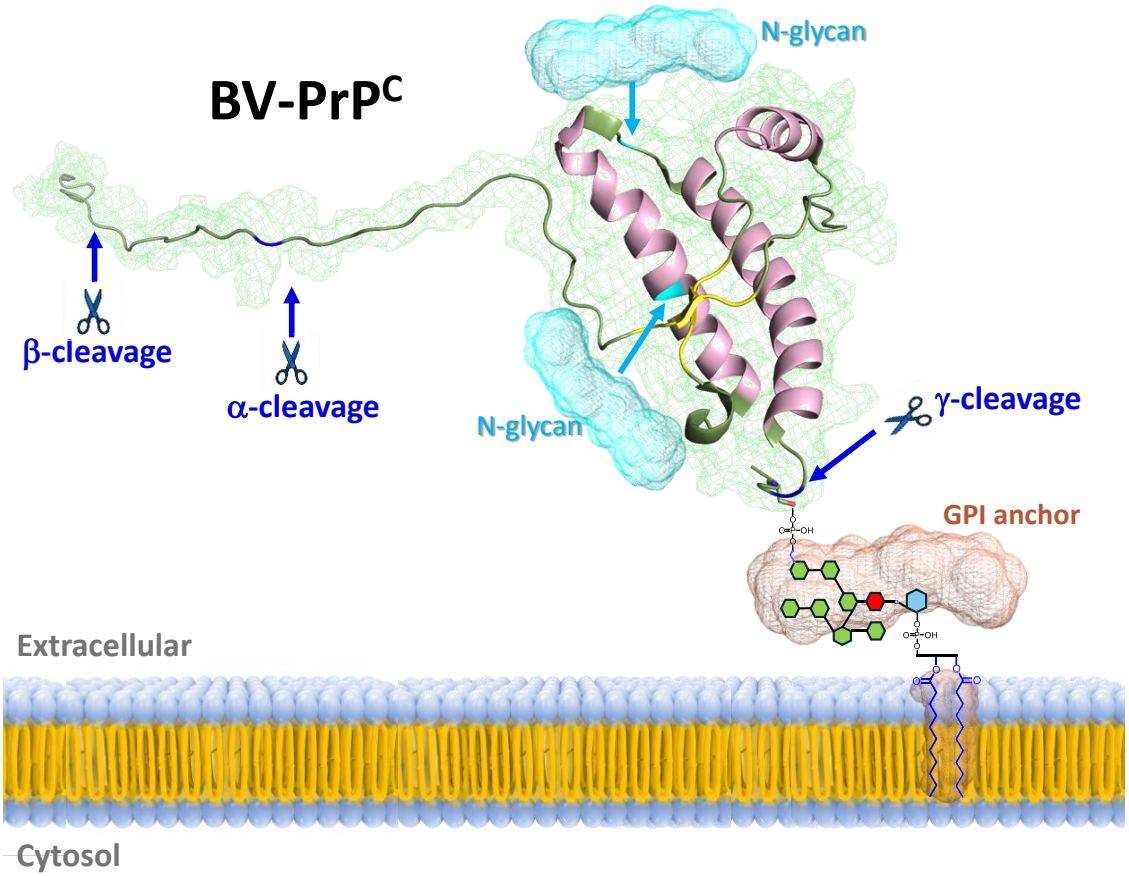

Figure 2 Cartoon of membrane-anchored Bank-Vole cellular prion protein ($BVPrP^C$). The coordinates of the disordered N-terminal region and the Folded Domain (FD) are based on the published structure (PDB: 2K56) and represented together with the two N-glycosidic sites and main physiological proteolytic cleavage sites.

On the other hand, PrP^{Sc} undergoes an extensive structural post-translational refolding with increased content of β-sheet and reduced α-helical structure (13,56). The resulting conformation has partial protease resistance, insolubility, and an overwhelming tendency to form amyloid-

like fibrils (57,58). It has proven challenging to describe the precise atomic-level structure of PrP^{Sc} because it is heterogeneous and insoluble. While from early on it was clear that PrP^{Sc} contained a substantially higher proportion of β-strand secondary structure, based on Fourier Transform Infrared Spectroscopy (FTIR) measurements, and that PrP^{Sc} formed amyloid fibrils, many different and highly incompatible theoretical structural models were put forward (59).

However, as more indirect experimental constraints continued to accumulate, many of these were gradually abandoned. For example, limited proteolysis studies (60) demonstrated that no significant α-helical secondary structure remained in PrP^{Sc}, contrary to earlier misinterpretation of FTIR absorption bands (59). This led to a consensus that PrP^{Sc} necessarily was a succession of short β-strands connected by short coils, with individual PrP^{Sc} subunits stacked to form an amyloid protofilament with the characteristic cross-β architecture (59). As to the specific disposition of the β-strands and connecting short coils, two hypotheses emerged, eventually leading to two final contending PrP^{Sc} models. One suggested that PrP^{Sc} fibrils might feature parallel-in-register intermolecular β-sheets (PIRIBS) (**Fig. 3A**), so that each PrP^{Sc} subunit was flat, with all β-strands and coils in the same 4.75 Å plane (61). This model was championed by Caughey and collaborators, based on recombinant PrP fibrils made *in vitro*. These usually take on PIRIBS-based shapes and show resistance to proteases; however they lack infectivity compared to real brain-derived prions (61–63), The other, that each PrP^{Sc} subunit was a four-rung β-solenoid (4RβS) (**Fig. 3B**), with β-strands and coils spiralling along four 4.75 Å layers (64). In this case, the stack of 4RβS subunits would be a thinner protofilament, and a typical fibril would consist of two intertwined protofilaments. Such model was championed by the Requena and Wille groups, and it was based on earlier low resolution 2D crystallography-based models developed by Wille, Prusiner and coworkers (65,66) .

Each one of these two proposals had their pros and cons, as extensively discussed in a historical roundtable at the 2018 International Prion Conference celebrated in Santiago de Compostela (67).

The first high-resolution structures of fully infectious prions became available shortly thereafter due to momentous advances in cryo-electron microscopy (cryo-EM). Thus, the Caughey group published in 2021 the atomistic structure of the hamster-adapted 263K prion strain, definitively showing that it consists of helical fibrils made of stacked PrP monomers (residues ~95-227) arranged in a PIRIBS pattern (**Fig. 3A**). These fibrils have GPI anchors and glycans asymmetrically attached (68). Shortly thereafter, to show the structural differences among strains, Manka and colleagues reported the structures of wild-type mouse RML prions (69), and even more recently, of the murine 22L and ME7 PrP^{Sc} strains (70). Hoyt et al. in turn independently described the structure of GPI anchorless RML PrP^{Sc} (71), that is identical to the structure reported by Manka et al. More recently, the structure of CWD PrP^{Sc} has also been reported (72). These findings reveal what lies behind disease characteristics, transmission barriers, and strain specificity (73).

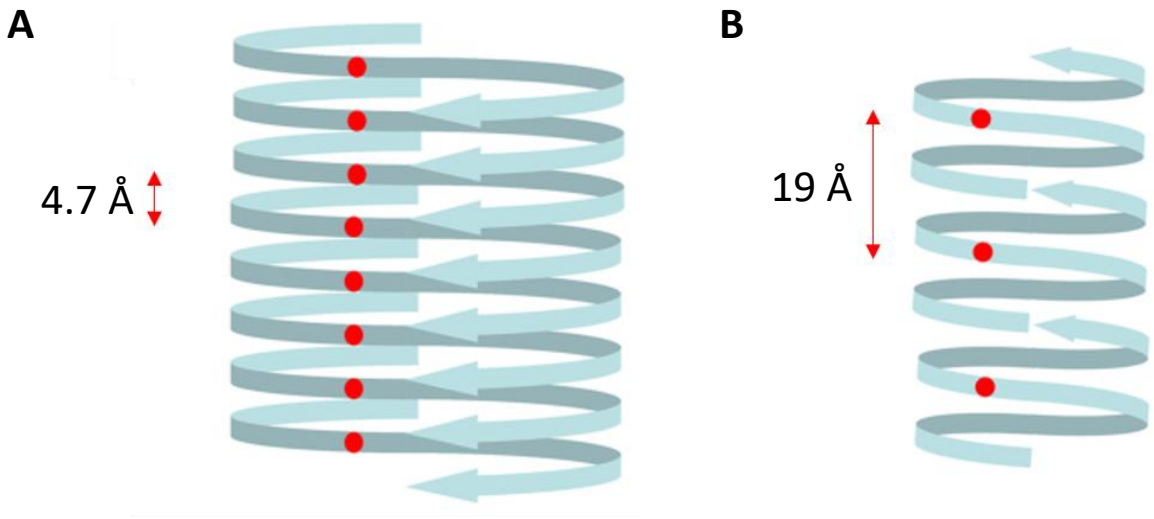

Figure 3 Structural arrangements of PrP^{Sc} monomers in prion fibrils. A) Parallel In-Register β-Sheet stack (PIRIBS) and **B)** β-solenoid stack. The red dots mark identical residues in each monomer, highlighting the different distances in the two arrangements. Adapted from (Shewmaker, 2009)(74), under Creative Commons CC-BY license).

1.3 The paradox of PrP^{C}-templated conversion of PrP^{C} to PrP^{Sc}

Nearly three decades after the atomic structure of the cellular prion protein (PrP^{C}) was elucidated (54), the elucidation of the structure of its pathogenic counterpart, PrP^{Sc}, marks a pivotal moment in prion research. It opens the door to understanding the molecular basis of prion propagation, defined as the conversion of PrP^{C} into PrP^{Sc}, facilitated by pre-existing PrP^{Sc} molecules.

Prion propagation is one of the two defining features defining a prion (8) the other is the ability of PrP^{Sc} to transmit between hosts, typically from the brain of an affected individual to that of a new host. In natural settings, and in the absence of human intervention (e.g., iatrogenic transmission), this inter-host spread usually occurs via the oral route, and its mechanisms have been well elucidated (50,75,76) . Therefore, the main challenge remaining to understand the PrP^{Sc} prion is determining how it catalyzes the conformational conversion of PrP^{C} into the alternatively folded PrP^{Sc} conformation.

Contemplation of PrP^{C} and PrP^{Sc} immediately suggests the first step of conversion: the N-terminal ~23-120 domain of PrP^{C} is intrinsically disordered and the corresponding ~90-120 domain of the templating surface of PrP^{Sc} (68–71), offers an array of unpaired -NH and -CO moieties that are highly predisposed to form hydrogen bonds with -CO and -NH groups in equivalent residues of PrP^{C}. The decrease in entropy resulting from the transition from disordered to cross-β conformation is generously offset by the higher decrease in enthalpy resulting from the extensive array of hydrogen bonds in the newly molded PIRIBS array. This

well-known mechanism commonly referred to as “seeded amyloid propagation” is driven by specific molecular interactions often described as “lock and dock” events (77,78).

However, once the disordered ~90–120 segment of PrP^{C} has adopted the PrP^{Sc} conformation, the remaining FD (residues ~121–231) presents a more complex challenge. This globular region of PrP^{C} comprises three α-helices, two short antiparallel β-strands, and several well-defined connecting loops (9,50,79). The corresponding region in PrP^{Sc} is structurally inert, lacking dynamic features and functions primarily as a passive template. Its role would be limited to capturing segments of PrP^{C} that have already undergone partial unfolding. This templating surface can be likened to a “procrustean bed” (80) , requiring the incoming FD to conform precisely to its extended topology. To achieve this, the FD must first undergo unfolding, a prerequisite for its subsequent refolding into the PrP^{Sc} structure.

Initially, the FD likely remains suspended facing the templating surface, unable to engage until structural rearrangement occurs. Importantly, the FD is a compact, roughly spherical domain composed of two subdomains: β1–α1–β2 and α2–α3, connected by a flexible hinge regions (13) panning residues ~164–168 (9,79), (Suppl. Fig. S2). For successful templating, these subdomains must separate and align with the extended N- and C-terminal lobes of the PrP^{Sc} surface (68,81).

A substantial body of research has investigated the unfolding behavior of PrP^{C} (82–90). Most of these studies have employed elevated temperatures to accelerate unfolding a process that naturally occurs over days so that it can be observed within minutes. However, these investigations primarily focus on spontaneous amyloid formation, which differs from PrP^{Sc}-templated conversion even though both processes are likely to share some mechanistic elements. It is noteworthy that amyloids generated *in vitro* under conditions of simple PrP misfolding *v.g.*, shaking under denaturing conditions, typically have structures with short C-terminal PIRIBS cores that are quite different from those of bona fide PrP^{Sc} (91,92). We are specifically interested in the very early events, before partially unfolded PrP^{C} conformers enter a pathway of spontaneous generation of PrP amyloids that are different from PrP^{Sc}. In other words, we are interested in identifying early events within the PrP^{C} FD that result in partially unfolded conformations that can be trapped by the templating PrP^{Sc} surface in the context of PrP^{Sc} propagation.

Here we describe studies aimed at identifying such early unfolding events, using solution NMR and MD simulations. We compare our data with results from earlier studies and build a tentative timeline of early FD unfolding, which should be a first step for our aim: building an atomistic model of PrP^{Sc} propagation.

2. HYPOTHESIS AND OBJECTIVES

The purpose of this thesis is to elucidate the stepwise unfolding pathway of PrP^{C}, more specifically its folded domain (FD; residues ~121–231), in the context of prion propagation. Its key underlying hypothesis is that its structural destabilization is a prerequisite for its refolding into the infectious PrP^{Sc} conformation.

In contrast to classical views emphasizing active templating by PrP^{Sc}, we propose a "passive templating" model: PrP^{Sc} serves primarily as a structurally inert surface that captures transient, partially unfolded states of PrP^{C}. Thus, the conversion process is driven predominantly by intrinsic dynamics within PrP^{C}, rather than active catalysis by PrP^{Sc}.

To probe this conversion mechanism, the main experimental approach used was variable-temperature (VT) solution NMR spectroscopy. The results obtained were combined with data from a parallel project of the research group based on molecular dynamics (MD) simulations. This dual approach allowed monitoring conformational changes at residue-level resolution, assessing thermal stability.

The central objective was to map the early thermally induced conformational changes of PrP^{C}, identifying regions of elevated lability, candidates to initiate unfolding of the FD.

To achieve this general objective, the following specific (partial) objectives were established:

Objective 1: Characterization of Thermal Dynamics and Early Unfolding Events by VT_HSQC

1. To investigate the conformational dynamics of PrP^{C} under thermal variation using incremental-temperature ^{1}H-^{15}N HSQC (VT-HSQC) spectroscopy.
2. To determine the temperature range over which PrP^{C} maintains full conformational reversibility and to quantify temperature coefficients of the combined chemical shift deviation in both ^{1}H and ^{15}N nuclei (CCSD) for backbone amide groups across residues and identifying potential unfolding hotspots.
3. To calculate temperature coefficients (T_C) from VT-HSQC data to identify residues involved in stable hydrogen bonding or solvent exposure based on temperature-dependent amide proton shifts.

Objective 2: Dynamic Profiling Through NMR Relaxation and Solvent Accessibility

1. To measure ^{15}N_NMR longitudinal (R_1) and transverse (R_2) relaxation rates and use R_2/R_1 ratios to map residue-specific flexibility under thermal stress, generating time-resolved profiles of conformational dynamics and early unfolding transitions.
2. To assess thermal changes in solvent accessibility related to the early unfolding events using CLEANEX-PM experiments.

Objective 3: Identification of Latter Irreversible Structural Transitions

In the course of VT-HSQC studies, unanticipated formation of soluble aggregates was observed at higher temperatures. While such aggregates would be off track in a hypothetical PrP^{Sc}–templated conversion, they contain useful information on relevant partially unfolded conformers trapped in them. Therefore, a set of additional specific objectives were designed when they were detected to tap on the information they offered:

1. To use VT-HSQC spectra as sensitive fingerprints of structural changes under thermal stress, monitoring signal broadening and loss indicative of aggregation or oligomerization. Furthermore, these spectra are also useful to assess the presence (or absence) of recalcitrant residues that exhibit high resistance to unfolding, thereby providing insights into the protein′s structural stability and folding behavior.
2. To employ Diffusion-Ordered Spectroscopy (DOSY) for the determination of diffusion coefficients, enabling differentiation of molecular species by size.

Long-Term Goals:

The long-term goal of this line of research is to build a complete atomistic model of PrP^{Sc}-templated conversion of PrP^{C} into PrP^{Sc}, i.e., of PrP^{Sc} propagation.

3. METHODS

3.1 EXPRESSION AND PURIFICATION OF BVPrP^{C}(90–231)

The coding sequence for Bank vole PrP^{C} (90–231) with the I109 polymorphism (93) was amplified via PCR from genomic DNA and cloned into the pOPINE expression vector, a plasmid from the pOPINE series designed for recombinant protein expression in E. coli (84,85,94–96)

N-terminal 6x-His tag used to facilitate purification was retained for practical reasons, as has been done previously (84,85,94–96). It has been experimentally established that the His6 tag, at the end of the intrinsically unfolded ~90-120 segment, does not influence unfolding of the FD (84).

A single E. coli BL21 (DE3) colony transformed with the expression plasmid (or a frozen glycerol stock stored at –80°C) was inoculated into 50 mL of LB broth in a 250 mL Erlenmeyer flask and cultured overnight at 37°C with orbital shaking at 225 rpm.

The overnight culture was used to inoculate two 500 mL cultures of defined minimal medium in 2 L Erlenmeyer flasks. The composition of the minimal medium was as follows: 3 g/L uniformly labeled ^{13}C-glucose for isotopic labeling, 1 g/L ^{15}N-NH_4Cl for isotopic labeling, 1 mM $MgSO_4$, 0.1 mM $CaCl_2$, 1 µg/mL thiamine, 1 µg/mL biotin, and 100 µg/mL ampicillin. Cultures were incubated at 37°C with shaking at 225 rpm until the optical density at 600 nm (OD_{600}) reached 0.8–1.2.

Protein expression was induced by adding isopropyl β-D-1-thiogalactopyranoside (IPTG) to a final concentration of 1 mM. Cultures were incubated overnight under the same conditions to allow expression of recombinant PrP^{C}. Bacteria were then pelleted by centrifugation for 15min at 5000 g and 4°C, pellets were frozen for 2h at -80°C. Subsequently, bacteria were lysed with 60 mL of lysis buffer for 1h under shaking at 225 rmp and centrifuged 20 min at 20000 g and 4°C to obtain the inclusion bodies containing the expressed protein. Inclusion bodies were then solubilized in the buffer of solubilization of inclusion bodies and centrifuged for 1 h at 20000 g and 4°C.

The clarified supernatant was applied to a HisTrap FF Crude 5 mL column (GE Healthcare, Amersham) pre-equilibrated with equilibration buffer consisting of 20 mM Tris-HCl, 500 mM

NaCl, 5 mM Imidazole and 2 M guanidine-HCl (pH 8.0). Bound His_6-tagged PrP^C (residues 90–231) was eluted with the same buffer supplemented with 500 mM imidazole. Eluted fractions were collected and stored on ice for subsequent refolding and characterization steps. Purified protein fractions were analyzed by SDS-PAGE gels (BioRad), followed by staining with BlueSafe (NZYTech, Lisbon) to assess purity and molecular weight. Guanidine-HCl was added to a final concentration of 6 M for complete denaturation and stored at -80 C until use. Folding of $BVPrP^C$(90-231) was initiated by dialysis against 10 mM sodium acetate buffer (pH 5.0) using 2 kDa cutoff membrane Slide-A-Lyzer™ cassettes with three changes of dialysis buffer, to gradually remove guanidine. Aggregated material was removed by centrifugation at 18000 g for 10 min (Beckman Microfuge 22R).

Protein concentration was determined spectrophotometrically at 280 nm using a molar extinction coefficient of 26,000 $M^{-1}\cdot cm^{-1}$ and a molecular weight of 17.02 kDa (residues 90–231). The protein remained soluble under isotopic labeling conditions, yielding ~5 mg/L of folded protein. It was concentrated as needed using Amicon centrifugal devices and used immediately for structural and functional assays or stored short-term at 4°C. Purity was confirmed by SDS-PAGE, and correct folding was validated by CD spectroscopy and ^1H–^{15}N HSQC NMR.

3.2 Circular Dichroism (CD) Spectroscopy

Circular dichroism (CD) spectroscopy was employed to assess the secondary structure content and thermal stability of the protein in its native and denatured states. This method offers a global, yet rapid, evaluation of conformational changes.

CD samples were adjusted to a protein concentration of 0.7 mg/mL in 10 mM sodium acetate, pH 5. Far-UV CD instruments (180–260 nm): Jasco J-1100 or Jasco715 CD spectropolarimeters. Cuvette path length: 1 mm quartz. Temperature: Temperature ramp from 25 to 85°C in steps of 1°C. Temperature is controlled by a Peltier-controlled system (±0.1°C). Averaging: 12 accumulations per spectrum .CD data as a function of temperature was fitted by SciDavis software to a single-state sigmoidal Boltzmann model to calculate the percentage of unfolding (Eq. 1).

$$Unfolding(\%) = \frac{(A_1 - A_2)}{(1+\frac{\exp(x-x_0)}{dx})} + A_2 \qquad \text{Eq. 1}$$

Fitting parameters derived from Origin software were:

x_0= Midpoint of the transition
A_1= Minimum value
A_2= Maximum value

dx = Time constant

CD data of the naturally folded protein at 25ºC and the same sample after heating at 75ºC and cooling down to 25ºC were measured. The CD spectra were deconvoluted to estimate the changes in % of the secondary structure elements.

3.3 Nuclear Magnetic Resonance Spectroscopy (NMR)

NMR samples of the protein were prepared in high-quality 0.5 mm outer diameter (OD) NMR tubes. The protein concentration was 0.62 mM (corresponding to 5 mg/mL) or 0.17 mM (1.4 mg/mL), consisting of uniformly $^{13}C/^{15}N$ double-labeled or ^{15}N single-labeled protein. The samples were prepared in water with a 10% D_2O for deuterium lock. Samples were prepared at pH 5 by addition of 10 mM sodium acetate buffer and the final sample volume was 500 µL.

All NMR experiments were performed on a Bruker AV-NEO 750 MHz spectrometer equipped with a PA-TXI-HFCN ($^{1}H–^{19}F/^{13}C/^{15}N$) triple-resonance probe featuring a deuterium lock and an automated tuning and matching system. Data acquisition and processing were carried out using TopSpin 4.0.x software.

3.3.1 NMR signal assignment of BVPrP^{C} (90-231)

Experimental part

NMR signal assignment of BVPrP^{C} (90-231) was carried out with a set of double and triple resonance NMR experiments (2*D* ^{1}H-^{15}N Heteronuclear Single Quantum Coherence spectroscopy (HSQC), and the following 3*D* spectra: HNCA, intra-HNCA, HN(CA)CO, HNCO, HN(CO)CA, CBCANH, intra-CBCANH, HNHA, HNCAHA, HCCH-TOCSY, ^{15}N and ^{13}C edited TOCSY-HSQC and ^{15}N and ^{13}C edited NOESY-HSQC were performed at 25 and 45 °C on a $^{13}C/^{15}N$-labeled sample to assign backbone resonances. The spectra were processed with TopSpin and analyzed with CCPN software v3.2 (97) assisted by the chemical shifts reported by Christen *et al*. for BVPrP^{C}(125-231) (79) and deposited under the BMRB accession code *15824*. Additional unpublished chemical shift values at 25°C were kindly provided by Simone Hornemann, University Hospital, Zürich. The ^{1}H, ^{13}C and ^{15}N chemical shifts. The assignment of N-terminal residues 90-124 was assisted by comparison with mouse Q216R-PrP (87).

The canonical list of backbone triple resonance experiments required for de-novo NMR assignment in proteins consists of the following 6 types of spectra: HNCA, HN(CO)CA, HN(CA)CO, HNCO, HNCACB, and HN(CO)CACB or CBCA(CO)NH (98,99).

Conceptual Basis for NMR signal assignment of proteins

A brief description is provided below on the use of HNCA and HN(CO)CA spectra for the assignment of HN, N and CA resonances of of $BVPrP^{C}$(90-231). A description of the assignment of proton signals by combination of ^{15}N edited TOCSY and ^{15}N edited NOESY is also described.

***HNCA*:** this spectrum provides sequential and intra-residue correlations between amide proton (HN) its directly attached nitrogen (N) and the Cα atoms of a given residue (i) and its predecessor (i-1), facilitating backbone assignments. HNCA provides two correlations: Hi/Ni/CAi (strong), and Hi/Ni/CAi-1 (weak) (**Fig. 4**)

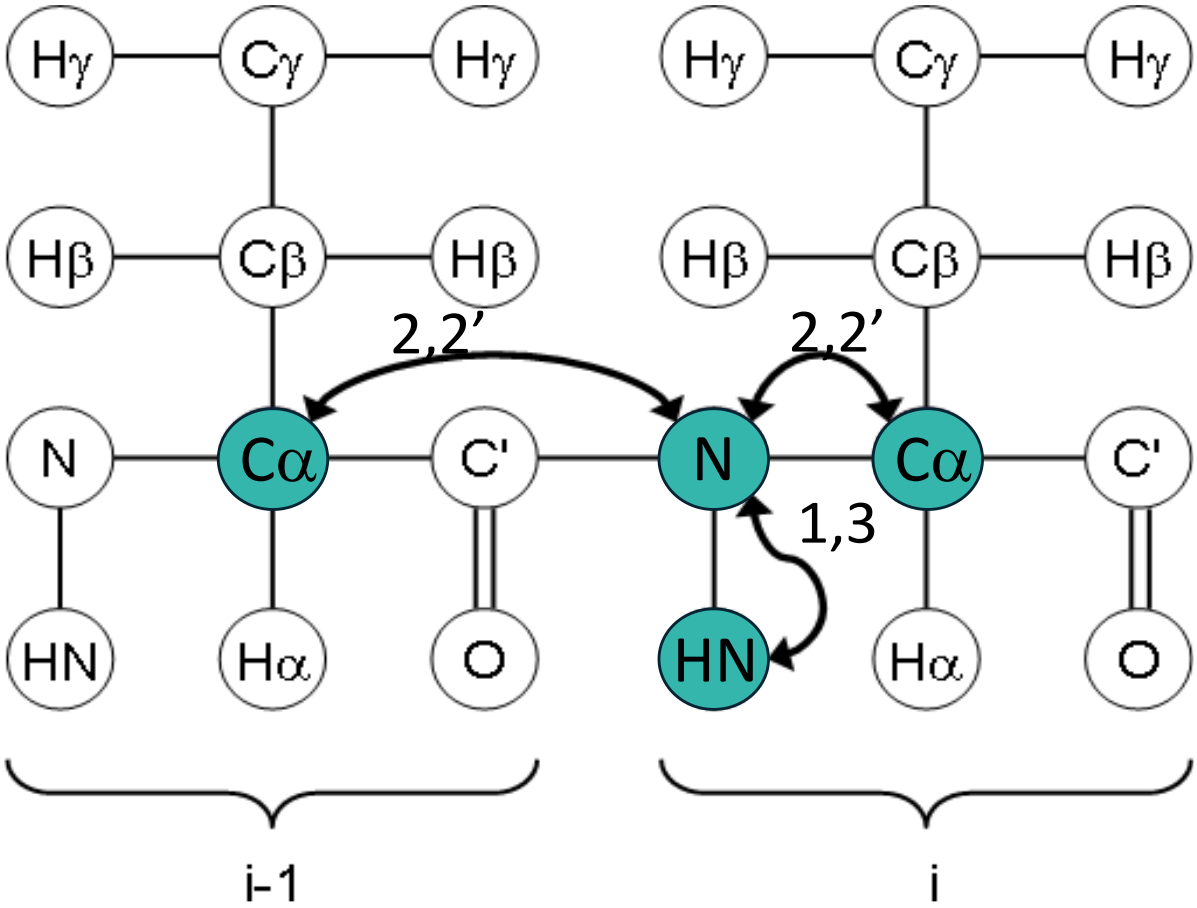

Figure 4. Magnetization pathway in a 3D HNCA spectrum of a peptide. The numbers describe the pathway of the magnetization and the labelling the atoms along the three dimensions of the spectrum. Number 1 is the transfer from NH to N. Number 2 and 2′ represents, respectively, the transfer from N to Cα and from Cα to N. Number 3 is the transfer from N to NH.

HN(CO)CA: this spectrum provides a sequential correlation between amide proton (H) its directly attached nitrogen (N) and the Cα atoms of the precedent residue (i-1) facilitating backbone assignments. HN(CO)CA provides the correlation: $H_i/N_i/CA_{i-1}$ (strong) (**Fig. 5**)

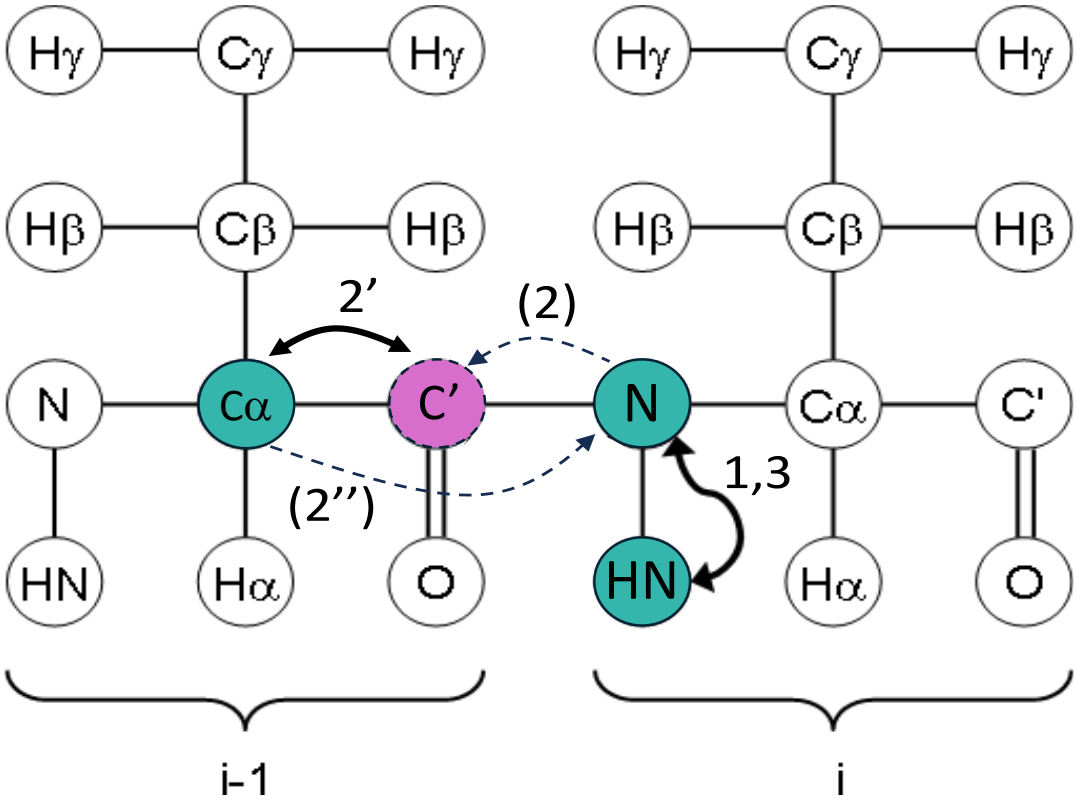

Figure 5 Magnetization pathway in a 3D HN(CO)CA spectrum of a peptide. The numbers describe the pathway of the magnetization and the labelling the atoms along the three dimensions of the spectrum. Number 1 is the transfer from NH to N. Number (2) represents the transfer from N to C' (C' is carbonyl). Number 2′ is the transfer from C' to Cα. Number (2″) is the transfer from Cα to NH. Number 3 is the transfer from N to NH. Numbers with parenthesis do not generate dimensions in the spectrum.

After assigning the backbone atoms, analyzing ^{15}N-edited NOESY and ^{15}N edited TOCSY spectra (3D TOCSY-HSQC_^{15}N and 3D NOESY-HSQC_^{15}N, respectively) enables the assignment of Hα and many side-chain protons. The NOESY cross-peak intensity between two assigned protons is useful because it permits them to deduce their interproton distance. A number of those distances, both intra- and inter-residual, are usually required to deduce the conformational preferences of a protein in solution. The inter-residual proton-proton distances are particularly important for understanding local folding and the organization of secondary and tertiary structural elements. The comparison of these types of distances enables the detection of potential conformational changes in the spatial arrangement of secondary structure elements (e.g. local secondary structure, tertiary contacts, etc.) as result of a change in the experimental conditions such as temperature, concentration, pH, addition or a ligand or cofactor, among others.

3D ^{15}N edited TOCSY: this spectrum involves two key magnetization transfer processes, which can be implemented in either order. From all the protons in the protein, the first step selects only the magnetization of the amide protons (HN) exploiting their direct attachment and scalar coupling to a ^{15}N nucleus. The second is a TOCSY mixing period that enables sequential transfer of the HN magnetization via scalar couplings ($^{n}J_{HH}$, where n is the number of bonds, typically 2 or 3) to other protons covalently attached within the same amino acid residue. Thus,

magnetization propagates initially from a given HN to its adjacent Hα and from there to other protons in the amino acid side chain (e.g. $NH_i \rightarrow H\alpha_i \rightarrow H\beta_i \rightarrow H\gamma_i \rightarrow$ …etc.). This propagation along the network of coupled protons is effectively interrupted whenever a weak vicinal coupling occurs in the side chain (e.g., when $^3J_{HH} < 2.5$ Hz) (**Figs. 6** and **7**).

Notably, all correlations observed in the ^{15}N-edited TOCSY experiment necessarily originate from protons within the same amino acid residue, conferring inherent residue-specificity. This feature is particularly valuable for assigning the Hα and other side-chain protons of that residue.

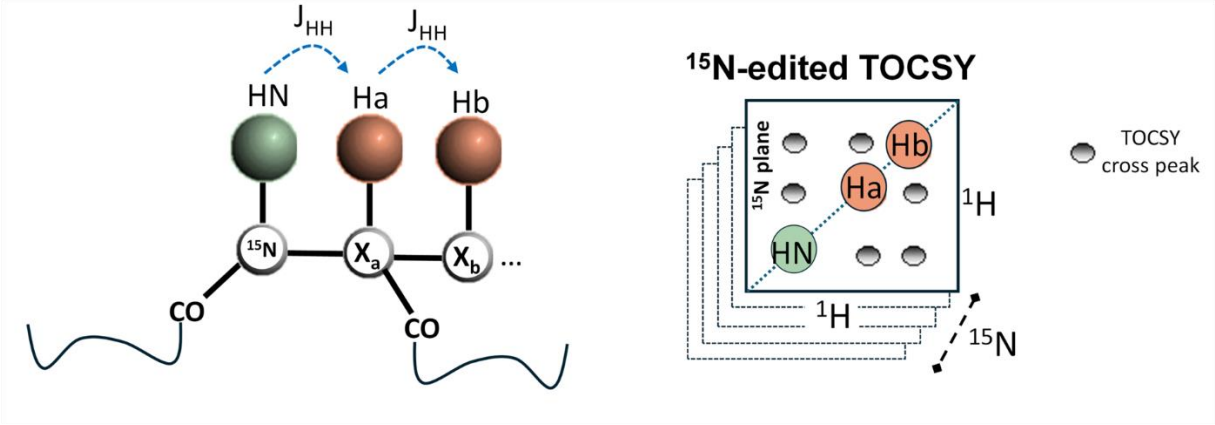

Figure 6 Scheme of the ^{15}N-edited TOCSY experiment. Only protons directly bonded to ^{15}N, such as amide HN, are edited (selected) by the experiment in its third dimension. During the mixing time, a series of TOCSY cross peak between HN and a network of scalar-coupled protons (up to three bonds apart) such as Ha, Hb is generated. Ha, Hb can be any proton in the molecule, it is not required to be directly attached to a ^{15}N nucleus.

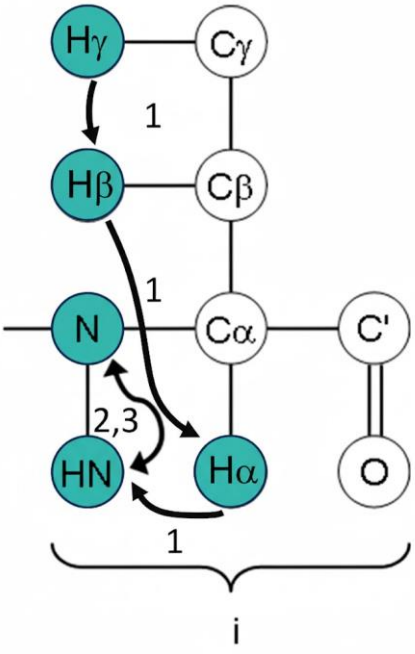

Figure 7 Magnetization pathway in a 3D ^{15}N-edited TOCSY spectrum of a peptide. The numbers describe the pathway of the magnetization and the order of the labelling of the atoms in each of the three dimensions of the spectrum. In dimension 1, all the protons in the same network of couplings (e.g. HN, Hα, Hβ and Hγ in the residue of the figure) appear. Dimensions 2 and 3 correspond to the two dimensions of N_HSQC. All the correlated nuclei by this experiment belong to the same residue.

3D ^{15}N edited NOESY: this spectrum provides structural information through cross-peaks whose intensities are modulated by the nuclear Overhauser effect (NOE), arising from through-space dipolar relaxation between interacting nuclei (e.g., protons) and scaling inversely with the sixth power of their internuclear distance (r^{-6}). This effect thus reflects the spatial proximity of the protons.

The ^{15}N-edited NOESY experiment involves two key magnetization transfer processes, which can be implemented in either order. From all the protons in the protein, the first step selects only the magnetization of the amide protons (HN) exploiting their direct attachment and scalar coupling to a ^{15}N nucleus. The second process is the NOESY mixing period, during which through-space dipolar relaxation transfers magnetization from the initially selected HN proton to surrounding protons, generating cross-peaks of sufficient intensity only for those in close spatial proximity (typically <5 Å) (**Figs. 8** and **9**).
Analyzing the NOEs of a protein yields multiple NOE interproton distances, enabling determination of the 3*D* structure of the protein in solution.

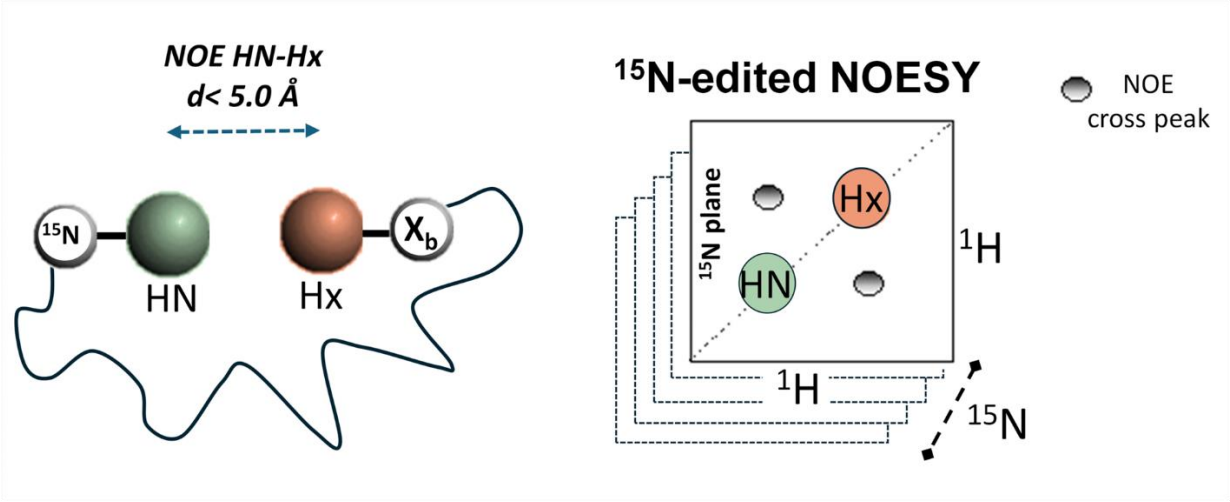

Figure 8 Scheme of the ^{15}N-edited NOESY experiment. Only protons directly bonded to ^{15}N, such as amide HN, are edited (selected) by the experiment and it is the nucleus (atom) that originates the NOE during the mixing time. A NOE cross peak between HN and a nearby proton Hx is observed when Hx is in proximity (d < 5.0 Å). Hx can be any proton in the molecule, it is not required to be directly attached to a ^{15}N nucleus.

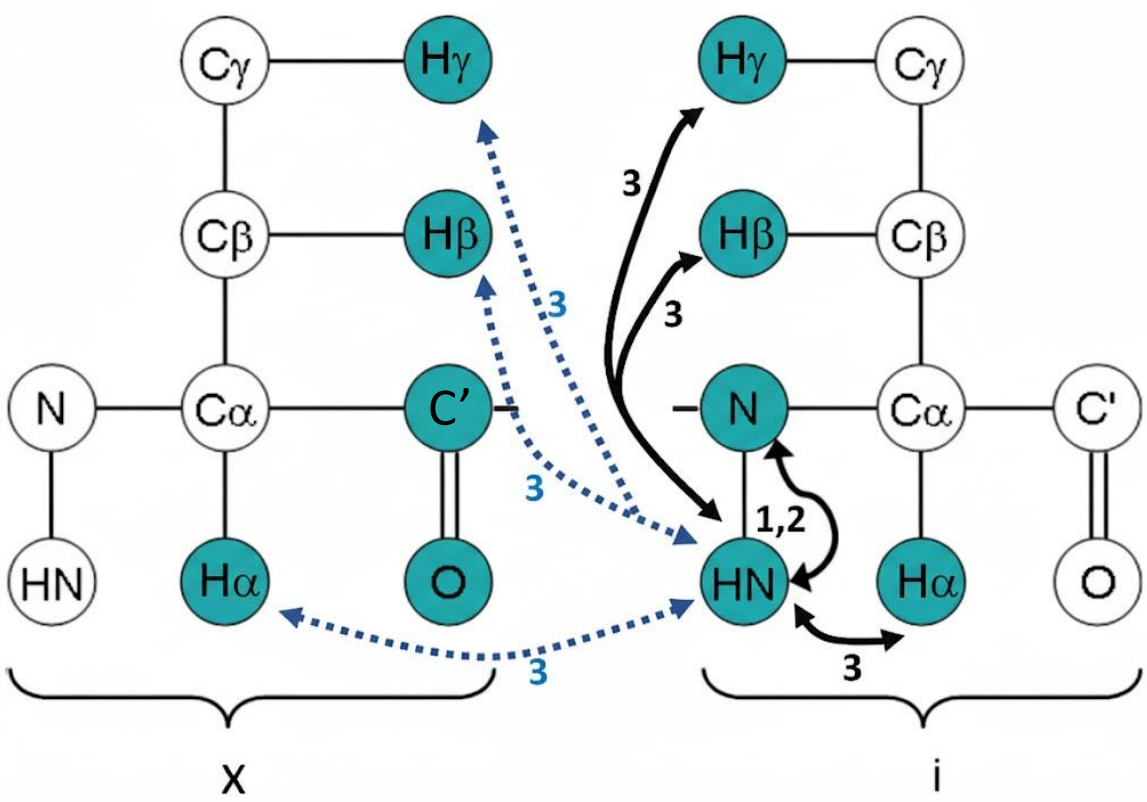

Figure 9 Magnetization pathway in a 3D ^{15}N-edited NOESY spectrum of a peptide. The spectrum detects ^{1}H-^{1}H NOEs between the amide proton of a residue i and other protons of the proteins located in the same or any other residue (x) of a protein. The numbers describe the pathway of magnetization and the order of the labelling the atoms in the three dimensions of the spectrum. The numbers 2 and 3 correspond to the two dimensions of N_HSQC. The protons in dimension 1 are either intra-residue (black arrows) or inter-residue (blue stripped arrows) located at a distance up to a maximum of ca. 5 Å from the amide proton of residue i.

3.3.2 Variable Temperature study of BVPrP^{C}(90-231) by ^{1}H–^{15}N HSQC (VT N-HSQC)

Experimental part

VT N-HSQC spectra were acquired at the following eight temperatures: 15, 20, 25, 30, 35, 40, 42.5 and 45°C. Each spectrum was referenced using 2,2-dimethyl-2-silapentane-5-sulfonate (DSS) as primary reference or the acetate signal of the buffer as secondary reference, and chemical shift changes for each amide proton-nitrogen (HN) cross-peak were tracked across the temperature range. The assignment of N and proton HN resonances at each temperature was carried out by tracking peak drift in the series of VT N-HSQC spectra. The spectra were processed with TopSpin and the peak positions were analyzed using MestreNova software (Mestrelab, Inc.).

3.3.3 Temperature coefficients (T_C) for the detection of hydrogen bonds

Experimental part

Temperature coefficients were determined by analyzing the chemical shift of the amide proton (100) of each residue in the series of VT N-HSQC spectra from 15 to 45ºC. The proton NH chemical shift versus temperature for each amino acid was linearized by fitting to an analogue equation to Eq. 3 using Excel software, and the temperature coefficient (T_C, in ppb/K) was taken from the slope. T_C values were plotted along the BVPrP^C(90-231) sequence. Residues with T_C between 0 and -4.6 ppb/K were interpreted as participating in stable hydrogen bonds or being buried within the protein core, whereas values of T_C were more negative than -4.6 ppb/K indicated solvent exposure or dynamic behavior. Large positive T_C >+4.6 ppb/K, were interpreted as temperature-induced conformational change and increased average distance between amide proton and an aromatic ring upon heating (101,102).

3.3.4 Combined Chemical Shift Difference (CCSD) to detect early unfolding events

Experimental part

The ^{1}H and ^{15}N drift of a peak in the N-HSQC spectrum at a certain temperature of the series from 15 to 45 ºC was analyzed by the Combined Chemical Shift Difference (CCSD) (87,103) parameter given by Eq. 2:

$$\mathrm{CCSD} = \sqrt{(\Delta\delta^{\mathrm{HN}})^2 + (\Delta\delta^{\mathrm{N}}/5)^2} \qquad \text{Eq. 2}$$

Where $\Delta\delta^{\mathrm{HN}}$and $\Delta\delta^{\mathrm{N}}$is, respectively, the change in ^{1}H and ^{15}N chemical shift respect to the reference values of the spectrum acquired at the lowest temperature of the series. Factor 5 in the denominator of (Eq. 2) is used to account for the fact that nitrogen shifts are spread over a much larger range than proton shifts. CCSD of a given amino acid respect to temperature was linearized and the residual were plotted against temperature (104,105) .

The experimental CCSD for a specific amino acid at each temperature was linearized using Microsoft Excel by fitting the data to the following equation (Eq. 3):

$$CCSD^{calc} = A + B \cdot T \qquad \text{Eq. 3}$$

Here, CCSD^{calc} represents the calculated linearized CCSD value for each data point, T is the temperature, and A and B are the regression coefficients. The residual error (defined as CCSD - CCSD^{calc}) was calculated and plotted against temperature (104,105) either using SciDAVis software (scidavis.sourceforge.net) or a homemade vibe coded python script based in the matplotlib library. Residues showing linear or non-linear behavior were identified by visually inspecting the plots and quantitatively confirmed through second-order linearization of the residuals (i.e. curvature of the residuals) and calculation of the Root-Mean-Square Deviation

(RMSD) factor. Residues exhibiting RMSD values 1.4 times greater than the mean were classified as having non-linear CCSD. These residues were identified as having the highest tendency to adopt alternative conformations within the temperature range of 15 to 45°C.

Conceptual Basis

This technique enhances traditional Δδ/ΔT measurements by considering the changes in the chemical shift (i.e. Chemical Shift Perturbations) for the combination of amide protons ($\Delta\delta^{HN}$) and amide ^{15}N atoms ($\Delta\delta^{15N}$) of the backbone as result of a change in temperature.

For a protein residue with a single conformation, the amide ^{1}H and/or ^{15}N chemical shifts are expected to exhibit a linear trend with temperature. This arises from the temperature-dependent modulation of chemical exchange between the amide proton and water protons, as well as the influence of temperature on molecular dynamics. Non-linear behavior (curvature) in these shifts suggests the presence of multiple conformational states in equilibrium, impacting the specific residue's backbone and indicating transitions between the native conformation and secondary conformations.

3.3.5 Detection of residues of BVPrP^{C}(90-231) experiencing slow-conformational exchange: peak-intensity study of VT N_HSQC

Experimental part

Peak intensities in the ^{15}N_HSQC spectrum of BVPrP^{C}(90-231) were quantified at each temperature across the range from 15 to 45°C measured in steps of 5°C (or 2.5°C). To improve measurement sensitivity, peak volumes were determined using MestreNova software by integrating the signal within a narrow region centered on the peak maximum, and the resulting temperature-dependent intensities were plotted with a custom vibe coded python script.

Conceptual basis

Under specific experimental conditions, the NMR signal-intensity, defined as the maximum intensity relative to the noise level, depends on the relaxation properties of the nucleus or nuclei generating the peak. The transversal relaxation rate R_2 ($^{15}N\_R_2$ and $^{1}H\_R_2$) of a signal in N_HSQC is inversely related with the peak maximum intensity and its linewidth. For instance, an increase in R_2 broadens the linewidth and reduces the intensity, while the total signal area remains unchanged. In general, an increase in temperature enhances molecular mobility, which reduces the transverse relaxation rate (R_2) and thereby increases signal intensity. However, for exchangeable protons such as amide HN protons, higher temperatures also weaken hydrogen bonds and accelerate the rate of chemical exchange with solvent water. This exchange contribution adds to R_2 (as R_{2ex}), causing additional line broadening that often dominates and leads to a net reduction in signal intensity.

In presence of conformational exchange, the experimental transversal relaxation (R_2^{exp} for ^{1}H or ^{15}N) is the sum of the pure dipolar relaxation component (R_2^0) of the ^{15}N-^{1}H amide and an

additive exchange term (R_{2ex}). Specifically, $R_2^{exp} = R_2^0 + R_{2\text{ex}}$. Both terms R_2^0 and $R_{2\text{ex}}$ are temperature dependent.

The signature of slow conformational exchange for the temperature evolution of the cross-peak intensity is a U-shaped profile like the plot represented in (**Fig. 10**) taken from the paper of (106).

To understand the U-shaped profile of **Fig. 10** it is useful to disregard for a moment the effect of water-HN exchange with temperature (which simply tends to reduce peak intensity) and consider only the spectral effects for a dynamic equilibrium of interconversion between two conformations A and B that experience different magnetic environments (i.e. chemical shifts). The exchange rate k_{ex} (s^{-1}), which increases with the temperature, of the equilibrium determines the aspect and intensity of the signals the spectrum as can be seen in the simulation of **Fig. 11**.

When conformational exchange (i.e., interconverting equilibrium between conformers) is considered, the equilibrium rate k_{ex} relative to the difference of frequency of the signals affects both the appearance and intensities of the signals involved. These effects for two-site conformational exchange are illustrated in the simulation shown on **Fig. 11**. It can be seen in this figure that in the slow-exchange regime ($k_{ex} \ll \Delta\nu$), where the exchange rate is much slower than the frequency difference between the two sites, distinct signals are observed for each conformation, with intensities proportional to their respective populations. In the fast-exchange regime ($k_{ex} \gg \Delta\nu$), a single sharp signal appears at the population-weighted average chemical shift, with intensity equal to the sum of the two individual contributions. In the intermediate-exchange regime ($k_{ex} \approx \Delta\nu$), the signals are broadened and distorted, appearing at an intermediate position with significantly reduced peak intensity. The minimum intensity occurs at the coalescence point, where the two signals completely merge into a single peak with the maximum broadness (lowest intensity).

The U-shaped intensity profile shown in **Fig. 10** is consistent with this behavior of increasing the conformational exchange starting from the high intensity in the intermediate or slow-exchange regime (280 K), decreasing through the intermediate regime to a minimum at coalescence (300 K), and then increasing again as the system enters the fast-exchange regime (305 to 318K). This interpretation can be extended to water-exchangeable protons, as the reversal of slope, from negative to positive, in the U-shaped profile cannot be plausibly accounted for only by HN-water chemical exchange and the change in the molecular mobility.

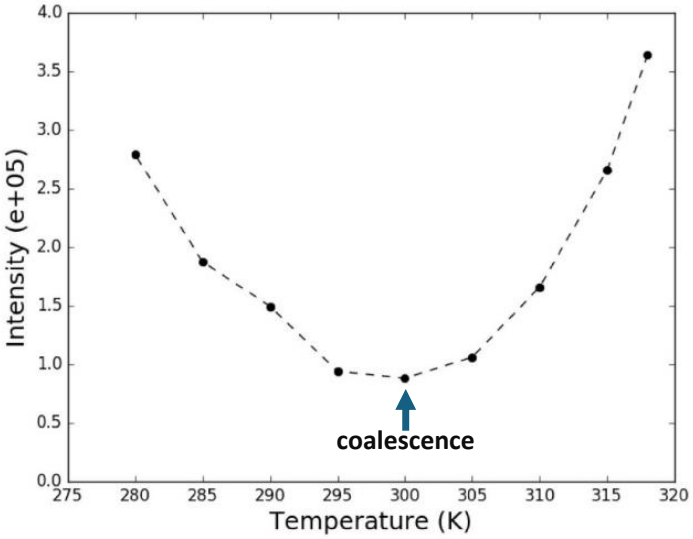

Figure 10 Temperature-dependent N_HSQC intensity profile revealing conformational exchange in a protein. The figure is for residue S13 of *Naja naja atra* chymotrypsin inhibitor protein and it was taken from the paper of Lin et al. (106). At the lowest temperature of 280 K, essentially a single conformer is populated, yielding a sharp signal with maximum intensity. As the temperature is raised to 300 K, multiple conformers become populated in slow exchange (on the chemical shift timescale), leading to progressive signal broadening and a concomitant reduction in intensity. As the temperature is then raised from 300 K to 317 K, the exchange rates among the conformers accelerate, resulting in gradual signal sharpening and an increase in intensity. (This is the fig. 4b adapted from reference Lin 2025(106) autorized for reproduction by creative commons CC-BY licence).

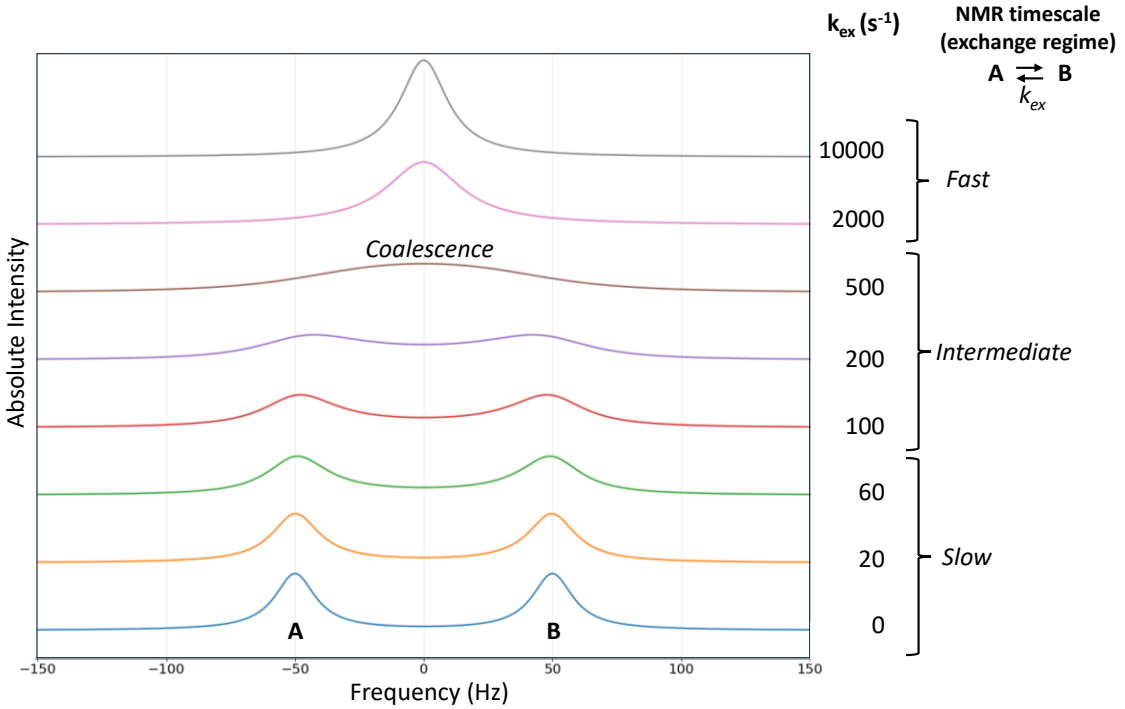

Figure 11 NMR line-shape simulation for the conformational interconverting equilibrium of two species. Two species A and B are simulated with chemical shift difference Δν = 100 Hz, R2 = 60 Hz for both sites and equal populations. As the kex is increased the lineshapes of A and B are affected by the equilibrium. The coalescence occurs at kex ~500 s-1 which is characterized by a single signal that appears in an average frequency position between A and B with the maximum broadness and the minimum intensity.

It is worth noting that, for water-exchangeable protons, an inverted U-shaped intensity profile as a function of temperature does not necessarily indicate slow conformational exchange. An alternative explanation involves a two-step mechanism: an initial increase in signal intensity due to enhanced molecular mobility (which reduces R_2) without a proportional acceleration of HN-water chemical exchange, for example, if the amide proton remains protected by a persistent partial H-bond, followed by a subsequent decrease in intensity as rising temperatures weaken the H-bond and markedly accelerate exchange with solvent water.

3.3.6 Water-Amide proton chemical exchange rate (k_{ex}) and solvent exposure to study early unfolding events

Experimental part

Solvent exposure and hydration changes were assessed using the CLEANEX-PM (Phase-Modulated CLEAN chemical EXchange) experiment (107). CLEANEX-PM spectra were measured at 15, 25 and 45ºC for a U-^{13}C,^{15}N labelled sample of naturally folded BVPrP^{C}(90-231). Samples were studied at 6 mg/ml pH 5. Each spectrum was measured (sequence fhsqccxf3gpph of the Bruker library) with 2048 and 128 points for dimensions ^{1}H (F_2) and ^{15}N (F_1), respectively. The spectral width in F_2 and F_1 was 15.9 and 35 ppm, respectively. The number of scans was 32. At each temperature the spectrum was acquired at the following mixing times: 5, 10, 20, 35, 50, 75, 100, 150 and 200 ms. The measurement time of each spectrum was ca. 1.4 hours. The spectral processing and the cross-peak intensity analysis of each backbone amide were done by MestreNova software and the fitting to (Eq. 4) was done with SciDavis and represented with a homemade vibe coded python script.

At a given temperature, the chemical exchange rate constant (k_{ex}) for a backbone amide proton (HN) with solvent water can be determined by acquiring 2D CLEANEX-PM spectra at a series of mixing times and fitting the initial buildup of water-amide cross-peak intensities to the following exponential function (107,108) (Eq. 4).

$$V(t) = V_0\left(\frac{k_{ex}}{k_{ex}+R_1}\right)\left[1 - e^{-(k_{ex}+R_1)t}\right] \qquad \text{Eq.4}$$

where V(t) is the peak volume in the experiment measured at a mixing time t, V0 is the reference intensity in the HSQC spectrum and R1 is the effective longitudinal relaxation rate during CLEANEX mixing time.

Conceptual basis

The CLEANEX-PM experiment is specific to study water accessibility and exchange. It is based on the initial selective excitation of the water peak (with a nulling by defocusing of all the amide HN protons) which is followed by the transfer of water magnetization to the amide HN protons of the protein via exchange (or spatial proximity) during a certain mixing time (**Fig.**

12). Specifically, it enables the detection of HN amide protons of the backbone that are in rapid exchange with H_2O and to determine the water chemical exchange rate constant (k_{ex}) of the amide residue.

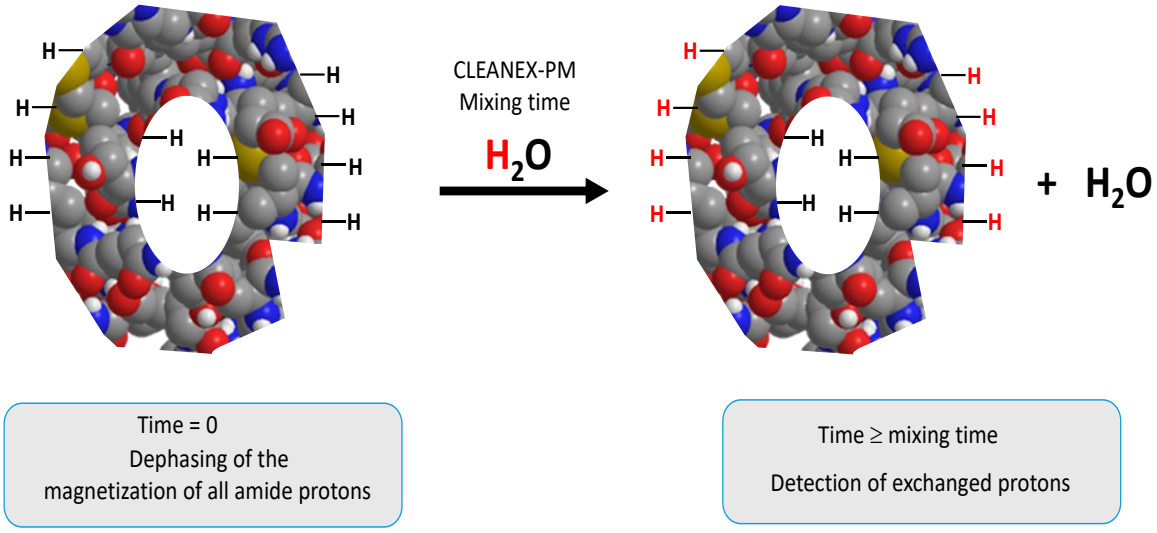

Figure 12 Diagram explaining the basis of the CLEANEX-PM experiment. A folded protein may have NH amide protons with varying degrees of solvent exposure. CLEANEX-PM begins by dephasing all NH amide protons (black color), while leaving the H_2O and other protons unaffected (red color). Dephasing causes the signals of those protons originally attached to the nitrogen of the amide group to be undetected in the spectrum. During the mixing period (typically from 40 to 100 ms), the NH amide groups exposed to the exterior can be replaced by fresh H_2O protons, whereas those in the interior do not exchange or do so very slowly. After mixing, the renewed protons of NH amide groups that were never dephased contribute to the cross-peak in the spectrum (in red).

3.3.7 Study of the changes in the water-accessible area of BVPrP^C(90-231) during early unfolding events: water-T_2 study at variable temperature

Experimental part

The T_2 transverse relaxation time of the water proton signal was measured for a fresh sample of BVPrP^C(90–231) (5 mg/mL, pH 5) and for the post-75ºC heated oligomerized sample of this protein at the same concentration. For comparison, the measurement of T2 was also measured an aqueous sample of the same buffer used for the protein sample preparation. The measurements were done in a Bruker NEO-750 spectrometer (proton frequency of 750 MHz). The spectra were acquired using the CPMG pulse sequence. The CPMG consists on a train of spin-echoes separated by a delay of 10 ms. The following times (t) were explored: 0.3, 0.5, 0.8, 1.0, 1.5, 1.8, 2.0, 2.3, 2.5, 3.0, 3.5, 4.0, 4.5, 5.0, 5.5, 6.0, 6.5, 7.0, 7.5, 8.0, 8.5, 9.0, 10.0, 16.0 s. The spectra were measured with 2 scans and with an inter-scan delay d_1 of 10 s. The FID acquisition time (aq) was 0.68 s and the spectral width was 15.8 ppm. The water-T_2 measurement was carried out at the following temperatures for the fresh and oligomerized protein: 15.0, 20, 22.5, 25, 27.5, 29, 30, 31, 32.5, 34, 35, 36, 37.5, 38, 40, 41, 42.5, 44 and 45 °C. For the buffer sample the temperatures were 15, 20, 25, 30, 35, 40 and 45 °C. Each spectrum was processed and analyzed with MestreNova software. The intensity of the water signal was analyzed and non-linear fit to the three parameters equation (Eq. 5) to determine proton T_2.

$$I(t) = I_0 \cdot exp\left(-\frac{t}{T_2}\right) + I_{offset} \quad \text{Eq. 5}$$

where t is the total time, I_0 is the intensity at time zero and I_{offset} is the intensity offset.

Conceptual basis

In the hydration of a solute, different types of H_2O molecules can be identified based on their residence time when bound to the solute molecule (see figure below). The first hydration shell (water bound layer) consists of H_2O molecules with a long residence time. Residues such as amide NH protons exposed to H_2O that do not form hydrogen bonds undergo chemical exchange with H_2O and exhibit an intermediate residence time. Finally, the bulk solvent H_2O is far more abundant than the solute, resulting in an additional layer of H_2O molecules surrounded by the solvent (H_2O_{bulk}) (**Fig. 13**).

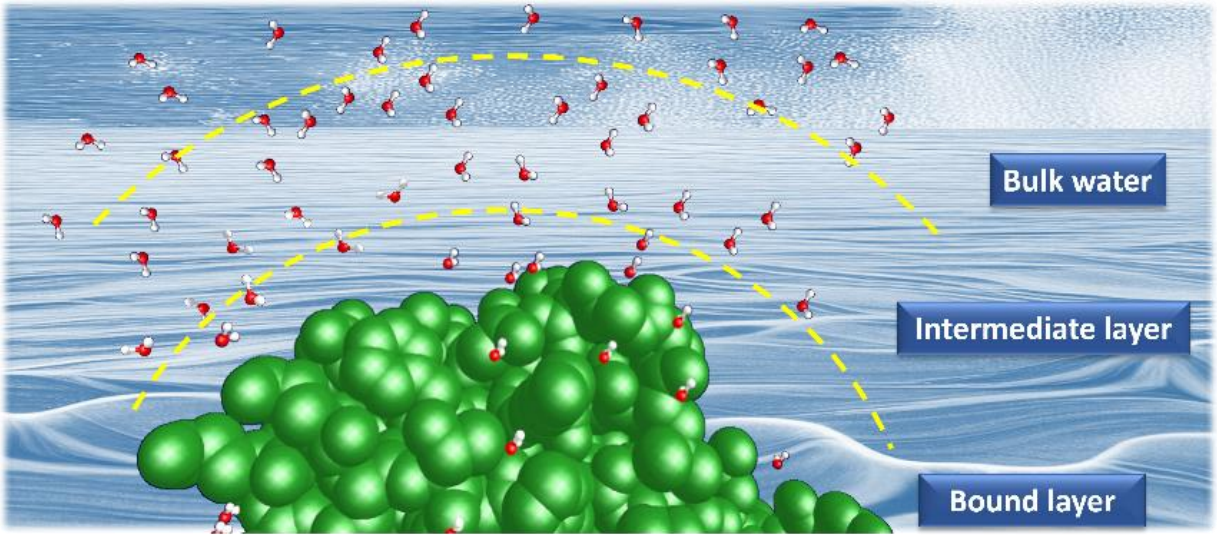

Figure 13 Diagram of binding interaction water-solute. Water molecules experience different interactions with a solute.

In the case of proteins of moderate size in aqueous solvent, the different types of water molecules have substantial differences of mobility and therefore different T_2's and the experimentally observed T_2 is a weighted average of these contributions. In contrast, for proteins of a large size that tend to form aggregates, the contribution from T_2^{bound} can be neglected.

A conformational change in a protein that leads to its structural expansion in size (e.g., oligomerization, formation of protofibrils, and fibrils) tends to increase the surface area and the number of bound waters. The bound water in the first hydration layer is highly compacted and restricted in its rotational motion, so it can be considered to have low kinetic energy and low T_2 (109). In contrast, the bulk water has the opposite properties. When bound water is released

from the protein due to a conformational change, this molecule rapidly adopts the kinetic energy from the free water molecules which is experimentally reflected in an increase in T_2.

3.3.8 Protein dynamics studied by ^{15}N-Relaxation

Experimental part
The following heteronuclear relaxation experiments based in the ^{15}N-HSQC detection (110,111) were measured at 25 and 45°C for the naturally folded monomeric state of the protein at 5 mg/ml, pH 5.

^{15}N_R_1 (Longitudinal Relaxation Rate): (Bruker sequence: hsqct1etf3gptcwg3d). A total of 12 relaxation delays were explored between 20 ms and 1200 ms with 24 scans and d_1 2.0 s.

^{15}N_R_2 (Transverse Relaxation Rate): (Bruker sequence: hsqct2etf3gptcwg3d). A total of 12 relaxation delays with the CPMG block were explored between 15.6 ms and 343 ms with 24 scans and d_1 2.0 s.

Steady-State ^{15}N{^{1}H} heteronuclear NOE (^{15}N_NOE): (Bruker sequence: hsqcnoef3gpsi). The spectrum was measured as a pseudo-3D by acquiring two interleaved 2D N-HSQC spectra collected with (S^{sat}) and without (S^0) an initial proton saturation period (3 s) during the 5 s recycle delay. Both spectra were collected with 24 scans.
For determining ^{15}N_R_1 and ^{15}N_R_2, the intensity of a given cross peak in the N-HSQC correlation at each relaxation delay τ, $I(\tau)$, was measured and the curve was non-linearly fit to the mono-exponential equation (Eq. 6) to determine I_0 and R_x.

$$I(\tau) = I_0 \, exp\,(-\tau \cdot R_x) \qquad \text{Eq. 6}$$

Where R_x refers to either ^{15}N_R_1 or ^{15}N_R_2, and I_0 is the initial intensity at $\tau = 0$.
The ^{15}N_NOE of a given protein cross-peak is determined by measuring its intensity in the saturated (S^{sat}) and reference (S^0) spectra using (Eq. 7).

$$N\_NOE = \frac{S^{sat}}{S^0} - 1 \qquad \text{Eq. 7}$$

For a given temperature (25 or 45°C) a plot of ^{15}N_R_2/ ^{15}N_R_1 ratio vs. residue number and another plot of N_NOE vs. residue number was used to infer rigidity/flexibility, local mobility, and potential conformational exchange at the residue level in a time scale from ps to tenths of ns.

Conceptual basis
Nuclear spin relaxation (NMR relaxation) involves the transfer of energy or a loss of spin coherence (order) from one spin to other spins and/or between one spin and its surroundings

(112). This energy transfer is quantized, so relaxation via molecular motions only occurs via motions with specific energies (frequencies) as dictated by the NMR experimental conditions (type of NMR experiment, nuclei involved, magnetic field strength, relaxation mechanism, etc.). The rotational motions of molecules in solution often have the adequate range of frequencies for NMR relaxation. These motions exhibit a gaussian-shaped continuous distribution of frequencies centered around a characteristic frequency, which depends on the motion type (e.g., global rotation, side chain rotations, or methyl rotation to name a few) (113).

In this work longitudinal ($^{15}N\_R_1$), transverse ($^{15}N\_R_2$) relaxation rates, and steady-state $^{15}N\{^1H\}$ NOE were measured, they are based on the mechanism of dipolar relaxation and are sensitive to the rotational dynamics of proteins at the residue level. These parameters inform of the motions of the backbone NH group in the picosecond-to-nanosecond timescale, which includes global rotational motions of the protein, fast small-amplitude vibration/libration motions in solution. The case of $^{15}N\_R_2$ is special because it may contain an additional contribution of the so-called conformational exchange term, R_{2ex}, which makes it sensitive large-amplitude motions μs to ms timescale such as folding/unfolding processes. By analysis of these relaxation parameters the level of intramolecular rigidity or flexibility of each residue can be determined which is influenced by factors such as hydrogen bonding and hydrophobic interactions. This study focused on detecting not only conformational changes but also alterations in internal dynamics during the early stages of temperature-induced protein unfolding.

The $^{15}N\_R_1$ reports on the return of ^{15}N magnetization to equilibrium along the z-axis of the vector-model. It is primarily sensitive to rapid local motions in the picosecond–nanosecond range. Regions of high flexibility typically display higher R_1 values compared to well-ordered secondary structure elements.

The $^{15}N\_R_2$ describes the rate at which the transverse magnetization of the ^{15}N nucleus (in the xy-plane of the rotating frame of the vector model) decays due to loss of order (coherence) which is a non-radiative entropic process in the sense that the excess of energy is redistributed between the spin-pair ^{15}N and ^1H but it does not involve the emission of any electromagnetic radiation. Like R_1 it is primarily sensitive to rapid local motions in the picosecond–nanosecond range. However, another significant contributor to $^{15}N\_R_2$ in proteins is chemical exchange (R_{ex}), which arises when the ^{15}N nucleus experiences different chemical environments due to intermediate conformational changes or binding events on the microsecond-to-millisecond timescale. Elevated R_2 values therefore often reporters of conformational heterogeneity, transient interactions, or unfolding events.

The $^{15}N\_NOE$ complements these rates by probing spatial correlation between an amide proton and its directly bonded ^{15}N nucleus. High positive NOE values indicate restricted backbone motions, characteristics of well-folded regions, while low or negative NOE values reveal enhanced flexibility typical of disordered or partially unfolded segments.

Together, with appropriate experiments these three NMR relaxation parameters can provide a residue-specific map of protein backbone dynamics, allowing identification of rigid secondary structure elements, flexible loops, and residues undergoing conformational exchange (113).

3.3.9 3D ^{15}N-edited-NOESY to measure inter-proton distances

Experimental part

NOEs ^{1}H-^{1}H were measured at 25 and 45ºC for a U-^{13}C,^{15}N labelled sample of naturally folded BVPrP^{C}(90-231) at a concentration of 6 mg/ml and pH 5.0. At each temperature two spectra were acquired using a mixing time of 80 ms and 120 ms and the following conditions. A total of 2048, 40 and 128 complex points were measured for dimensions ^{1}H (F3) and ^{15}N (F2) and ^{1}H (F1), respectively. The spectral width in F3, F2 and F1 was 12.8, 28 and 12.8 ppm, respectively. The number of scans was 24 and the NUS factor was 50%. Each spectrum was measured in 21.9 hours. A third ^{15}N-edited NOESY spectrum was measured at each temperature with a mixing time of 60 ms and a higher number of points. The number of points acquired was 2048, 64 and 450 complex points for dimensions 1H (F3) and 15N (F2) and 1H (F1), respectively. The spectral width in F3, F2 and F1 was 12.8, 28 and 12.8 ppm, respectively. The number of scans was 16 and the NUS factor was 40%. The spectrum was measured 63.4 hours. NOE cross-peak intensities were converted to proton–proton distances by first normalizing each to the intensity of its corresponding diagonal peak, taken from the ^{15}N_HSQC plane of the 3D ^{15}N-edited NOESY spectrum. The average intensity of the 3% strongest normalized intra-residue peaks was then calibrated to a reference distance of 2.5 Å. Remaining proton–proton distances were calculated using the relationship $I \propto r_{ij}^{-6}$ (114).

3.3.10 Diffusion-Ordered SpectroscopY (DOSY)

Experimental part

Diffusion-Ordered SpectroscopY (DOSY) spectra were measured at 25ºC for the intact BVPrP^{C}(90-231) sample (conc. 6 mg/ml, pH 5.0) and for the same sample at 25ºC post-heated 75ºC during more than 2 hours. DOSY spectra were measured with the One-shot sequence (115) that incorporates a Watergate 3-9-19 scheme for the strong suppression of the water peak (Bruker sequence stebpgp1s19). The diffusion delay Δ was 100 ms; the bipolar gradient pulses (δ) used to encode/decode diffusion have a total duration of 4 ms and were smooth-square shaped (Bruker SMSQ10.100). Their power varied linearly between 2.5 and 50.3 G/cm to detect 30 points in the diffusion dimension with 24 scans per point. The pre-scan delay (d_1) was 1s and the measurement time is 27 min. Each DOSY spectrum was processed along the chemical shift dimension (F2) with MestreNova and the most-intense proton signals of the protein in the exclusive region where most β protons appear from 2.7 to 3.4 ppm were integrated along the 30 points of the diffusion dimension (F1). The integrals were non-linearly fitted to the corresponding mono- or biexponential type of Stejskal-Tanner equation governing the

experiment, (Eqs. 8 or 9), respectively to determine one or two self-diffusion coefficients for either one or two molecular species in the solution, respectively (116). The plot of the intensity and the fit to (Eqs. 8 or 9) to determine D was carried out with Sci-Davis software.

$$I(G) = I(0) \cdot \exp\left(-D_a\, \gamma^2\, \delta^2\, G^2\right)\left(\Delta - \frac{\delta}{3}\right) \quad \text{Eq. 8}$$

$$I(G) = \exp\left(\gamma^2\, \delta^2\, G^2\right)\left(\Delta - \frac{\delta}{3}\right)\left[I_{0a} \cdot \exp(-D_a) + I_{0b} \cdot \exp(-D_b)\right] \quad \text{Eq. 9}$$

where the parameters are:

D_x = Self-Diffusion coefficient ($m^2 \cdot s^{-1}$) for the species, x (x= a for monomer and b for oligomer)

I_{0x} = Initial intensity and weighting factor for the species, x (x = a for monomer and b for oligomer)

G = gradient strength, varied during the experiment (G/m)

γ = magnetogyric ratio of the proton (26752.2205 $G^{-1}\ s^{-1}$)

δ = gradient pulse duration (4 ms)

Δ = diffusion delay (100 ms)

The molecular weight (M) (in g/mol) for monomer or oligomer was estimated from the D value (in $m^2 \cdot s^{-1}$) using the empirical relationship for globular proteins valid from 4 to 120 kDa (117), (Eq. 10).

$$D = 3413.3 \cdot 10^{-12} \cdot M^{-0.37203} \quad \text{Eq. 10}$$

Experimental change in the D value helped detect aggregation events even before turbidity or visible aggregates appeared

Conceptual basis

Diffusion-Ordered Spectroscopy (DOSY) is a multidimensional NMR technique that quantifies the self-diffusion coefficient (D) of molecular components in pure samples or mixtures, enabling their virtual separation based on diffusive behavior without requiring physical separation.

The value of D quantifies a molecule's average displacement due to Brownian motion over a given time interval, and is inversely related to its hydrodynamic size, shape, and intermolecular interactions via the Stokes–Einstein equation (**Fig. 14**).

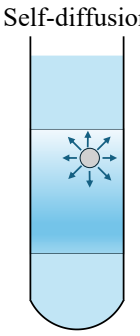

Stokes-Einstein equation

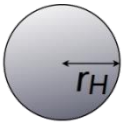

$$D = \frac{k_B T}{6\pi \eta r_H}$$

Where k_B is the Boltzmann constant, T temperature, η viscosity of the solution, and r_H effective radius of the solute molecule including the solvation layer.

Figure 14 Concept of self-translational diffusion of a molecule in solution (NMR tube) and Stokes-Einstein equation.

In a DOSY experiment, molecular positions are encoded at a given time using a pulsed-field gradient (PFG) of a certain strength, followed by a diffusion delay during which molecules move randomly. A second PFG of the same magnitude then decodes their new positions. Molecules with higher diffusion coefficients (typically smaller species) experience greater positional changes, resulting in stronger signal attenuation (**Fig. 15**).

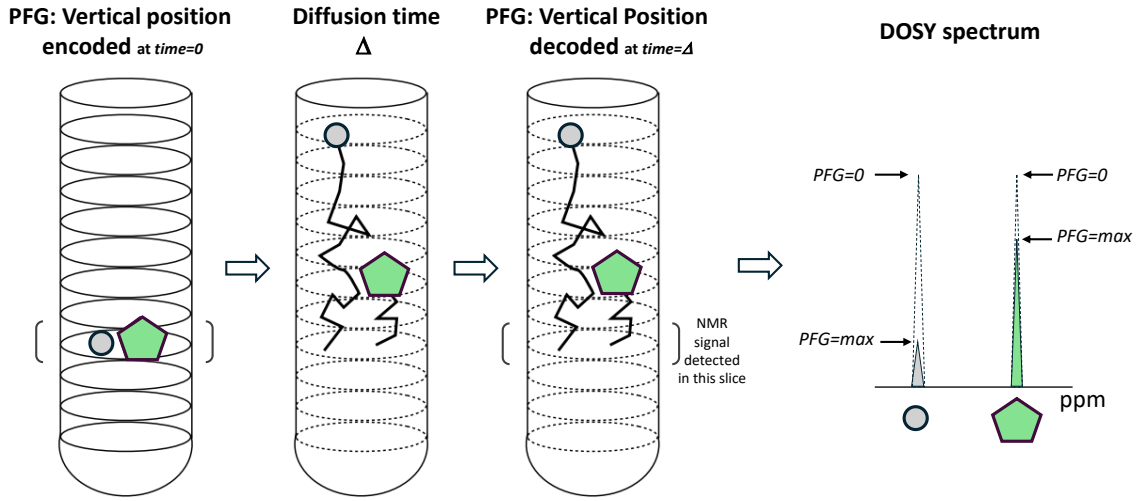

Figure 15 Schematic of the key components in a DOSY pulse sequence. The initial pulsed field gradient (PFG) encodes the position of each molecule along a series of vertical slices in the NMR tube. During the subsequent diffusion interval (Δ), self-diffusion causes molecules to displace to adjacent slices. The decoding PFG then rephases the magnetization only for spins that remain in their original slice, resulting in signal attenuation that depends on the diffusion coefficient (D) and the effective slice thickness. This thickness is systematically varied across experiments by adjusting the PFG amplitude, which bears an inverse relationship to the attenuation. In the resulting DOSY spectrum, the signal from the smaller molecule (gray circle) exhibits greater attenuation relative to the larger one (green pentagon), compared to the reference spectrum acquired with zero PFG strength.

The DOSY spectrum can be represented as a stack of 1D spectra in which the intensity of the signals are attenuated as a function of the PFG gradient strength or, alternatively, as a pseudo-2D spectrum which correlates conventional chemical shift (F2 dimension) with the diffusion coefficient (F1 dimension) of the species that generates the NMR signal, enabling the separation, identification, and characterization of molecular species based on their diffusion behavior. The relationship between signal attenuation and diffusion is described by the adequate type of Stejskal–Tanner equation (118).

3.3.11 Chemical Exchange Saturation Transfer (CEST) and Dark state Exchange Saturation Transfer (DEST) to study conformational variability and oligomerization

Experimental part

The ^{15}N_CEST (119–122) spectrum was acquired at 25ºC and 45ºC for U-^{13}C,^{15}N natively folded monomeric sample (6 mg/ml, pH 5). The spectrum is measured as a pseudo-3D experiment (Bruker sequence: hsqc_cest_etf3gpsitc3d) (123) probing a series of 105 unique ^{15}N saturation sites, with a spectrum collected for each site. In the series, the selective saturation was applied during 0.4 s at a ^{15}N frequency ranging from 103 to 134.2 ppm with the saturation frequency incremented linearly in steps of 0.3 ppm and a saturation B_1 field strength of 25 Hz. The ^{15}N_CEST spectrum was processed with TopSpin by applying a Fourier transformation in ^{1}H and ^{15}N dimensions followed by phase correction and baseline correction in both dimensions. The processed spectrum was extracted as a series of 2*D* sub-spectra with a home-made TopSpin macro and then imported and stacked in MestreNova software for the analysis of the intensities. The intensity (I) of each amide cross-peak in the ^{1}H and ^{15}N dimensions was evaluated at each CEST saturation frequency (^{15}N frequency) divided by the intensity of the reference CEST spectrum (I^0) without saturation. The point of minimum and maximum intensity was normalized to 0% followed by a second normalization to set the point of maximum intensity to 100%. The CEST spectrum of each cross-peak was represented with a homemade vibe coded python script based on the matplotlib library.

The ^{15}N_DEST spectrum (119,124), was measured at 25ºC for the oligomeric post-75 sample of BVPrP^{C}(90-231). The spectrum is measured as a pseudo-3D experiment (Bruker sequence: hsqc_cest_etf3gpsitc3d) (123) probing a series of 105 unique ^{15}N saturation sites, with a spectrum collected for each site. In the series, the selective saturation was applied during 0.4 s at a ^{15}N frequency ranging from 103 to 134.2 ppm, with the saturation frequency incremented linearly in steps of 0.3 ppm. The B_1 field strength of the saturation was 25 Hz. The ^{15}N_DEST spectrum was processed with TopSpin by applying a Fourier transformation in ^{1}H and ^{15}N dimensions followed by phase correction and baseline correction in both dimensions. The processed spectrum was extracted as a series of 2*D* sub-spectra with a home-made TopSpin macro and then imported and stacked in MestreNova software for the analysis of the intensities. The intensity (I) of each amide cross-peak in the ^{1}H and ^{15}N dimensions was evaluated at each DEST saturation frequency (^{15}N frequency) divided by the intensity of the reference DEST

spectrum (I^0) without saturation. The point of minimum and maximum intensity was normalized to 0% followed by a second normalization to set the point of maximum intensity to 100%. The DEST spectrum of each cross-peak was represented with a homemade vibe coded python script based on the matplotlib library.

Conceptual basis of CEST

Chemical Exchange Saturation Transfer (CEST) (119–123,125,126), are a class of NMR spectra aimed to detect a conformational equilibrium of a molecule. This is the case of the exchange of minority conformation and a dominant conformation of lower energy. One key advantage of CEST is its ability to detect low-population conformations (~1%) that are invisible in conventional spectra such as N_HSQC.

CEST is sensitive to dynamic exchange with a kinetic constant (k_{ex}) between 50 and 400 s^{-1} (120). This timescale is characteristic of large-scale domain reorientations, folding/unfolding transitions, reversible oligomerization, ligand-binding allostery, and enzyme catalysis, among other dynamic processes.

CEST involves measuring the reduction in longitudinal magnetization when a specific nucleus (e.g., ^{15}N, ^{13}C, ^{1}H) is saturated. The effect is modulated by the parameters of the saturation namely its duration (milliseconds to seconds), the B_1 field strength (10–500 Hz), and the frequency offset (ppm).

The scheme of **Fig. 16** explains the basic concepts of the CEST methodology which is general for several types of CEST spectra including ^{15}N_CEST, and methyl-CEST. CEST consists on applying selective irradiation in a series of frequency positions of the spectrum (ppm) of a certain type of nucleus. The position is incrementally swept, acquiring one spectrum at a time, until the entire spectral window of the target nucleus is covered. At a position in which saturation targets the frequency of a visible signal in the spectrum, its intensity decreases, producing a pronounced drop in the CEST curve, referred to as a "dip" in NMR terminology.

The CEST spectrum is constructed by plotting signal intensity against the frequency of the applied saturation, a type of spectrum that is often referred as a “Z-spectrum” (named for the exchange of longitudinal magnetization during the saturation period). The key feature of CEST is its ability to detect minor conformations that do not produce observable signals in the spectrum. In favorable cases, when the saturation targets the frequency of a nucleus in a minor conformation, distinct from that of the major conformation, and the two conformers interconvert at a sufficient rate, the saturation can be transferred from the minor to the major conformation. This results in an additional secondary dip in the CEST spectrum. By fitting the CEST spectrum to a conformational equilibrium model involving two or more exchanging sites using the Bloch-McConnell equations (127), quantitative details are obtained, including exchange rate/s and the chemical shifts of the conformational species that exchange.

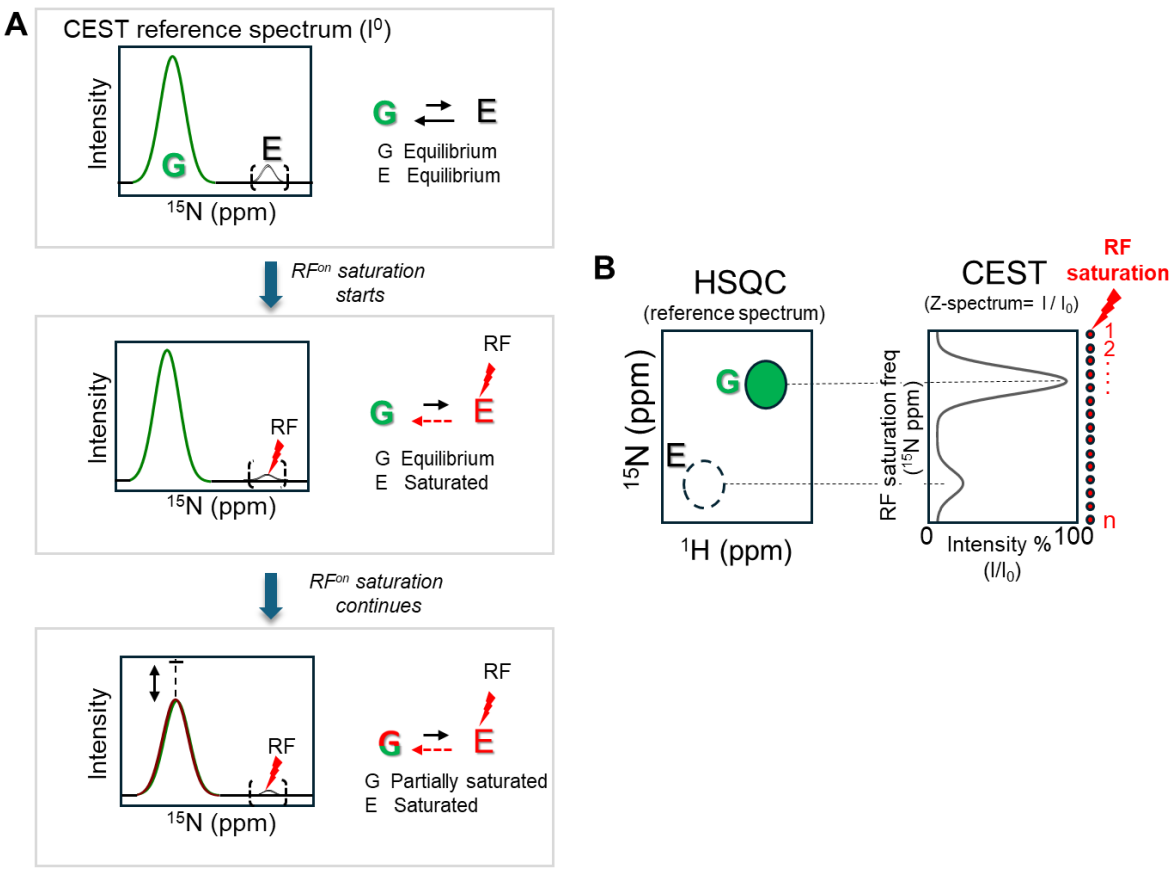

Figure 16 Scheme of ^{15}N_CEST for probing exchange with low populated conformations. (G) is the highly populated ground conformational state (green signal) and (E) is the low populated excited conformational state (black dotted signal), both comprising the same low-molecular-weight molecule (e.g., monomeric state). **A)** Selective RF saturation at E is partially transferred to G state, reducing its intensity. **B)** The full ^{15}N_CEST involves acquiring a series of N_HSQC spectra, each with selective RF saturation applied at incremental offsets across the ^{15}N frequency range providing a series of signal intensities I. A reference spectrum without saturation provides intensity I^0. The resulting Z-spectrum, calculated as the ratio (I / I^0) shows dual dips and confirms the equilibrium. Quantitative fitting of the Z-spectrum yields parameters such as the population ratio pE/pG and the difference in their ^{15}N chemical shift ($\Delta\omega_{EG}$).

Conceptual basis of DEST

Dark State Exchange Saturation Transfer (DEST) probes chemical exchange equilibrium between two or more species of different molecular size such as a monomer in a transient equilibrium with its aggregate forms (oligomers, protofibril, fibrils). Although experimentally highly analogous to CEST, Dark-state Exchange Saturation Transfer (DEST) (119,124) provides fundamentally distinct insights into biomolecular dynamics. DEST probes chemical exchange between distinct species that differ markedly in size, leveraging large differences in transverse relaxation rates (ΔR_2). In contrast, CEST detects conformational variability within the same molecule, exploiting chemical shift differences ($\Delta\omega$) between ground and excited states. The scheme of **Fig. 17** explains the basic concepts of the DEST methodology.

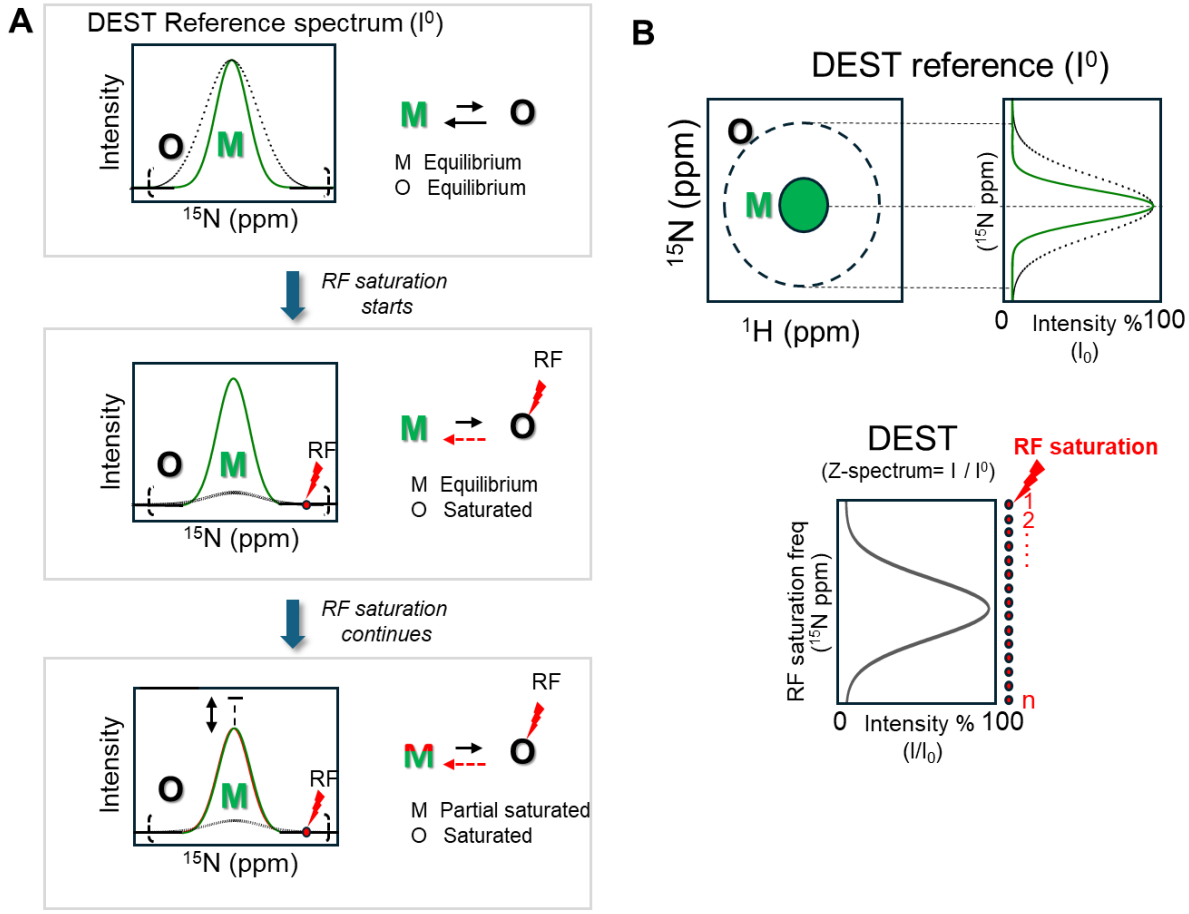

Figure 17 Scheme showing the principle of the ^{15}N_DEST. The experiment probes chemical exchange equilibrium between a low molecular weight monomeric state (M) (green signal), whose signals are observed in the spectrum, and an invisible oligomeric or polymeric state (O) (black dotted signal), formed through its self-aggregation via non-covalent interactions. A) selective RF saturation of invisible signals of O (dark state) leads to partial transfer of saturation to the visible M reducing its intensity. B) The full ^{15}N_DEST acquisition involves acquiring a series of N_HSQC spectra, each with selective RF saturation applied at incremental offsets across the ^{15}N frequency range providing a series of signal intensities I. A reference spectrum without saturation provides intensity I^0. The resulting Z-spectrum, calculated as the ratio (I / I^0), reveals evidence of broadness, confirming equilibrium. Quantitative fitting of the Z-spectrum yields parameters such as the population ratio p_M/p_O and the exchange rate constant (k_{ex}).

3.3.12 Measurements of methyl-CEST and methyl-DEST spectra to detect conformational variability affecting the side chain of amino acids containing methyl groups

Experimental part

Methyl ^{13}C Chemical-Exchange-Saturation-Transfer spectrum (methyl-CEST) (128) was acquired at 25ºC for U-^{13}C,^{15}N natively folded monomeric sample (6 mg/ml, pH 5). The methyl_DEST spectrum was measured under identical conditions for oligomeric post-75 sample of BVPrP^{C}(90-231) (6 mg/ml, pH 5). The spectrum is acquired as a pseudo-3D (Bruker sequence: *mehsqccest3d*) by collecting a series of 81 sub-spectra in which the selective saturation varies in a ^{13}C frequency range from 4.3 to 28 ppm, with the saturation frequency incremented linearly in steps of 0.3 ppm. The saturation was applied during 0.4 s with a B_1 field strength of 20 Hz. The spectrum was processed with TopSpin by applying Fourier

transformations in ^{1}H and ^{13}C dimensions followed by phase correction and baseline correction in both dimensions. The processed spectrum was extracted as a series of 2*D* sub-spectra with a home-made TopSpin macro and then imported and stacked in MestreNova software for the analysis of the intensities. The intensity (I) of each methyl cross-peak in the ^{1}H and ^{13}C dimensions was evaluated at each CEST saturation frequency (^{13}C frequency) divided by the intensity of the reference CEST spectrum (I^{0}) without saturation. The point of minimum and maximum intensity was normalized to 0% followed by a second normalization to set the point of maximum intensity to 100%. The CEST spectrum of each cross-peak was represented with a homemade vibe coded python script based in the matplotlib library.

3.4 Size Exclusion Chromatography (SEC)

Samples subjected to different temperatures (*vide supra*) and cooled back to 25°C were subjected to SEC using a 90 cm TSK4000SW (7 mm×600 mm) column eluted with 10 mM sodium acetate at 1 ml/min. A_{280} of the effluent was monitored. This column was previously calibrated for molecular mass using low and high molecular mass calibration kits (Amersham). Before each run the column was equilibrated with at least four column volumes of elution buffer and each run was performed at 20°C (129).

3.5 Transmission Electron Microscopy (TEM) with Negative Staining

To visualize the morphology of oligomeric assemblies of recBVPrP^{C} (90–231), negative stain transmission electron microscopy (TEM) was performed using standard protocols with minor optimizations for sample type. Sedimented recBVPrP^{C}(90–231) oligomer sample were first collected by centrifugation and gently resuspended in a minimal volume of ultrapure water to avoid structural disruption. A 10 µL aliquot of the oligomer suspension was then applied to a carbon-coated gold grid (Electron Microscopy Sciences), which had not undergone glow discharge. The grid was incubated at room temperature for 1 minute to allow the sample to absorb onto the grid surface. Following adsorption, excess sample was carefully wicked off using filter paper, and the grid was washed two times with ultrapure water to remove unbound material and buffer components that could interfere with staining or increase background contrast.

After the adsorption and washing steps, grids were subjected to negative staining with 2% (w/v) uranyl acetate, which had been freshly prepared and filtered through a 0.22 µm syringe filter to eliminate particulates. A 10 µL drop of the stain was placed on each grid and incubated for 20 seconds at room temperature and excess stain was then wicked off with Whatman filter paper, and the grids were air-dried completely on a clean bench at ambient conditions before imaging.

Grids were imaged using a JEOL JEM 1011 transmission electron microscope operating at an acceleration voltage of 100 kV. Imaging was conducted under low-dose conditions to minimize radiation damage, particularly important for negatively stained biological samples. Images were

captured using a high-resolution direct electron detector or MegaView G3 camera, and magnifications ranged from 20,000× to 200,000×, depending on the sample and the level of structural detail required.

Multiple regions of each grid were examined to assess consistency and reproducibility, and representative micrographs were selected for figure preparation and quantitative analysis where applicable.

3.6 Molecular Dynamics (MD) simulations

MD simulations were performed on the supercomputer Finis Terrae II (CESGA, Santiago de Compostela, Spain). A model representing a BVPrP^{C}(90-231) monomer with its 90-120 flexible tail attached to a PrP^{Sc} stack was constructed. We used the experimentally determined structure of BVPrP^{C}(121-23) (PDB: 2K56). Since no BVPrP^{Sc} structure has been resolved yet, we used RML MoPrP^{Sc}(PDB: 7td6) (69), as an approximation. To the tetramer of this PrP^{Sc}, we added a 90-120 MoPrP rung to which we manually attached the 121-231 FD of BVPrP^{C}(121-231). It should be noted that the 90-120 sequences of MoPrP and BVPrP differ in residue 109 only: L in mouse and I/M in BV (I in the construction used in this study). Motions of the PrP^{Sc} tetramer were restricted, to simulate the situation of a hypothetically much more stable >>4-mer stack, and because at this point only the trajectory of the attached PrP^{C} FD interests us. However, a recent MD study has shown that the surface of a PrP^{Sc} stack does have fluctuations that should be taken into consideration in future studies (130). The resulting structure underwent energy minimization and equilibration using a standard protocol in GROMACS-2022, employing the V-rescale thermostat to maintain a constant temperature and the Parrinello-Rahman algorithm for pressure coupling (131) MD production simulations were carried out in the NPT ensemble, maintaining the same conditions used during equilibration. One run of 200 ns was performed at 310 K and three independent runs of 300 ns each were done at 400 K.

In parallel we carried out MD simulations of BVPrP^{C}(90-231) with its tail free, just as in our experiments. In this case the model was constructed by adding to the BV121-231 structure (PDB: 2K56) the flexible N-terminal region. This N-terminal tail was modeled based on the solution NMR structure of the human PrP molecule (PDB: 7FHQ), which includes residues 91-120. Moreover, residue 90 was added to complete the sequence. To match the BV sequence, residues N97, I109, and V112 were mutated accordingly. The topology was generated using the CHARMM36 force field, which is specifically optimized to accurately model both structured and unstructured regions of proteins. The structure underwent energy minimization and equilibration (*vide supra*). MD production simulations were carried out as detailed for the model described above. Three independent 200 ns production runs were performed at 400 K, and two at 310.

4. RESULTS

4.1 Thermal unfolding of BVPrP^{C}(90–231) as evaluated by Far-UV Circular Dichroism (CD)

To investigate the thermal stability of recombinant BVPrP^{C}(90–231), we monitored the change in secondary structure by tracking the ellipticity at 222 nm, a spectral feature characteristic of α-helical content, using far-UV CD spectroscopy. As shown in **Fig. 18A** gradual and cooperative unfolding transition was observed between 25 °C and 75 °C, characterized by a sigmoidal unfolding curve when plotted as a function of temperature.

The unfolding transition fitted well to a single-state Boltzmann sigmoidal model, suggesting the absence of significant thermodynamically stable intermediate, suggesting a direct native to unfolded state shift (**Fig. 18A**). The irreversibility shown on **Fig. 18B**, with a 50% intensity drop and beta-sheet shift in the 75 °C sample after it was cooled back to 25 °C, points to a soluble altered conformation. The lack of precipitation (post-centrifugation at 16,000g for 15 minutes) suggests the absence of insoluble aggregates under these experimental conditions.

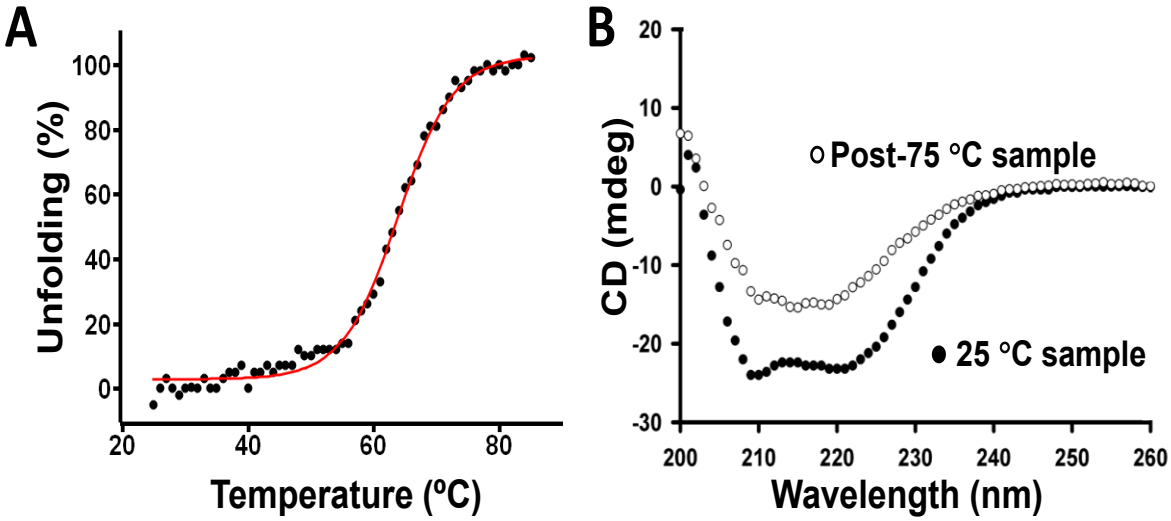

Figure 18 CD analysis of temperature-induced unfolding of BVPrP^{C}(90-231). A) Unfolding curve evaluated as decrease in CD signal at 222 nm (α-helix content) over temperature; the datapoints were fitted to the Boltzmann sigmoidal function (Eq. 1). The fitted parameters were A_1=2.78, A_2=102.67, x_0=63.80, dx=4.41. **B)** Overlaid CD spectra at the beginning (25 °C) and after heating at 75 °C and cooling down to 25 °C.

4.2 NMR signal assignment of BVPrP^{C}(90-231)

While CD provides global information about the secondary structure of a protein and its evolution over different experimental conditions (in our case, temperature), solution NMR

provides structural and dynamic information about individual atomic nuclei. It yields a range of observables, including chemical shifts, coupling constants, NOEs, and relaxation parameters that are highly sensitive to the local environment of each nucleus (i.e. atom) and that can be modulated by temperature variations. Analysis of these parameters reveals subtle molecular details, such as a protein's solution structure, hydrogen bond formation, conformational equilibria, global dynamics, internal flexibility, and intermolecular interactions. A critical prerequisite for deriving such insights is the peak assignment of each spectral peak to a specific nucleus in the protein.

Due to the numerous atoms in a typical protein and its spectral range, signal overlap occurs, which is addressed by using multidimensional NMR techniques. The standard NMR approach for protein signal assignment integrates multiple NMR spectra (98,99) using nuclei like ^{1}H, ^{13}C, and ^{15}N which requires samples of the protein prepared with uniform labeling in both ^{13}C and ^{15}N isotopes. The first step focuses on achieving the most complete assignment of the protein's backbone atoms (HN, N, CA, and CO). Later, the side chain atoms (CB, CG, CD, CE, etc.) of each protein residue can be assigned with other dedicated types of NMR spectra.

In the present study of BVPrP^{C}(90-231), its initial assignment was based on the published data by Christen *et al*. for BVPrP^{C}(125-231) (PDB entry 2k56) (79) and also in the assignment of an analogue sequence of mouse Q216R-PrP^{C} for the N-terminal residues (90-118) (PDB entry 51007) (87). It should be noted that the residue numbering in the published Q216R-PrP^{C} sequence is offset by one compared to the numbering used herein for BVPrP^{C}. It is experimentally established that the ~90-122 segments of both MoPrP^{C}(22-232) and BVPrP^{C}(90-231) are disordered and that the Mo and BVPrP^{C}(90-120) sequences are identical in this segment, except for L109I mutation in the case of BV sequence, which allows comparison of their signals in an N_HSQC spectrum feasible. Because these previous NMR assignments were obtained from similar but not identical conditions (pH, concentration…), the transfer of the NMR assignment required a further step of validation or reassignment for the actual sample under study. The task was accomplished using standard NMR methodologies based on 3*D* spectra (HNCA, HN(CO)CA, HNCACB, etc.) to achieve the most complete set of NH, N, CO, CA, CB, CG and HA assignments. The assignment table is provided in Table in Appendix.

The combination of 3*D* HNCA and 3*D* HN(CO)CA experiments is commonly employed to verify the consistency of assignments for amide HN, ^{15}N, and $^{13}C\alpha$ resonances via the so-called sequential assignment-walk method. In this approach, the ^{15}N planes from the aforementioned 3*D* spectra are displayed as ordered strip plots for a given protein segment, facilitating residue-by-residue tracing along the backbone. Examples of the sequential backbone assignment-walk for three segments of BVPrP^{C}(90-231) are shown in **Fig. 19**. To start with the assignment the ^{15}N plane of the HNCA spectrum corresponding to a given HN residue in the N_HSQC can be considered. It contains two CA cross-peaks, the stronger corresponding to the intra-residue signal and the weaker to the preceding residue. The same plane in the HN(CO)CA experiment identifies which one is the preceding residue, as it is the only signal observed. For instance,

starting from the known assignment of HN and N of R156 (**Fig. 19A**) it is possible to connect one by one with the preceding residues of the segment with full consistency of their NH, N and the Cα resonances.

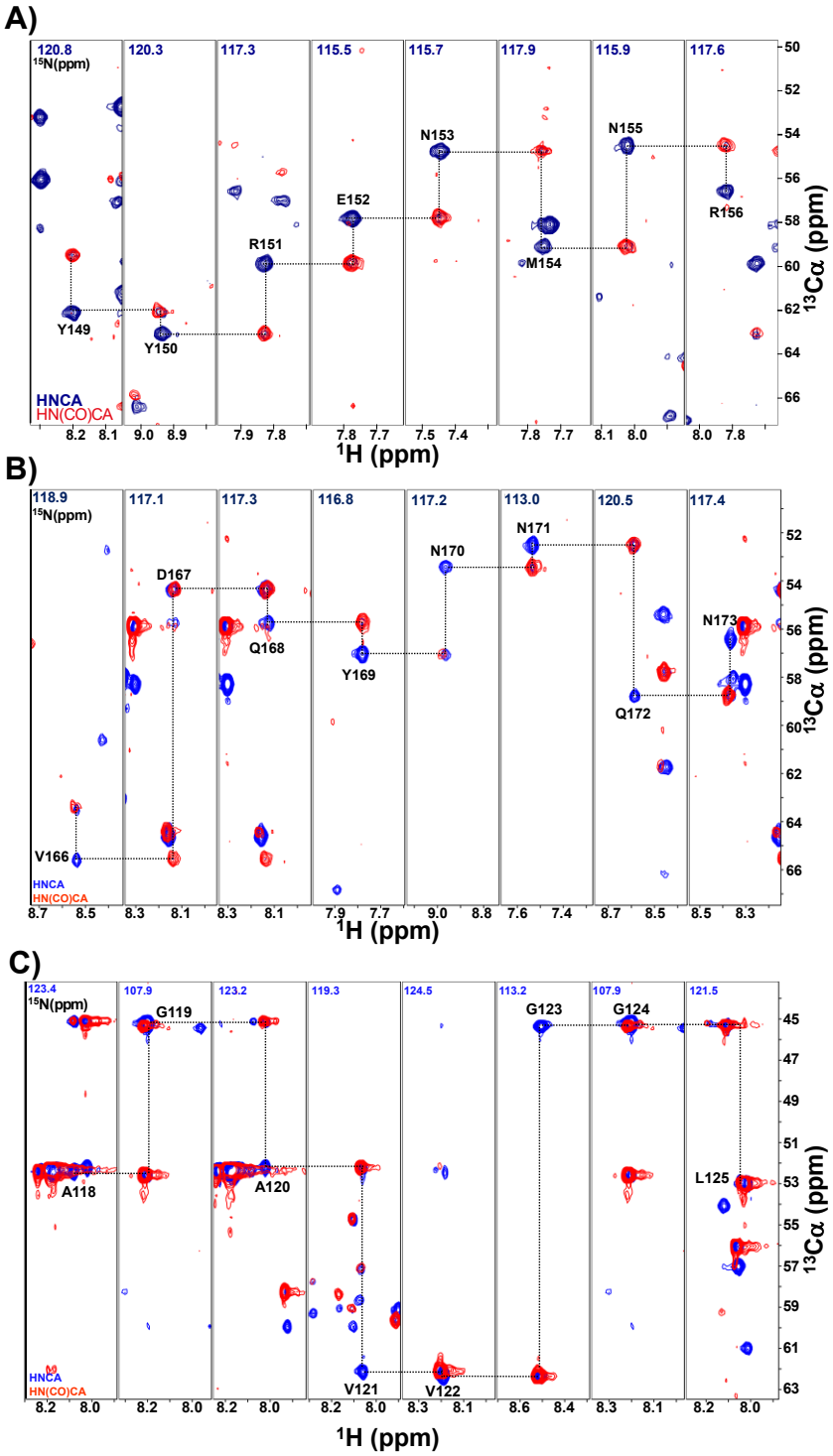

Figure 19 Sequential assignment-walk for the backbone atoms of BVPrP^{C}(90-231) at 25°C. **A)** Assignment-walk for the segment (Y149-R156). **B)** Assignment-walk for the segment (V166-N173). **C)** Assignment-walk for the segment (A118-L125). Strip plots of HNCA (blue) and HN(CO)CA (red) spectra. In each strip the two spectra are superimposed. The number in blue in the upper part refers to the ^{15}N chemical shift plane of the corresponding 3D spectra. The stripped lines show the Cα sequential assignment walk.

The assignment of CB was obtained by combining 3*D* intra-HNCACB and 3*D* HNCACB spectra. The 3*D* HNHA spectrum provided the assignment of Hα's. These data are reported in Table in Appendix.

Using the backbone assignment-walk method described above, the chemical shift assignment of HN, ^{15}N, ^{13}Cα, and other resonances were verified and found to align well to those reported by Christen et al. (79) for the truncated BVPrP^{C}(121-231). The assignment was extended to the extra residues of the BVPrP^{C}(90-231) construct studied herein. The achieved assignment covers 94% of the backbone amides (129 out of 137 non-proline residues), as shown in the ^{15}N_HSQC spectrum in **Fig. 20**. This spectrum exhibits well-dispersed peaks for residues (128–225), indicative of proper folding in the globular folded domain (FD). In contrast, the N-terminal residues (90–127) display poor peak dispersion, characteristic of flexible and intrinsically disordered regions, consistent with prior literature.

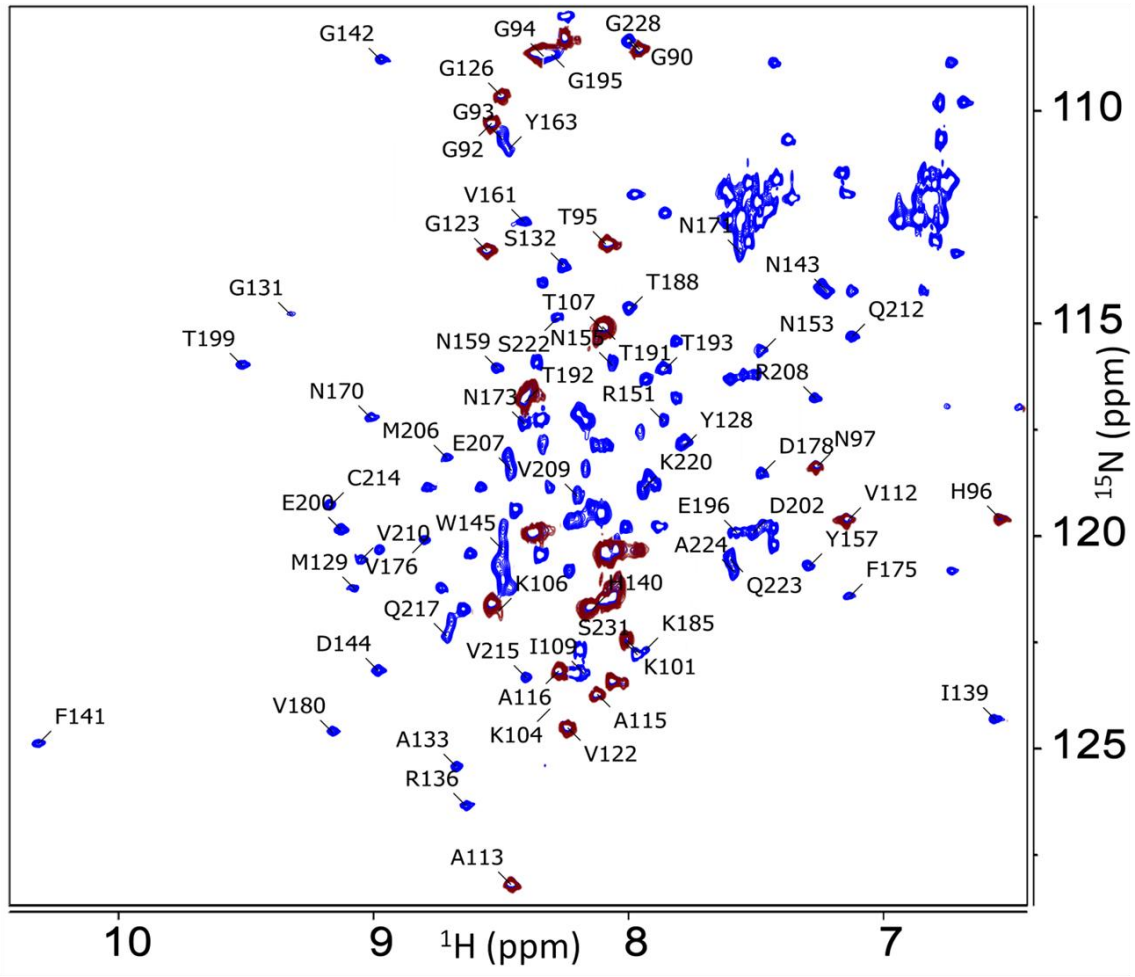

Figure 20 2*D* HSQC_N spectrum of natively folded BVPrP^{C}(90-231). showing the assignment at 25ºC (6 mg/ml, pH 5, 750 MHz). The peaks in red correspond to the N-terminal residues (G90-G127) and the blue color to FD (Y128-S231). There is overlap between some peaks of the N-terminal and FD.

4.3 Discovery of two different regimes of temperature induced unfolding of BVPrP^{C} (90-231) by VT-HSQC ^{15}N

A series of VT-N_HSQC spectra of BVPrP^{C}(90-231) were measured exploring temperatures from 15 to 75°C in small increments of 5°C (or 2.5°C), some of these spectra are shown in **Fig. 21.** An expansion of the spectra obtained at some of the temperatures is given **Fig. 22**.

The nuclear magnetic resonance (NMR) chemical shift of a nucleus (typically ^{1}H, ^{13}C, or ^{15}N in proteins) is highly sensitive to its local electronic environment, which induces a shielding/deshelling of a given nucleus which adds to the NMR external magnetic field and therefore affects its chemical shift (132). It is well known that the chemical shifts of a protein exhibit pronounced temperature dependence. This arises from multiple factors, including the effect of conformational variability and chemical exchange reactions affecting labile protons The later effect manifests specially for the backbone HN amide protons that may exchange with the bulk water protons, a process whose rate escalates with increasing temperature and predominantly affects solvent-exposed residues not involved in hydrogen bonding (100). The water exchange causes the HN chemical shift to be a population-weighted average, dominated by the vast excess of solvent water protons over HN amide protons, thereby shifting the HN resonance toward the bulk water signal (~4.7 ppm at 25°C).

At temperatures up to 50°C, the peaks in the N_HSQC spectra remained well-dispersed, with most peaks retaining their original intensity and width (**Fig. 21**). In this regime of temperatures gradual changes of chemical shifts induced by temperature were observed, consistent with the expected dependence of amide proton and nitrogen shifts (132) but the signal dispersion is retained confirming that the FD remains intact and dynamically stable within this range. Notably, the temperature changes induced are reversible when samples are heated to ≤50°C since when the sample is taken back to 25°C, the original N_HSQC spectrum of the native protein shown in (**Fig. 21**) were fully restored, confirming complete structural reversibility and preservation of FD within this temperature range for the intact protein.

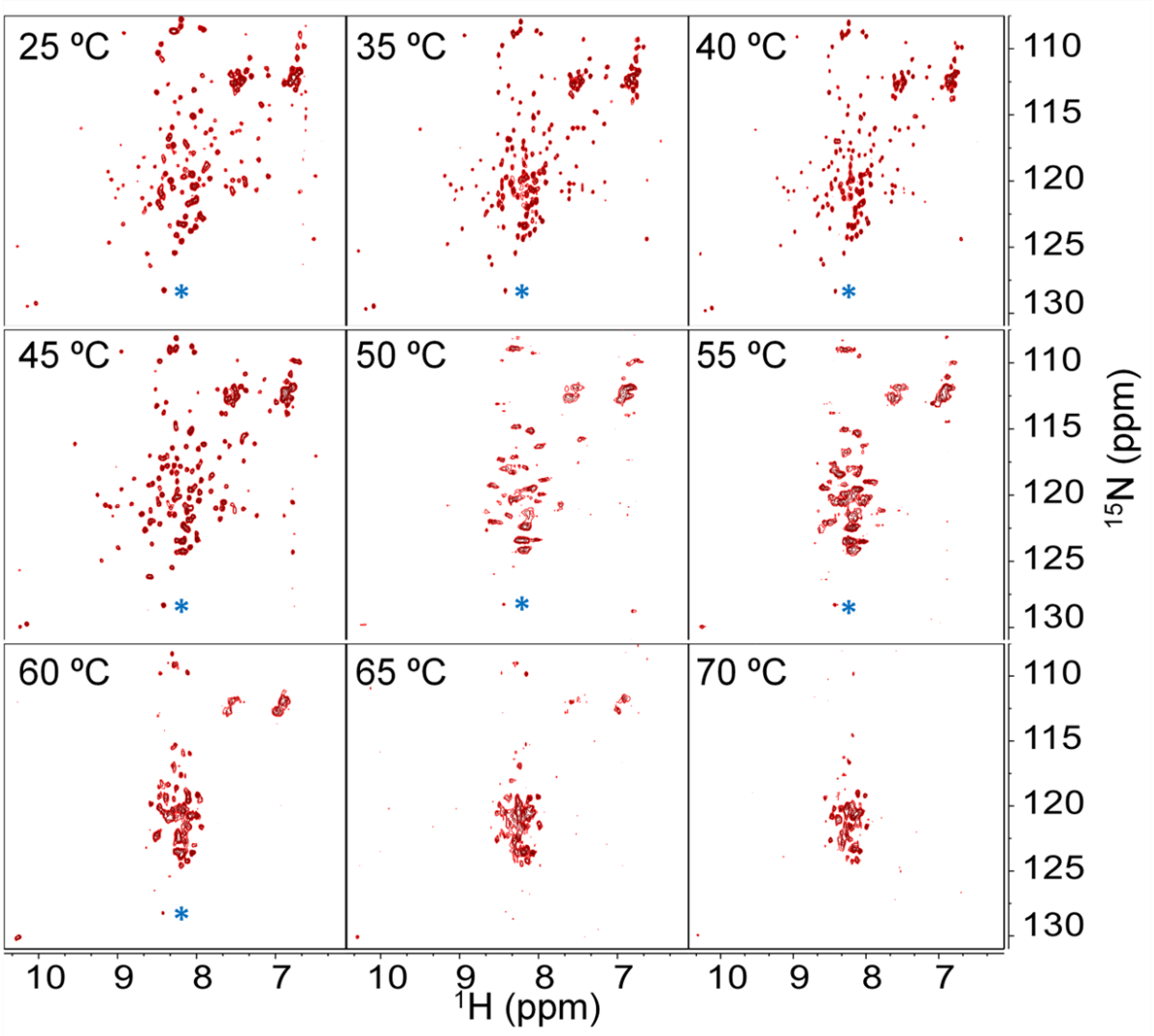

Figure 21 Temperature-induced unfolding of BVPrP^{C}(90-231) tracked with solution NMR. N-HSQC-^{15}N spectra of the backbone amides from 25 to 70°C. Each spectrum was recorded at the indicated temperature. The chemical shifts were referenced to the signal marked with the asterisk and are represented at the same level above the noise.

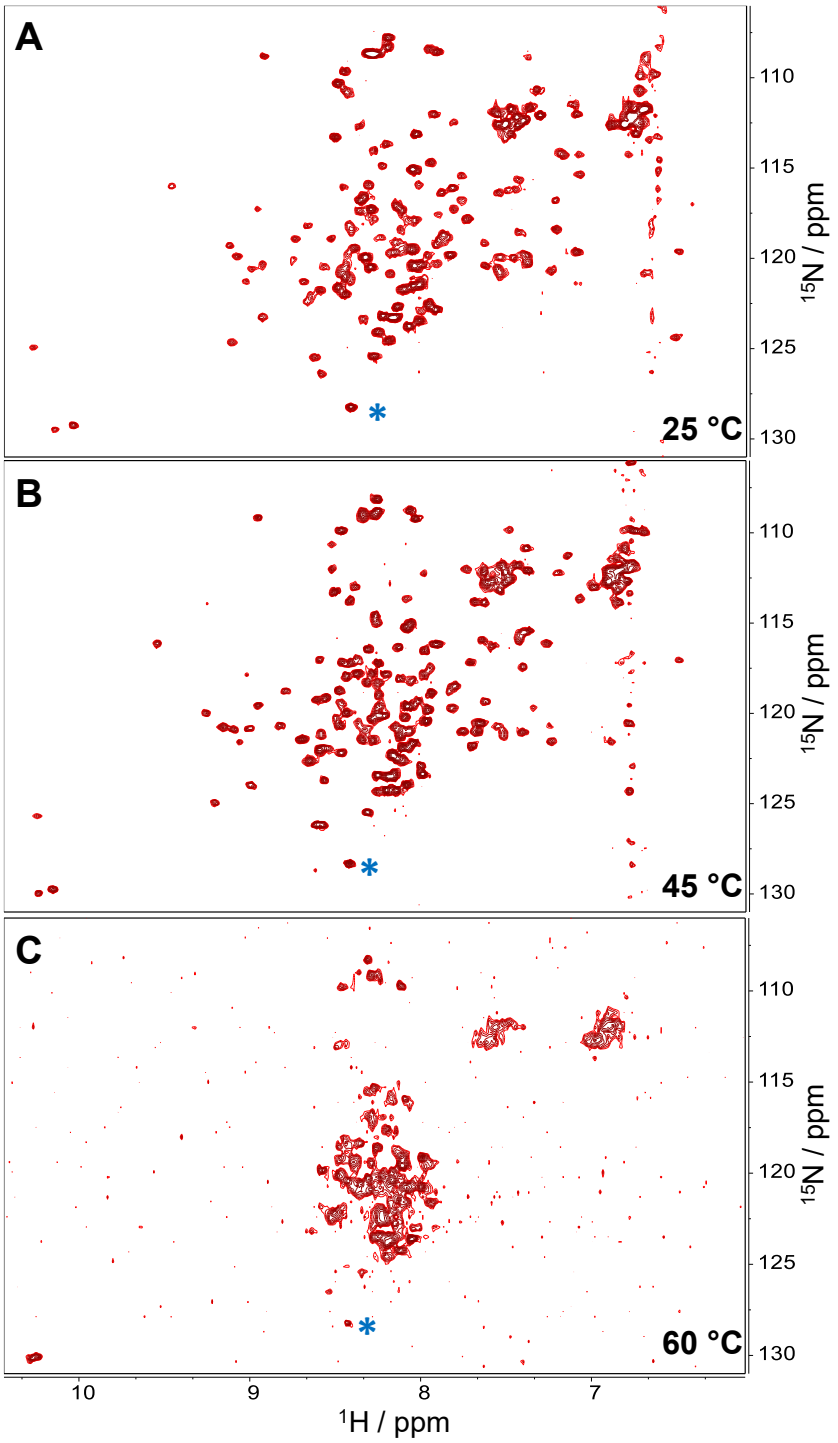

Figure 22 Expanded ^{1}H-^{15}N HSQC view highlighting backbone amide resonances of BVPrP^{C}(90-231). A) 25ºC **B)** 45ºC and **C)** 60ºC. The chemical shifts were referenced to the signal marked with the asterisk and are represented at the same level above the noise.

Beginning at ca. 50 °C, significant alterations in the spectral features became evident. A general peak broadening, intensity reduction, and in some cases complete disappearance of signals was observed (**Fig. 21**). The spectra plateaued between 55°C and 65°C, with no further significant

alteration up to 70°C. Interestingly, once the sample is heated to 55°C for about 1 hour and then cooled back to 25°C, the original N_HSQC spectrum of the natively folded protein given in (**Fig. 24B**) is not recovered. The result is that only 36% of the signals are visible while the remaining 64% of the peaks either disappear or exhibit significantly reduced intensity due to peak broadening effects, implying that irreversible structural alterations occur above this temperature threshold ≥55°C.

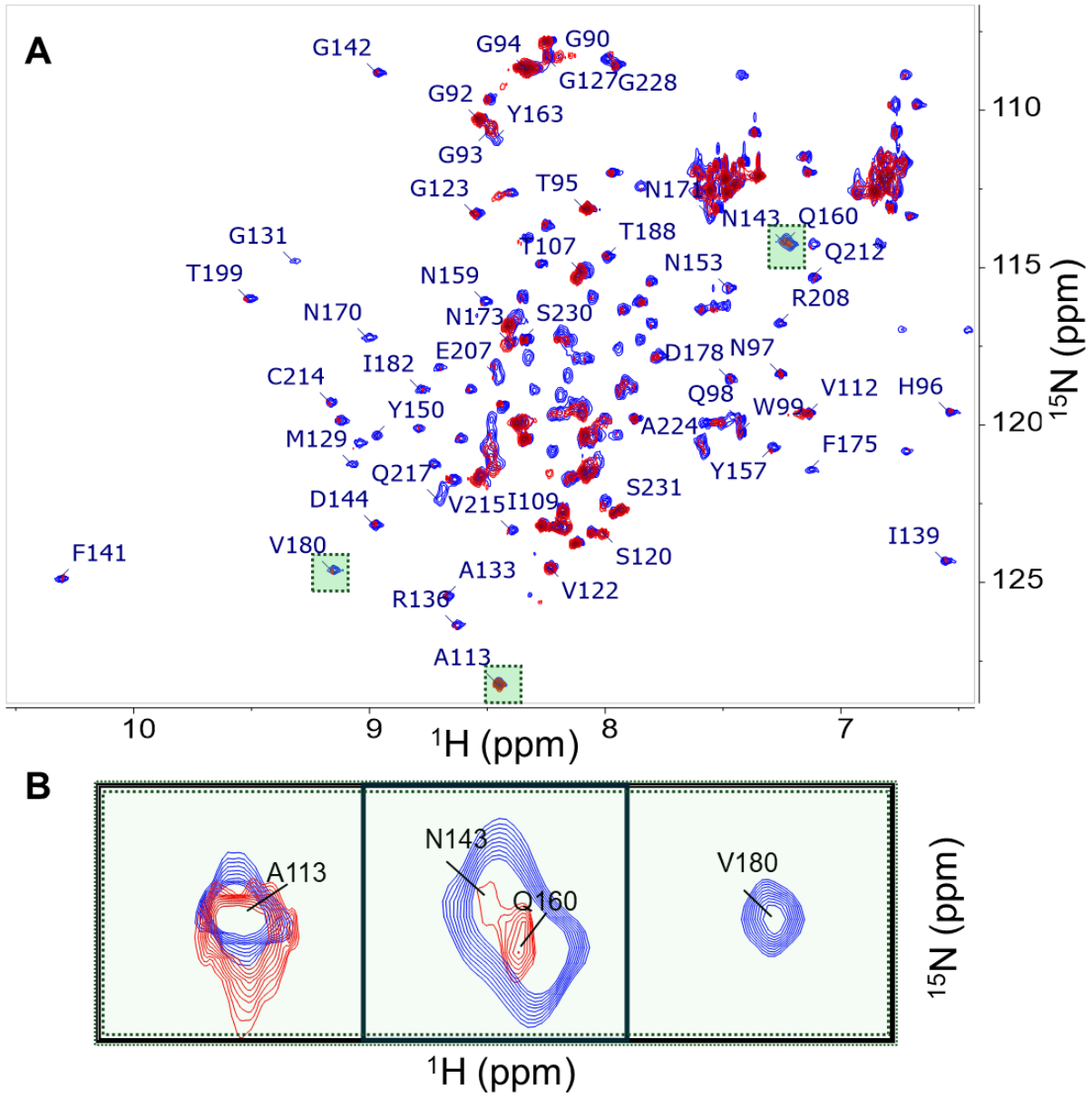

Figure 23 Superimposition of N_HSQC spectra of BVPrP^{C}(90-231) with different thermal history. **A)** N_HSQC of intact folded sample at 25°C (blue), and after being heated at 70°C and cooled back to 25°C (red). The spectra are represented at the same intensity scale. **B)** Enlargement of three regions highlighted in green with examples of residues whose signals are still detected (A113, N143/Q160) or have disappeared (V180) and therefore must be in substructures partially detached from the oligomer core to maintain a partially independent motion regime.

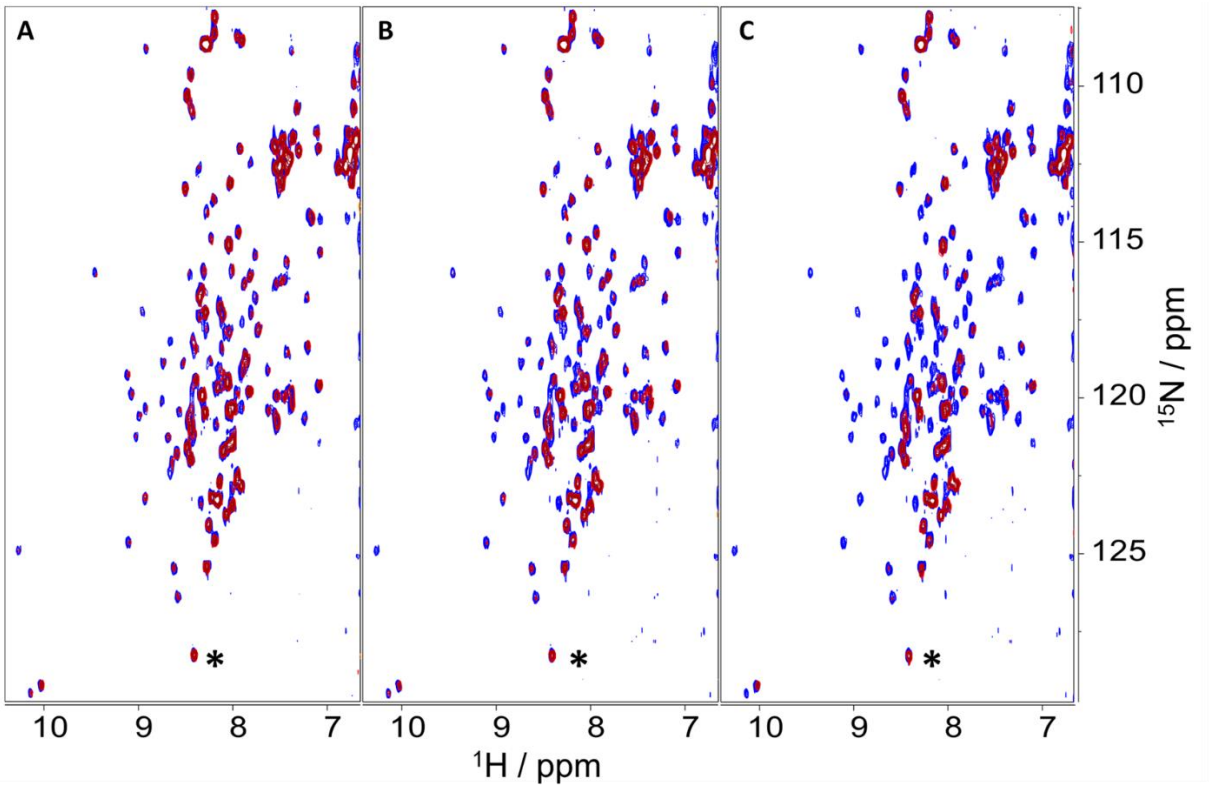

Figure 24 Reversibility/irreversibility of changes in ^{15}N-HSQC spectrum of BVPrP^{C}(90-231) upon heating. A) Superimposition of spectra recorded at 25˚C, of the unheated sample (blue) and of the same sample at 25˚C post heated at 50˚C (red). **B)** Superimposition of spectra recorded at 25˚C, of the unheated sample (blue) and of the same sample at 25˚C post heated at 55˚C (red). **C)** Superimposition of spectra recorded at 25˚C, of the unheated sample (blue) and of the same sample at 25˚C post heated at 60˚C (red). The spectra are represented at ca. the same noise level respect to the signal labelled with an asterisk.

As an initial conclusion of the VT-N_HSQC study of BVPrP^{C}(90-231), we identified two regimes for the temperature induced unfolding, one reversible regime at temperatures below ~50°C and another irreversible regime at temperatures above ~50°C. In what follows we present a further study of these two regimes independently.

4.3.1 Study of thermal unfolding of monomeric BVPrP^{C}(90-231) in the reversible temperature regime: 15 to 45°C

Temperature is known to modulate the global protein dynamics, and its increase can potentially enable access to higher-energy secondary conformations. The backbone amide HN and N chemical shift are good reporters of the conformational and dynamic preferences of each backbone amide group. Their changes in response to temperature can be evaluated and classified as linear or non-linear (104,105) Linear chemical shift behavior is anticipated when only enhanced global dynamics and/or changes in the HN proton exchange rate with water protons dominate. Non-linear behavior is expected for residues that in addition to the mentioned temperature effects also tend to adopt alternative higher energy conformations at the residue level.

A temperature-dependent N_HSQC study was performed on the protein over a temperature range of reversibility from 15 to 45°C (**Fig. 21**). The results were analyzed by Temperature Coefficients (T_C) and Combined Chemical Shift Difference (CCSD), peak-area or peak-integral analysis of N_HSQC signals, VT CLEANEX-PM, VT T_2 proton relaxation of water, ^{15}N-relaxation, proton-proton NOEs, CEST and methyl-CEST. This type of study offers residue specific insight into local flexibility, early unfolding events, and domain stability across different structural motifs of the protein.

4.3.1.1 VT-study to distinguish amide HN residues engaged in strong intramolecular hydrogen bonds from those susceptible to solvent exchange: T_C study

The analysis of a series of VT N-HSQC spectra allows to determine Temperature-Coefficients (T_C) of the backbone HN amide protons of a protein which inform of their ability to participate in a stable hydrogen-bond under the measurement conditions in solution proton (100). The method consists in tabulating the chemical shift variation of HN ($\Delta\delta_{HN}$) as a function of temperature. An increase in temperature enhances the molecular mobility and backbone flexibility, resulting in general upfield shifts of HN due to faster exchange of amide protons with solvent water. Under the temperature range explored, the HN chemical shift drift has a linear dependence on temperature for residues with stable conformations. The slope of this drift ($\Delta\delta/\Delta T$) in ppb/K units is the so-called Temperature coefficient (*T*c). A Tc value between 0 and −4.6 ppb/K is typically interpreted as evidence of solvent protection, involvement in a stable hydrogen bond, or restriction from bulk water, resulting in limited mobility. In contrast, a value more negative than −4.6 ppb/K suggests solvent exposure or dynamic behavior (disorder) and/or the absence of intramolecular hydrogen bonding (87,101,132). In other words, *T*c values provide indirect insight into the conformational stability of residues due to hydrogen bonding which is expected for those residues with secondary structural elements of the FD.

The *T*c were determined by analyzing a series of VT-N_HSQC in the reversible temperature regime between 15 and 45ºC (see **Fig. 25**). Most residues within the disordered N-terminal tail (residues 90–120) exhibit *T*c values < −4.6 ppb/K. The exception is the ~H96–K101 segment, a charged region containing prolines P102 and P105, which may confer transient structure and thus reduced disorder. Residues from ~T107 to W145, which include the remainder of the disordered tail, the ~V121–G128 transition coil (*vide infra*), the coil connecting β1 and α1 and just two residues at the beginning of α_1 form a compact block with moderately to strongly negative *T*c values (highlighted residues in **Fig. 25**), consistent with weak intramolecular HN bonds and a propensity to unfold.

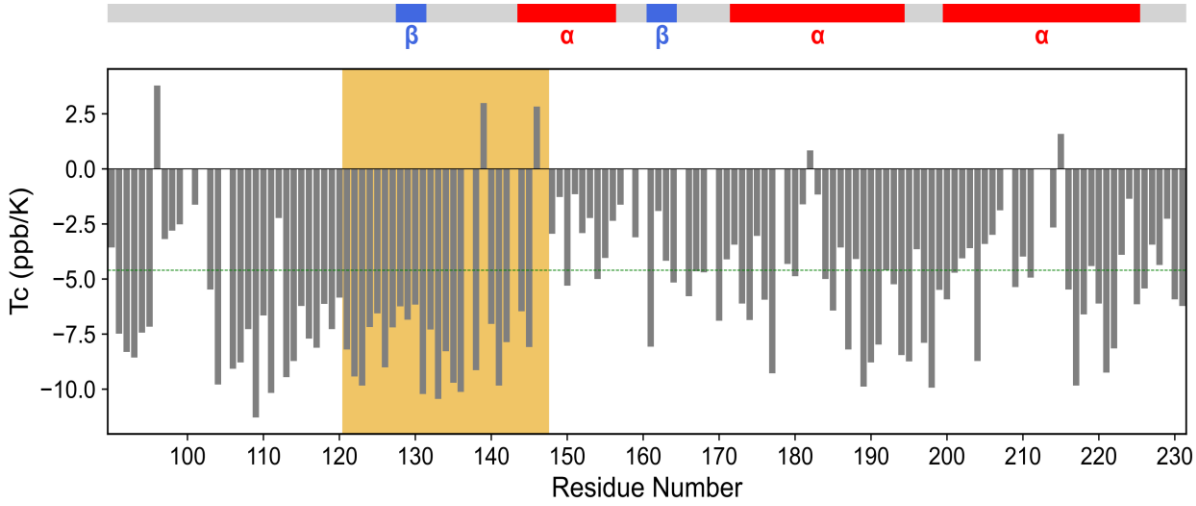

Figure 25 Temperature Coefficients by analysis of backbone proton amide chemical shifts. The bar-plot shows the temperature coefficients T_C (ppb/K) of amide proton (HN) signals in the 15-45ºC range represented along the primary sequence. Signals with values > -4.6 ppb/K are considered protected from the solvent or involved in permanent hydrogen bond and vice versa. The stripped red line marks the aforementioned limit to guide the eye. The region shadowed in orange represents a continuous block of residues with high negative (*Tc* < -4.6 ppb/K) *Tc* values, contiguous to the flexible 90-120 tail. The secondary structure elements are shown on the top. Residues with non-linearity behavior of their *Tc* are omitted from the analysis.

The remainder of α_1 display *Tc* values > −4.6 ppb/K, indicating hydrogen bond and possibly greater relative rigidity. Residues in β_2 and the loop connecting β_2 to α_2 exhibit a mixture of low and large *Tc* values. The large negative values of this loop could be part of the so-called "rigid loop", a misnomer given that its peculiar NMR properties are explained by alternative conformations (79,133) suggesting structural complexity. This loop links not only β_2 and α_2, but also the two "clam-like" FD subdomains, β_1–α_1–β_2 and α_2–α_3.

The α_2-loop-α_3 display a pattern of *Tc* with many values < −4.6 ppb/K between the terminal part of α_2 to the initial part of α_3 and the end part of α_3 indicating greater flexibility there. The remainder residues of this segment are considerably more rigid.

Four residues H96 (coil) and I139 (coil), I182(α2) and V215 (α3) display unusually positive *Tc* (>0 ppb/K), indicating an increase in HN chemical shift with increasing temperature (**Fig. 25**). Such positive Tc values are uncommon and have been previously associated with either temperature-induced conformational changes or an increase in the average distance between the amide proton and a nearby aromatic side chain upon heating (101,102) . On the basis of secondary chemical shifts (134) two types of conformational transitions are known to produce absolute positive Tc for amide protons: (i) α-helix → random coil or (ii) random coil → β-sheet. Alternatively, the observed positive Tc may arise from the anisotropic ring-current effects of nearby aromatic side chains (e.g., Phe, Tyr, Trp, or His. These effects typically shield the HN proton when it is positioned above or below the aromatic ring. Upon heating, thermal motion or subtle structural loosening can increase the average distance or alter the relative orientation,

thereby reducing shielding and resulting in a downfield (more positive) shift of the HN resonance. To sum up, positive Tc values can be grouped together with highly negative (> −4.6 ppb/K) values as suggestive of flexibility/motions.

4.3.1.2 Combined Chemical-Shift Difference coefficients (CCSD) from VT-N_HSQC spectra

Backbone amide HN and N chemical-shift changes with temperature can be analyzed together by the Combined Chemical Shift Difference (CCSD) parameter (87,103) calculated by Eq. 2. In principle, CCSD provides a superior approach for mapping residue-specific structural perturbations caused by a temperature change compared to the individual change of chemical shift for any of these two atoms. This is because CCSD better represents and is more sensitive to the local environment of the amide backbone (e.g., hydrogen bonding and solvent exposure) while offering improved noise reduction and structural robustness.

The linearity or non-linearity of CCSD is related with the conformational stability/instability of the residue (104,105) which includes the alteration of its chemical environment arising from its dissociation or association from/to other protein domains. To determine the linearity propensity of each residue we did a linear fit of VT-CCSD values and calculated the residuals (defined as CCSD - $CCSD^{calc}$) at each temperature. Two examples are given in the plots of **Fig. 26C**. A plot of the residuals and the curvature obtained after the linearization of CCSD is given for each residue of $BVPrP^{C}$(90-231) in **Figs. 27** and **28** show these CCSD results represented over the 3*D* structure of the protein, as well as the primary sequence.

It can be seen in **Figures 26 to 28** that most residues in the folded domain (FD) have a linear dependence of CCSD with temperature indicating conformational stability. However, significant deviations (non-linear CCSD residuals) were observed in residues located primarily within or near β1 and β2 strands, especially the segment from V121 to G131 which involves residues M129 to G131 in β_1, and residues Y163 to N170 which involves residues Y163 and R164 in β_2 (**Fig. 27**). The residues of these β-strands form part of a short antiparallel β-sheet (β1–β2), which emerged as a key region with high conformational plasticity. Given their non-linear temperature response, these residues are likely to be early participants in unfolding transitions, strongly suggesting a hotspot of conformational flexibility, likely an initiation point for early thermal perturbation responses or unfolding, and therefore they likely have a critical role in the thermodynamic stability of the FD.

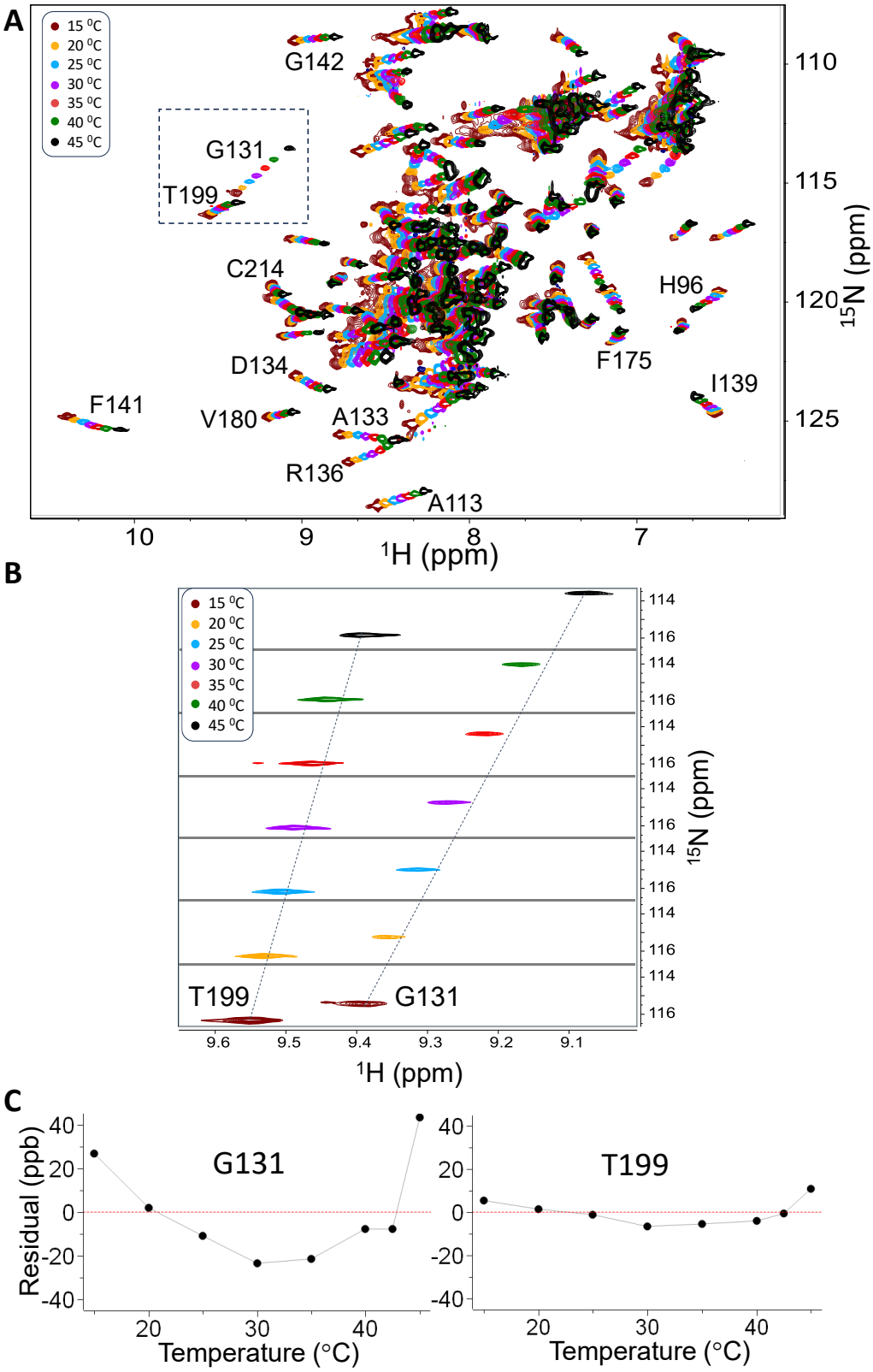

Figure 26 Thermal induced partial unfolding of BVPrP^{C}(90-231) tracked by solution NMR. CCSD study in the reversible regime between 15 and 45°C. Deviation from linearity of temperature dependent on HN chemical shifts reports on conformational change. **A)** Superimposition of VT-N_HSQC spectra. **B)** Detail of stacked HN signals from Thr199 (linear) and Gly131 (non-linear) in N_HSQC spectra recorded between 15 and 45 °C. The striped lines are shown to guide the eye. **C)** Residual CCSD deviation plots for residues G131 and T199.

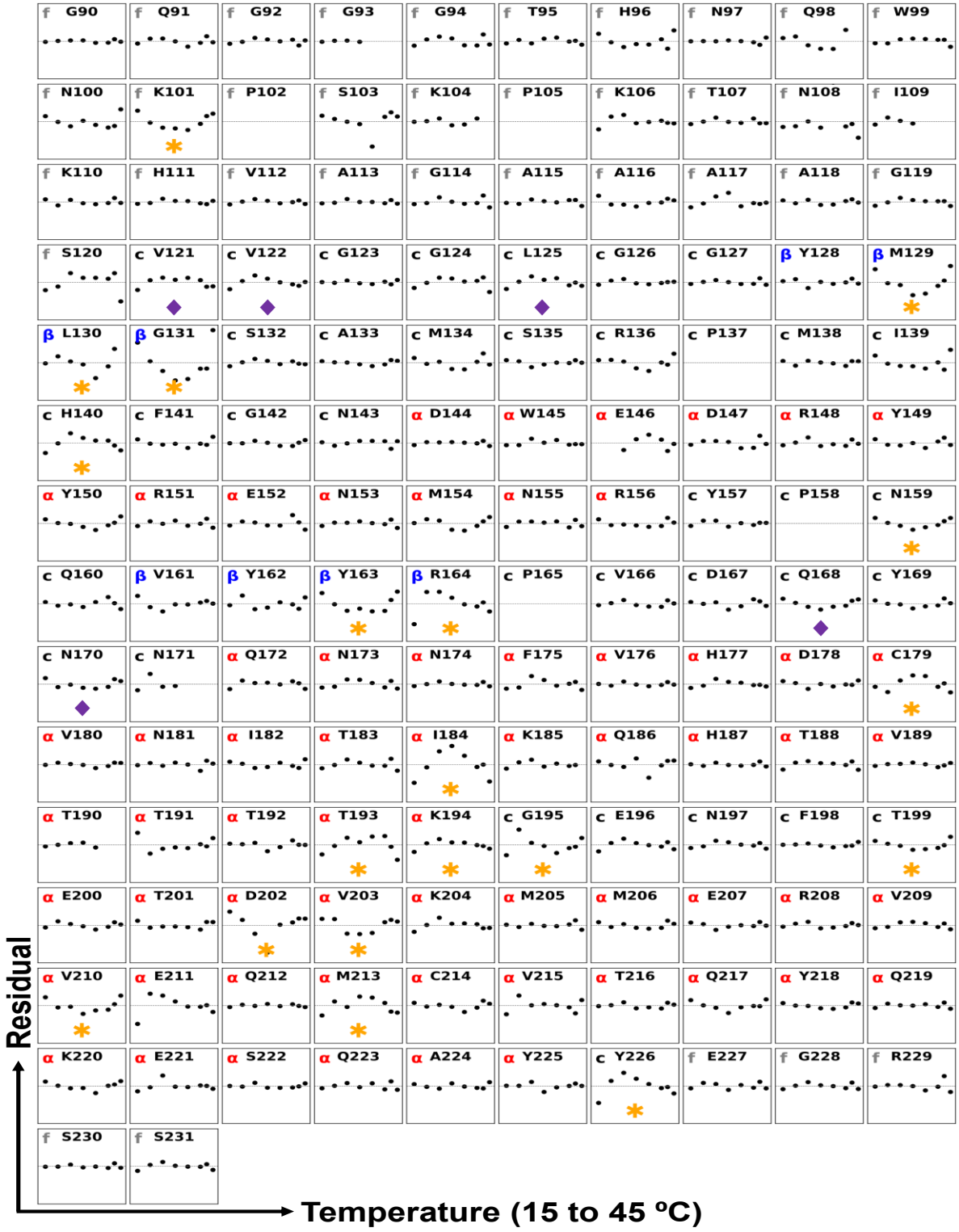

Figure 27 Plot of CCSD residual error for backbone amides of individual BVPrP^{C} (90-231) amino acid. Implicating residues vs. temperature and CCSD values for each residue are calculated by Eq. 2 through peak tracking across the series of VT N_HSQC spectra. They were fitted to a linear regression model with Eq. 3. Each plot represents the residual error (defined as CCSD - CCSD^{calc}) against temperature (104,105). In each plot the amino acid is indicated, and the letter code refers to f=flexible (disordered), α=helix, β=sheet or c=coil. The orange asterisk and purple diamond denote a residue with strong and intermediate non-linear variation of their chemical shifts with temperature, respectively.

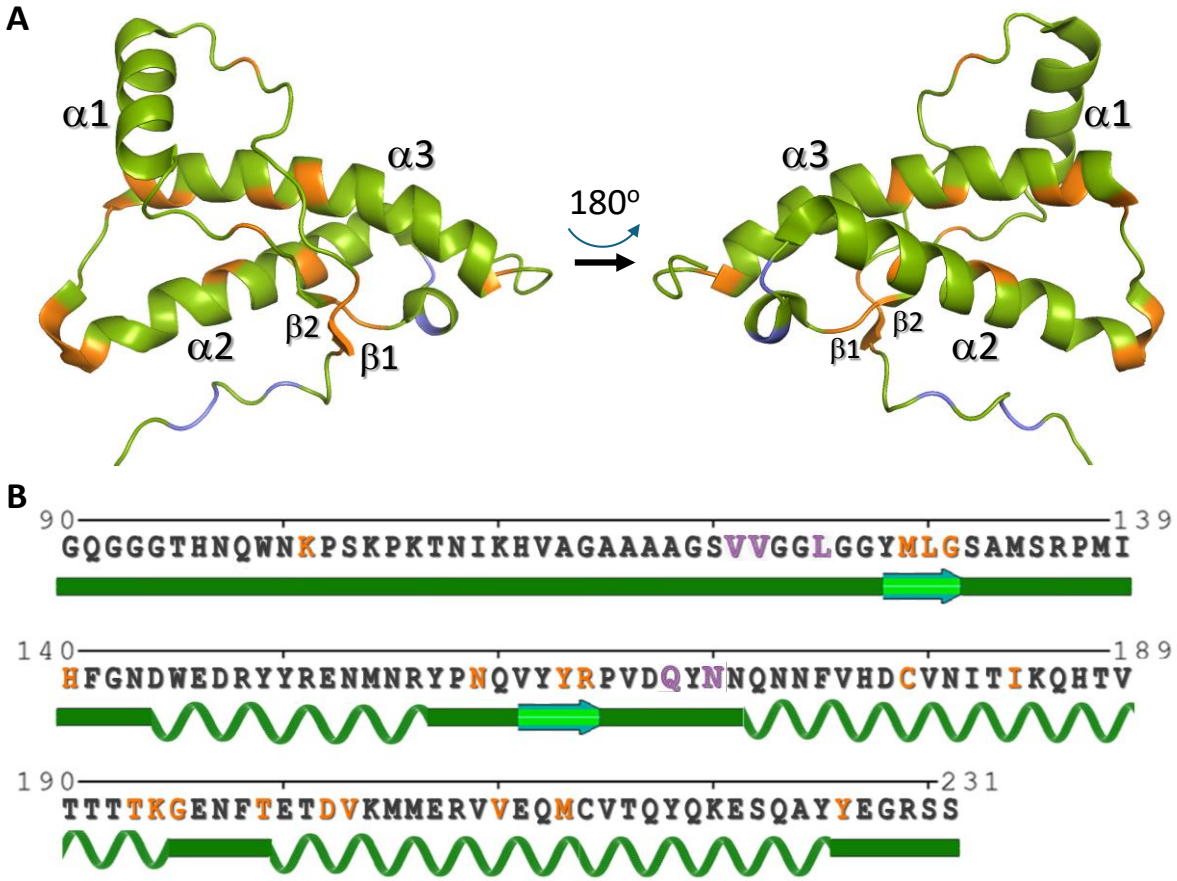

Figure 28 Thermal induced partial unfolding of BVPrP^{C}(90-231) tracked by solution NMR. CCSD study in the reversible regime between 15 and 45°C. **A)** Non-linear CCSD responses are marked in orange over the 3D structure of the protein. Highlighted orange in the 3D structure of the protein. **B)** Cartoon showing residues with strong and medium non-linear CCSD response to temperature in orange and purple characters, respectively.

There are a few specific highly non-linear CCSDs hotspot residues in α2 and α3 such as residues C179, I184, and the segment T193-G195 in α_2 and D202, V203, V210, and M213 in α_3. The remaining highly non-linearities of CCSDs are in sparse residues in the N-terminal and C-terminal region where a high dynamical behavior is expected in concordance with ^{15}N relaxation and MD simulations and a few sparse residues in the connecting loops of the FD.

4.3.1.3 Detection of residues of BVPrP^{C}(90-231) experiencing slow-conformational exchange: peak-intensity study of VT N_HSQC spectra

The analysis of cross-peak intensity in the series of VT-N_HSQC spectra from 15 to 45ºC complements the results of T_C and CCSD sections for studying cases of conformational exchange at the residue level, indicative of early unfolding events. As detailed in Section 3.3.5, an increase of temperature influences several factors that affect NMR signal intensity: it enhances global molecular mobility, thereby accelerating overall tumbling reducing R_2 which increases the intensity; it can also promote conformational exchange, enabling exploration of alternative conformations and introducing an additional exchange contribution (R_{2ex}) that in

the case of the intermediate exchange regime (motions in μs to ms timescale) reduces the intensity; weakens H-bonds and in general accelerates the chemical exchange rate between amide HN protons and solvent water which also reduces the intensity.

The intensity results for BVPrP^{C} (90–231) in the reversible temperature range of 15-45°C is shown in **Fig. 29**. The more clear signature of slow conformational exchange for the temperature evolution of the cross-peak intensity of an amide HN proton of a protein is a U-shaped intensity profile vs. the increment of temperature like the plot represented in **Fig. 10** in the methodology section (106). Therefore, the simplest case of U-shaped profile will be analyzed first and then the cases of reversed-U-shaped profile.

For the analysis of U-shaped profiles in **Fig. 29** the criterium of quality followed is that the intensity should vary consistently (up or down) in at least three consecutive temperature points. Intensity fluctuations due to low signal-to-noise ratio or peak overlap were excluded. Only five residues, K101 (N-terminal), G127 (N-terminal), I184 (α2), V189 (α2), V203 (α3) and M213 (α3), exhibited profiles consistent with slow conformational exchange on the chemical shift timescale (residues marked with cyan stars in **Fig. 29**). Notably, K101, I184, V203 and M213 were previously identified as having conformational exchange by CCSD (**Figs. 26 to 28**). The CCSD method is sensitive conformational exchange, but it does not identify the rate of exchange. Intensity analysis provided further information for these residues, since it indicates that this exchange is slow at the temperature of minimum intensity corresponding to the coalescence point (coalescence is explained in **Fig. 11**).

The U-shaped intensity profile of V189 (α2) **(Fig. 29)** is a less obvious case to interpret. This residue does not form H-bond according to Tc (**Fig. 25**) and has a linear CCSD profile respect to temperature (**Fig. 27**). Moreover, its relaxation data R_2/R_1 ratio shows an extremely low value at 25ºC and an average value at 45ºC (**Fig. 35C and D**) which, contrary to the expected and to the previous cases considered above, indicates that its relative flexibility is higher at 25ºC than at 45ºC. A plausible explanation for the U-shaped profile of V189 is as follows: the initial decrease (from 15°C to 25°C) arises from a combination of faster water-amide hydrogen exchange rates and progressive rigidification of the local structure. Once this rigidification reaches a maximum at 30ºC, the subsequent recovery in intensity (35 to 45ºC can be attributed to enhanced global molecular motions induced by thermal energy. This is a special case of conformational exchange in which increasing the temperature causes a residue, initially sampling a broad ensemble of high amplitude conformations in fast-exchange, transitions to a narrower ensemble with reduced amplitude, passing through a coalescence regime in fast-exchange the maximum rigidity. The V189 case illustrates how temperature-induced mobility in most regions of the protein creates an entropic benefit that outweighs the local entropic cost, thereby stabilizing order in a small number of specific sites.

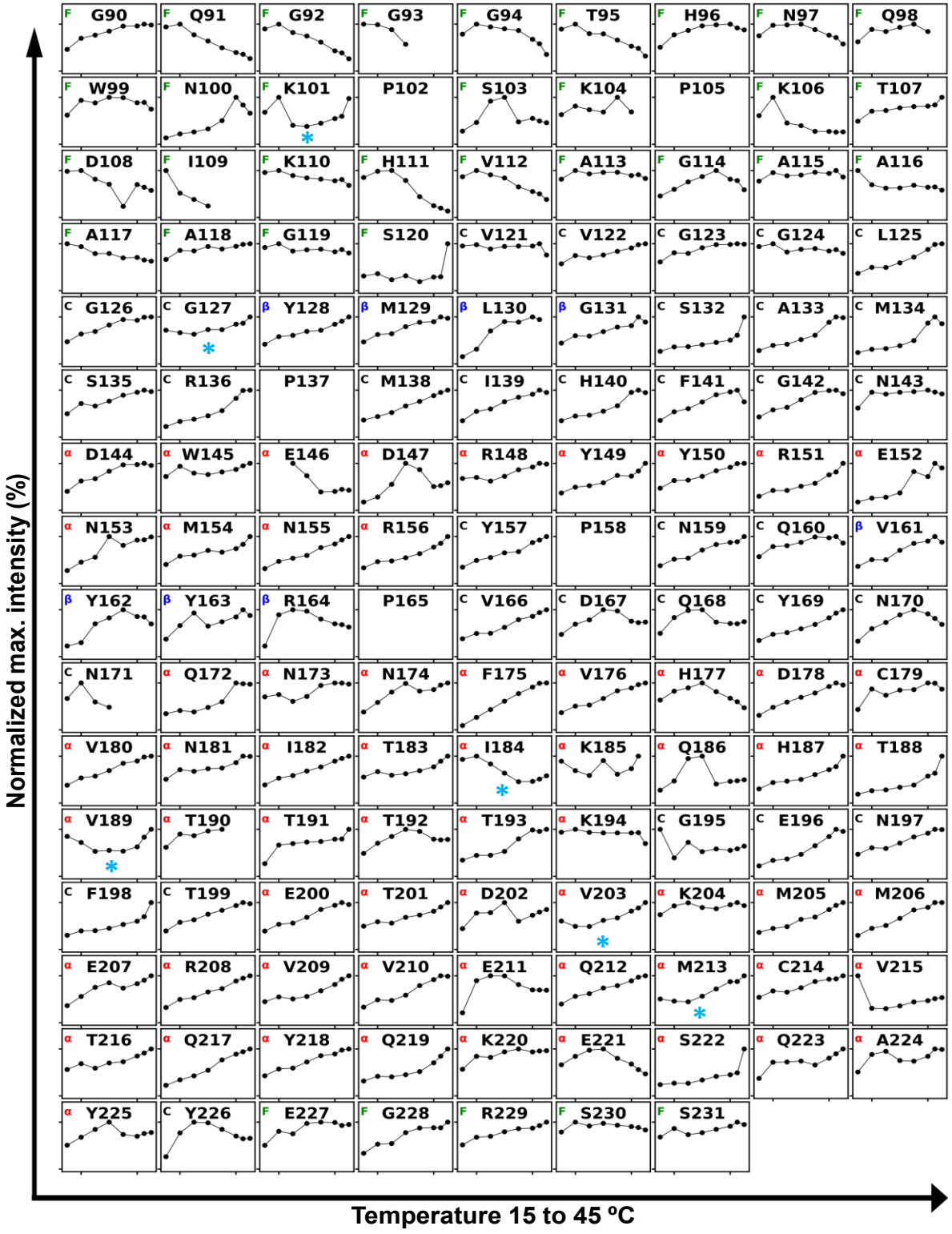

Figure 29 Intensity analysis of VT-N_HSQC of BVPrP^{C}(90-231) in the reversible regime between 15 to 45°C. The plots display normalized intensity versus temperature. The asterisks show residues with a profile consistent with conformational exchange. To enhance the accuracy of peak intensity determination and minimize contributions of noise and small errors in the peak-peaking position, the integral was measured over a small rectangular region in both dimensions (0.05 ppm in ^{1}H and 0.7 ppm in ^{15}N) around the center on each peak in the N_HSQC spectrum. In each plot the amino acid is indicated, and the letter code refers to f=flexible (disordered), α=helix, β=sheet or c=coil.

Analysis of the BVPrP^{C}(90–231) data (*vide infra*) showed certain residues exhibit an inverted U-shaped intensity profile as a function of temperature. This profile arises from competing dynamic processes and does not necessarily indicate slow conformational exchange. For instance, it could be interpreted by a two-step mechanism: firstly, an initial rise in intensity, attributable to enhanced overall protein mobility without a commensurate increase in solvent exchange at the HN proton; and secondly a subsequent decline in intensity, driven by accelerated exchange with H_2O.

4.3.1.4 VT-study to measure water-amide HN exchange rates (k_{ex}): CLEANEX-PM study

The CLEANEX-PM spectrum (107) yields a ^{1}HN /^{15}N correlation map of backbone amide peaks. The cross-peak intensity is primarily governed by the rate of chemical exchange of the labile HN amide proton with the water solvent (k_{ex}), with negligible influence from the residue's motional rigidity or flexibility, provided the peak is sufficiently intense, to be observed in the conventional N-HSQC spectrum. Fitting the intensities of amide signals in CLEANEX-PM spectra, acquired at a series of mixing times, to Eq. 4 yields the k_{ex} for individual HN residues in the protein, with values typically ranging from 1 to 100 s^{-1} (108).

A simple qualitative indication of the absence of H-bond can be obtained from CLEANEX-PM experiments: the mere appearance of a signal in the spectrum indicates that its HN is not involved in a stable H-bond. Thus, the qualitative comparison of CLEANEX-PM at several temperatures can probe discrete changes in solvent accessibility and H-bond arising from protein unfolding and/or alterations that make the residue more/less accessible to water-exchange.

The quantitative measurement of k_{ex} by CLEANEX-PM is relevant because it is one of the most direct experimental reporters of per-residue structural persistence, solvent protection, and dynamic opening events in proteins. It is particularly useful for identifying mobile, non-H-bonded regions, while slower-exchange regimes (detected by H/D exchange followed by N_HSQC) probe the stably folded core.

For amide residues, CLEANEX-PM is a powerful complement to temperature coefficient (T_C). T_C reflects an empirical putative H-bond over a temperature series, whereas CLEANEX-PM (via qualitative or quantitative k_{ex} analysis) is based in the physical property and directly captures changes in H-bond and/or water accessibility between two discrete temperatures, thereby highlighting potential conformational transitions associated with unfolding. Of particular interest for this study is the observation that, at a given temperature, certain amide protons identified as involved in H-bond based on Tc exhibit substantially weakened, or even apparently non-stable, H-bonds when their signals qualitatively appear in the CLEANEX-PM spectrum. Conversely, the absence of a CLEANEX-PM signal should be interpreted with caution because it does not necessarily confirm the presence of a stable H-bond. In such cases,

Tc remains the more reliable indicator of H-bond and the absence of CLEANEX-PM peak only suggests its stability (Table 1).

Table 1 **Qualitative interpretation of CLEANEX-PM in combination with T_C used for the study of BVPrP^C(90-231).**

CLEANEX-PM peak observed	H-bond according to Tc	Structural interpretation
YES	YES	Amide proton exposed to water. Non-stable H-bond
YES	NO	Amide proton exposed to water
NO	YES	CLEANEX-PM not informative. Stable H-bond is a possibility.
NO	NO	CLEANEX-PM not informative

The CLEANEX-PM spectra of the protein were acquired at 15, 25, and 45°C for a series of mixing times between 5 and 200 ms. **Fig. 30** shows the spectra obtained for the mixing time of 200 ms. It can be appreciated that, in general, the number and intensity of the peaks increase with temperature and so does the number of observable residues, owing essentially to the enhancement in k_{ex} as expected.

The quantitative analysis of each signal in the CLEANEX-PM spectrum at the series of mixing times by Eq. 4 yielded the water-amide exchange rates, k_{ex}, for each observable residue of the protein at 15, 25, and 45 °C. An example of the k_{ex}, determination for residue T95 of BVPrP^C(90-231) at the three temperatures is shown in **Fig. 31**. The observation of this residue in the CLEANEX-PM experiment at the three temperatures clearly indicates that it is not engaged in stable H-bond and the k_{ex} follows the expected trend of increasing with temperature. The analysis of, k_{ex}, was only possible for residues showing sufficient intensity and no peak overlap in the CLEANEX-PM spectrum (see **Fig. 32**). **Fig. 32** also marks all observed residues, whether quantifiable or not.

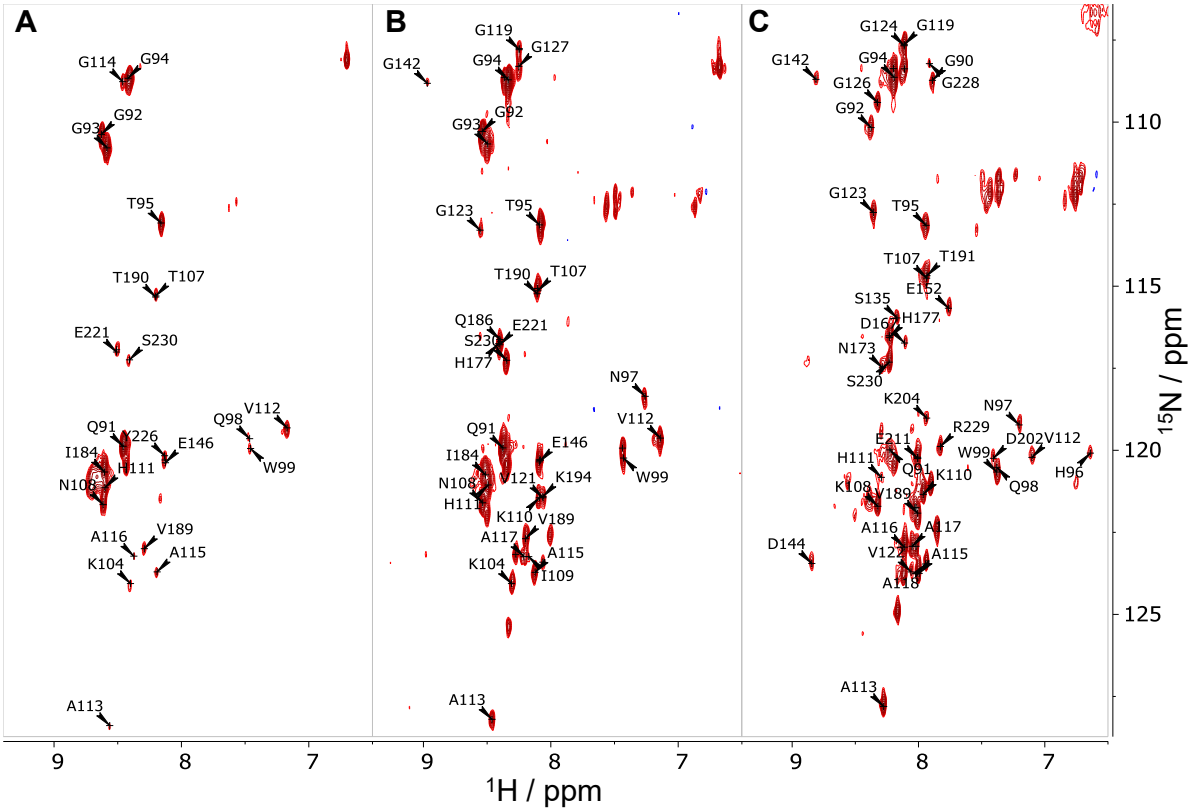

Figure 30 CLEANEX-PM spectra of monomeric BVPrP^{C}(90-231) showing solvent-exposed residues. Spectra acquired at **A)** 15ºC. **B)** 25ºC. **C)** 45ºC. The mixing time of the spectra is the same, 200 ms, and are represented at the same level above the noise. The assignment of the residues is shown.

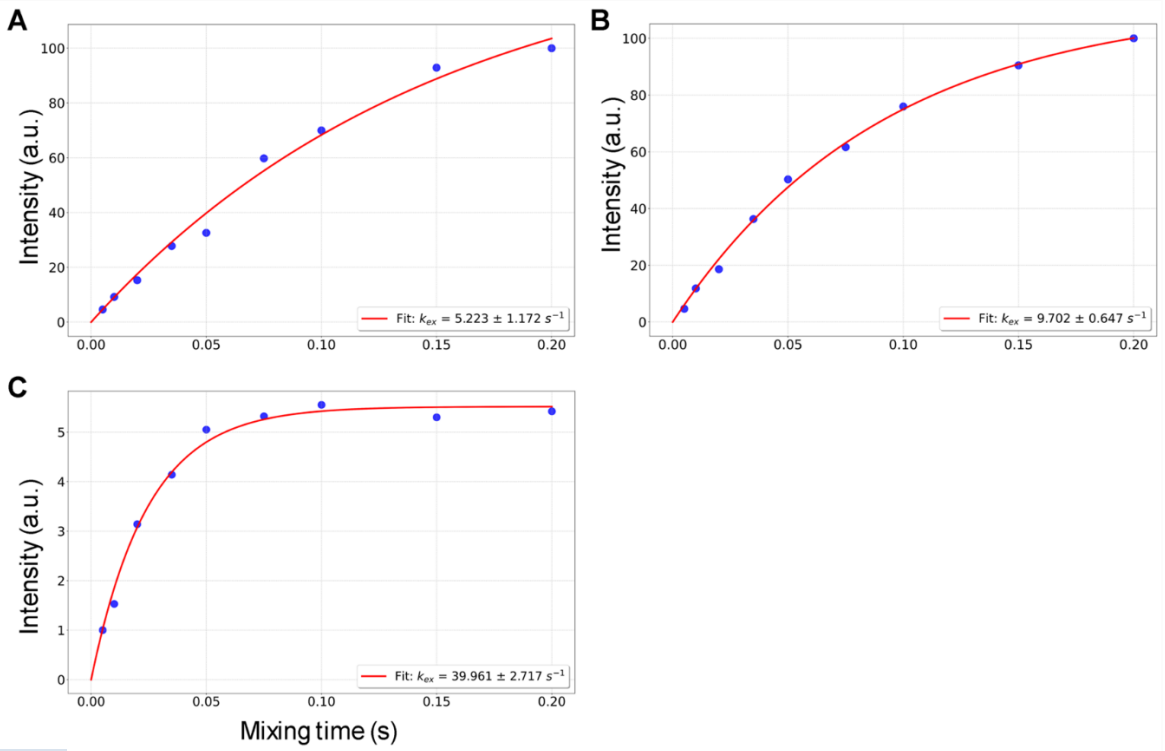

Figure 31 Water-amide HN exchange rate, k_{ex}(s^{-1}), of residue T95 of BVPrP^{C}(90-231). Data obtained at **A)** 15ºC, **B)** 25ºC and **C)** 45ºC. The k_{ex} is shown at the bottom of each plot and was obtained by fitting CLEANEX-PM intensities to Eq. 4.

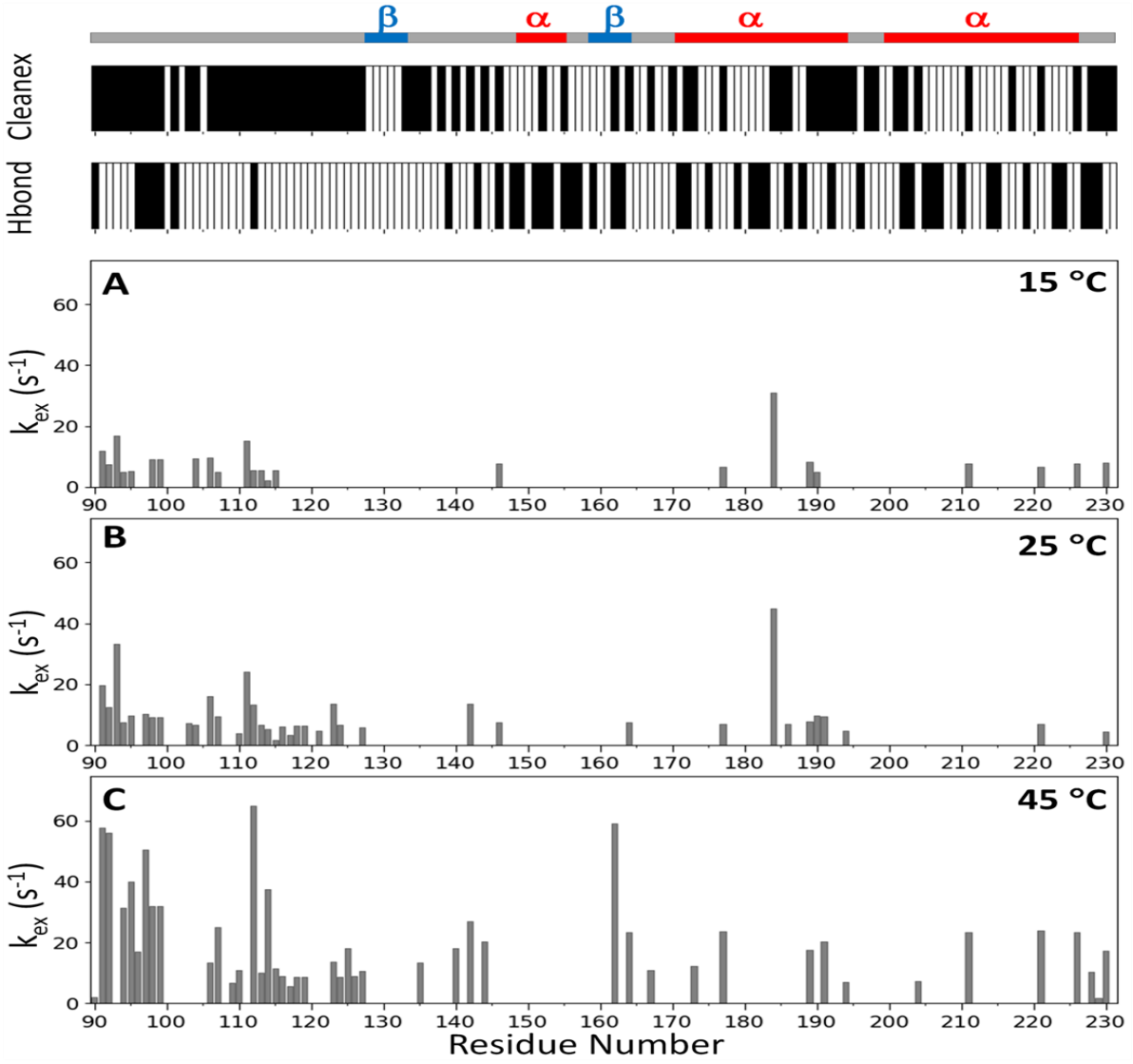

Figure 32 Amide exchange rates, k_{ex} (s^{-1}), and structural correlations for BVPrP^{C}(90-231). Bar plots display the water-amide exchange rates. **A)** 15ºC, **B)** 25ºC and **C)** 45ºC determined only for the quantifiable residues of the naturally folded BVPrP^{C}(90-231). The upper panel shows the secondary elements. The other two panels indicate CLEANEX-PM signal observed in at least one of the temperatures (black = yes) and residue involved in H-bond according to amide Tc.

Fig. 32 reveals that most amide resonances from the N-terminal segment (G90–G127) are detectable in the CLEANEX-PM experiment at least at one of the temperatures investigated. This observation aligns with the pronounced flexibility and solvent accessibility of this intrinsically disordered tail and further suggests that the H-bonds found for these residues by Tc analysis are not retained at 45ºC.

For the short β1 strand (residues Y128-G131) no residues appear to participate in stable H-bond according to the temperature coefficients (Tc) and somewhat unexpected, no signals from this region were detected in any of the CLEANEX-PM spectra analyzed in **Fig. 32**. However, no firm conclusion can be drawn (see Table 1), as the absence of CLEANEX-PM signal may arise from several factors, including k_{ex} rates outside the detectable window of the experiment or from conformational exchange broadening. The latter possibility is supported by significant

CCSD values for residues M129–G131 (**Fig. 27**), which cause line broadening and reduced sensitivity.

For α1 (residues D144 to R156), only two out of 16 residues are observed in CLEANEX-PM: D144 and E146. No firm conclusions can be drawn regarding the unobserved residues. Their lack of signal is compatible with solvent exposure and/or the presence of stable H-bond in this region.

For the short β2 strand (residues V161-R164) no residues are observed in CLEANEX-PM at 15°C. However, at 45°C, two residues, Y162 and R164, become visible (see **Fig. 32** for Y162). Notably, R164 shows evidence of H-bond according to its Tc, yet its detection in CLEANEX-PM at 45°C indicates that this H-bond is not retained (i.e., it is transiently broken or significantly weakened) at the higher temperature of 45ºC.

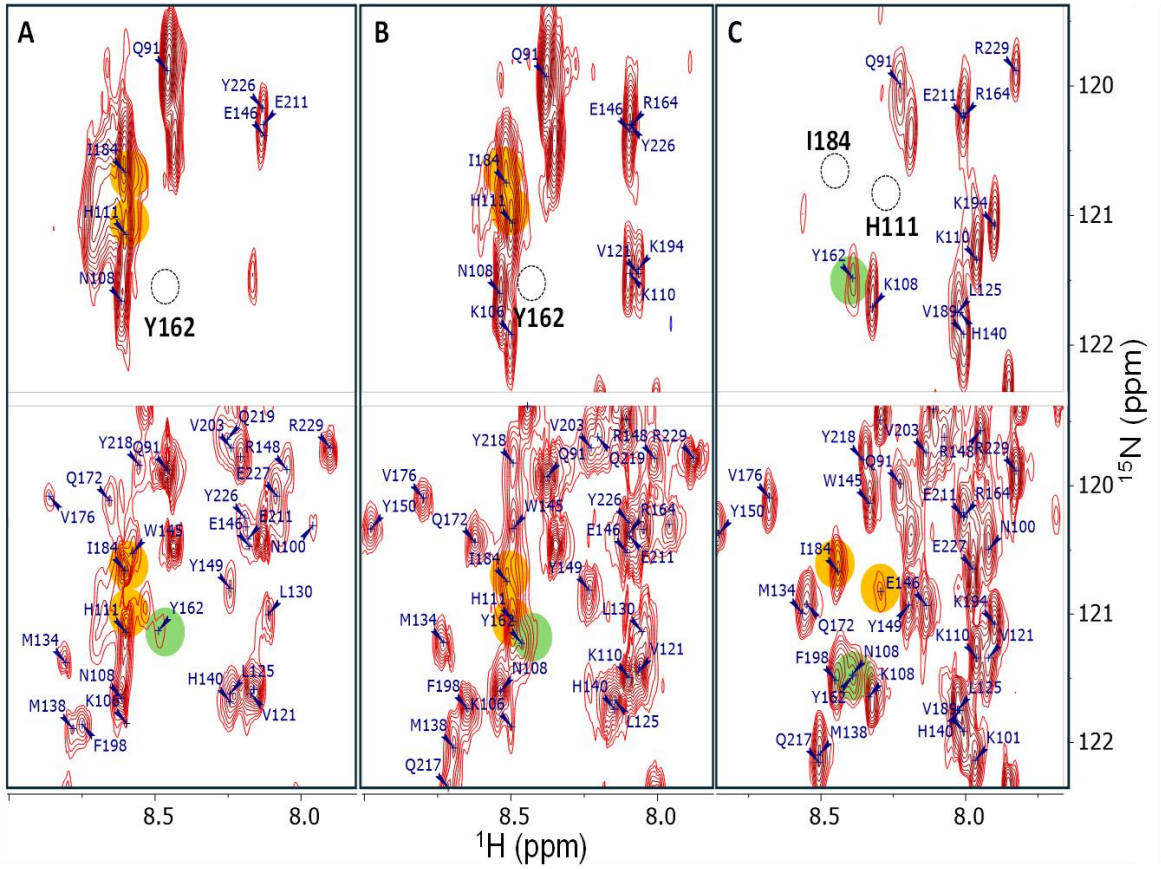

Figure 33 Temperature-dependent visibility of CLEANEX-PM signals. Comparison of CLEANEX-PM cross-peaks (upper panels) and corresponding ^{1}H-^{15}N_HSQC reference spectra (lower panels) at **A)** 15˚C, **B)** 25˚C, and **C)** 45˚C. Residues H111 and I184 (highlighted in orange) and Y162 (highlighted in green) demonstrate contrasting exchange behaviors: signals present at lower temperatures vanish at 45 ˚C, or vice versa. Stripped open circles indicate positions where signals disappear in the CLEANEX-PM spectra despite remaining visible in the HSQC reference. All spectra are shown at a consistent intensity level above the noise.

For residues in α2 (Q172-K194) the CLEANEX-PM detects residues at the beginning (Q172, N173 and H177) and in the end part (V189 to K194) and a few sparse residues in between. Residues N173, H177, V189, T190 and T191 were forming H-bond according to Tc and its observation in CLEANEX-PM is an indication that the H-bond is not retained at the higher temperature of 45ºC.

For residues in α3 (E200-Y225) the CLEANEX-PM detects water-exchange for residues specially at the beginning T201, D202 and K204 together with very few sparse additional residues. Residues T201 and K204 were forming H-bond according to Tc and the emergence of the CLEANEX-PM peak at 45ºC indicates that this H-bond is not retained.

4.3.1.5 Study of the changes in the water-accessible area of monomeric BVPrP^{C}(90-231) during early unfolding events: water-T_2 study at variable temperature

The T_2 transverse relaxation of the water solvent (water-T_2) has been used to study molecular interactions (135). A recent NMR work by Chakraborty et al. (109) explored the time evolution of water-T_2 at constant temperature to monitor spontaneous aggregation of samples of amyloid proteins in aqueous solution. This solvent relaxation approach demonstrated that it effectively tracks perturbations in the hydration shell dynamics as result of key events in the unfolding, oligomerization, and/or fibrillation pathways. The water-T_2 study of amyloid proteins of Chakraborty et al. (109) also demonstrated that the rate and characteristic pathways of these processes are very sensitive to the exact sample conditions such as protein sequence, concentration and temperature.

In this study, the aggregation propensity of BVPrP^{C}(90–231) was found to be negligible or exceedingly slow at room temperature. In contrast, elevated temperatures (50°C) induced spontaneous and rapid oligomerization within minutes, too fast for conducting a water-T_2 study. Due to this time constraint, the objective here is to monitor water-T_2 changes across a series of temperatures that promotes the partial unfolding of the protein within the reversible regime of conformational variability (15–45°C). In principle, provided the protein concentration is sufficiently high, such measurements could detect alterations in protein hydration arising from changes in the first hydration shell. These changes may be induced by conformational transitions, such as partial unfolding or domain reorientation, or more in general by any perturbation in the protein's solvent-accessible surface area (e.g., protein contraction or expansion). Obviously, unlike the study by Chakraborty et al. (109), the temperature variation introduced here must be accounted for when interpreting the results.
The plot in **Fig. 34A** shows experimental water-T_2 values for the protein sample across a range of temperatures from 15 to 45ºC, with an aqueous 10 mM acetate buffer-only sample shown for comparison (i.e. the same buffer conditions used for the preparation of the protein). In the buffer, which contains only free water molecules, water-T_2 increases with temperature owing to enhanced molecular mobility, as anticipated. In contrast, as can be better appreciated in the

expansion of **Fig. 34B**, the curve of the protein has different trends. As the temperature rises from the minimum to the maximum several regimes were identified with letters in **Fig. 34B**.

In the temperature regime from *a* to *b* (15–27°C), T_2 exhibits the steepest positive slope and increases substantially, indicating a purely mobility-driven enhancement of free water molecules, with no significant conformational changes.

Between points *b* and *c* (27–38°C), the slope flattens as the water-T_2 curve reaches a maximum at 35°C and begins to decline, signifying diminished solvent dynamics due to minor conformational rearrangements that initiate monomer unfolding.

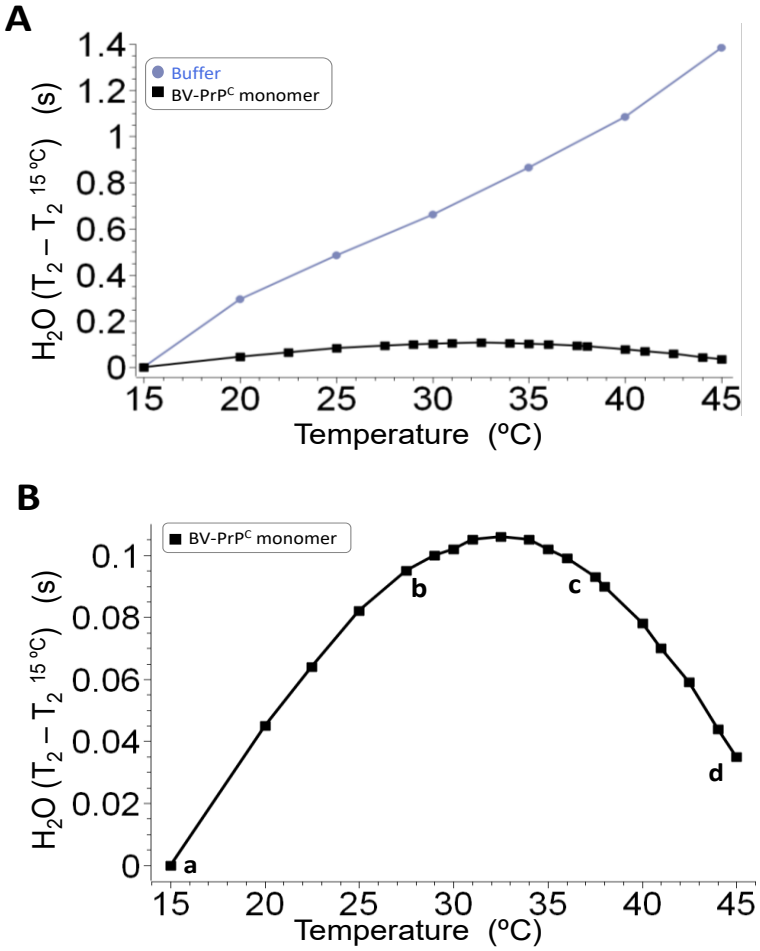

Figure 34 Plot of the water-T_2 relaxation time vs. temperature at 750 MHz. A) The black squares correspond to a fresh sample of monomeric BVPrP^C(90-231) (5 mg/ml, pH 5) prepared in acetate buffer 10 mM. The circles to an aqueous sample that contains exclusively the 10 mM sodium acetate buffer component (pH 5). **B)** Expansion of the water-T_2 curve of monomeric BVPrP^C(90-231). The letters indicate several temperatures regimes that are commented on the text.

Finally, from points *c* to *d* (38–45°C), water-T_2 decreases gradually, consistent with water adsorption onto the protein's first hydration shell. This likely indicates a conformational transition that leads to a more extended structure that increases the solvent-accessible surface area for bound water molecules. Importantly, this transition leaves secondary structural elements unperturbed, as evidenced by N_HSQC spectra in the reversible regime of temperatures from 15 to 45ºC (see **Figs. 21** and **22**) in the VT-N_HSQC section) and aligns

well with the dissociation of some labile secondary structure element/s from the FD core as could be the case of the labile subdomain β1-α1-β2 as discussed in other sections of this thesis.

4.3.1.6 Temperature unfolding induces differential changes in the internal mobility (flexibility) at specific residues of BVPrP^{C}(90-231): ^{15}N-NMR relaxation study

Relaxation measurements were carried out to assess the fast (ps-ns) dynamics of BVPrP^{C} (90–231), to gain insights into the very early unfolding events that facilitate adaptation of the folded domain to the templating surface of PrP^{Sc}. Specifically, R1, R2, and ^{15}N {1H} NOE values allowed us to distinguish structured versus flexible regions, detect conformational exchange processes associated with destabilization, and identify residues in the β1–β2 region most prone to early partial unfolding. These dynamic readouts complement the structural and thermal unfolding data, providing a mechanistic view of how local destabilization initiates the broader unfolding pathway relevant for prion conversion.

To characterize the residue-specific backbone dynamics of BVPrP^{C} (90–231), we measured ^{15}N_R$_1$, ^{15}N_R$_2$ and ^{15}N_NOE at 25°C and 45 °C. The study at the two temperatures at which the structural changes are reversible is useful to study how the dynamics and local flexibility and rigidity evolve when the increase in the temperature induces the early stages of unfolding in the structure.

The ^{15}N_NOE is highly sensitive to fast-timescale internal motions of backbone amide groups, with positive values reflecting restricted mobility typical of ordered secondary structure, and negative values reflecting disordered, solvent-exposed regions. At 25°C (**Fig. 35A**), the NOE data revealed a bipartite architecture of BVPrP^{C}(90–231). Residues in the N-terminal segment (90–120) showed negative or near-zero NOEs, confirming high flexibility and lack of stable secondary structure. Within this otherwise disordered block, a short cluster of residues between Q98 and N108 displayed weakly positive values, suggesting transient or partially structured conformations embedded in the flexible tail. In contrast, residues belonging to the folded domain (121–231) consistently exhibited strongly positive NOE values, confirming their restricted mobility within a well-ordered tertiary fold. The transition between these two regimes was gradual, extending across residues V121–G126, where NOE values progressively increased from negative to positive. This gradient defines a structural boundary region that is neither fully ordered nor fully disordered.

At 45°C (**Fig. 35B**), the overall pattern was retained, but systematic changes were observed. The N-terminal residues (90–120) became more negative, indicating further enhancement of disorder upon heating. The transition zone residues V121–G126 remained intermediate, but the slope of the increase in NOE values was shallower than at 25°C, indicating a blurring of the ordered/disordered boundary. Within the folded domain (130–231), most residues retained positive NOE values, consistent with overall preservation of rigidity. However, local decreases were evident in the β_1–α_1–β_2 assembly and in portions of α_2, suggesting incipient destabilization

of these structural elements at elevated temperature. These results agree with previous data reported for and human PrP^C(90–231), mule deer PrP^C(90–231) or Syrian hamster PrP^C(90–230) (55,89,136). Also, in agreement with these studies, the border between these two disordered/ordered subdomains is characterized by a group of residues (~V121-G126) with values that cross the zero line and slowly and steadily increase until reaching positive values of the same magnitude as the mean value of FD residues. These residues are therefore neither fully ordered nor disordered, showing increasing rigidity from the N to C ends of the ~V121-G126 segment.

The R_2/R_1 ratio of an amide residue provides a more reliable indicator of its dynamic characteristics than the independent analysis of $^{15}N\_R_2$ and $^{15}N\_R_1$.The R_2/R_1 ratio is sensitive to the effective global correlation time of the residue enabling discrimination between more mobile and rigid regions in a way that is rather independent of motional model assumptions (106).

Low R_2/R_1 values are typical of highly mobile or disordered residues, whereas high values are characteristic of compact, folded regions with slow motions or increased slow conformational exchange contributions.

The R_2/R_1 results obtained for BVPrPC(90-231) at 25°C are represented along the primary sequence in Fig. 34.C. Most residues in the N-terminal region 90–127 consistently exhibited very low R_2/R_1 ratios (<5), consistent with high mobility and disorder. The only exception is K101. By contrast, residues in the folded domain (130–231) displayed significant higher ratios in the range of 10–25, characteristic of residues within well-ordered globular structures. The change between these two regions with different dynamic characteristics seems to start at ca. 120 with some intermediate values, reinforcing the transition zone identified by NOE data. Only residue G131, located at the C-terminal end of β1, which exhibits an exceptionally high R_2/R_1 ratio exceeding 30, deviated markedly from these baseline patterns. Such an anomaly is unlikely to reflect rigidity alone and is more plausibly explained by contributions from intermediate conformational exchange on the microsecond-to-millisecond timescale which suggest that around G131 there is a hotspot for additional local conformational dynamics within specific structural elements of the FD.

At 45°C (**Fig. 35D**), the differences between the two aforementioned dynamical regions seem to be still present but it is less evident because the R_2/R_1 ratios of all the residues significantly decrease as expected due to the higher mobility imposed by the thermal motions at this higher temperature. Three residues in the FD have very high R_2/R_1 ratio that deviates from the mean baseline pattern. One is the previously commented G131 in β1. The other two are residues V161 and Y163 located in β2. These findings suggest again the presence of local conformational exchange dynamic in the microsecond-to-millisecond around these residues probably involving large scale amplitude motions.

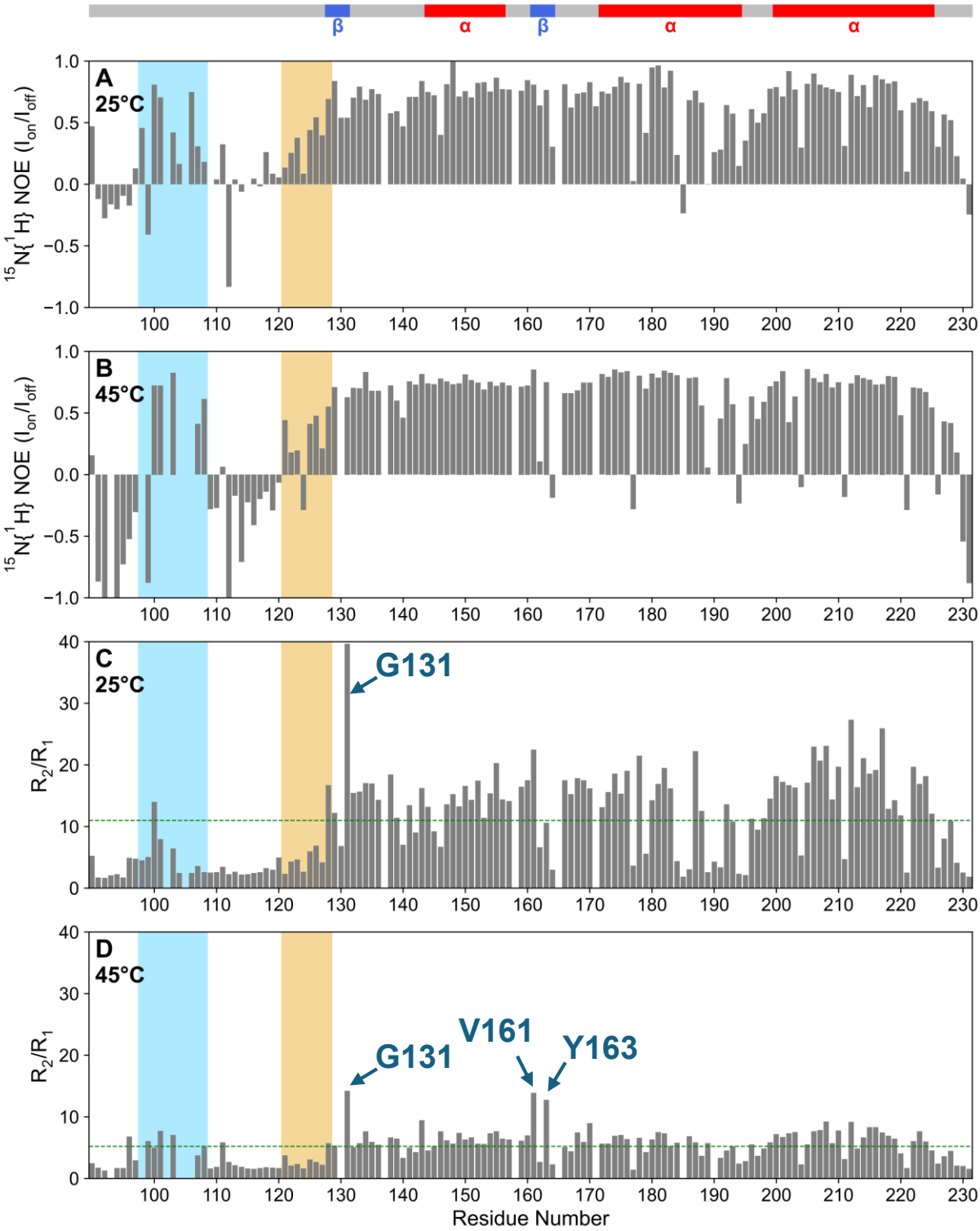

Figure 35 ^{15}N-NMR relaxation analysis of BVPrP^{C}(90-231). ^{15}N_NOE at **A)** 25°C and **B)** 45°C; R_2/R_1 ratios at **C)** 25°C; D: 45°C. The red striped line in C and D represents the mean value. The mean value at 25°C is in the 10-20 range, typical of well folded domains. The region shadowed in orange represents a continuous stretch of residues with Tc < -4.6 ppb/K values contiguous to the flexible 90-120 tail (see main text). The secondary structure elements are shown on the top.

As seen for ^{15}N_NOE, a transition zone with incremental values is seen for the residues at the border between these two blocks (~121-130) (Figs. **35 A and B**). Residue G131, located at the

end of β1, exhibits an abnormally high positive R_2/R_1 at both 25°C and 45ºC which for a residue in a FD is interpreted as a signature of intermediate conformational exchange in the μs-ms regime. A similar situation occurs for V161 and Y163 at 45ºC.

4.3.1.7 Temperature unfolding induces subtle changes of the distances between secondary structure elements of BVPrP^C(90-231): ^{1}H-^{1}H NOE study

The intensity of an NOE cross-peak between two protons enables determination of their inter-proton distance, as it is proportional to the inverse sixth power of their separation (r_{ij}^{-6}). The ensemble of measured NOEs for a protein can thus reveal its conformational preferences (137). Fewer NOEs are typically detected in flexible regions, while structured domains yield more abundant and diverse signals. Typically, a minimum of approximately 12 NOE distance restraints per residue is required to achieve a high-quality structure of a folded protein domain (137).

Interpreting variable-temperature (VT)-induced changes in NOE distances is challenging, first by the expected change in the molecular tumbling correlation time and second and more importantly because heating can not only lead to a partial unfolding but also can cause protein regions to adopt multiple conformations. Because NOE reflects a population-averaged distance, a minor subset of conformations with substantially altered interproton distances can disproportionately affect the measured NOE intensity potentially leading to over- or underestimation of the overall conformational changes.

Despite these limitations in rigorously interpreting NOE-derived distances, qualitative assessments of VT-induced changes in these distances could be valuable for investigating the thermal unfolding of BVPrP^C(90-231). In particular, they enable detection of alterations in key NOE distances, such as long-range NOEs that define the FD structure. Such changes often signal local destabilization, e.g., helix fraying or loop expansion, prior to cooperative global denaturation or oligomerization.

For this study 3D ^{15}N-edited NOESY spectra were acquired for BVPrP^C (90-231) at 25 and 45ºC along with 3D ^{15}N-edited TOCSY spectra to aid in the assignment. Proton-proton NOE distances were calculated and compared at both temperatures. A total of 20 key long-range (i.e. more than 4 residues apart) inter-residual NOEs were observed (Table 2). This is a very limited number of NOE cross-peaks compared with the large number obtained by Christen *et al,*(79) who used up to ~3x protein concentrations compared to ours (79). This limitation is also attributable to the differences of sensitivity of our experimental setup because no cryoprobe was available in our lab and in a lower extend by the accelerated Non-Uniform Sampling (NUS) factors of 50% or 40% used, respectively, to acquire the ^{15}N-edited NOESY spectra (138).

It can be seen in Table. 2 that 12 out of the long-range inter-residual 20 NOE distances decreased by more than ~0.45 Å when heating from 25 to 45ºC, two increased by a similar

magnitude, and six remained essentially unchanged. The NOE plane of four illustrative residues, (residues M129, Y149, Y162 and V180) that changed inter-residual distances when heating from 25 to 45ºC are shown in **Fig. 36**.

Table 2 **Evolution of long range inter-residual NOE distances of BVPrP^{C}(90-231) involving amide protons with other protons upon heating from 25 to 45° C.**

Amide proton	proton	25°C NOE distance (Å)	45°C NOE distance (Å)	Secondary structural elements involved
M129	Y163 NH	4.74	3.50	β1 → β2
G131	V161 NH	6.22	4.86	β1 → β2
A133	Q160 HB	4.24	4.05	coil β1-α1 → coil α1-β2
M134	Q160 HA	3.23	3.17	coil β1-α1 → coil α1-β2
N143	E146 HB	4.33	4.44	coil β1-α1 → α1
W145	R148 HD	3.54	4.24	α1 → α1
R149	M205 HE	3.86	4.31	α1 → α3
M154	Y157 HD	3.42	2.84	α1 → coil α1-β2
Q160	M213 HE	4.32	3.00	coil α1-β2 → α3
Y162	T183 HG	4.28	3.42	β2 → α2
Y162	I182 HG	4.89	3.72	β2 → α2
V166	Y225 HD	4.73	4.25	coil β2-α2 → α3
Q168	R229 HD	3.71	3.51	coil β2-α2 → N-ter coil
N173	V176 HG	4.04	4.02	α2 → α2
D178	N181 HA	4.48	3.70	α2 → α2
V180	V210 HG	3.92	3.35	α2 → α3
I184	V210 HG	4.02	3.92	α2 → α3
T199	D202 HB	4.73	4.14	coil α2-α3 → α3
E207	V210 HG	4.47	3.37	α3 → α3
Q212	V215 HG	4.80	3.82	α3 → α3

The changes of NOE distances observed in Table. 2 between 25 and 45ºC included shortened distances between M129 and Y163, and G131 and V161, indicating a closer average distance for the β1/β2 ensemble. Notably, residues M129, Y163, and G131 displayed a non-linear trend

in the chemical shifts of their backbone amide groups in the VT-CCSD study (detailed in section 4.3.1.2), clearly indicating that these residues are conformational hotspots undergoing significant structural changes. This finding aligns well with the NOE analysis and suggests the destabilization of the two beta-sheet cores.

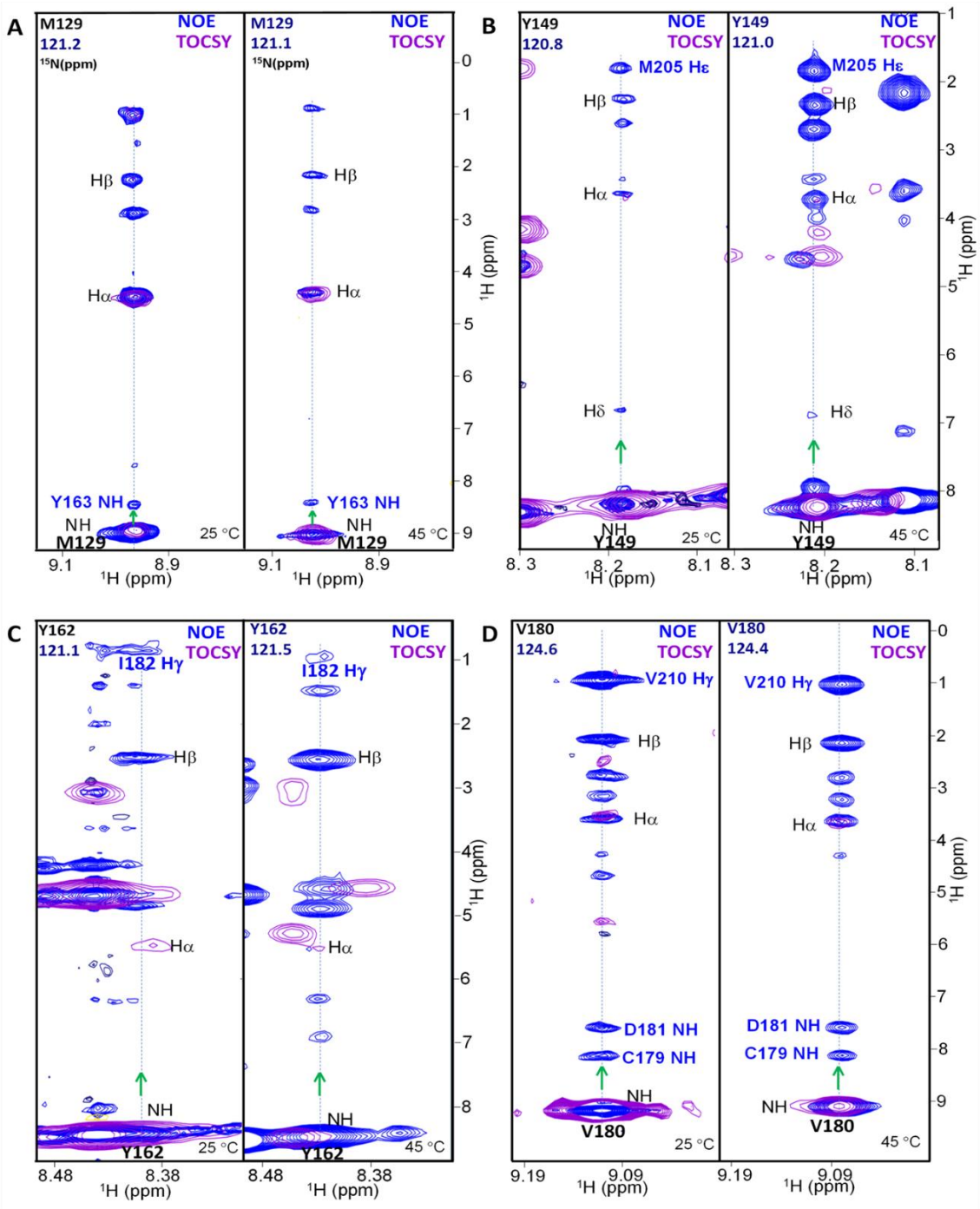

Figure 36 Superimposition of 3D ^{15}N edited TOCSY and NOESY planes of BVPrP^{C}(90-231). Comparison of TOCSY (purple) and NOESY (blue) spectra at 25°C (left) and 45°C (right) for residues **A)** M129, **B)** Y149, **C)** Y162, and **D)** V180. The blue numbers at the top indicate the specific ^{15}N chemical shift plane for each 3D spectrum. Green arrows and striped lines mark the NOE correlation tracks originating from the amide proton indicated at the bottom. Intra-residue NOEs (black labels) are confirmed by overlapping with TOCSY peaks, while inter-residue NOEs (blue labels) appear only in the NOESY spectra, allowing for unambiguous spatial assignment.

The distance (W145-HN, R148-HD) increased by 0.7 Å, suggesting partial unraveling of helix α1 or reordering of R148 side chain but not to the backbone conformation which is consistent with the linearity observed for the backbone amide group of these two residues in the VT-CCSD study (see section 4.3.1.2). Similarly, the NOE distance (R149-HN, M205-HE) increased, potentially reflecting an incipient separation of the β_1-α_1-β_2 and α_2-α_3 subdomains, supporting a hinge displacement at P165–N171 (Table 2 and **Fig. 37**). In this case the four residues show linearity for their amide group in the VT-CCSD study, possibly indicating that the local folding of these residues is not significantly affected by the mentioned hinge rearrangement.

Globally, these results indicate that heating this protein from 25 to 45°C induces multiple conformational rearrangements at the interfaces between subdomains, especially between α_1 and the α_1-β_2 coil. Conversely, the distance between V166 (in the P165–N171 hinge region) and Y225 (HD proton, in helix α_3) shortened, further supporting a hinge-like rearrangement that may facilitate subdomain separation. Similarly, the shortening of the distance between M154 and Y157, both within helix α_1 or the adjacent α_1-β_2 coil, suggests a sidewise displacement of α_1 relative to the coil, potentially enhancing subdomain flexibility. None of these residues exhibit VT-CCSD non-linearities of their backbone amide group possibly indicating that the rearrangement affects the side chain instead of the backbone. An intriguing observation was the shortened distance between Q160 (in the α_1-β_2 coil) and the Hε proton of M213 (in helix α_3). This change appears counterintuitive given the hypothesized separation of the β_1-α_1-β_2 and α_2-α_3 subdomains but may be explained by a concomitant twist and separation of α_1 from the α_1-β_2 coil, allowing transient proximity of these residues. Again, the residues involved are linear in the VT-CCSD study which possibly indicates that the NOE changes are referred to the side-chains.

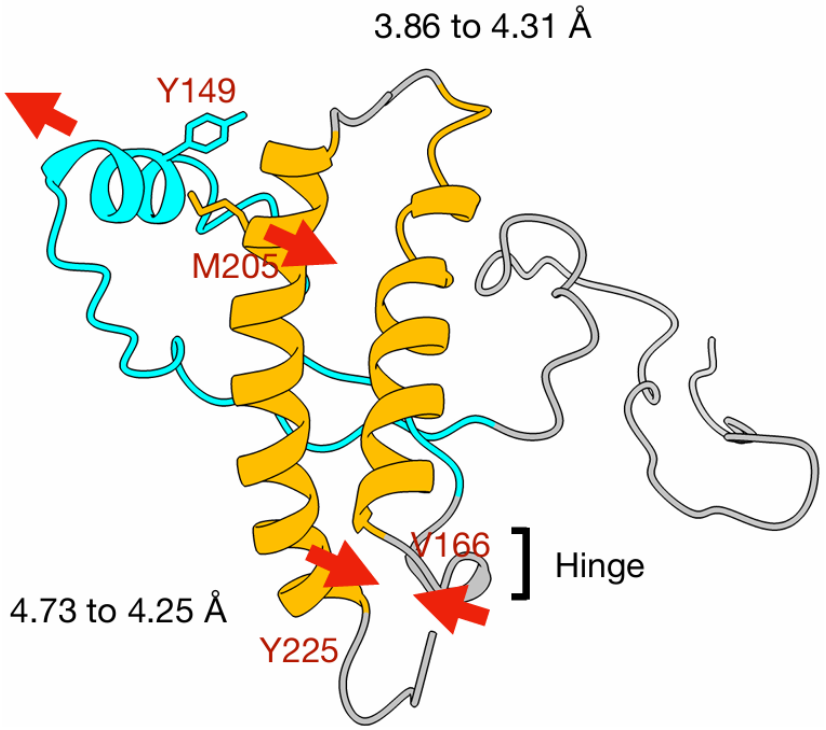

Figure 37 Temperature-induced conformational changes in BVPrP^{C}(90-231). Cartoon representation of plausible structural evolution of the protein between 25°C and 45°C, based on the expansion or contraction of inter-residue NOE distances. The β1-α1-β2 subdomain is highlighted in cyan, while the α2-α3 subdomain is colored orange. The model illustrates how heating alters the spatial proximity and relative orientation of these subdomains.

4.3.1.8 Exploring conformational variability in the amide backbone atoms of native folded monomeric BVPrP^{C}(90-231) by ^{15}N-CEST

^{15}N_CEST spectrum (119–122) allows detecting conformational exchange between native, unfolded, and intermediate conformational states of proteins (139) and has been applied as well to the study of prionic proteins (140). It is particularly valuable for characterizing low-populated (minor) conformational states that are in dynamic equilibrium with the dominant folded state, even when the minor species are invisible in conventional NMR spectra due to their low abundance (<~5%). CEST is sensitive to large conformational exchange processes occurring on the slow timescale, typically between ~5 and 200 ms.

Thermal study of native folded BVPrP^{C}(90–231) within the reversible temperature range (15–45°C) revealed, through analysis of backbone ^{15}N–^{1}H CCSDs and inter-residue ^{1}H–^{1}H NOEs, non-linear temperature-dependent changes in amide chemical shifts and significant variations in certain inter-proton distances, respectively, which strongly suggest of conformational changes occurring in the protein. CEST experiments are ideally suited to discriminate between two scenarios: (i) the conformational change is the product of a single cooperative conformational transition, and (ii) the conformational change leads to a dynamic equilibrium involving the coexistence of two (or more) distinct populated conformational states. The presence of secondary dips in the ^{15}N CEST profiles of specific residues would directly demonstrate scenario (ii). Nevertheless, lack of observable secondary dips does not rule out

conformational exchange, as the process may lie outside the CEST timescale window, the ^{15}N chemical shifts of the two states may be nearly identical or other reasons.

The ^{15}N_CEST spectra of BVPrP^{C}(90-231) were measured for the native folded monomeric protein at 25°C and 45°C. The ^{15}N_CEST curves for each residue are shown on **Figs. 38. 39**, respectively. Most ^{15}N_CEST spectra exhibit the anticipated symmetric and prominent dip at the exact ^{15}N frequency of the amide cross peak, but none show clear evidence of secondary dips that could be interpreted as a signature of slow conformational exchange. Additional ^{15}N_CEST spectra were measured to pursue this objective, employing selective ^{15}N saturation pulses with different bandwidths apart from the one used here of 25 Hz (B_1 field strengths of 15 and 60 Hz) at 25°C. However, neither condition provided evidence of slow conformational exchange (data not shown).

There are several peaks with a single dip and a substantially noisier profile than others. They are the cases of K104, K106 and S120 at 25 ºC (**Fig. 38**) and Q91, G92, and N170 at 45ºC (**Fig. 39**). The effect can be explained by a faster exchange of its amide proton with the water protons during the relatively long saturation time of 0.4 s used for ^{15}N_CEST. The explanation is that a signal to be detected in ^{15}N_CEST requires a transfer of saturation from ^{15}N to the directly attached amide proton, but this process competes with water-exchange equilibrium, which replaces the saturated amide proton with an unsaturated one from water, thereby the detected signal intensity when the FID (Free Induction Decay) is recorded at the scan's end shows no or little effect of saturation. The extreme situation is when the water-exchange is so efficient that the residue shows no dip in the ^{15}N_CEST spectrum. At 25°C (**Fig. 38**), residues H96, N97, Q98, W99, K104, and V112 show no dip, while at 45°C, residues H96, N97, W99, H111, V112, and D202 are similarly absent of dips (**Fig. 39**). There are few residues without ^{15}N_CEST spectrum at 45ºC (**Fig. 39**), the reason is the lack of intensity of these signals in the N_HSQC spectrum at this temperature again as result of temperature effect that increases the water-exchange rate.

Interestingly, residue G131 displays a significantly broader dip at 25°C (**Fig. 38**) compared to other residues in the FD, suggesting it may be involved in a conformational equilibrium with alternative and relative populated conformation(s) with ^{15}N frequencies relatively close to the major conformation. This possibility is further supported by the variable temperature (VT) study, where G131 shows pronounced non-linearity in its CCSD curve (see **Fig. 27**), consistent with this hypothesis. At 45°C, the CEST profile of G131 sharpens and becomes comparable in width to those of the other FD residues. This observation indicates that the higher temperature allows G131 to overcome the energy barrier separating the conformations, shifting the exchange regime toward fast exchange on the chemical-shift timescale (**Fig. 39**). No other residues exhibited significant broadening of their CEST profiles at either 25°C or 45°C (**Figs. 38 and 39**).

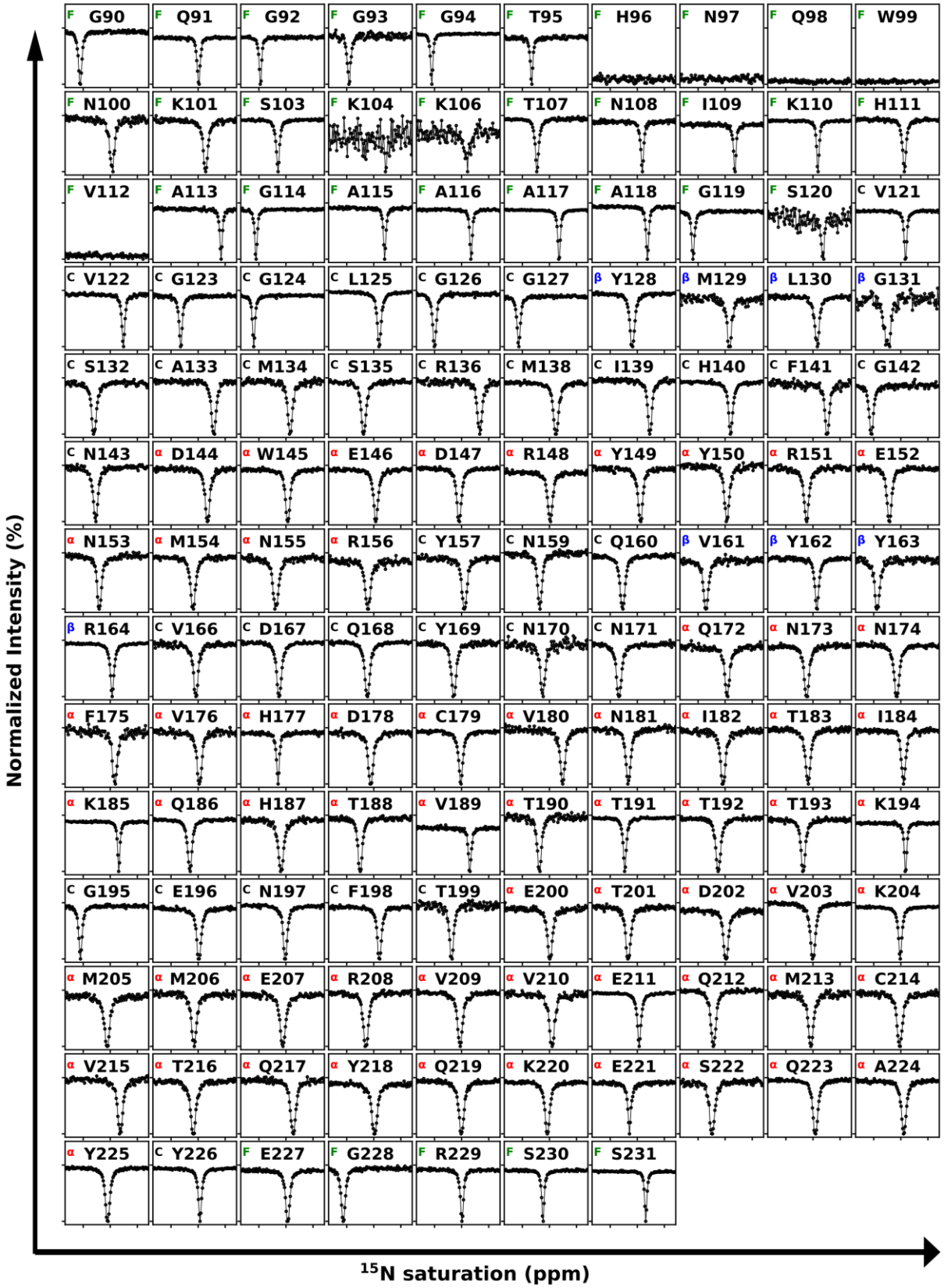

Figure 38 ^{15}N_CEST profiles of the backbone amides NH of the naturally folded monomeric BVPrP^{C}(90-231) at 25°C. In each spectrum the amino acid is indicated, and the letter code refers to f=flexible (disordered), α=helix, β=sheet or c=coil.

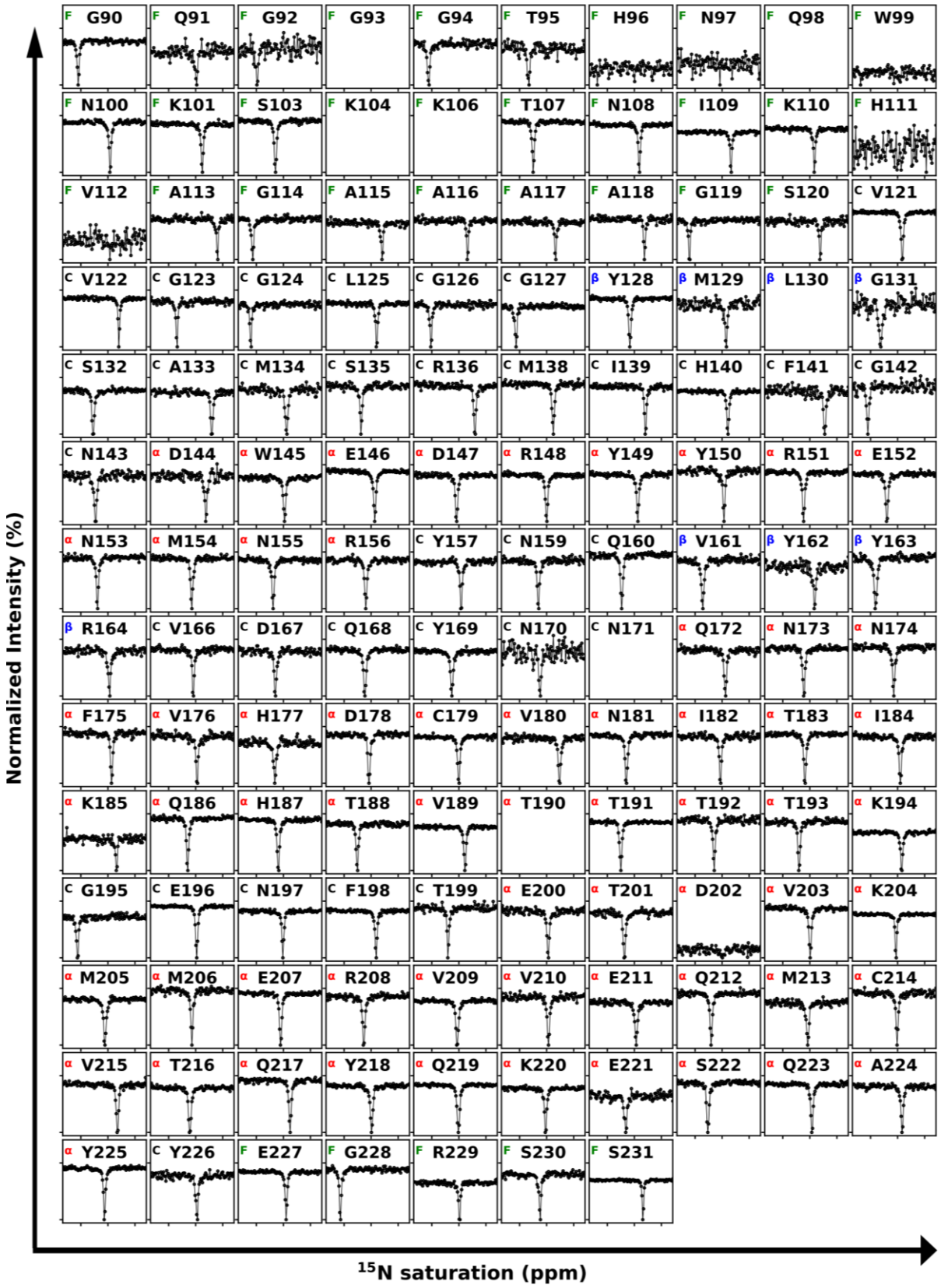

Figure 39 ^{15}N_CEST profiles of the backbone amides NH of the naturally folded monomeric BVPrP^{C}(90-231) at 45°C. In each spectrum the amino acid is indicated. The letter code refers to f=flexible (disordered), α=helix, β=sheet or c=coil. Empty spectra correspond to peaks that are not observed in N_HSQC at this temperature due to fast exchange with the water.

In summary, beyond the nuances relative to residue G131 and others, as reported, the CEST experiment tells us that in the >45°C regime there are motions within specific regions of the FD, but none of them corresponds to sampling of discrete and significantly populated alternative conformations.

4.3.1.9 Exploring conformational variability in methyl groups of native folded monomeric BVPrP^{C}(90-231) by methyl-CEST

Methyl groups are found in the side chains of the six amino acids Ile, Met, Ala, Thr, Val, and Leu and can serve as effective probes for protein structure and dynamics (121). The three methyl protons, with their rapid rotation, are equivalent in NMR, yielding signals with high sensitivity and favorable relaxation properties that are largely unaffected by molecular size. The 2*D* HSQC ^{1}H, ^{13}C spectrum, or alternatively the methyl-TROSY for large systems, provides a cross-peak for each methyl group of the molecule. In proteins, the specific fingerprint of the methyl region of those spectra allows the assignment of each cross-peak to one of the six mentioned amino acid types containing methyl groups, as it is shown in **Fig. 40**, though with some ambiguity.
Methyl-CEST methodology offers the opportunity to detect conformational variability of the methyl groups in the side chain of certain amino acids of proteins operating in a millisecond-to-minute timescale. Methyl groups in proteins are valuable reporters of the structure and dynamics specially because they tend to have favorable relaxation properties for their detection even in large aggregates, and also they often appear at the interface between oligomers in complexes and in the interior of protein cores (121).

The methyl-CEST spectrum of naturally folded monomeric BVPrP^{C} (90-231) was measured at 25°C (**Fig. 40**). A total of 40 methyl unique signals were identified. To simplify the analysis, arbitrary numbers were assigned to the peaks, as their specific assignment to individual residues in the protein requires measuring a number of spectra with selective isotopic labeling strategies, as described earlier, which are beyond the scope of this thesis. Nevertheless, based on ^{15}N edited TOCSY and ^{15}N edited NOESY spectra the side chain methyl groups (Mγ and Mδ) of the four Ile of the protein, residues I109, I139, I182 and I184, could be assigned (**Fig. 41**).

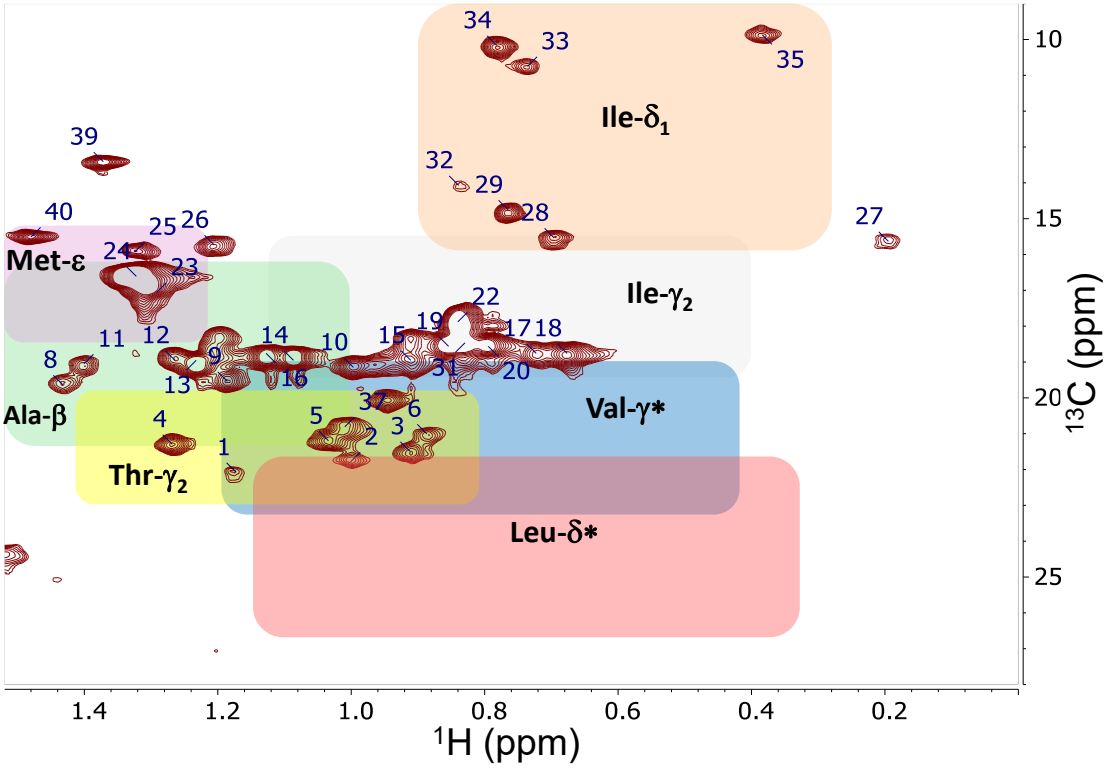

Figure 40 2D Methyl-CEST reference spectrum of BVPrP^{C}(90-231) at 25°C. This spectrum, analogous to a ^{13}C_HSQC, displays the characteristic chemical shift fingerprints for the six types of methyl-containing amino acids. Ovals delineate the regions corresponding to each residue type (based on Fig. 2a in Kurauskas, 2017)(141). Due to the lack of residue-specific assignments, signals are labeled with arbitrary numerical identifiers.

Here, the focus will be on detecting potential alternative conformations of these methyl groups that may differ between the protein's monomeric and oligomeric states (the methyl-CEST study for the oligomeric state is given in section 4.3.2.6).

To build a 1D methyl-CEST intensity profile, the procedure is the same as for a 1D ^{15}N-CEST profile. First, a methyl peak from the 2D methyl-CEST spectrum is selected (**Fig. 39**). Then, the intensity of this peak is evaluated while applying saturation at different ^{13}C frequencies. For each saturation point, the peak intensity is divided by the intensity measured in a reference experiment without saturation. Plotting these values gives the 1D methyl-CEST profile. This profile shows how much the signal is reduced by the saturation. The largest reduction always occurs when the saturation frequency matches the exact ^{13}C chemical shift of the methyl group, which produces the main dip (or peak) in the 1D profile. If the methyl group can adopt alternative conformations, smaller additional dips may appear at other ^{13}C positions.

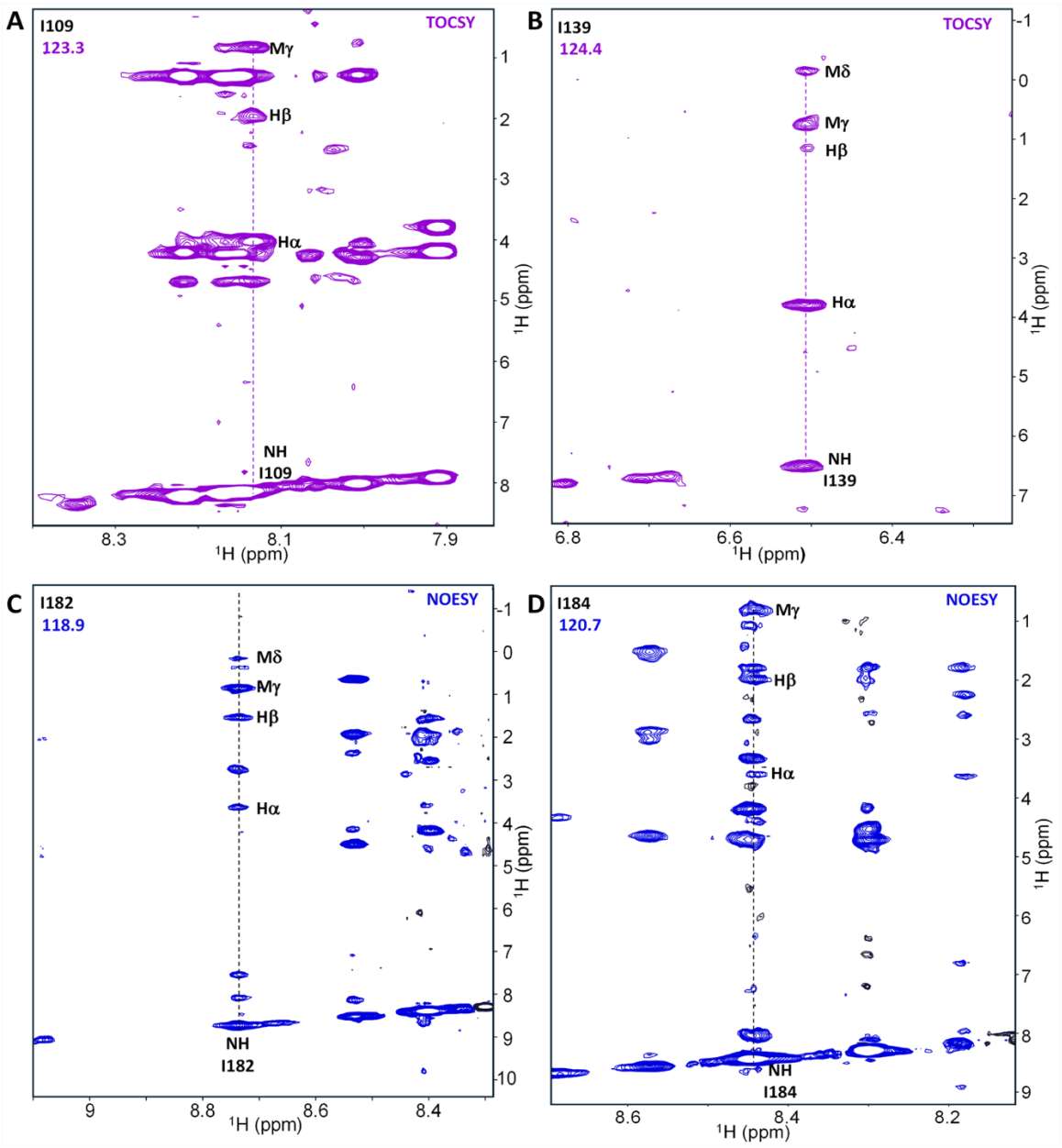

Figure 41 Assignment of Ile methyl groups in BVPrP^{C}(90-231). Panels show ^{15}N-edited TOCSY planes for **A)** I109 and **B)** I139, and 15N-edited NOESY planes for **C)** I182 and **D)** I184. The residue number and corresponding ^{15}N chemical shift plane are indicated in the upper left of each panel. Striped lines mark the tracks of TOCSY or NOE correlations originating from the specific amide proton labeled at the bottom diagonal. These correlations facilitate the unambiguous assignment of isoleucine methyl resonances by linking the side-chain signals to the assigned backbone amide.

The methyl-CEST spectrum shows the expected symmetric and prominent dip at the exact ^{13}C frequency of each methyl group signal. Two methyl groups, arbitrarily numbered as peaks 17 and 33 in **Fig. 39**, exhibit weak secondary dips in their ^{13}C CEST profiles. The chemical shifts of peak 17 (^{1}H/^{13}C: 0.72/18.75 ppm) corresponds to a methyl group at the γ_2 position of Ile, while peak 33 (^{1}H/^{13}C: 0.73/10.79 ppm) corresponds to a methyl group at the δ_1 position of Ile.

In principle these peaks could correspond to any of the four Ile residues in the BVPrP^{C}(90-231) sequence, specifically I109, I139, I182, or I184. Based on the ^{1}H chemical shift assignments for these four Ile residues in **Fig. 41**, some of the possible assignments can be ruled out if they are inconsistent with the ^{1}H chemical shifts observed in the spectrum of **Fig. 40**. According to this criterium, peak 17 can be assigned to I182 or I184 in helix-α_2, while peak 33 can be assigned to I182, I184 or I139 (coil). This indicates that these particular methyl groups of the correspondingly Ile side chain are sampling alternative conformations with slow or intermediate dynamics, even though this does not affect the backbone torsion angles (φ and ψ) of the corresponding Ile residue, for which no secondary dip was observed in the ^{15}N CEST experiment (**Fig. 38**).

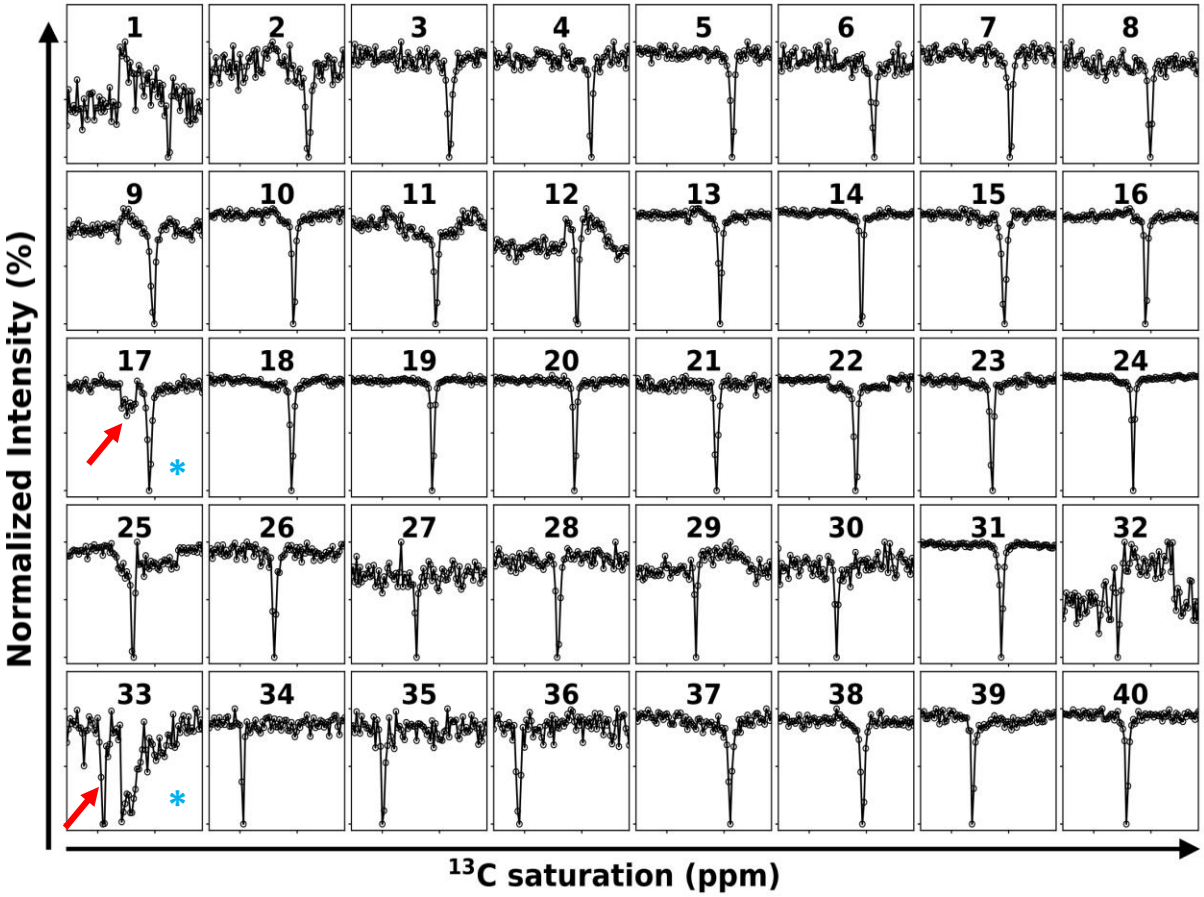

Figure 42 1D Methyl-CEST intensity profiles of BVPrP^{C}(90-231) side chain methyl groups. Profiles acquired at 25°C, with numerical identifiers corresponding to those established in **Figure 39**. The asterisk denotes a spectrum with a secondary dip, indicated with a red arrow, which indicates the presence of a minor conformational state in exchange with the ground state.

4.3.2 Study of Oligomeric State of BVPrP^{C}(90-231)

It was seen in section 4.3 that beginning at ca. 50°C and above, that significant and permanent alterations in the N_HSQC spectral features of BVPrP^{C}(90-231) occur (see **Fig. 21**). This preliminary study suggested the formation of a stable soluble oligomer of BVPrP^{C}(90-231)

induced by temperature which is corroborated by the analyses carried out in this section (*vide infra*). These soluble oligomers are an off-track artefact in the sense that they do not correspond to the deposition and templating of a PrP^{C} monomer on the growing PrP^{Sc} stack.

In what follows samples in which this oligomeric state is formed will be referred as "post-70°C" spectra, where 70ºC denotes the highest temperature to which the sample was heated for more than 2 hours. An early observation is that the post-70ºC sample upon cooling to 25ºC did not recover the original signals of the N_HSQC indicating the occurrence of irreversible changes (**Fig. 23**), in contrast with the reversible changes observed for the naturally folded monomeric sample when heated between 15 to 45ºC (this reversible regime was studied in section 4.3.1).

This section aboard the characterization of the oligomeric state formed in the post-70ºC samples of the protein by using NMR and other techniques and a comparison with the native folded protein in the monomeric state. The following properties/experiments are studied here: signal intensity analysis of N_HSQC, SEC and TEM, DOSY diffusion study, ^{15}N_CEST and methyl-CEST.

4.3.2.1 Structural features of the oligomeric state of BVPrP^{C}(90-231) by analyzing N_HSQC peak intensities

The N_HSQC of the protein of the post-70ºC sample (1.3 or 6 mg/ml and pH 5) measured at 25ºC features substantially alterations compared to the original natively folded spectrum at the same temperature (**Fig. 23**). The post-70ºC N_HSQC is characterized by widespread peak broadening, diminished signal intensities, and even complete peak disappearance (**Fig. 23B**). These spectral perturbations indicate a substantial elevation in the transverse relaxation rate (R_2) of many residues, primarily driven by the emergence of high-molecular-weight species and strongly suggests the formation of soluble oligomers of the protein by self-aggregation.

The quantitative analysis of the peak intensities in the N_HSQC spectrum of the 25ºC post-70ºC sample shows only 46 peaks with appreciable intensity, while the remaining 64% of peaks either disappear or show significantly reduced intensity (**Fig. 43A**). Most of the visible peaks correspond to residues located in the intrinsically disordered N-terminal (~90-120) and short C-terminal (~227-231) sequences (**Fig. 43**). However, several signals from residues within the FD remain detectable in the oligomeric sample; these must belong to structural elements that do not contribute to the oligomer core, retain their original fold (as indicated by unchanged chemical shifts), and maintain a degree of local flexibility independent of the oligomer's overall slow tumbling. The majority of these residues (Q172, N174, D178, V180, N181, Q186, H187, T190, T191, and T193) are in helix α2, comprising 43% of its sequence. Residues G195 and E196, situated at the C-terminal edge of α2 in the short coil connecting to α3, are also detected. In contrast, only two residues from α3, D202 and E222, appear prominently in the spectrum. Similarly, two residues from α1 (D147 and R148, representing 15% of that helix) and two from β2 (V161 and Y162, 50% of its sequence) are observed with high intensity (**Fig. 43A**).

In summary the peaks detected in the N_HSQC spectrum of the 25ºC post-70ºC sample fall into three categories: (a) a majority corresponding to residues in the ~90-121 and ~225-231 unfolded regions; (b) peaks from residues within the folded domain (FD) with unchanged chemical shifts; and (c) a very small number of new peaks (2-4) not present in the original 25°C spectrum **(Fig. 23)**. These observations substantiate the hypothesis of the formation of soluble oligomers caused upon heating and cooling and a plausible cartoon scheme compatible with the observations is shown in **Fig. 43C.**

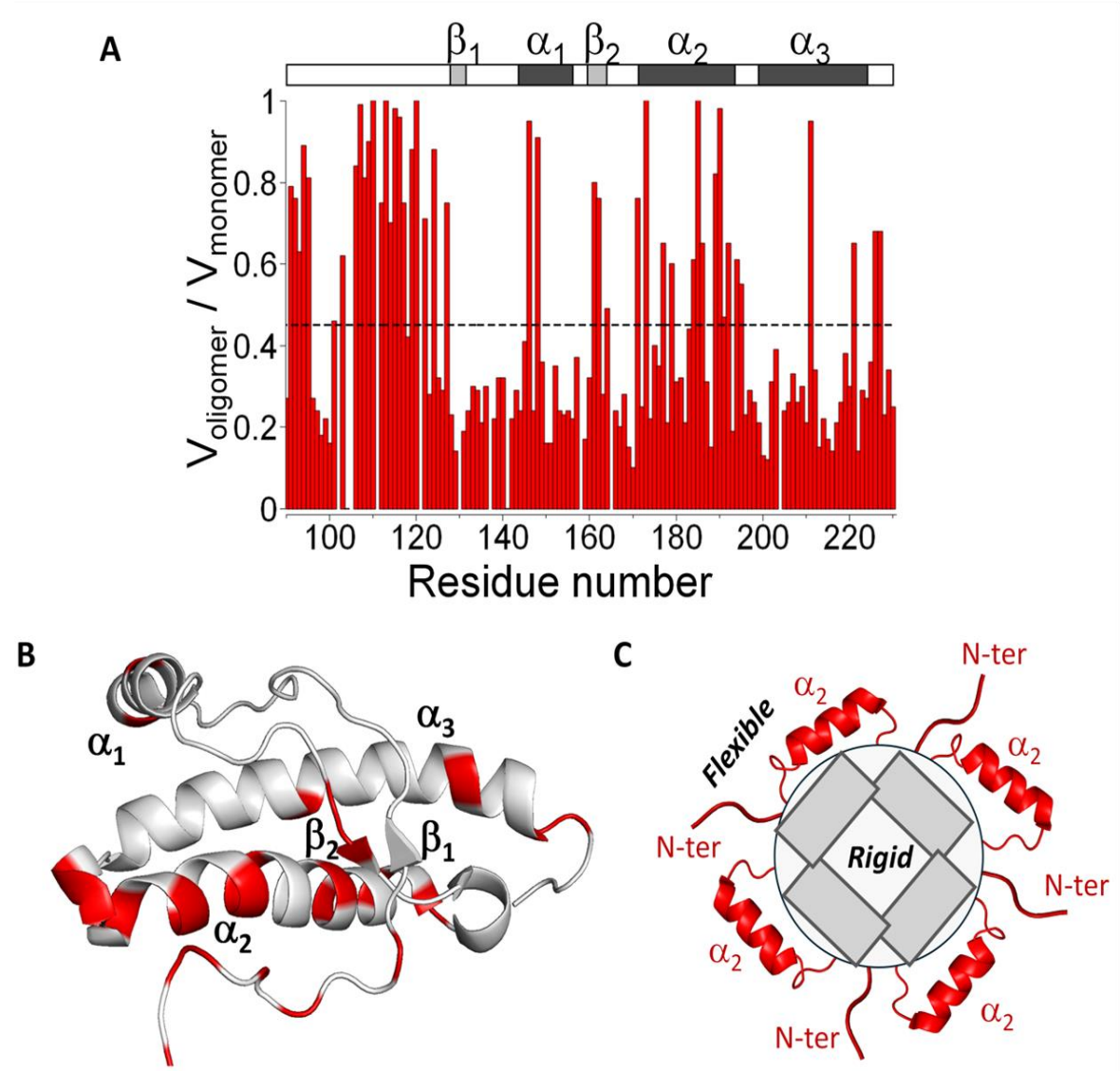

Figure 43 Comparison of the post-heated BVPrP^{C}(90-231) sample with the native monomeric state. Analysis of the sample at 25ºC after heating to 70ºC, relative to the native folded monomer (6 mg/mL, pH 5). **A)** Bar plot showing the normalized volume ratio; the dashed line at 0.45 indicates the mean ratio across all residues. **B)** 3*D* structure of the native protein, with residues retaining visible intensity highlighted in red. **C)** Schematic of a proposed oligomer model featuring "dangling" portions; these regions maintain independent conformational mobility and remain detectable in the N_HSQC spectrum.

4.3.2.2 Evidence of the oligomeric state of BVPrP^{C}(90-231) by Size Exclusion Chromatography (SEC) and Transmission Electron Microscopy (TEM) analysis

We performed size exclusion chromatography (SEC) on post-50°C, post-60°C, and post-70°C samples. The post-50°C chromatogram shows a single peak corresponding to the BVPrP^{C}(90-231) monomer (**Fig. 44A**). However, the post-60°C chromatogram displays a second peak, corresponding to an earlier-eluting (larger) species, with an elution time consistent with a ~12-mer based on the column calibration. In the post-70°C chromatogram, this peak is also present, with its relative area increasing at the expense of the monomer peak, reaching an oligomer-to-monomer ratio of approximately 2:3.
Finally, negative stain Transmission Electron Microscopy (TEM) of 25°C, post-50°C, post-60°C, and post-70°C samples revealed numerous spherical particles (~10-15 nm diameter) in the post-60°C and post-70°C samples, but not in the 25°C or post-50°C samples (**Fig. 44B**).

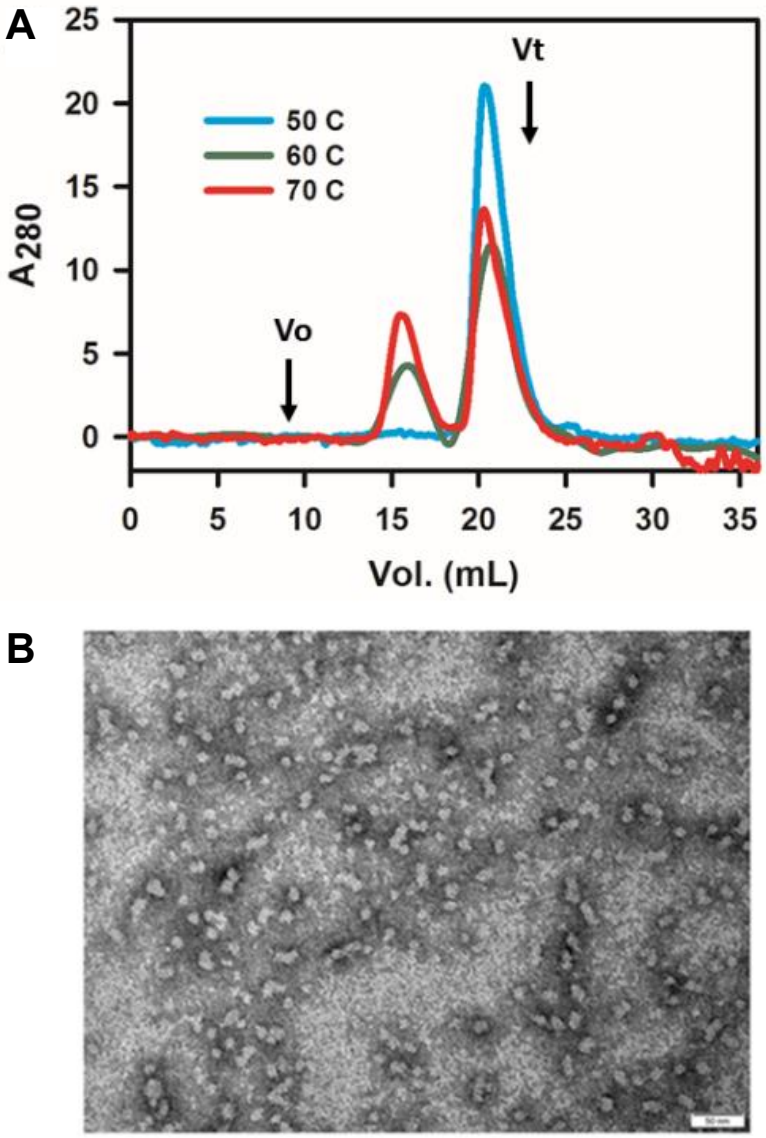

Figure 44 Partially unfolded BVPrP^{C}(90-231) collapses into soluble oligomers at >50°C. A) SEC analysis. Areas under the two peaks correspond to relative amounts of ~2:3. **B)** Negative stem TEM of the oligomer.

4.3.2.3 Analysis of the size of the oligomeric state of BVPrP^{C}(90-231) by DOSY

In the previous section, the oligomeric state was assessed by SEC, a technique that physically separates species based on their hydrodynamic volume. In this section, diffusion-ordered spectroscopy (DOSY) NMR is employed to determine the size (and thus the oligomeric state) of the oligomer directly under the identical experimental conditions (pH, temperature, concentration, buffer, etc.) used for the main NMR studies. This complementary approach eliminates potential biases or artifacts that may arise from SEC, such as interactions with the column matrix, dilution effects during elution, or non-native conditions in the mobile phase.

The self-diffusion coefficient (D) in solution provides a valuable probe for assessing molecular self-aggregation, owing to its inverse relationship, via the Stokes–Einstein equation or analogues, with the hydrodynamic radius (and thus effective molecular size and weight) of the species. DOSY is a multidimensional NMR technique to measure D of molecular components in pure samples or mixtures.

DOSY spectra were measured at 25ºC (conc. 1.4 mg/ml, pH 5.0) for the intact native folded BVPrP^{C}(90-231) sample and for the same sample at 25ºC post-heated 70ºC during more than 2 hours (**Fig. 45**). The analysis of DOSY was carried by signal integration of regions corresponding to non-exchangeable protein protons, they are highlighted in yellow in both spectra (**Fig. 45A** and **45B**). The fitting of the DOSY intensities of each of these two spectra to a single diffusion component by using Eq. 8 are shown in **Fig. 45C**. The values of D obtained were 0.96±0.04 × 10^{-10} m²/s and 0.63±0.04 × 10^{-10} m²/s, for the native folded monomer and the post-heated 70ºC samples, respectively, indicating the larger size of the species in the later sample, which is consistent with the formation of oligomers.

However, the post-heated 70°C sample is known to contain a mixture of monomer and oligomer in a 2:3 ratio, as determined by SEC in **section 4.3.2.2**, and the ^{1}H spectra of these species completely overlap in the aliphatic region. Consequently, the D value obtained from single-exponential fitting of the DOSY spectrum represents a weighted average of the diffusion coefficients for the monomeric and oligomeric species, yielding an apparent D that does not reflect the true size of the oligomer. To derive a more accurate D for the oligomeric species, the DOSY spectrum was instead fitted to a bi-exponential model (Eq. 9) (116), using the established D value of 0.96 ± 0.04 × 10^{-10} m²/s for the native folded monomer and the 2:3 monomer:oligomer ratio from SEC. This analysis yielded a D of 0.32 ± 0.03 × 10^{-10} m²/s for the oligomer. Assuming a globular shape, the calculated Mw by Eq. 9 for this diffusion value is ~280 kDa, or approximately 16 mers (see Materials and Methods).

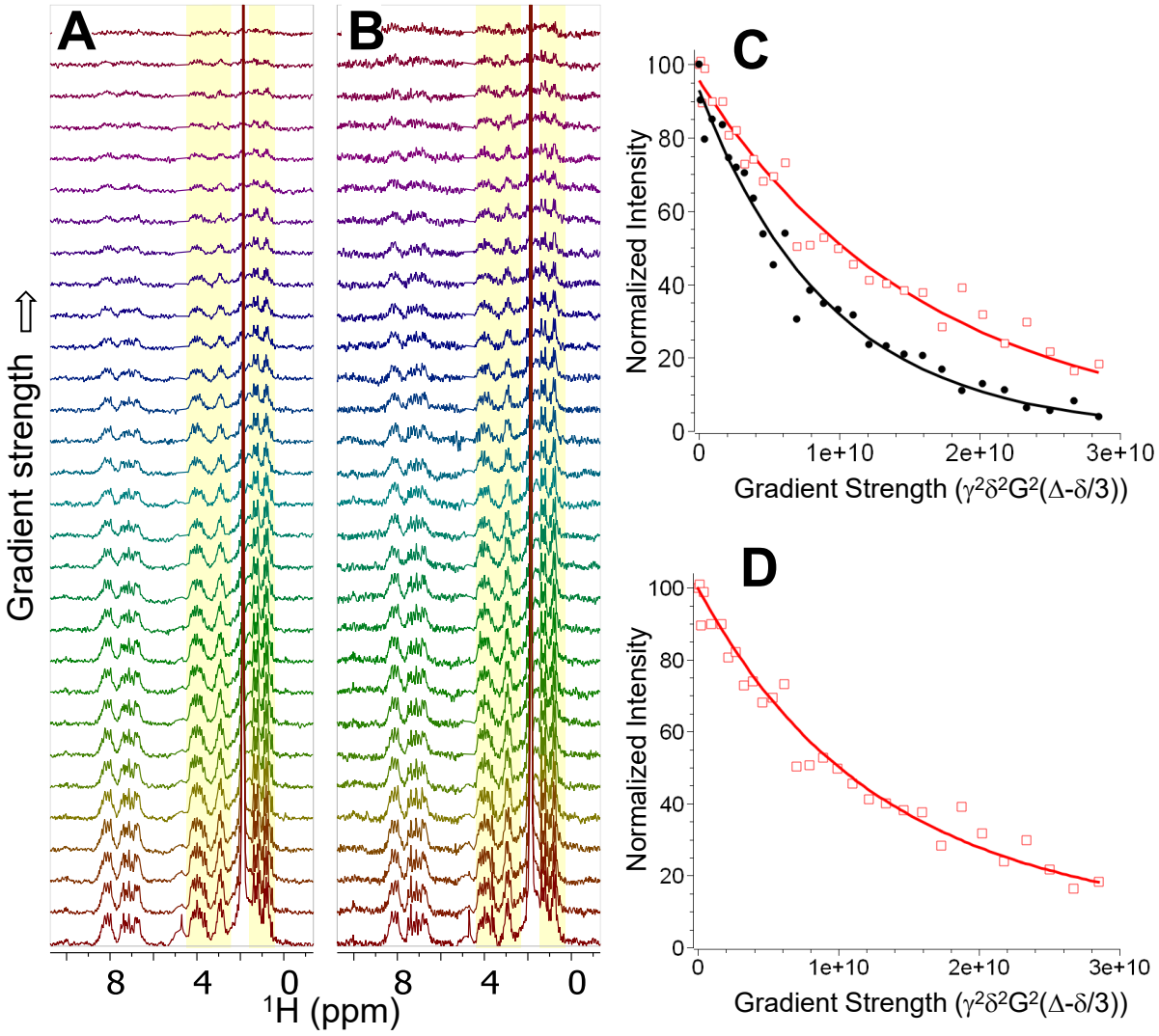

Figure 45 DOSY study of native folded and post-heated 70°C samples of BVPrP^C(90-231) measured at 25°C (1.4 mg/ml, pH 5). A) 1D traces of the DOSY spectrum of the native folded protein. **B)** 1*D* traces of the DOSY spectrum of the post-70°C sample. The signal integral in the regions highlighted in yellow in A and B were analyzed. **C)** Plot of DOSY integral versus gradient strength. Black circles and open red squares represent the native sample and the post-70°C sample, respectively. Solid lines show fits to the mono-exponential Stejskal-Tanner equation (Eq. 8), yielding diffusion coefficients D of 0.96±0.04 × 10^{-10} m^2/s for the native sample and 0.63±0.04 × 10^{-10} m^2/s for the post-70°C sample. **D)** Plot of DOSY integral versus the gradient strength of the post-70°C sample fitted to a double-exponential equation (Eq. 9) used to determine the diffusion of the oligomeric species.

4.3.2.4 Study of the conformational stability of the oligomeric BVPrP^C(90-231): water-T_2 study at variable temperature

The time evolution of the T_2 transverse relaxation of the water solvent (water-T_2) has been used to study molecular interactions (135) and to track perturbations in hydration shell dynamics during spontaneous aggregation processes at constant temperature, such as oligomerization or amyloid fiber formation (109).

In this study, the water-T_2 was investigated for pre-formed oligomers derived from the post-70°C sample of BVPrP^C(90-231) over a temperature range of 15–45°C. The objective was to probe the conformational stability of these oligomers in response to temperature changes, based on the sensitivity of water-T_2 measurements to perturbations in the first hydration shell arising from de-aggregation, unfolding, or domain reorientation or any other effect that perturbates the water accessible surface of the oligomer.

The plot in **Fig. 46** shows experimental water-T2 values for the oligomeric protein sample as a function of temperature, with those of the monomeric protein already discussed in Section 3.3.7 for comparison. For the oligomer, water-T_2 values increase monotonically with temperature and reach a plateau at ca. 35ºC and remain stable up to 45ºC, reflecting the enhanced mobility of the predominant free water molecules and indicating no major alterations in oligomeric shape or aggregation state. By contrast, the monomeric protein exhibits a marked decrease in water T_2 relaxation time over the higher temperature range. This has been interpreted as resulting from partial unfolding, as detailed previously. Overall, these water-T_2 measurements assess the conformational stability of the thermally formed oligomeric state of BVPrP^C(90-231) in the temperature range of 15-45ºC.

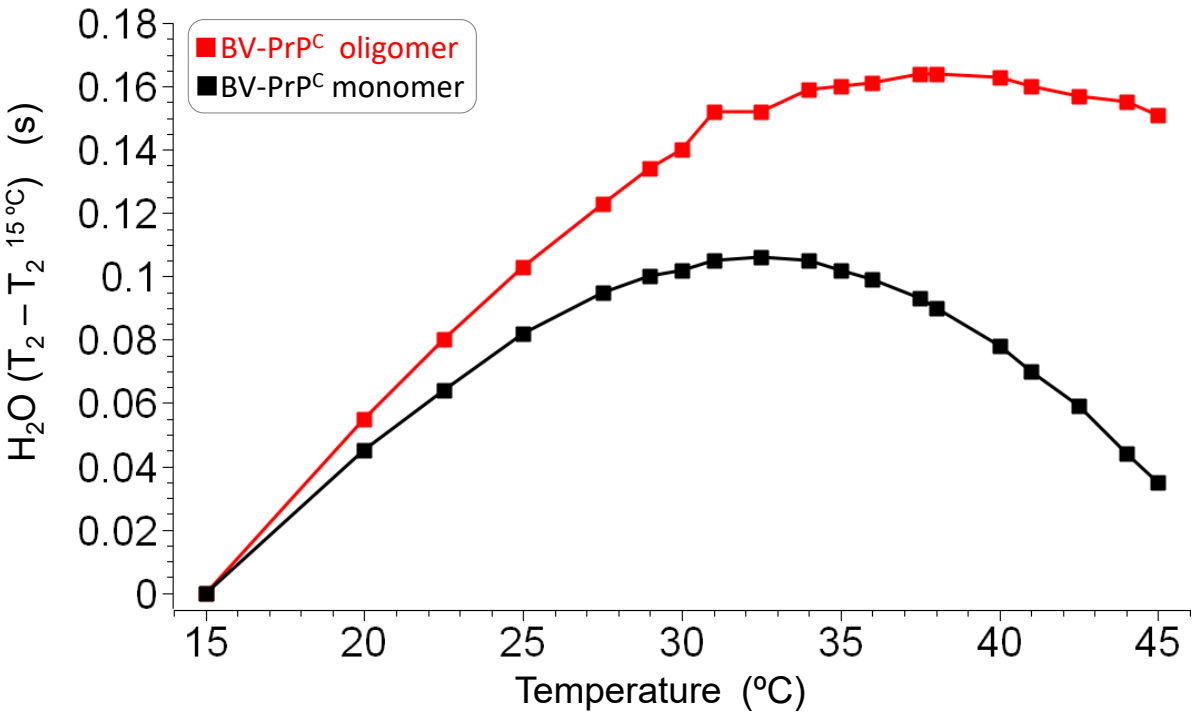

Figure 46 Plot of the water-T_2 relaxation time of water signal vs. temperature at 750 MHz. The red filled squares correspond to the post-70°C oligomeric state of BVPrP^C(90-231) (5 mg/ml, pH 5) and the black squares correspond to a fresh sample monomeric state of the protein (5 mg/ml, pH 5).

4.3.2.5 Exploring conformational equilibrium between monomeric and oligomeric forms of BVPrP^{C}(90-231) by ^{15}N-DEST

The ^{15}N_DEST (Dark-statE chemical exchange Saturation-Transfer) spectrum (119,142) has been applied to study large protein assemblies in exchange with its monomeric state (119) as it is the case of amyloid fibrils (143)

In this section, the ^{15}N_DEST spectrum was measured at 25ºC for the U-^{13}C,^{15}N post-75 labelled sample of BVPrP^{C}(90-231) (6 mg/mL, pH 5). This sample was determined by size-exclusion chromatography (SEC) to exhibit an oligomer-to-monomer ratio of approximately 2:3 and DOSY spectra estimate a size of the oligomeric of ca. 16 mers (see section 4.3.2.2). The objective of ^{15}N_DEST is to detect the transient binding equilibrium between the oligomeric and monomeric forms.

The ^{15}N_DEST spectra for those residues exhibiting sufficient signal intensity in the oligomeric sample of the protein are presented in **Fig. 47**. Their general aspect is substantially noisier than the comparable residues in the ^{15}N_CEST spectrum of the pure monomer sample (**Fig. 38**). Such intensity loss is attributable to the presence of the large size oligomers. It can be appreciated that ^{15}N_DEST spectra of the sample suffer from a substantial broadness compared to the visible signal in the N_HSQC spectrum. In other words, the effect demonstrates the presence of a weak binding equilibrium between monomer and oligomer with the monomer species coming in and out of the oligomer. The formation of this complex is likely favored by a variety of non-covalent stabilizing forces (hydrophobic, electrostatic, H-bond, π-stacking, etc.).

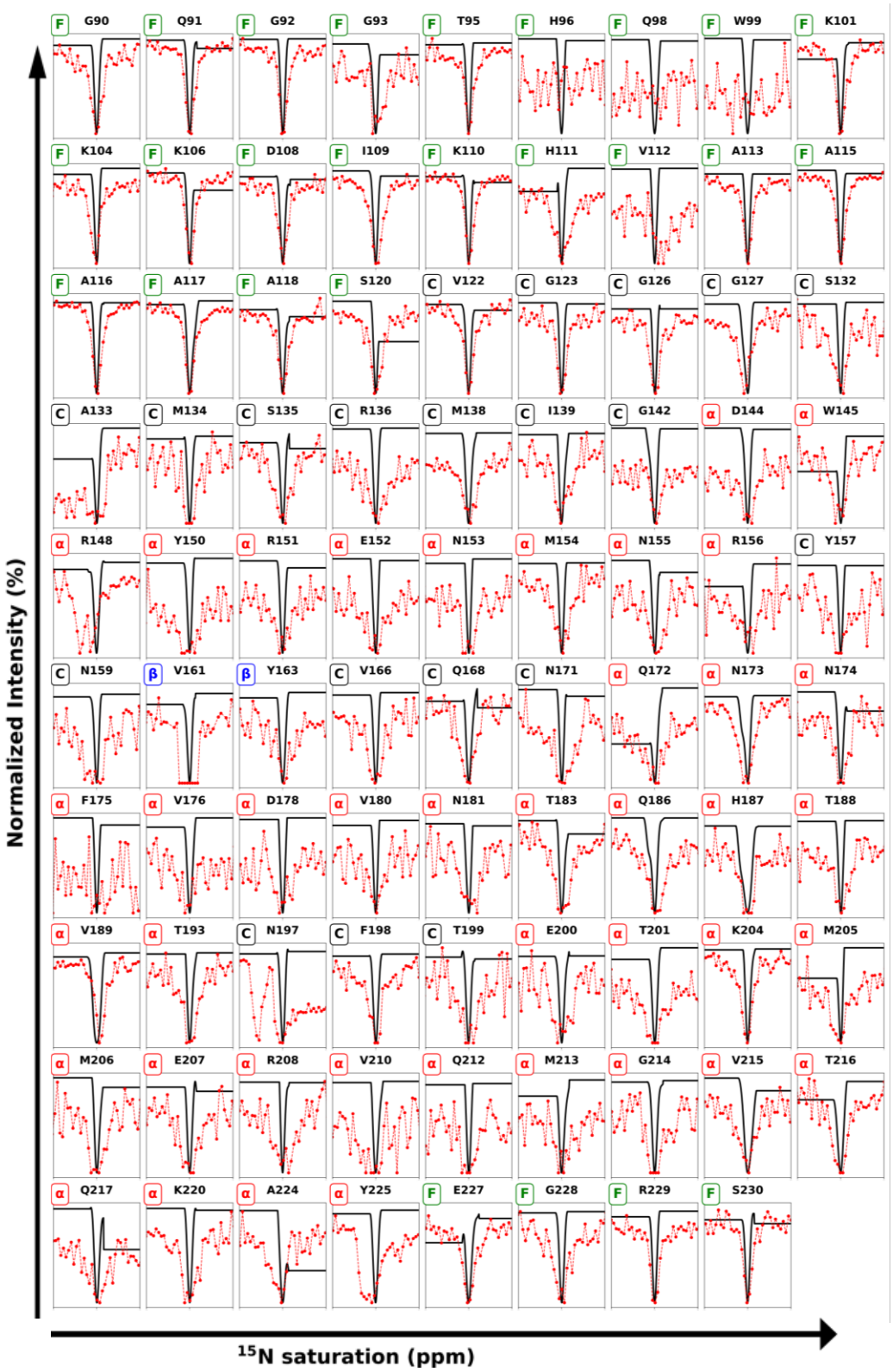

Figure 47 ^{15}N_DEST profiles of the backbone amides NH of the oligomeric BVPrP^{C}(90-231) at 25°C (post-70°C). In each spectrum the amino acid/s is/are indicated. The spectra are centered around the exact ^{15}N chemical shift of the residue and span 10 ppm. The red trace (connected by points) represents the subtracted DEST on-off normalized intensities, while the continuous black trace shows the corresponding normalized reversed intensity from the DEST off reference spectrum which is given for comparison purposes. The letter code refers to f=flexible (disordered), α=helix, β=sheet or c=coil.

4.3.2.6 Exploring conformational variability in methyl groups of oligomeric BVPrP^{C}(90-231) by methyl-CEST

The methyl-CEST spectrum of the BVPrP^{C}(90-231) oligomeric state at 25°C post-70 is shown in **Fig. 47**. The spectrum exhibits all 40 methyl signals previously identified in the analogue spectrum of the monomer (**Fig. 42**), but most exhibited significantly reduced intensity and were obscured by elevated noise levels, hindering detection of potential secondary dips. The broadness/narrowness reflects the inherent rigidity/flexibility experienced by the specific methyl side chain within the oligomer, and it likely correlates with the visibility (or invisibility) of the corresponding residue in the ^{15}N_HSQC spectrum of the oligomer (**Fig. 23**).
None of the methyl-CEST spectra of the oligomer displayed clear signs of secondary dips suggestive of slow conformational exchange phenomena. In particular, the substantial noise in the methyl-CEST spectrum of the oligomeric protein (**Fig. 47**) precludes identification of whether signals 17 and 33 display the secondary dips observed in the methyl-CEST spectrum of the monomeric protein (**Fig. 40**).

In conclusion, no secondary conformations were found for methyl-side chains in the oligomer in contrast with the two cases found for the monomeric state.

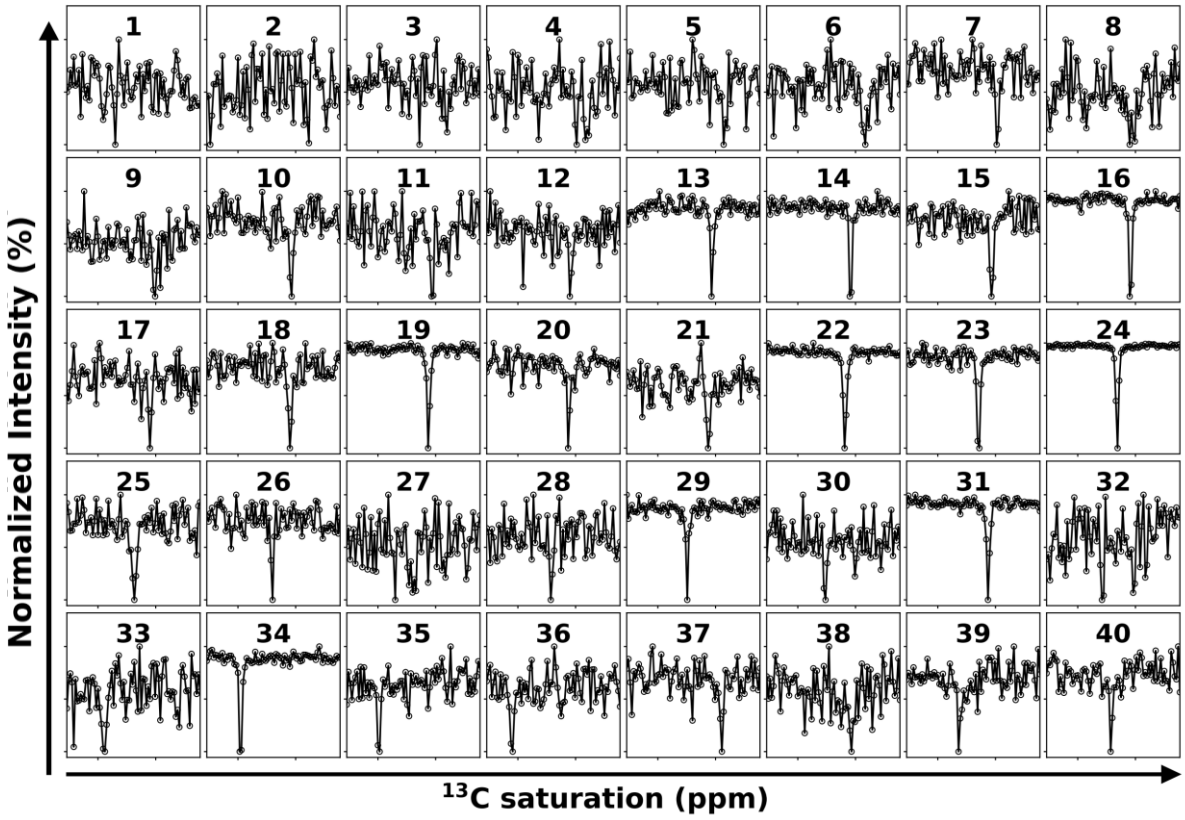

Figure 48 Methyl-CEST intensity profiles of the oligomeric state of BVPrP^{C}(90-231). The spectra were measured at 25°C (post-heated sample at 75ºC). The arbitrary number used to refer to each signal is identical to **Figure. 39**.

4.3.2.7 Unified interpretation of the oligomeric state of BVPrP^{C}(90-231)

SEC and DOSY and other spectra proved the formation of a stable ~16-mer oligomer by thermal heating of the monomeric species in solution over 50ºC. The CD study showed a substantial reduction of the signal at 220 nm for the post-75ºC sample which clearly indicates a reduction α-helix content in the oligomer respect to the monomeric state. The N_HSQC showed that the oligomer has a rigid core in which most of the residues are packed except N-ter and C-ter together and a fraction of α2 which are exposed to the water and with substantial flexibility (**Fig. 43**). Water-T_2 measurements proved that that the compactness of the oligomer is not substantially affected by temperature in contrast with the monomeric species. ^{15}N_CEST spectra proved a weak binding equilibrium of the oligomer with the monomeric species.

4.3.2.8 Molecular Dynamics (MD) analysis

The experimental observations obtained in this study consistently highlight the instability of β1 and its adjacent coil, particularly within the V121-E146 segment, which emerges as the principal hotspot for early unfolding. NOE analysis further revealed expansion of the β1-α1-β2 domain (144,145), underscoring its intrinsic flexibility relative to the more stable α2-α3 subdomain. Based on these findings, it can be hypothesized that partial unfolding of β1 and its flanking coil facilitates domain separation and may provide the structural plasticity required for PrP^{C} to undergo fit-induced adjustment at the PrP^{Sc}-PrP^{C} interface during the initial stages of conversion. Therefore, plain MD simulations were carried out as an alternative and complementary approach to probe PrP^{Sc}-assisted unfolding of BVPrP^{C}(90-231). Unlike solution NMR, this method allows exploration of an ensemble where the disordered N-terminal tail, up to residue A120, is attached to a PrP^{Sc} templating surface and adopts the PrP^{Sc} conformation. To model this, MD simulations were performed for BVPrP^{C}(93-231) with its 93-120 tail attached to a stacked tetramer of PrP^{Sc}, serving as a surrogate for a longer PrP^{Sc} stack. Since no BVPrP^{Sc} structure has yet been resolved, RML MoPrP^{Sc} (PDB: 7td6) (71) was used as an approximate model of BVPrP^{Sc}. Accordingly, the BVPrP^{C}(121-231) FD was attached to the C-terminus of an RML MoPrP^{Sc} tetramer with an extra 93-120 upper rung **(Fig. 49)**.

An initial 300 ns simulation at 310 K showed that the FD structure was maintained throughout, with the three α-helices remaining intact, although undergoing considerable vibrational motions. The extreme N-terminus of the attached tail detached early from the PrP^{Sc} surface and fluctuated throughout the simulation, detaching and reattaching.

To accelerate unfolding, the simulation was repeated at 400 K. The results, representative of three trajectories, resembled those at 310 K but displayed more intense fluctuations. However, once again, the three helices emerged unscathed from the simulation. More intense motions were also seen for the connecting coils, particularly 121-143, which underwent extensive

changes of conformation. While the focus of these simulations is the FD, it is of interest that at this temperature the 93-120 coil initially attached to the PrP^{Sc} surface exhibited substantial fluctuations, with its N- and C-terminal sections detaching from the template, while its central ~103-110 segment remained more stably attached to it (**Fig. 49**). Quantitative RMSF analysis (**Fig. 50**) revealed very high fluctuations in the disordered N- and C-terminal sequences, while coils β1-α1, β2-α2, and α2-α3, along with most of α1 and the termini of α2 and α3, showed RMSF values that were also elevated but not as much. The central regions of α2 and α3 around the disulfide bridge exhibited low RMSF values, as did the β1 and β2 strands and the α1-β2 coil.

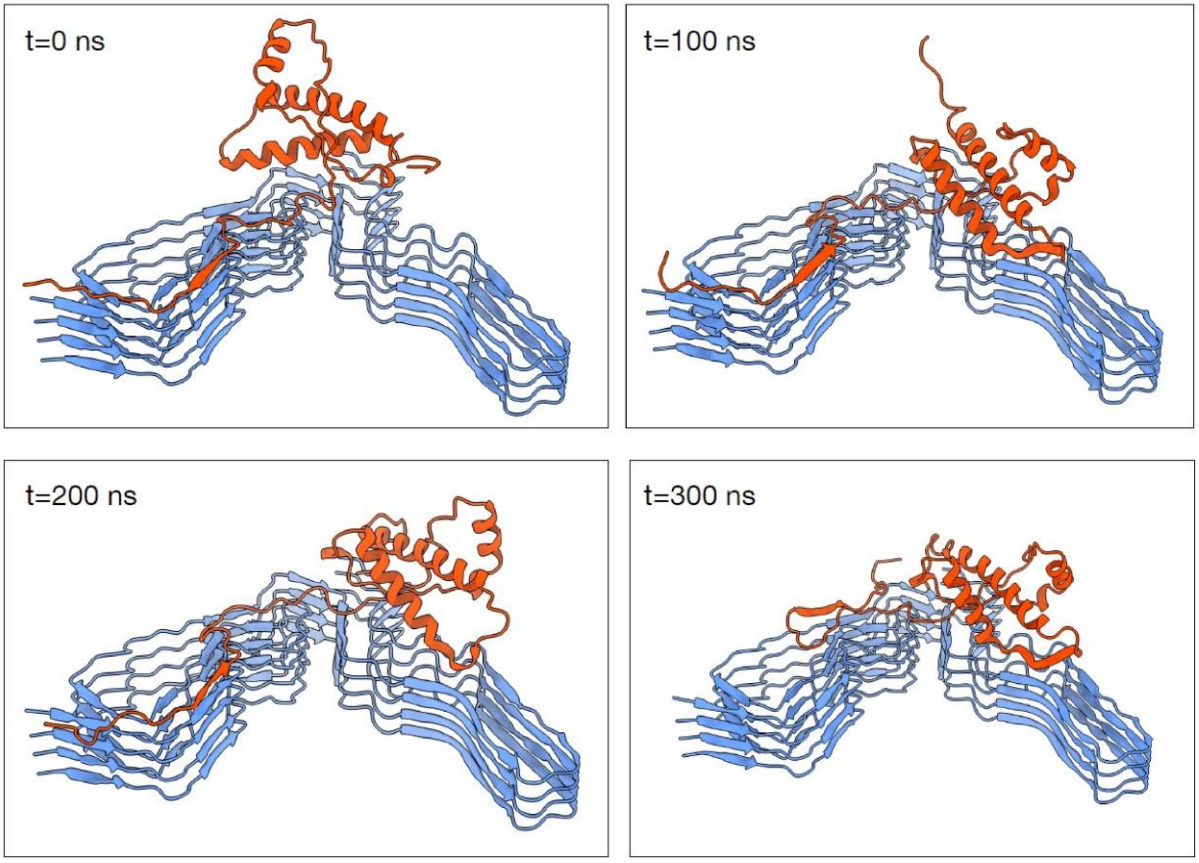

Figure 49 MD simulation of BVPrP^{C}(93-231) with its 93-120 tail attached to PrP^{Sc}. The tail was already converted to the PrP^{Sc} conformation. Trajectories were obtained at 400 K in explicit water. The trajectory time is indicated.

MD simulations of the free BVPrP^{C}(90-231) were also carried out, without the N-terminus attached to a PrP^{Sc} surrogate tetramer, at both 310 and 400 K. Some trajectories, one of two at 310 K and two of three at 400 K, resembled those of the attached system, albeit with somewhat larger fluctuations (see RMSF plots in **Fig. 50**). However, in one 310 K and one 400 K trajectory, motions were considerably more intense overall, including a drift and separation of α1 from the rest of the FD ensemble (**Fig. 51**).

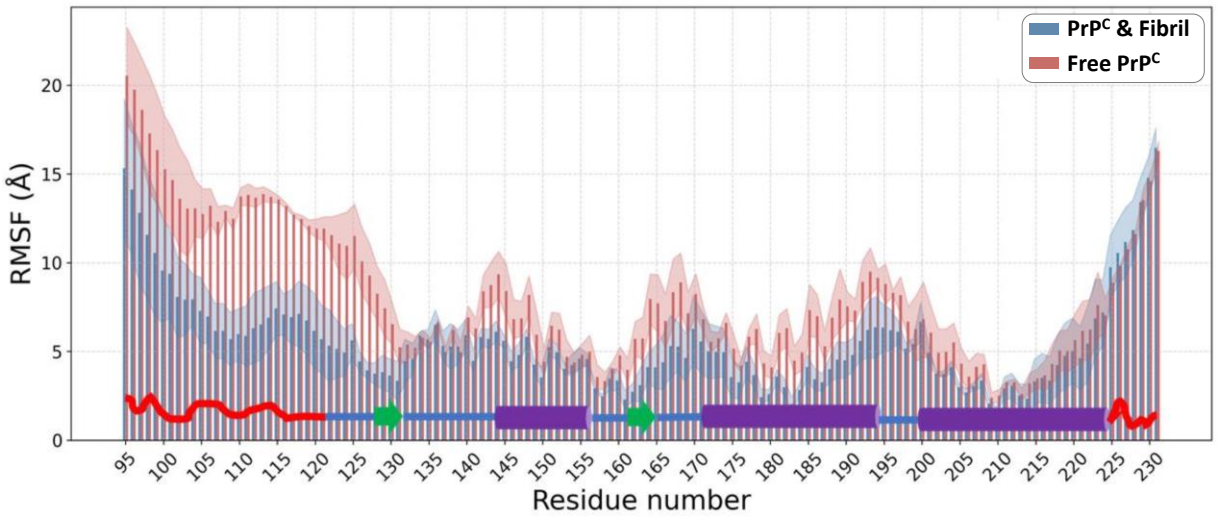

Figure 50 Amino acid residue RMSF throughout MD simulations at 400 K of BVPrP^{C}(93-231). Blue: 93-120 tail attached to a PrP^{Sc} trimer. Red: 93-120 tail free. MD simulations are 300 ns. Bars represent means of 3 trajectories. Shaded areas cover +/- sd. Superimposed: secondary structure elements.

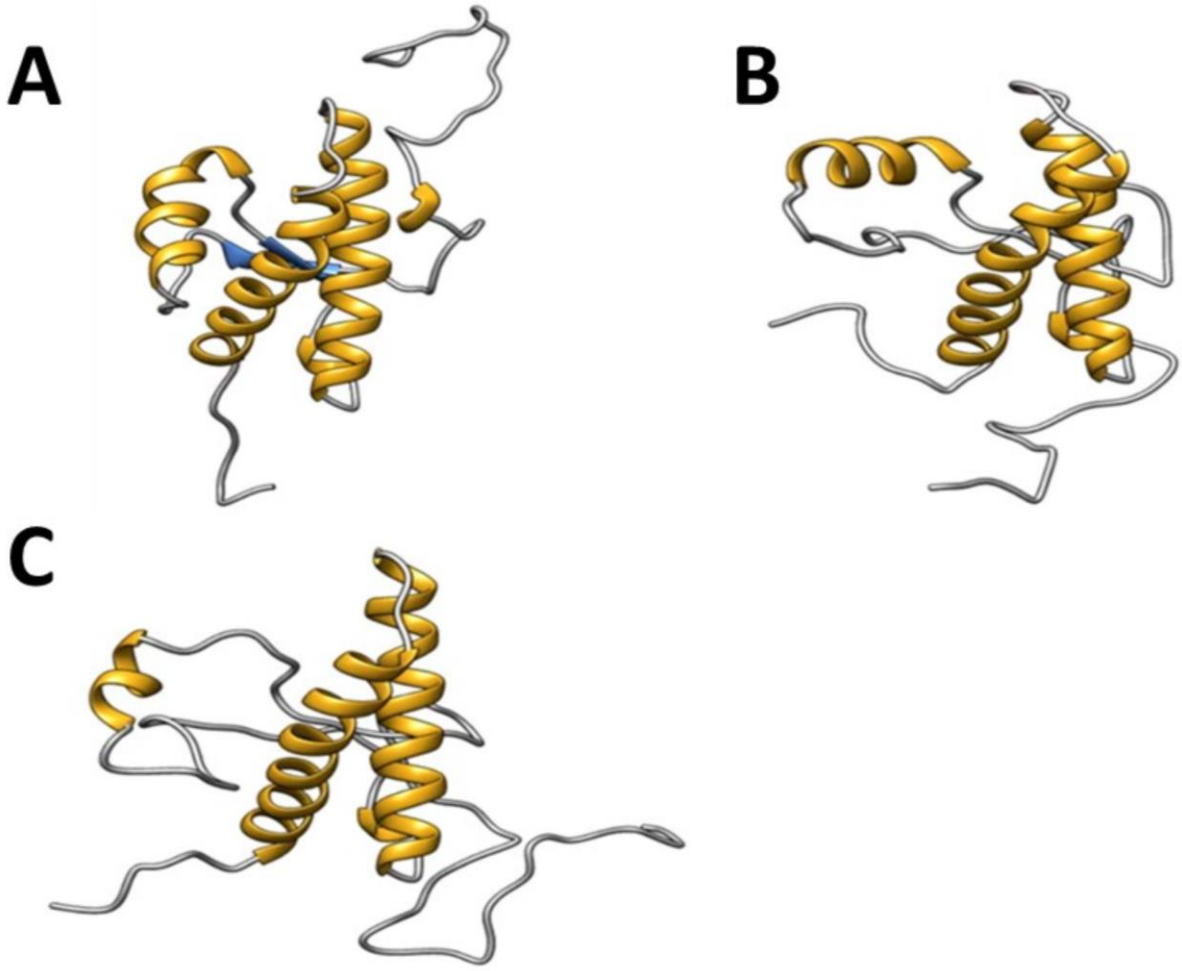

Figure 51 Snapshots of a MD trajectory of BVPrP^{C}(90-231) at 400 K. **A)** t = 0. **B)** t = 120 ns. **C)** t = 175 ns. Note the separation of α1 from the rest of the FD ensemble (t =120 ns vs. t= 0).

5. DISCUSSION

The fundamental molecular process underling prion diseases is the PrP^{Sc}-templated conversion of PrP^{C} to PrP^{Sc}. This event triggers a series of biochemical and structural changes that ultimately cause neurodegeneration and neuronal dysfunction. Defining how the spread of prions occurs, as well as identifying targets of therapy, hinges on understanding the molecular basis of this conversion.

The PrP^{Sc} templating surface acts as a relatively inert mold, which means that the FD of PrP^{C} has to adapt through unfolding and subsequent refolding to match the β-sheet-rich architecture of PrP^{Sc}. This study focused on the initial stages of FD unfolding, employing variable temperature to promote structural rearrangements due to the thermal perturbation. To investigate these structural and dynamic changes in $BVPrP^{C}$, solution NMR was combined with complementary techniques including CD, SEC, and MD simulations to interpret the results.

Although a construct encompassing solely the folded domain (FD), $BVPrP^{C}$(121–231), would appear to be the most appropriate choice for investigating the intrinsic unfolding properties of the FD, since this segment coincides precisely with the structured domain and excludes the unstructured N-terminal residues, in this study, $BVPrP^{C}$(90–231) was selected to enable direct comparison with previous biophysical studies that utilized related constructs (e.g., 121–231, 113–231, or 90–231) under a variety of unfolding conditions (89,102,146–150).

In principle, the most informative experimental approach would involve analyzing the FD when tethered to PrP^{Sc}, thereby providing direct insight into its conformational rearrangements during conversion. However, such experiments remain technically intractable owing to the insolubility and strong aggregation propensity of PrP^{Sc} assemblies. Consequently, the recombinant $BVPrP^{C}$(90–231) fragment we investigated in isolation, under the assumption that the fundamental unfolding behavior of the FD is largely conserved between the free and PrP^{Sc}-bound states, albeit modulated by intermolecular interactions with the PrP^{Sc} surface *in vivo*.

The choice of the bank vole PrP^{C} sequence was deliberate, as $BVPrP^{C}$ exhibits exceptional adaptability to diverse PrP^{Sc} strain conformations (151,152). This "generic convertibility" may stem from a diverse ensemble of conformers within the $BVPrP^{C}$ folding/unfolding landscape, facilitating accommodation to various PrP^{Sc} templates. These experimental results relying on thermal unfolding of this protein were followed by several spectroscopic or analytical techniques, including CD and sophisticated NMR spectra such as ^{15}N_CEST, Methyl-CEST, NMR relaxation, temperature coefficients (*Tc*), CLEANEX-PM, Combined Chemical Shift Deviations (CCSD), and Nuclear Overhauser Effect (NOE) data. Collectively, they provided a detailed map of the thermal unfolding of $BVPrP^{C}$ FD. These findings were complemented by

molecular dynamics (MD) simulations, providing a multifaceted view of the early conformational transitions that could lead to the conversion to the PrP^{SC} form.

5.1 Disruption of the antiparallel β-sheet as an early event in unfolding

According to the NMR data obtained, a key early event in the unfolding pathway is the disruption of the short antiparallel β-sheet comprising β1 (Y128-G131) and β2 (V161-R164). This structural element seems to be central to the FD's stability in native PrP^{C}. It confers compactness to the FD by compensating for the entropic penalty of maintaining α1 in close proximity to α2 and α3, in accordance to the published NMR structure (BMRB entry #15824) (79) . The following observations suggest the disruption of the antiparallel β-sheet due to the thermal perturbation:

First, temperature coefficients (*T*c) of amide proton chemical shifts provide insight into hydrogen bonding integrity. All residues of β_1 and one of the four residues of β_2 (**Fig. 25**) weaken their intramolecular H-bond at 45ºC, consistent with solvent exposure and partial unfolding. The CLEANEX-PM analysis (**Fig. 32**) does not provide information for β_1; however, it confirms the breaking of another H-bond for a second β_2 residue (R164) at 45ºC.

Second, nonlinear temperature dependence of CCSDs over 15–45°C underscores specific unfolding events. Multiple residues in β1 and β2 and some adjacent residues show pronounced nonlinearities (**Figs. 27** and **28**). This is particularly evident in the segment adjacent to β1 and suggest dynamic equilibrium between native and partially unfolded states. The unfolding event could be either a conformational change in these parts of the structure or alteration in their chemical environment, such as that arising from the dissociation or association from/to other parts of the protein.

Third, ^{15}N relaxation data (R_2/R_1 and ^{15}N-NOE) exhibits high mobility (**Fig. 35**) in the region from the N-terminal to β1 (approximately residues 121-127), serving as a transition zone between the disordered N-terminal tail (~90-120) and the ordered FD (79,153). Residue G131 (β1) exhibits the highest R_2/R_1 ratios at both 25°C and 45°C, with values ca. 3 times greater than the average of the residues in the FD (128-225). This anomalous elevation of the R_2/R_1 ratio is consistent with conformational flexibility on the intermediate timescale. A similar interpretation can be inferred for residues V161, Y162, and Y163 in β2 which exhibit elevated R_2/R_1 values, albeit only at 45°C. These motions affecting the β1/β2 suggest temperature-dependent intensification of local conformational disorder at 45ºC likely reflecting fraying at the β-sheet edges, weakening inter-strand hydrogen bonds and predisposing the sheet to dissociation.

Fourth, NOE intensities for the monomeric protein indicate an apparent shortening of the β1-β2 separation at 45°C with respect to room temperature (**Fig. 37**; Table 2). A plausible explanation for this shortening is that the β1-α1-β2 motif moves away together from the α2-α3 subdomain while still maintaining at least partially its original secondary structure. **Fig. 37** illustrates these changes consistent with the inter-residual ^{1}H-^{1}H NOE distances upon heating from 25 to 45°C.

Fifth, water-T_2 measurements indicate that the monomeric protein incorporates a higher amount of bound water in its first hydration shell at 45°C than at 25°C, owing to an increase in solvent-accessible surface area. These observations suggest that early unfolding events in the temperature-reversible regime lead to a less compact structure at 45°C, consistent with other observations that indicate that certain parts of the FD domain separate, rendering the structure more accessible to the solvent.

Sixth, MD simulations show transient separation of β1-α1-β2 motif from α2-α3 and also the transient breaking of the antiparallel β-sheet of β1 and β2 sheet (**Figs. 50** and **51**), where it "breathes" in the sense that disappear but often recovers during MD, highlighting its resilience yet vulnerability.

In summary, the observables indicate that thermal unfolding of native PrP^{C} begins with disruption of the hydrophobic core and detachment of the β1-α1-β2 subdomain from α2-α3, increasing solvent exposure. The antiparallel β-sheet is a fragile core whose inter-strand interactions are readily disrupted by thermal energy, enhancing conformational sampling. This is consistent with a model of β1 acting as a "pre-assembly unit" in PrP^{Sc} suggesting its dynamics in PrP^{C} is tuned for conversion. Even without complete β1 unfolding, a plausible propagation mechanism (**Fig. 52**) involves transient detachment of β1 as an intact block that docks onto the PrP^{Sc} surface since the strand conformation is already compatible for further stabilization by H-bonds.

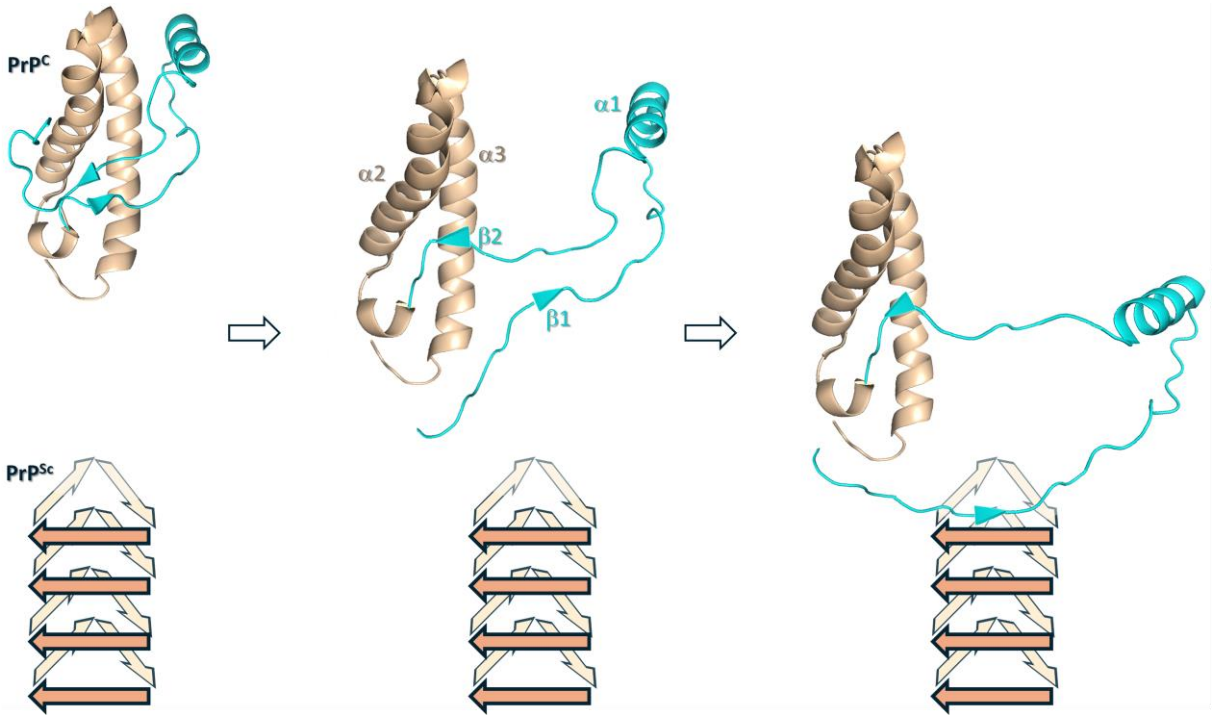

Figure 52 Cartoon illustrating the antiparallel ß-sheet disruption and structural decompaction of BVPrP^C at ca. 45°C. This thermally induced change suggests a mechanism where the resulting exposed ß1 strand may bind to the cross–ß motif on the PrP^{Sc} surface, facilitating the initial stage of the growing amyloid aggregate.

5.2 Additional Sites of Early Flexibility

Besides the V121-D144 segment, the T_C data identify additional sites of early flexibility, namely: (1) the C-terminus of α2 through the α2-α3 coil and into α3's N-terminus (*i.e.*, residues 187-201); (2) the C-terminus of α3; and (3) the region adjacent to β2 (α1-β2 coil, β2, β2-α2 coil). These sites are shorter and less prominent than the ~121-144, as judged by Tc magnitude and extension. For example, the 187-201 α2-α3 coil spans 15 residues with highly negative Tc values, compared to 24 residues in 121-144 (**Fig. 25**), a similar situation occurs for the shorter C-terminal stretch of α3 (216-225). The α3 C-terminal segment (216-225) shows flexibility, potentially linked to the short-disordered C-terminal tail (Y226-S231). This is supported by MD simulations showing resilience in helices but breathing motions, with RMSF highlighting coil regions (**Fig. 50**). The implications are that these secondary sites might act as "release valves" for structural strain, allowing the FD to adapt without immediate global unfolding.

In detail, the non-linear CCSD for residues like those in the α2-α3 coil (**Figs. 27** and **28**) suggests sampling of alternative conformations, possibly involving loop restructuring. This aligns with prior observations of excited states in these areas and underscores their role in modulating stability. The integration of *Tc*, CLEANEX-PM, and CCSD data provides a multi-dimensional view, revealing how hydrogen bonding, solvent exchange, and chemical shift perturbations converge to signal early flexibility.

However, the shorter and less prominent *Tc* magnitude, together with the shorter non-linear CCSD extension in the α2–α3 segment and additional considerations relative to the geometry of the PrP^{Sc}-attached FD ensemble, discussed below, indicate that these regions are less likely candidates for initiating unfolding of the FD. Nevertheless, the possibility that alternative or parallel unfolding/refolding pathways may operate cannot be ruled out.

5.3 Alignment of the present data with Prior PrP^{C} unfolding studies

The results obtained herein support the conclusion that the ~121-144 region, encompassing the coil N-terminal to β1, β1, the β1-α1 coil, and α1's N-terminus, emerges as the most active, likely due to its exposure and lower protection factors, and strong candidates to initiate the unfolding of the FD following attachment of the 93-120 flexible coil to PrP^{Sc}, in a zipper-like fashion. By "zipper" we do not mean that unfolding proceeds in a continuous, residue after residue manner from V121 to D144; rather, it refers to the fact that the V121-D144 segment as a whole is contiguous to the ~90-120 segment that initiates the templating. These flexible sites, once unfolded, enter a high-energy state, making them highly susceptible to templated conversion. In this state, they can be readily captured by PrP^{Sc}, making them highly susceptible to templated conversion.

The findings in this study broadly concur with previous studies on PrP^{C} misfolding, though we distinguish between unfolding and misfolding. The objectives of this study focus in exploring the early steps of unfolding of the FD that are of relevance in a situation in which such FD is attached to the surface of PrP^{Sc}. In contrast, "misfolding" would refer to a more extensive process by which the FD converts all the way to a stable conformer, typically of an amyloid nature, that is typically considered to be a surrogate of PrP^{Sc}. The vast majority, if not all previous studies have taken this second perspective, to model spontaneous generation of PrP^{Sc}. Of course, the first steps of such misfolding process require unfolding. Thus, Russo et al. (89) identified β1, β2, α1, and the α2-α3 coil as part of an "excited state" in human PrP^{C} (90-231), with α2 and α3 preserved, mirroring our early flexibility sites. However, $HuPrP^{C}$(90-231) (but not $HuPrP^{C}$(23-231)) formed a Partial Unfolded Form (PUF) at 61°C (**Fig. 53**), absent in our $BVPrP^{C}$(90-231) experiments (**Fig. 18**), indicating species-specific differences.

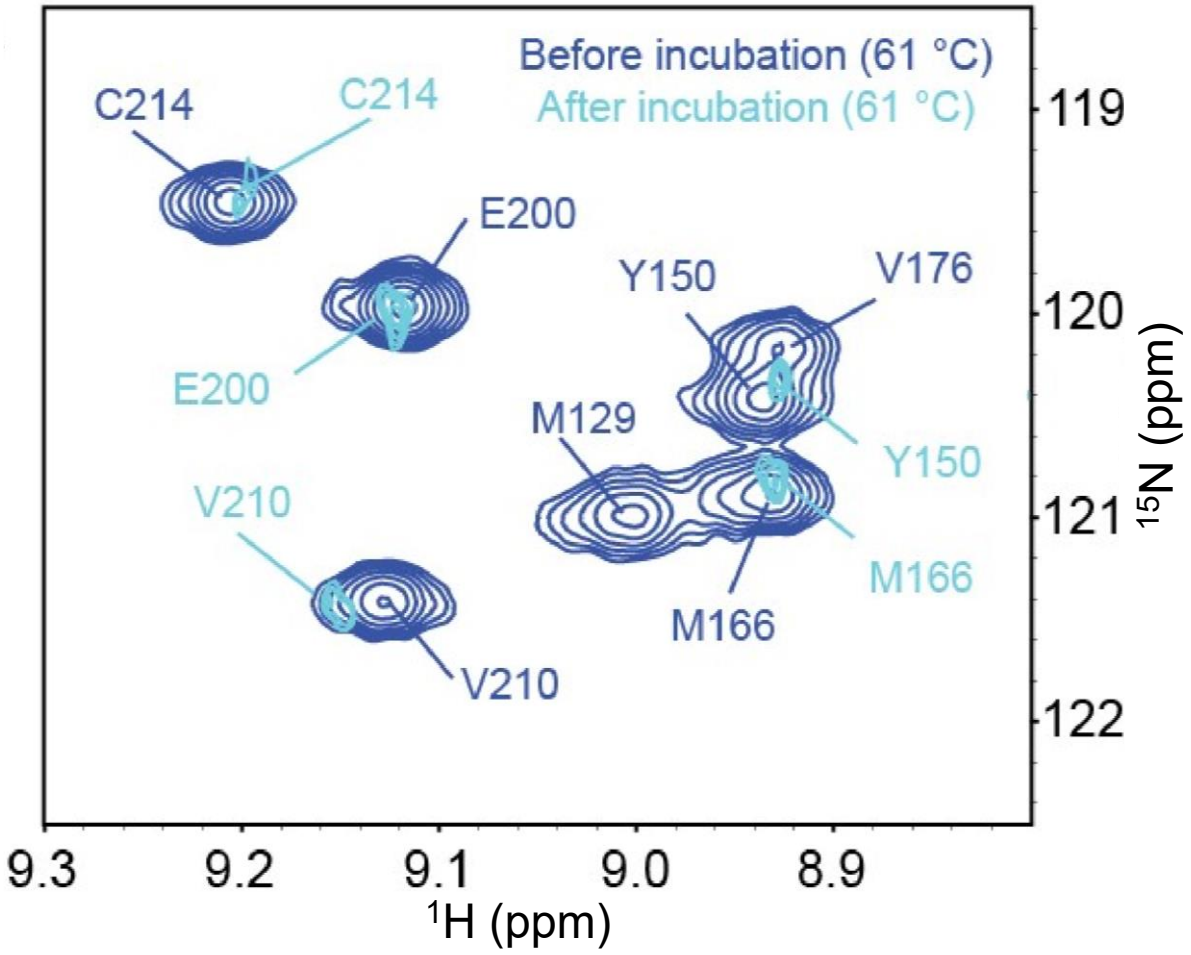

Figure 53 Temperature effects on N_HSQC spectra of HuPrP^{C}(90-231). Superimposition of the spectrum acquired at 25°C, before (blue) and after (cyan) incubation at 61°C (15 hours) This is panel A from Supplementary Fig. S16 of (Russo et al, 2022)(89). Reproduced with permission under the Creative Commons Attribution 3.0 under License (CC BY 3.0).

5.4 Characterization and Implications of Thermally Induced Oligomers

What is stated in the previous section might seem contradictory with the analyses carried out in this study of the oligomers generated in the >50°C temperature regime (**Figs. 23** and **24**), as these are clearly off-pathway with respect of a hypothetical templated conversion in the presence of PrP^{Sc}, or in other words, they are on-pathway for another route which is the formation of non-propagating oligomers or non-PrP^{SC} amyloids. However, it should be noted that while their size, shape and other biophysical characteristics (**Fig. 44**) are indeed irrelevant features for the purpose of this study, the fact that they contain some elements of the FD with unchanged conformation (**Fig. 23**) provides information about a partially unfolded conformer existing immediately prior to their emergence. In other words, hypothetically the oligomers are right on the border between "unfolding" and "misfolding" and can provide a bonus of useful information.

The solubility, slow tumbling due to the elevated size and irreversible nature of the oligomers formed in the BVPrP^C(90–231) post-70°C sample was evidenced because only a fraction of the N_HSQC peaks was observed at room temperature 25°C, in contrast to the full set of peaks seen in the unheated sample (**Fig. 23**).

The formation of soluble oligomers of PrP^C different means and under different conditions (very low pH, high salt, temperature and combinations thereof) has been extensively reported, although their atomistic structure has not been deciphered to date. They exhibit, β-sheet enrichment, and concurrent oligomerization /structural changes, akin to those induced by acidic pH, denaturants, or salts (85,94–96,148,154–160). Thermal induction alone has been noted previously (129,144,161) .

Kinetic traces showing simultaneous β-sheet increase and oligomerization of mouse and Syrian hamster PrP (156) suggest these oligomers trap fleeting monomeric unfolding conformers, as has been stated at the beginning of this section. Overall, the literature suggests, based on indirect data, that such hypothetical intermediates preserve much of α2-α3 while β1-α1-β2 partially refolds into β-sheet structure and suggest that it might involve separation of these subdomains and domain-swapping-like interactions. Thus, Honda *et al*. (85) showed, using deuterium exchange coupled with NMR analysis, that protection factor across the β1-α1-β2 subdomain is orders of magnitude lower than that of the α2-α3 subdomain immediately prior to oligomerization. This strongly suggests generalized unfolding of β1-α1-β2, with some α1 and coil segments eventually converting to β-sheet and collapsing into the oligomeric form.

While PrP^C oligomers are very soluble, and therefore amenable to solution NMR analysis, studies had consistently shown disappointingly uninformative spectra in which only signals arising from the long N-terminal and short C-terminal intrinsically disordered stretches (~23/90-120 and ~225-231, respectively) are detected (94,95,148) , This is a consequence attributable to severe line broadening resulting from slow tumbling of the large oligomer in solution, together with partially independent fast motions of the disordered flexible “tails” (86,94). This suggests that our oligomers have some distinct architectural characteristics, given that their HSQC spectrum does contain signals from the FD. Namely, β2 is preserved, and together with α2 and at least part of α3, it constitutes an ensemble that likely juts out of the oligomeric core (**Fig. 43**).

Nevertheless, our findings are consistent with those recently reported by Russo et al. (89). These authors observed that incubating HuPrP^C (90–231) for 1 hour over a temperature range of 15–80°C resulted in fully reversible unfolding; however, prolonged incubation for several hours at 61 °C produced irreversible oligomers (**Fig. 53**), just as in this study, although the yield appeared lower than that obtained here. This different behavior might result from intrinsically different unfolding properties of both proteins. When they compared the ^1H-^{15}N HSQC spectra of this “post-61°C” sample and the original one, both at 25°C, they observed, like in this work

(see **Fig. 23**), signal loss and broadening for many residues in the FD without significant chemical shift changes. Also, in analogy to this work, some residues located within the FD were less affected, namely most residues in α1, the C-terminus of α2. Except for residues in β2, that were severely suppressed, there is a good coincidence with this study. The mixture of oligomers and monomers ~40:60 in this work, ~10:90 in theirs (R. Fattorusso, personal communication at *Prion 2025 Conference*), adds complication to the interpretation of data. All in all, it suggests that both BVPrP^{C}(90-231) and HuPrP^{C}(90-231) can generate a partially unfolded late intermediate in which a substantial portion of α2 is preserved and that collapses to form oligomers. However, such intermediate is more accessible to BVPrP^{C}(90-231), given that HuPrP^{C}(90-231) requires a higher temperature (>61°C *vs* >50°C), and longer incubation times, and yields are lower.

Studies on PrP^{C} oligomers, particularly by Rezaei and Serpa (96,129,161) characterized then as direct precursors to fibril assembly and their formation was linked to disease pathology. This thesis defends the interpretation that these oligomers are non-PrP^{Sc}-capable amyloids. Nevertheless, their study remains valuable, as they share key early unfolding intermediates with the on-pathway species that lead to PrP^{Sc}-competent oligomers. The group of Rezaei described heterogeneous, β-rich prion oligomers (PrP$^{\beta}$) of variants of sheep-PrP^{C} as nucleation-competent precursors with pathogenic properties, capable of templating aggregation. The work of Serpa provided structural insights into PrP$^{\beta}$ oligomers of Syrian hamster-PrP^{C}(90-232), proposing that a structured loop region dissociates from the FD core, resulting in exposure of hydrophobic residues and the creation of a new putative β-structure nucleation site. Broader amyloid literature emphasizes oligomeric structural diversity and β-sheet enrichment, with ongoing debate about whether certain oligomers are on-pathway species or off-pathway towards the generation of amyloid.

It is noteworthy that the oligomers obtained towards generation of a HuPrP(90-231) amyloid by Russo *et al*. (89) were shown to be "on-pathway", underscoring the differences between studying misfolding and unfolding in the context of PrP^{Sc}-templated propagation, even though some conformers (in this case those immediately preceding the oligomers) might be common. In contrast to Russo *et al*. (89), the present study examines the transient unfolded species that exist immediately prior to their collapse into oligomers. The oligomers of this work are considered "off pathway" intermediates, and the primary interest lies in the pre-oligomeric unfolded states rather than the oligomers themselves, as already stated. The working hypothesis here is that in the presence of the PrP^{Sc} template, such unfolded conformers, tethered as they are to PrP^{Sc} through their N-termini, would collapse onto the templating surface as depicted in **Fig. 52**, rather than self-aggregate with a similar partially unfolded PrP^{C} to form oligomers.

To delve deeper, the fast and irreversible nature of oligomer formation of BVPrP^{C}(90-231) above 50°C, as evidenced by non-recovery of the native spectrum upon cooling, highlights a kinetic trap in the unfolding landscape. The partially unfolded conformation that forms BVPrP^{C}(90-231) above 50°C is an exciting state that exhibits a strong tendency to interact with

stabilizing agents in an irreversible way, such as potentially could be a PrP^{Sc} template. In the present study, this propensity manifests as self-aggregation, which is promoted by the relatively high protein concentrations used herein (1.3 and 5 mg/mL). This irreversible behavior contrasts with observations in other PrP systems: full-length human-PrP^{C} exhibits greater resistance to aggregation and typically forms irreversible oligomers under forcing conditions (89), whereas certain truncated constructs, such as human PrP^{C}(23–231) (162), and recombinant hamster PrP^{C} (163) can form reversible oligomers under specific in vitro conditions.

These observations strongly emphasize how sequence differences and experimental conditions influence oligomeric conversion susceptibility and a lower barrier to form oligomeric states of BVPrP's could correlate with their easier adaptation to various PrP^{Sc} strains. Future isolation of these oligomers via SEC (**Fig. 44A**) could enable detailed structural studies, potentially revealing domain-swapped interfaces akin to those proposed by Serpa et al .(96)

5.5 Insights from Molecular Dynamics Simulations

Molecular dynamics (MD) simulations provide plausible models of the initial unfolding events in free BVPrP^{C}(90-231) and allow simulation of its binding to the PrP^{Sc} surface and the subsequent templated conversion to PrP^{Sc}, thus complementing the NMR data presented here. These simulations were performed by Dr. Marta Rigoli (University of Trento) and are included to enrich the discussion.

The initial structure for these MD simulations was set to the known NMR structure of BVPrP^{C}(90-231) (79). Simulations were carried out for the free (unattached) protein and for the protein with the N-terminal tail (90-120) tethered to a static RML MoPrP^{Sc} tetramer surface. These simulations were done at 310K and at 400K to accelerate unfolding.

The MD trajectories of BVPrP^{C}(90-231) of the free protein showed that flexible coils dominate mobility (RMSF plots, blue bars in **Fig. 50**), while α-helices and β-strands are resilient, stretching/breathing but recovering to their original conformation, without losing their structure. The same is true for the two β sheets, that keep on separating transiently from one another and temporarily lose their canonic parameters, only to recover them. These observations are apparently inconsistent with the increased proximity between β1 and β2 detected by NOE at 45ºC respect to 25ºC. These NOEs likely represent a population-weighted average over an equilibrium mixture of folded and partially unfolded conformations in this region (**Fig. 37** and Table 2). This suggests a dynamic tendency of the β1-α1-β2 and α2-α3 subdomains to separate, particularly with α1 drifting away from the rest of the FD via torsion in the Y157–Q160 coil that links it to β1. In two of the MD trajectories, the referred separation of α1 from the rest of the FD was seen (**Fig. 51**). However, the occurrence of this event only in some of the trajectories suggests that it is rare and therefore it could take place at later times throughout the unfolding process. Separation of the β1-α1-β2 and α1-α2 subdomains is *sine qua non* to complete templating of the FD by the flat PrP^{Sc} surface for obvious geometrical reasons and

additional evidence of the occurrence of such molecular event has been gathered experimentally by FRET.

The MD trajectories of BVPrP^{C}(90-231) with the free N-terminal tail attached to PrP^{Sc} exhibited overall behavior (red bars in RMSF plot of **Fig. 50** and **Fig. 51**) very similar to that seen in the MD of the unattached-tail system at similar temperature, including the rare event in some of the trajectories of the separation of α1 from the rest of the FD. The major difference is found in the overall mobility of the tail attached residues that were noticeably reduced in the analogous MD simulation when the tail was attached.

5.6 Hypothetical pathway conversion of BVPrP^{C} into PrP^{Sc} and Speculative Elements

Based on the early unfolding characteristics of BVPrP^{C}(90-231) presented in this thesis, the following timeline pathway for unfolding of BVPrP^{C}(90-231) in the context of its templated conversion into PrP^{SC} can be proposed (**Fig. 54**): (A) PrP^{C} encounters PrP^{Sc}; (B) The disordered ~90-120 tail attaches and is easily templated into PrP^{Sc}; (C) destabilization of~V121-D144, especially the flexible residues ~121–125 together with concomitant separation of β1-β2 followed by templating of β1 into PrP^{Sc}. As result of that the V121-D144 region is the first major FD segment to unfold and be trapped, the remaining part of the sequence is a shortened ~140-231 FD connected to the templating surface through a small ~138-144 coil. (D) This shortened FD may exhibit increased flexibility in its β2–α2 loop. This possibility is consistent with the findings of Hosszu et al. (150) for a recombinantly expressed truncated HuPrP(137–231) which entirely lacks the β1 strand and a substantial portion of the adjacent hydrophobic segment and it is significantly less stable than HuPrP(119–231). In that study, Chemical Shift Index-derived order parameters (CSI-S^2) showed that the overall structure of the truncated domain is preserved, yet the β2–α2 loop displays greater flexibility compared to the complete folded domain. Key evidence includes CD data indicating an ~10°C reduction in thermal melting temperature, reduced protection factors in hydrogen-deuterium exchange experiments (reflecting greater dynamic unfolding), and a substantially enhanced propensity for fibrillization. (E) in the last step, α2-α3 must separate from the β1-α1-β2 block, part of which will have already been converted to the PrP^{Sc} conformation and gravitate towards the C-terminal lobe of the PrP^{Sc} templating surface. MD simulations suggest that this happens at a later stage. A substantial portion of α2 and bits of α3 resists in its native conformation at high temperatures but they subsequently will be captured and templated by the PrP^{Sc} surface.

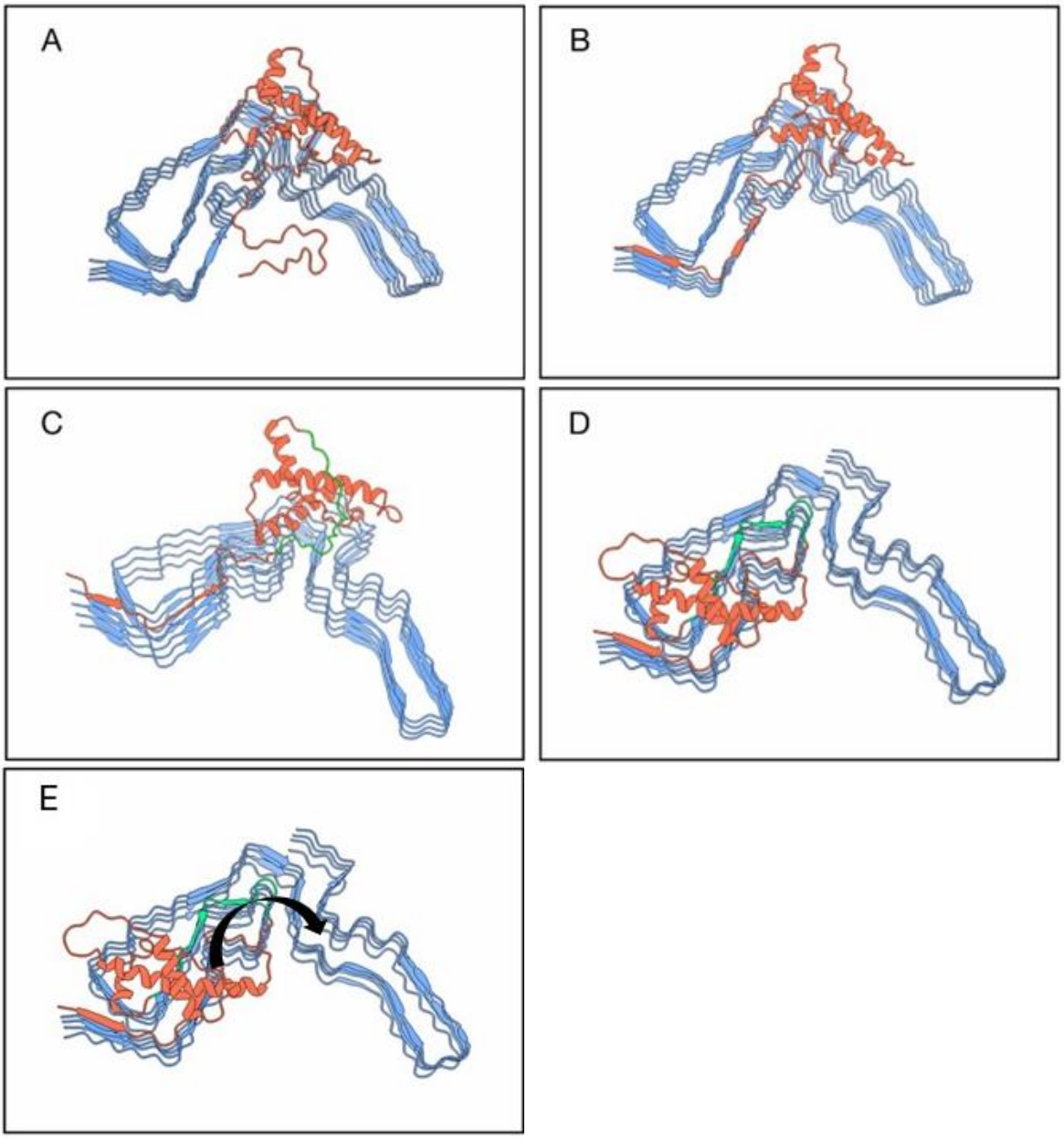

Figure 54 Cartoon model of the trapping of PrP^{C} intro PrP^{Sc}. **A)** PrP^{C} encounters PrP^{Sc} on the cell surface. **B)** The flexible/disordered stretch (~90-120) of PrP^{C} is easily trapped and templated by the (~90-120) templating surface of PrP^{Sc}. **C)** The PrP^{C} FD now hovers in front of the essentially inert PrP^{Sc} surface; while stable, some regions within the FD explore partial unfolding. The ~V121-D144 region (green), encompassing the coil N-terminal to ß1, ß1, the ß1-α1 coil and the N-terminal stretch of α1, constitutes the most active region. **D)** The partially unfolded ~V121-D144 region is the most likely to be trapped by the templating surface. The FD is now reduced to ~140-231 and lacks ß1. **E)** α1 and the ß2-α2-α3 ensemble drift apart around the a1-ß2 coil, and eventually α2-α3 from ß2 around the ß2-α2 "rigid" coil to gravitate towards the C-terminal "wing" of PrP^{Sc}. Given that no BV PrP^{Sc} structure has been resolved yet, the structure of RML, a mouse PrP^{Sc} (PDB 7td6) has been used, which does not affect the conclusions of this cartoon-level analysis.

5.7 Limitations, Implications, and Future Directions

The proposed unfolding pathway timeline for the conversion of BV-PrP^{C}(90-231) into PrP^{SC} described in the previous section includes speculative elements but aligns well with experimental and modeling data. One limitation that can be argued is that the BV-specific

sequence employed in this study may not represent a universal pathway for the conversion of PrP^{C} to PrP^{Sc} that is broadly applicable to other prion sequences. However, given that, as mentioned, $BVPrP^{C}$ is a "universal acceptor" of PrP^{Sc} prions, it is more likely that its unfolding involves universal features than the opposite. On the other hand, alternative pathway timelines are possible; for example, the disordered C-terminal Y226-S231 segment could attach to the PrP^{Sc} surface before the N-terminal region. However, this is less likely due to steric constraints from the GPI anchor and the segment's short length, which may cause detachment before further extension (**Fig. 55**). Another possibility is that, following the attachment or conversion of the ~90-120 tail, a region other than ~121-144, such as the G195-T199 coil may initially undergo unfolding, envelop surrounding areas, and become trapped. However, the FD's geometry and the distance to this segment's corresponding "docking site" on the PrP^{Sc} surface make this less feasible. While multiple reaction coordinates occurring in parallel cannot be ruled out, the proposed pathway integrates experimental and modeling data, offering a structural framework for future atomistic models of PrP^{Sc} propagation.

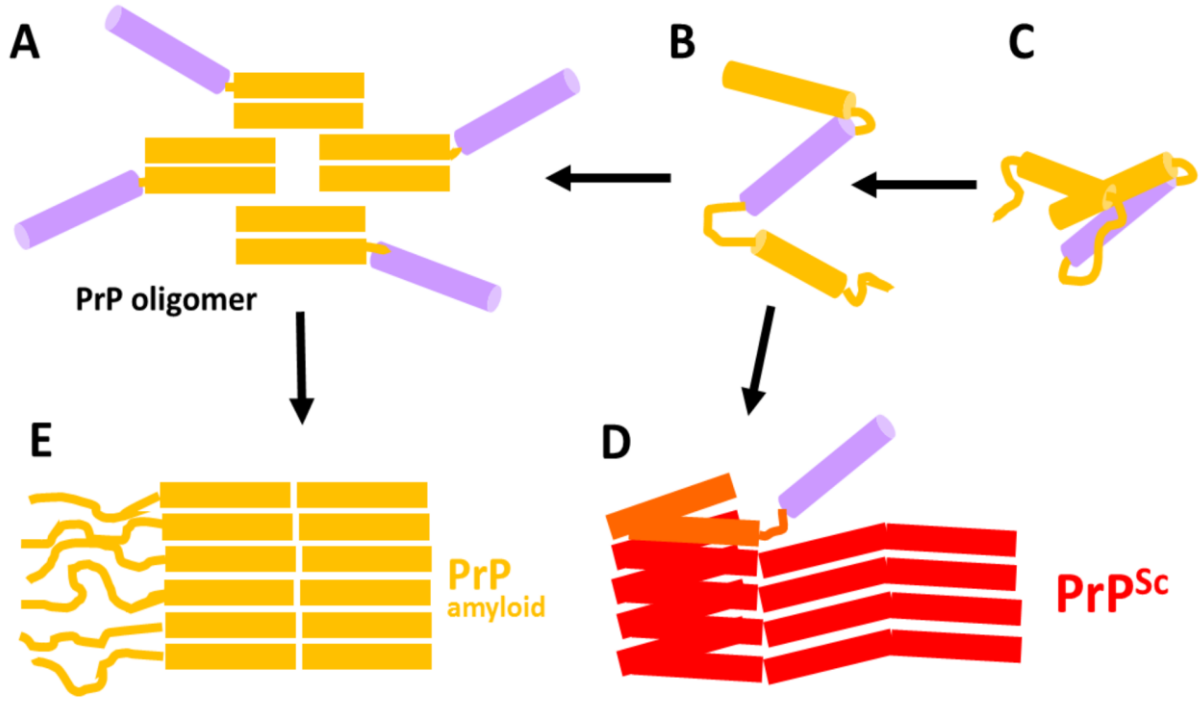

Figure 55 Off-track oligomers as intermediate stage of the unfolding of $BVPrP^{C}$. The existence of thermically-induced soluble $BVPrP^{C}$ oligomers **A)** with preserved structural elements necessarily requires the existence of a partially unfolded BVPrP species in which such structural elements are also preserved **B).** Other elements of partially unfolded $BVPrP^{C}$ at such stage would have unfolded into an unstable conformation that would lead to oligomerization, likely with simultaneous conversion to ß-structure. The **B** partially unfolded species must in turn originate from an earlier species in which partial unfolding is reversible **C),** as seen by reversible changes detected by NMR and described in the main text. Hypothetically, the putative partially unfolded species existing in stage **B)** and surmised from **A),** if attached to the templating surface of a PrP^{Sc} assembly, would not collapse into oligomers, but rather, would collapse onto the templating surface and further template into the PrP^{Sc} conformation **D).** This presupposes that similar intermediate unfolding stages occur in the presence and absence of a PrP^{Sc} template. Finally, as seen in many studies, PrP oligomers **A)** can evolve to PrP amyloids with structures that are different from PrP^{Sc} and exhibit no or little infectivity **E).** In conclusion, oligomers are off-track to PrP^{Sc} but provide useful information on the unfolding process of BVPrP, suggesting which $BVPrP^{C}$ structures are more resilient than others and likely to convert at a more advanced stage of unfolding.

Another common limitation in studies of PrP unfolding pathways is the frequent use of truncated constructs that isolate the flexible domain (FD). The N-terminal region may play a substantial role in conformational stability and initial binding to PrP^{Sc} (89,150). Therefore, full-length (non-truncated) constructs are preferable for such studies as it is the case of the present. In this regard, extending the study to include membrane-anchored PrP^{C} would be ideal; however, producing such constructions in the quantities and purity required for structural characterization remains a significant challenge.

More in general, the *in vitro* conditions employed in this and other studies typically involve relatively high protein concentrations, chemical denaturants (e.g., urea or detergents), elevated temperatures, and variations in pH and salinity to induce unfolding. These conditions markedly differ from physiological in vivo conditions and may promote alternative unfolding pathways, including the formation of oligomeric artifacts.

The integrative experimental approach used (NMR, CD, SEC, TEM) is expected to prove valuable for complementary investigations. Future research will benefit from comparisons with other sequence-specific or mutant PrP constructs work (currently ongoing). These comparisons are expected to delineate the conserved features of the unfolding mechanism while identifying sequence-dependent variabilities. Furthermore, advancements in molecular dynamics (MD) simulations could provide deeper insights into the unfolding process. Collectively, these approaches will help to elucidate the full scope of prion unfolding mechanisms across species. The goal of this line of research is completing a full reaction coordinate of the FD unfolding process and using it to develop an MD-based atomistic model of PrP^{Sc}-templated conversion of PrP^{C} into PrP^{Sc}, in other words, of PrP^{Sc} propagation. Such model should clarify key aspects of prion biology, including strain adaptation and cross-species transmission, while providing a framework for developing targeted therapies.

6. CONCLUSIONS

The integrative experimental (NMR, CD, SEC, TEM) methodology used herein applied to the study of the thermal unfolding of BVPrP^{C} (90-231) lead to the following conclusions that allowed building a plausible model of early unfolding/conversion pathway in its way to conversion into PrP^{Sc}:

1. BVPrP^{C}(90-231) revealed two distinct temperature-dependent regimes: a) 15–45°C: The protein remains monomeric, and structural changes are reversible. b) >50°C: Irreversible oligomerization occurs, yielding β-sheet-rich aggregates.

2. The β1–β2 sheet (β1: Y128–G131; β2: V161–R164) represents an early unfolding hotspot. Notably, β1 exhibits, nonlinear CCSDs, T_C indicating weak H-bond features and anomalously high R_2/R_1 ratio due to conformational exchange, all of them consistent with high local flexibility and low stability.

3. The 121-144 segment appears as the most likely region to unfold first, given the high mobility and lack of H-bonds in consonance to the global uninterrupted low and negative Tc values.

4. The CLEANEX-PM measurements in monomeric BVPrP^{C} were interpreted with Tc values and provided evidence of H-bond instabilities as the temperature is raised from 15, 25 to 45°C. Specific hydrogen-bond breaking at 45°C was detected for specific residues in the FD.

5. Water-T_2 relaxation data reveal a temperature-dependent reorganization of the monomeric BVPrP^{C}(90-231) toward a more extended conformation, commencing moderately at approximately 30°C and becoming substantially more pronounced from 36 to 45ºC right below the temperature threshold >50°C for its oligomerization.

6. Proton-proton NOEs reveal moderate temperature-dependent reorganization of secondary structure in the <45°C range, particularly involving a compaction of β1–β2 and a trend towards separation of the β1–α1–β2 and α2–α3 subdomains.

7. ^{15}N_CEST on the monomeric state revealed no evidence of conformational exchange. Methyl-CEST detected minor dips in the side-chain resonances of I182 (α2), I184 (α2), and I139 (coil), consistent with slow conformational exchange for these methyl side-chain groups, without significantly perturbing the overall protein structure.

8. At temperatures exceeding 50°C, BVPrP^{C}(90-231) undergoes irreversible oligomerization, as indicated by a two-state transition in CD spectroscopy (Tm ≈ 63°C), increased β-sheet and decreased α-helical content, broadening and incomplete recovery in N-HSQC spectra and SEC, TEM and DOSY detection of collapsed 8–12mer oligomeric species.

9. Analysis of ^{15}N-HSQC peak intensities for the oligomeric state indicates that the oligomers comprise a rigid core flanked by highly dynamic regions, particularly in the N-terminal and α2 segments. While these oligomers are off-pathway from the PrP^{Sc}-templated conversion of PrP^{C} to PrP^{Sc}, they represent a valuable artifact, allowing key insights into later events of PrP^{C} unfolding, captured before the oligomer fully forms.

10. ^{15}N_DEST experiment on the mixture containing oligomeric and monomer species (molar ratio 2:3) revealed substantial broadening of the observable peaks. This broadening indicates the presence of a weak binding equilibrium (K_D = 1 to 10^{-3} mM) between the two species.

11. MD trajectories showed that the separation of the β1-α1–β2 segment from the α2–α3 domain is possible and the three helixes are very stable. MD aided to propose a plausible mechanism for the conversion of PrP^{C} and PrP^{SC} compatible with experimental observations.

7. REFERENCES

1. Prusiner SB, Scott MR, DeArmond SJ, Cohen FE. Prion Protein Biology Review. Cell. 1998 May 1;93(3):337–48.
2. Bian J, Khaychuk V, Angers RC, Fernández-Borges N, Vidal E, Meyerett-Reid C, et al. Prion replication without host adaptation during interspecies transmissions. Proc Natl Acad Sci. 2017 Jan 31;114(5):1141–6.
3. Son M, Wickner RB. Anti-Prion Systems in Saccharomyces cerevisiae Turn an Avalanche of Prions into a Flurry. Viruses. 2022 Sep 1;14(9):1945.
4. Bian J, Khaychuk V, Angers RC, Fernández-Borges N, Vidal E, Meyerett-Reid C, et al. Prion replication without host adaptation during interspecies transmissions. Proc Natl Acad Sci. 2017 Jan 31;114(5):1141–6.
5. Musher DM, Roig IL, Cazares G, Stager CE, Logan N, Safar H. Can an etiologic agent be identified in adults who are hospitalized for community-acquired pneumonia: Results of a one-year study. J Infect. 2013 Jul;67(1):11–8.
6. Caughey B, Baron GS, Chesebro B, Jeffrey M. Getting a Grip on Prions: Oligomers, Amyloids, and Pathological Membrane Interactions. Annu Rev Biochem. 2009 Jun 1;78(1):177–204.
7. Kraus A, Groveman BR, Caughey B. Prions and the Potential Transmissibility of Protein Misfolding Diseases. Annu Rev Microbiol. 2013 Sep 8;67(1):543–64.
8. Prusiner SB. Novel Proteinaceous Infectious Particles Cause Scrapie. Science. 1982 Apr 9;216(4542):136–44.
9. Riek R, Hornemann S, Wider G, Billeter M, Glockshuber, Rudolf, Wüthrich, Kurt. NMR structure of the mouse prion protein domain PrP(121-231). Nature. 1996 Jul 11;382(6587):180–2.
10. Bolton DC, Meyer RK, Prusiner SB. Scrapie PrP 27-30 is a sialoglycoprotein. J Virol. 1985 Feb;53(2):596–606.
11. Wüthrich K, Riek R. Three-dimensional structures of prion proteins. In: Advances in Protein Chemistry. Elsevier; 2001. p. 55–82.
12. Telling GC, Scott M, Mastrianni J, Gabizon R, Torchia M, Cohen FE, et al. Prion propagation in mice expressing human and chimeric PrP transgenes implicates the interaction of cellular PrP with another protein. Cell. 1995 Oct;83(1):79–90.
13. Safar J, Prusiner SB. Chapter 29 Molecular studies of prion diseases. In: Progress in Brain Research. Elsevier; 1998. p. 421–34.
14. Bessen RA, Marsh RF. Biochemical and physical properties of the prion protein from two strains of the transmissible mink encephalopathy agent. J Virol. 1992 Apr;66(4):2096–101.
15. Asher MI, García-Marcos L, Pearce NE, Strachan DP. Trends in worldwide asthma prevalence. Eur Respir J. 2020 Dec;56(6):2002094.
16. Requena JR, Wille H. The structure of the infectious prion protein: Experimental data and molecular models. Prion. 2014 Jan;8(1):60–6.
17. Collinge J, Clarke AR. A General Model of Prion Strains and Their Pathogenicity. Science. 2007 Nov 9;318(5852):930–6.
18. Wadsworth JDF, Joiner S, Linehan JM, Jack K, Al-Doujaily H, Costa H, et al. Humanized Transgenic Mice Are Resistant to Chronic Wasting Disease Prions From Norwegian Reindeer and Moose. J Infect Dis. 2022 Sep 13;226(5):933–7.
19. Biieler H, Aguzzi A, Autenried P, Ague M, Weissmann' C. Mice Devoid of PrP Are Resistant to Scrapie. Cell. 1993 Jul 2;73(7):1339–47.
20. Aguzzi Adriano, Heikenwalder Mathias. Pathogenesis of prion diseases: current status and future outlook. Nat Rev Microbiol. 2006 Oct 1;4:765–75.

21. Prusiner SB. Biology and Genetics of Prions Causing Neurodegeneration. Annu Rev Genet. 2013 Nov 23;47(1):601–23.
22. Bruce ME, Will RG, Ironside JW, McConnell I, Drummond D, Suttie A, et al. Transmissions to mice indicate that 'new variant' CJD is caused by the BSE agent. Nature. 1997 Oct;389(6650):498–501.
23. Collinge J. Prion Diseases of Humans and Animals: Their Causes and Molecular Basis. Annu Rev Neurosci. 2001 Mar;24(1):519–50.
24. Castilla J, Morales R, Saá P, Barria M, Gambetti P, Soto C. Cell-free propagation of prion strains. EMBO J. 2008 Oct 8;27(19):2557–66.
25. Imran M, Mahmood S. An overview of human prion diseases. Virol J. 2011 Dec;8(1):559.
26. Orrú CD, Groveman BR, Hughson AG, Zanusso G, Coulthart MB, Caughey B. Rapid and Sensitive RT-QuIC Detection of Human Creutzfeldt-Jakob Disease Using Cerebrospinal Fluid. Wickner RB, editor. mBio. 2015 Feb 27;6(1):e02451-14.
27. Zerr I, Kallenberg K, Summers DM, Romero C, Taratuto A, Heinemann U, et al. Updated clinical diagnostic criteria for sporadic Creutzfeldt-Jakob disease. Brain. 2009 Oct 1;132(10):2659–68.
28. Ironside JW, Ritchie DL, Head MW. Prion diseases. In: Handbook of Clinical Neurology. Elsevier; 2018. p. 393–403.
29. Gambetti P, Cali I, Notari S, Kong Q, Zou WQ, Surewicz WK. Molecular biology and pathology of prion strains in sporadic human prion diseases. Acta Neuropathol (Berl). 2011 Jan;121(1):79–90.
30. Kovacs GG, Molnár K, Keller E, Botond G, Budka H, László L. Intraneuronal Immunoreactivity for the Prion Protein Distinguishes a Subset of E200K Genetic From Sporadic Creutzfeldt-Jakob Disease. J Neuropathol Exp Neurol. 2012 Mar;71(3):223–32.
31. Brown DR. Consequences of manganese replacement of copper for prion protein function and proteinase resistance. EMBO J. 2000 Mar 15;19(6):1180–6.
32. Brandel JP, Culeux A, Grznarova K, Levavasseur E, Lamy P, Privat N, et al. Amplification techniques and diagnosis of prion diseases. Rev Neurol (Paris). 2019 Sep;175(7–8):458–63.
33. Seed CR, Hewitt PE, Dodd RY, Houston F, Cervenakova L. Creutzfeldt-Jakob disease and blood transfusion safety. Vox Sang. 2018 Apr;113(3):220–31.
34. Belay ED, Schonberger LB. Variant Creutzfeldt-Jakob disease and bovine spongiform encephalopathy.
35. Hsiao K, Baker H F, Crow T J, Poulter M, Owen F, Terwilliger J D, et al. Linkage of a prion protein missense variant to Gerstmann-Sträussler syndrome. Nature. 1989 Mar 23;338(6213):342–5.
36. Lugaresi E, Tobler I, Gambetti P, Montagna P. The Pathophysiology of Fatal Familial Insomnia. Brain Pathol. 1998 Jul;8(3):521–6.
37. Montagna P, Gambetti P, Cortelli P, Lugaresi E. Familial and sporadic fatal insomnia. Lancet Neurol. 2003 Mar;2(3):167–76.
38. Zou W, Puoti G, Xiao X, Yuan J, Qing L, Cali I, et al. Variably protease-sensitive prionopathy: A new sporadic disease of the prion protein. Ann Neurol. 2010 Aug;68(2):162–72.
39. Cracco L, Notari S, Cali I, Sy MS, Chen SG, Cohen ML, et al. Novel strain properties distinguishing sporadic prion diseases sharing prion protein genotype and prion type. Sci Rep. 2017 Jan 16;7(1):38280.
40. Gajdu DC. Unconventional Viruses and ti Origin and Disappearance of Kui. Science. 1977 Sep 2;197(4307):943–60.
41. Mead S, Whitfield J, Poulter M, Shah P, Uphill J, Beck J, et al. Genetic susceptibility, evolution and the kuru epidemic. Philos Trans R Soc B Biol Sci. 2008 Nov 27;363(1510):3741–6.
42. Andréoletti O, Litaise C, Simmons H, Corbière F, Lugan S, Costes P, et al. Highly Efficient Prion Transmission by Blood Transfusion. Bartz J, editor. PLoS Pathog. 2012 Jun 21;8(6):e1002782.
43. Houston F, Goldmann W, Foster J, González L, Jeffrey M, Hunter N. Comparative Susceptibility of Sheep of Different Origins, Breeds and PRNP Genotypes to Challenge with Bovine

Spongiform Encephalopathy and Scrapie. Kincaid AE, editor. PLOS ONE. 2015 Nov 20;10(11):e0143251.
44. Mathiason CK, Powers JG, Dahmes SJ, Osborn DA, Miller KV, Warren RJ, et al. Infectious Prions in the Saliva and Blood of Deer with Chronic Wasting Disease. Science. 2006 Oct 6;314(5796):133–6.
45. Haley NJ, Hoover EA. Chronic Wasting Disease of Cervids: Current Knowledge and Future Perspectives. Annu Rev Anim Biosci. 2015 Feb 16;3(1):305–25.
46. Saunders SE, Bartelt-Hunt SL, Bartz JC. Occurrence, Transmission, and Zoonotic Potential of Chronic Wasting Disease. Emerg Infect Dis. 2012 Mar;18(3):369–76.
47. Race B, Williams K, Chesebro B. Transmission studies of chronic wasting disease to transgenic mice overexpressing human prion protein using the RT-QuIC assay. Vet Res. 2019 Dec;50(1):6.
48. Mathiason CK. Large animal models for chronic wasting disease. Cell Tissue Res. 2023 Apr;392(1):21–31.
49. Will RG, Ironside JW, Zeidler M, Estibeiro K, Cousens SN, Smith PG, et al. A new variant of Creutzfeldt-Jakob disease in the UK. The Lancet. 1996 Apr;347(9006):921–5.
50. Prusiner SB. Prions. PNAS. 1998 Nov 10;95(23):13363.
51. Aguzzi A, Calella AM. Prions: Protein Aggregation and Infectious Diseases. Physiol Rev. 2009 Oct;89(4):1105–52.
52. Hornemann S, Glockshuber R. A scrapie-like unfolding intermediate of the prion protein domain PrP(121–231) induced by acidic pH. Proc Natl Acad Sci. 1998 May 26;95(11):6010–4.
53. Zahn R, Liu A, Lührs T, Riek R, Von Schroetter C, López García F, et al. NMR solution structure of the human prion protein. Proc Natl Acad Sci. 2000 Jan 4;97(1):145–50.
54. Riek R. NMR structure of the mouse prion protein. ETH Zurich; 1998.
55. Donne DG, Viles JH, Groth D, Mehlhorn I, James TL, Cohen FE, et al. Structure of the recombinant full-length hamster prion protein PrP(29–231): The N terminus is highly flexible. Proc Natl Acad Sci. 1997 Dec 9;94(25):13452–7.
56. Pan KM, Baldwin M, Nguyen J, Gasset M, Mehlhorn I, Huang Z, et al. Conversion of a-helices into,f-sheets features in the formation of the scrapie prion proteins. Proc Natl Acad Sci USA. 1993;
57. Caughey B. In Vitro Expression and Biosynthesis of Prion Protein. In: Chesebro BW, editor. Transmissible Spongiform Encephalopathies: Berlin, Heidelberg: Springer Berlin Heidelberg; 1991. p. 93–107. (Compans RW, Cooper M, Koprowski H, McConnell I, Melchers F, Nussenzweig V, et al., editors. Current Topics in Microbiology and Immunology; vol. 172).
58. Wille H, Bian W, McDonald M, Kendall A, Colby DW, Bloch L, et al. Natural and synthetic prion structure from X-ray fiber diffraction. Proc Natl Acad Sci. 2009 Oct 6;106(40):16990–5.
59. Requena JR, Wille H. The structure of the infectious prion protein: Experimental data and molecular models. Prion. 2014 Jan;8(1):60–6.
60. Vázquez-Fernández E, Alonso J, Pastrana MA, Ramos A, Stitz L, Vidal E, et al. Structural Organization of Mammalian Prions as Probed by Limited Proteolysis. Baskakov IV, editor. PLoS ONE. 2012 Nov 20;7(11):e50111.
61. Groveman BR, Dolan MA, Taubner LM, Kraus A, Wickner RB, Caughey B. Parallel In-register Intermolecular β-Sheet Architectures for Prion-seeded Prion Protein (PrP) Amyloids. J Biol Chem. 2014 Aug;289(35):24129–42.
62. Kim JI, Cali I, Surewicz K, Kong Q, Raymond GJ, Atarashi R, et al. Mammalian Prions Generated from Bacterially Expressed Prion Protein in the Absence of Any Mammalian Cofactors. J Biol Chem. 2010 May;285(19):14083–7.
63. Choi JK, Cali I, Surewicz K, Kong Q, Gambetti P, Surewicz WK. Amyloid fibrils from the N-terminal prion protein fragment are infectious. Proc Natl Acad Sci. 2016 Nov 29;113(48):13851–6.

64. Spagnolli G, Rigoli M, Orioli S, Sevillano AM, Faccioli P, Wille H, et al. Full atomistic model of prion structure and conversion. Supattapone S, editor. PLOS Pathog. 2019 Jul 11;15(7):e1007864.
65. Ce´ dric Govaerts, Holger Wille, Stanley B. Prusiner, Fred E. Cohen. Evidence for assembly of prions with left-handed β-helices into trimers. PNAS. 2004 May 21;101(22):8342–7.
66. Wille H, Michelitsch MD, Guénebaut V, Supattapone S, Serban A, Cohen FE, et al. Structural studies of the scrapie prion protein by electron crystallography. Proc Natl Acad Sci. 2002 Mar 19;99(6):3563–8.
67. Baskakov IV, Caughey B, Requena JR, Sevillano AM, Surewicz WK, Wille H. The prion 2018 round tables (I): the structure of PrP^{Sc}. Prion. 2019 Jan 1;13(1):46–52.
68. Kraus A, Hoyt F, Schwartz CL, Hansen B, Artikis E, Hughson AG, et al. High-resolution structure and strain comparison of infectious mammalian prions. Mol Cell. 2021 Nov;81(21):4540-4551.e6.
69. Manka SW, Zhang W, Wenborn A, Betts J, Joiner S, Saibil HR, et al. 2.7 Å cryo-EM structure of ex vivo RML prion fibrils. Nat Commun. 2022 Jul 13;13(1):4004.
70. Manka SW, Wenborn A, Betts J, Joiner S, Saibil HR, Collinge J, et al. A structural basis for prion strain diversity. Nat Chem Biol. 2023 May;19(5):607–13.
71. Hoyt F, Standke HG, Artikis E, Schwartz CL, Hansen B, Li K, et al. Cryo-EM structure of anchorless RML prion reveals variations in shared motifs between distinct strains. Nat Commun. 2022 Jul 13;13(1):4005.
72. Alam P, Hoyt F, Artikis E, Soukup J, Hughson AG, Schwartz CL, et al. Cryo-EM structure of a natural prion: chronic wasting disease fibrils from deer. Acta Neuropathol (Berl). 2024 Oct 24;148(1):56.
73. Manka SW. Breaking the Mould: How the First Structure of a Deer Prion Suggests the Framework for Interspecies Strain Diversity and Transmission Barriers. J Neurochem. 2025 Mar;169(3):e70050.
74. Shewmaker F, McGlinchey RP, Thurber KR, McPhie P, Dyda F, Tycko R, et al. The Functional Curli Amyloid Is Not Based on In-register Parallel β-Sheet Structure. J Biol Chem. 2009 Sep;284(37):25065–76.
75. Mabbott N. How do PrPSc Prions Spread between Host Species, and within Hosts? Pathogens. 2017 Nov 24;6(4):60.
76. Aguzzi A, De Cecco E. Shifts and drifts in prion science. Science. 2020 Oct 2;370(6512):32–4.
77. Jalali S, Zhang R, Haataja MP, Dias CL. Nucleation and Growth of Amyloid Fibrils. J Phys Chem B. 2023 Nov 16;127(45):9759–70.
78. Zhang W, Orrú CD, Foutz A, Ding M, Yuan J, Shah SZA, et al. Large-scale validation of skin prion seeding activity as a biomarker for diagnosis of prion diseases. Acta Neuropathol (Berl). 2024 Jun;147(1):17.
79. Christen B, Pérez DR, Hornemann S, Wüthrich K. NMR Structure of the Bank Vole Prion Protein at 20 °C Contains a Structured Loop of Residues 165–171. J Mol Biol. 2008 Nov;383(2):306–12.
80. Graves R. The Greek Myths. 1955.
81. Artikis E, Kraus A, Caughey B. Structural biology of ex vivo mammalian prions. J Biol Chem. 2022 Aug;298(8):102181.
82. Viles JH, Donne D, Kroon G, Prusiner SB, Cohen FE, Dyson HJ, et al. Local Structural Plasticity of the Prion Protein. Analysis of NMR Relaxation Dynamics. Biochemistry. 2001 Mar 1;40(9):2743–53.
83. Julien O, Chatterjee S, Thiessen A, Graether SP, Sykes BD. Differential stability of the bovine prion protein upon urea unfolding. Protein Sci. 2009 Oct;18(10):2172–82.
84. Julien O, Chatterjee S, Bjorndahl TC, Sweeting B, Acharya S, Semenchenko V, et al. Relative and Regional Stabilities of the Hamster, Mouse, Rabbit, and Bovine Prion Proteins toward Urea

Unfolding Assessed by Nuclear Magnetic Resonance and Circular Dichroism Spectroscopies. Biochemistry. 2011 Sep 6;50(35):7536–45.
85. Honda RP, Yamaguchi K ichi, Kuwata K. Acid-induced Molten Globule State of a Prion Protein. J Biol Chem. 2014 Oct;289(44):30355–63.
86. Sengupta I, Bhate SH, Das R, Udgaonkar JB. Salt-Mediated Oligomerization of the Mouse Prion Protein Monitored by Real-Time NMR. J Mol Biol. 2017 Jun;429(12):1852–72.
87. Bhate SH, Udgaonkar JB, Das R. Destabilization of polar interactions in the prion protein triggers misfolding and oligomerization. Protein Sci. 2021 Nov;30(11):2258–71.
88. Sanz-Hernández M, Barritt JD, Sobek J, Hornemann S, Aguzzi A, De Simone A. Mechanism of misfolding of the human prion protein revealed by a pathological mutation. Proc Natl Acad Sci. 2021 Mar 23;118(12):e2019631118.
89. Russo L, Salzano G, Corvino A, Bistaffa E, Moda F, Celauro L, et al. Structural and dynamical determinants of a β-sheet-enriched intermediate involved in amyloid fibrillar assembly of human prion protein. Chem Sci. 2022;13(35):10406–27.
90. Nicholson EM, Mo H, Prusiner SB, Cohen FE, Marqusee S. Differences between the prion protein and its homolog doppel: a partially structured state with implications for scrapie formation. J Mol Biol. 2002 Feb;316(3):807–15.
91. Wang LQ, Zhao K, Yuan HY, Wang Q, Guan Z, Tao J, et al. Cryo-EM structure of an amyloid fibril formed by full-length human prion protein. Nat Struct Mol Biol. 2020 Jun;27(6):598–602.
92. Wang LQ, Zhao K, Yuan HY, Li XN, Dang HB, Ma Y, et al. Genetic prion disease–related mutation E196K displays a novel amyloid fibril structure revealed by cryo-EM. Sci Adv. 2021 Sep 10;7(37):eabg9676.
93. Fernández-Borges N, Eraña H, Elezgarai SR, Harrathi C, Venegas V, Castilla J. A Quick Method to Evaluate the Effect of the Amino Acid Sequence in the Misfolding Proneness of the Prion Protein. In: Lawson VA, editor. Prions. New York, NY: Springer New York; 2017. p. 205–16. (Methods in Molecular Biology; vol. 1658).
94. Gerber R, Tahiri-Alaoui A, Hore PJ, James W. Oligomerization of the Human Prion Protein Proceeds via a Molten Globule Intermediate. J Biol Chem. 2007 Mar;282(9):6300–7.
95. Gerber R, Voitchovsky K, Mitchel C, Tahiri-Alaoui A, Ryan JF, Hore PJ, et al. Inter-Oligomer Interactions of the Human Prion Protein Are Modulated by the Polymorphism at Codon 129. J Mol Biol. 2008 Aug;381(1):212–20.
96. Serpa JJ, Popov KI, Petrotchenko EV, Dokholyan NV, Borchers CH. Structure of prion β-oligomers as determined by short-distance crosslinking constraint-guided discrete molecular dynamics simulations. PROTEOMICS. 2021 Nov;21(21–22):2000298.
97. Skinner SP, Fogh RH, Boucher W, Ragan TJ, Mureddu LG, Vuister GW. CcpNmr AnalysisAssign: a flexible platform for integrated NMR analysis. J Biomol NMR. 2016 Oct;66(2):111–24.
98. Sattler M. Heteronuclear multidimensional NMR experiments for the structure determination of proteins in solution employing pulsed field gradients. Prog Nucl Magn Reson Spectrosc. 1999 Mar 19;34(2):93–158.
99. Frueh DP. Practical aspects of NMR signal assignment in larger and challenging proteins. Prog Nucl Magn Reson Spectrosc. 2014 Apr;78:47–75.
100. Cierpicki T, Zhukov I, Byrd RA, Otlewski J. Hydrogen Bonds in Human Ubiquitin Reflected in Temperature Coefficients of Amide Protons. J Magn Reson. 2002 Aug;157(2):178–80.
101. Cierpicki T, Otlewski J. Amide proton temperature coefficients as hydrogen bond indicators in proteins. J Biomol NMR. 2001 Nov;21(3):249–61.
102. Andersen NH. Conformational Isomerism of Endothelin in Acidic Aqueous Media: A Quantitative NOESY Analysis. Biochemistry. 1992 Feb 11;31(5):1280–95.
103. Thielmann Y, Mohrlüder J, Koenig BW, Stangler T, Hartmann R, Becker K, et al. An Indole-Binding Site is a Major Determinant of the Ligand Specificity of the GABA Type A Receptor-Associated Protein GABARAP. ChemBioChem. 2008 Jul 21;9(11):1767–75.

104. Baxter NJ et al. Characterisation of Low Free-energy Excited States of Folded Proteins. J Mol Biol. 1998 Dec 18;284(5):1625–39.
105. Gupta S, Bhattacharjya S. NMR Characterization of the Near Native and Unfolded States of the PTB Domain of Dok1: Alternate Conformations and Residual Clusters. Driscoll PC, editor. PLoS ONE. 2014 Feb 28;9(2):e90557.
106. Lin YJ. Protein dynamics and estimation of additional relaxation from 13C to measured 15N relaxation, diffusion tensor and overall rotational correlation time using uniformly 15N/13C-labeled NACI. J Magn Reson. 2025 Jul;107939.
107. Hwang TL, Mori S, Shaka AJ, Van Zijl PCM. Application of Phase-Modulated CLEAN Chemical EXchange Spectroscopy (CLEANEX-PM) to Detect Water−Protein Proton Exchange and Intermolecular NOEs. J Am Chem Soc. 1997 Jul 1;119(26):6203–4.
108. Bertuzzi S, Gimeno A, Núñez-Franco R, Bernardo-Seisdedos G, Delgado S, Jiménez-Osés G, et al. Unravelling the Time Scale of Conformational Plasticity and Allostery in Glycan Recognition by Human Galectin-1. Chem – Eur J. 2020 Dec;26(67):15643–53.
109. Chakraborty I, Kar RK, Sarkar D, Kumar S, Maiti NC, Mandal AK, et al. Solvent Relaxation NMR: A Tool for Real-Time Monitoring Water Dynamics in Protein Aggregation Landscape. ACS Chem Neurosci. 2021 Aug 4;12(15):2903–16.
110. Farrow NA, Muhandiram R, Singer AU, Pascal SM, Kay CM, Gish G, et al. Backbone Dynamics of a Free and a Phosphopeptide-Complexed Src Homology 2 Domain Studied by 15N NMR Relaxation. Biochemistry. 1994 May 17;33(19):5984–6003.
111. Sapienza PJ, Lee AL. Using NMR to study fast dynamics in proteins: methods and applications. Curr Opin Pharmacol. 2010 Dec;10(6):723–30.
112. Jozef Kowalewski,, Lena Maler. Nuclear Spin Relaxation in Liquids. 1st Edition. CRC Press; 2006. 440 p.
113. Palmer Iii AG. NMR Probes of Molecular Dynamics: Overview and Comparison with Other Techniques. Annu Rev Biophys Biomol Struct. 2001 Jun;30(1):129–55.
114. Clore GM, Gronenborn AM. Determining the structures of large proteins and protein complexes by NMR. Trends Biotechnol. 1998 Jan;16(1):22–34.
115. Pelta MD, Morris GA, Stchedroff MJ, Hammond SJ. A one-shot sequence for high-resolution diffusion-ordered spectroscopy. Magn Reson Chem. 2002 Dec;40(13).
116. Ferreira ASD, Barreiros S, Cabrita EJ. Probing sol-gel matrices microenvironments by PGSE HR-MAS NMR. Magn Reson Chem. 2017 May;55(5):452–63.
117. Augé S, Schmit PO, Crutchfield CA, Islam MT, Harris DJ, Durand E, et al. NMR Measure of Translational Diffusion and Fractal Dimension. Application to Molecular Mass Measurement. J Phys Chem B. 2009 Feb 19;113(7):1914–8.
118. Nilsson M, Connell MA, Davis AL, Morris GA. Biexponential Fitting of Diffusion-Ordered NMR Data: Practicalities and Limitations. Anal Chem. 2006 May 1;78(9):3040–5.
119. Anthis NJ, Clore GM. Visualizing transient dark states by NMR spectroscopy. Q Rev Biophys. 2015 Feb;48(1):35–116.
120. Kay LE. New Views of Functionally Dynamic Proteins by Solution NMR Spectroscopy. J Mol Biol. 2016 Jan;428(2):323–31.
121. Yuwen T, Huang R, Kay LE. Probing slow timescale dynamics in proteins using methyl 1H CEST. J Biomol NMR. 2017 Jul;68(3):215–24.
122. Sekhar A, Velyvis A, Zoltsman G, Rosenzweig R, Bouvignies G, Kay LE. Conserved conformational selection mechanism of Hsp70 chaperone-substrate interactions. eLife. 2018 Feb 20;7:e32764.
123. Vallurupalli P, Bouvignies G, Kay LE. Studying “Invisible” Excited Protein States in Slow Exchange with a Major State Conformation. J Am Chem Soc. 2012 May 16;134(19):8148–61.
124. Alderson TR, Kay LE. Unveiling invisible protein states with NMR spectroscopy. Curr Opin Struct Biol. 2020 Feb;60:39–49.

125. Gu Y, Hansen AL, Peng Y, Brüschweiler R. Rapid Determination of Fast Protein Dynamics from NMR Chemical Exchange Saturation Transfer Data. Angew Chem Int Ed. 2016 Feb 24;55(9):3117–9.
126. Khandave NP, Hansen DF, Vallurupalli P. Increasing the accuracy of exchange parameters reporting on slow dynamics by performing CEST experiments with 'high' B1 fields. J Magn Reson. 2024 Jun;363:107699.
127. Palmer AG. Chemical exchange in biomacromolecules: Past, present, and future. J Magn Reson. 2014 Apr;241:3–17.
128. Bouvignies G, Kay LE. A 2D 13C-CEST experiment for studying slowly exchanging protein systems using methyl probes: an application to protein folding. J Biomol NMR. 2012 Aug;53(4):303–10.
129. Rezaei H, Eghiaian F, Perez J, Doublet B, Choiset Y, Haertle T, et al. Sequential Generation of Two Structurally Distinct Ovine Prion Protein Soluble Oligomers Displaying Different Biochemical Reactivities. J Mol Biol. 2005 Apr;347(3):665–79.
130. Artikis E, Roy A, Caughey B. How short is too short for amyloid fibrils?: Molecular dynamics of oligomers of infectious prion core structures. J Biol Chem. 2025 Jul;301(7):110390.
131. M. Parrinello, A. Rahman. Polymorphic transitions in single crystals: A new molecular dynamics method. J Appl Phys. 1981 Dec 1;52(12):7182–90.
132. Baxter NJ, Williamson MP. Temperature dependence of 1H chemical shifts in proteins. J Biomol NMR. 1997 Jun;9(4):359–69.
133. Christen B, Damberger FF, Pérez DR, Hornemann S, Wüthrich K. Structural plasticity of the cellular prion protein and implications in health and disease. Proc Natl Acad Sci. 2013 May 21;110(21):8549–54.
134. Shen Y, Delaglio F, Cornilescu G, Bax A. TALOS+: a hybrid method for predicting protein backbone torsion angles from NMR chemical shifts. J Biomol NMR. 2009 Aug;44(4):213–23.
135. Sakshi Bhagat, Bhawna Chaubey, Samanwita Pal. Solvent-Based NMR Approaches for the Assessment of Molecular Interactions: A Review of Current Practices. Magn Reson Chem. 2025 Oct 20;64(1):114–39.
136. Slapšak U, Salzano G, Ilc G, Giachin G, Bian J, Telling G, et al. Unique Structural Features of Mule Deer Prion Protein Provide Insights into Chronic Wasting Disease. ACS Omega. 2019 Nov 26;4(22):19913–24.
137. Liu S, Chu H, Xie Y, Wu F, Mu F, Wei J, et al. Assisting and accelerating NMR assignment with restrained structure prediction. Commun Biol. 2025 Jul 18;8(1):1067.
138. Darling WTP, Hyberts SG, Erdelyi M. Non-Uniform Sampling for Quantitative NOESY. Magn Reson Chem. 2025 Jul;63(7):495–507.
139. Jain S, Sekhar A. Elucidating the mechanisms underlying protein conformational switching using NMR spectroscopy. J Magn Reson Open. 2022 Jun;10–11:100034.
140. Ahn M, Streit JO, Waudby CA, Włodarski T, Figueiredo AM, Christodoulou J, et al. Amyloid Forming Human Lysozyme Intermediates are Stabilized by Non-Native Amide-π Interactions. Adv Sci. 2025 Sep;12(34):e03957.
141. Kurauskas V, Schanda P, Sounier R. Methyl-Specific Isotope Labeling Strategies for NMR Studies of Membrane Proteins. Methods in Molecular Biology. 2017 Jan 01, 1635:109-123.
142. Cawood EE, Karamanos TK, Wilson AJ, Radford SE. Visualizing and trapping transient oligomers in amyloid assembly pathways. Biophys Chem. 2021 Jan;268:106505.
143. Fawzi NL, Ying J, Ghirlando R, Torchia DA, Clore GM. Atomic-resolution dynamics on the surface of amyloid-β protofibrils probed by solution NMR. Nature. 2011 Dec 8;480(7376):268–72.
144. Eghiaian F, Daubenfeld T, Quenet Y, Van Audenhaege M, Bouin AP, Van Der Rest G, et al. Diversity in prion protein oligomerization pathways results from domain expansion as revealed by hydrogen/deuterium exchange and disulfide linkage. Proc Natl Acad Sci. 2007 May;104(18):7414–9.

145. Adrover M, Pauwels K, Prigent S, De Chiara C, Xu Z, Chapuis C, et al. Prion Fibrillization Is Mediated by a Native Structural Element That Comprises Helices H2 and H3. J Biol Chem. 2010 Jul;285(27):21004–12.
146. Zhang Y, Swietnicki W, Zagorski MG, Surewicz WK, Sönnichsen FD. Solution Structure of the E200K Variant of Human Prion Protein. J Biol Chem. 2000 Oct;275(43):33650–4.
147. Kuwata K, Kamatari YO, Akasaka K, James TL. Slow Conformational Dynamics in the Hamster Prion Protein. Biochemistry. 2004 Apr 1;43(15):4439–46.
148. O'Sullivan DBD, Jones CE, Abdelraheim SR, Thompsett AR, Brazier MW, Toms H, et al. NMR characterization of the pH 4 β-intermediate of the prion protein: the N-terminal half of the protein remains unstructured and retains a high degree of flexibility. Biochem J. 2007 Jan 15;401(2):533–40.
149. O'Sullivan DBD, Jones CE, Abdelraheim SR, Brazier MW, Toms H, Brown DR, et al. Dynamics of a truncated prion protein, PrP(113–231), from^{15} N NMR relaxation: Order parameters calculated and slow conformational fluctuations localized to a distinct region. Protein Sci. 2009 Feb;18(2):410–23.
150. Hosszu LLP, Sangar D, Batchelor M, Risse E, Hounslow AM, Collinge J, et al. Loss of Residues 119–136, Including the First β-strand of Human Prion Protein, Generates an Aggregation-competent Partially "Open" Form. J Mol Biol. 2023 Aug;435(15):168158.
151. Watts JC, Giles K, Patel S, Oehler A, DeArmond SJ, Prusiner SB. Evidence That Bank Vole PrP Is a Universal Acceptor for Prions. Mabbott NA, editor. PLoS Pathog. 2014 Apr 3;10(4):e1003990.
152. Espinosa JC, Nonno R, Di Bari M, Aguilar-Calvo P, Pirisinu L, Fernández-Borges N, et al. PrP^C Governs Susceptibility to Prion Strains in Bank Vole, While Other Host Factors Modulate Strain Features. Caughey BW, editor. J Virol. 2016 Dec;90(23):10660–9.
153. Calzolai L, Lysek DA, Güntert P, Von Schroetter C, Riek R, Zahn R, et al. NMR structures of three single-residue variants of the human prion protein. Proc Natl Acad Sci. 2000 Jul 18;97(15):8340–5.
154. Swietnicki W, Morillas M, Chen SG, Gambetti P, Surewicz WK. Aggregation and Fibrillization of the Recombinant Human Prion Protein huPrP90−231. Biochemistry. 2000 Jan 1;39(2):424–31.
155. Baskakov IV, Legname G, Prusiner SB, Cohen FE. Folding of Prion Protein to Its Native α-Helical Conformation Is under Kinetic Control. J Biol Chem. 2001 Jan;276(23):19687–90.
156. Baskakov IV, Legname G, Baldwin MA, Prusiner SB, Cohen FE. Pathway Complexity of Prion Protein Assembly into Amyloid. J Biol Chem. 2002 Jun;277(24):21140–8.
157. Sokolowski F, Modler AJ, Masuch R, Zirwer D, Baier M, Lutsch G, et al. Formation of Critical Oligomers Is a Key Event during Conformational Transition of Recombinant Syrian Hamster Prion Protein. J Biol Chem. 2003 Oct;278(42):40481–92.
158. Lu X, Wintrode PL, Surewicz WK. β-Sheet core of human prion protein amyloid fibrils as determined by hydrogen/deuterium exchange. Proc Natl Acad Sci. 2007 Jan 30;104(5):1510–5.
159. Schlepckow K, Schwalbe H. Molecular Mechanism of Prion Protein Oligomerization at Atomic Resolution. Angew Chem Int Ed. 2013 Sep 16;52(38):10002–5.
160. Pal R. Impact of innate immune modifications in prion disease pathogenesis. The University of Edinburgh; 2024.
161. Rezaei H, Choiset Y, Eghiaian F, Treguer E, Mentre P, Debey P, et al. Amyloidogenic Unfolding Intermediates Differentiate Sheep Prion Protein Variants. J Mol Biol. 2002 Sep;322(4):799–814.
162. Sasaki K, Gaikwad J, Hashiguchi S, Kubota T, Sugimura K, Kremer W, et al. Reversible monomer-oligomer transition in human prion protein. Prion. 2008 Jul;2(3):118–22.
163. Sangho Lee, David Eisenberg. Seeded conversion of recombinant prion protein to a disulfide-bonded oligomer by a reduction-oxidation process. Nature Structural & Molecular Biology volume. 2003 Aug 3;10(9):725–30.

8. APPENDIX

Appendix A: Chemical shifts for BVPrP^{C}(90-231).

Residue	N (HN)	CA (HA)	CB
GLY 90	108.6 (7.9)	45.3 (3.8)	
GLN 91	119.9 (8.3)	55.9 (4.7)	29.4
GLY 92	110.3 (8.5)	45.2 (3.9)	29.4
GLY 93	110.7 (8.4)	45.1 (3.9) (4.3)	29.4
GLY 94	108.5 (8.3)	45.4 (3.9)	
THR 95	113.1 (8.0)	62.0 (4.5)	70.1
HIS 96	119.6 (6.5)		
ASN 97	118.4 (7.2)	(4.7)	
GLN 98	119.9 (7.4)		
TRP 99	120.3 (7.4)	55.9	
ASN 100	120.3 (7.9)	53.7 (4.7)	38.8
LYS 101	122.5 (8.0)	54.3 (3.9)	32.4
SER 103	116.6 (8.3)	57.9 (4.3)	64.1
LYS 104	124.1 (8.2)	(4.5)	
LYS 106	121.9 (8.4)	56.3 (4.2)	
THR 107	115.1 (8.1)	61.4 (4.7)	61.4
ASN 108	121.6 (8.5)	52.9 (4.7)	38.9
ILE 109	123.3 (7.5)	62.3 (4.6)	
LYS 110	121.5 (8.0)	57.0 (3.9)	31.1
HIS 111	121.1 (8.4)	55.3 (4.6)	
VAL 112	119.6 (7.1)	(4.7)	
ALA 113	128.2 (8.4)	52.6 (4.2)	19.3
GLY 114	108.6 (8.3)	45.1 (3.9) (4.3)	
ALA 115	123.7 (8.1)	52.4 (4.2)	19.3
ALA 116	123.2 (8.2)	52.3 (4.7)	19.2
ALA 117	123.3 (8.2)	52.4 (4.2)	19.2
ALA 118	123.4 (8.0)	52.4 (3.8)	19.3
GLY 119	107.9 (8.1)	44.5 (3.9)	
ALA 120	123.3 (7.7)	49.8 (4.2)	48.1
VAL 121	119.2 (8.0)	62.1 (4.1)	34.1

Residue	N (HN)	CA (HA)	CB
VAL 122	124.5 (8.1)	62.3 (4.0)	32.7
GLY 123	113.2 (8.2)	45.1 (3.9) (4.7)	
GLY 124	107.9 (8.2)	45.1 (3.8) (4.7)	
LEU 125	121.5 (8.0)	55.4 (4.3)	39.8
GLY 126	109.7 (8.4)	46.6 (4.9) (3.8)	
GLY 127	108.3 (8.2)	45.7 (3.8)	
TYR 128	117.9 (7.7)	58.1 (4.4)	
MET 129	121.3 (9.0)	54.1 (4.4)	32.1
LEU 130	121.1 (8.0)	54.1 (4.3)	38.9
GLY 131	114.8 (9.3)	44.9 (4.4)	
SER 132	113.7 (8.2)	58.7 (4.4)	64.2
ALA 133	125.5 (8.3)	52.9 (4.3)	19.2
MET 134	121.3 (8.7)	53.9 (4.5)	30.0
SER 135	115.9 (8.3)	59.0 (4.3)	63.3
ARG 136	126.4 (8.6)	55.1 (4.2)	30.3
MET 138	122 (8.6)	54.2 (4.6)	
ILE 139	124.4 (6.5)	59.5 (3.8)	38.8
HIS 140	121.7 (8.1)	54.1 (4.8)	29.8
PHE 141	124.9 (10.3)	54.1 (4.2)	
GLY 142	108.8 (8.9)	45.7 (5.1) (4.0)	
ASN 143	114.2 (7.2)	52.5 (4.8)	41.5
ASP 144	123.3 (8.9)	57.9 (4.6)	41.4
RP 145	120.3 (8.4)	61.9 (4.1)	
GLU 146	120.5 (8.1)	58.1 (4.0)	29.4
ASP 147	118.8 (7.9)	58.4 (4.6)	40.6
ARG 148	119.9 (8.0)	59.8 (3.9)	29.9
TYR 149	120.8 (8.2)	62.6 (3.7)	38.2
TYR 150	120.3 (8.9)	62.9 (3.9)	38.4
ARG 151	117.3 (7.8)	60.3 (4.1)	28.6
GLU 152	115.5 (7.8)	57.9 (3.9)	30.1
ASN 153	115.7 (7.4)	54.9 (4.4)	
MET 154	117.9 (7.4)	58.9 (4.1)	34.5
ASN 155	115.9 (8.0)	55.0 (4.3)	39.2

Residue	N (HN)	CA (HA)	CB
ARG 156	117.6 (7.9)	57.5 (4.2)	
TYR 157	120.6 (7.2)	53.3 (5.0)	35.1
ASN 159	116.1 (8.5)	55.7 (4.5)	
GLN 160	114.0 (7.2)	54.3 (4.5)	
VAL 161	112.6 (8.4)	58.7 (4.6)	34.1
TYR 162	121.1 (8.4)	57.6 (5.2)	
TYR 163	111 (8.4)	56.4 (4.7)	38.6
ARG 164	120.3 (8.0)	52.7 (4.6)	29.3
VAL 166	118.9 (8.6)	65.6 (4.1)	
ASP 167	117.1 (8.2)	55.0 (4.4)	41.1
GLN 168	117.3 (8.1)	56.1 (4.5)	29.6
TYR 169	116.8 (7.8)	57.0 (4.6)	41.2
ASN 170	117.2 (8.9)	54 (4.7)	41.0
ASN 171	113.2 (7.5)	52.5 (4.7)	39.9
GLN 172	120.5 (8.6)	59.6 (4.7)	
ASN 173	117.4 (8.4)	56.4 (4.3)	35.2
ASN 174	118.2 (8.4)	56.9 (4.5)	38.4
PHE 175	121.4 (7.3)	56.1 (3.0)	39.2
VAL 176	120.1 (8.7)	67.6 (3.3)	
HIS 177	116.8 (8.3)	59.5 (4.3)	27.3
ASP 178	118.6 (7.4)	57.7 (4.5)	41.1
CYS 179	119.4 (8.1)	59.1 (4.3)	33.3
VAL 180	124.6 (9.1)	66.1 (3.6)	31.5
ASN 181	116.4 (7.5)	57.6 (4.2)	
ILE 182	118.9 (8.8)	62.6 (4.5)	36.6
THR 183	117.9 (8.1)	68.8 (4.0)	
ILE 184	120.7 (8.4)	66.4 (3.6)	
LYS 185	122.7 (7.9)	60.1 (4.0)	
GLN 186	116.5 (8.4)	57.9 (4.4)	28.4
HIS 187	117.9 (8.3)	58.1 (4.5)	
THR 188	114.6 (7.9)	64.5 (4.1)	69.1
VAL 189	122.7 (7.4)	61.9 (4.3)	32.9
THR 190	115.3 (7.4)	64.7 (4.2)	69.6
THR 191	115 (8.0)	64.5 (4.4)	69.9
THR 192	116.9 (7.7)	64 (4.4)	69.4
THR 193	116.0 (7.4)	64.2 (4.2)	69.2

Residue	N (HN)	CA (HA)	CB
LYS 194	121.5 (8.0)	57.2 (4.3)	32.4
GLY 195	108.6 (8.3)	46.5 (4.0) (4.7)	
GLU 196	119.9 (6.8)	55.7 (4.1)	31.2
ASN 197	119.4 (8.4)	52.9 (4.6)	
PHE 198	121.5 (8.6)	56.8 (5.1)	40.3
THR 199	116.0 (9.5)	60.6 (4.6)	72.3
GLU 200	119.9 (9.1)	60.3 (4.0)	29.1
THR 201	116.3 (7.9)	67.4 (3.7)	68.8
ASP 202	120.0 (7.5)	58.4 (4.6)	41.8
VAL 203	119.7 (8.2)	67.9 (3.3)	31.7
LYS 204	119.5 (8.1)	(4.3)	
MET 205	118.5 (8.1)	59.8 (4.1)	34.0
MET 206	118.2 (8.7)	59.9 (3.6)	32.9
GLU 207	118.4 (8.4)	61.2 (3.9)	28.5
ARG 208	116.8 (7.2)	58.5 (4.1)	30.0
VAL 209	119.0 (8.2)	66.1 (3.7)	32.7
VAL 210	120.6 (9.0)	66.4 (3.6)	
GLU 211	120.5 (8.1)	60.4 (3.8)	29.6
GLN 212	115.3 (7.1)	59.3 (3.9)	
MET 213	119.1 (8.2)	59.7 (4.5)	31.4
CYS 214	119.3 (9.1)	60.4 (4.3)	42.0
VAL 215	123.3 (8.3)	67.7 (3.4)	31.7
THR 216	118.0 (8.0)	67.1 (3.8)	68.5
GLN 217	122.3 (8.6)	58.8 (4.2)	29.5
TYR 218	119.8 (8.4)	62.0 (2.8)	37.3
GLN 219	119.6 (8.1)	59.4 (3.6)	27.7
LYS 220	118.9 (7.9)	59.2 (4.1)	31.9
GLU 221	116.8 (8.3)	57.9 (4.1)	29.9
SER 222	114.9 (8.2)	60.9 (3.9)	62.8
GLN 223	120.6 (7.5)	57.9 (4.1)	28.4
ALA 224	120.9 (7.5)	53.9 (4.1)	18.4
TYR 225	118.6 (7.5)	59.6 (4.2)	38.6
TYR 226	120.3 (8.0)	59.5 (4.2)	38.6
GLU 227	120.3 (8.0)	57.5 (4.1)	29.7
GLY 228	108.4 (7.9)	45.5 (3.8)	

Residue	**N (HN)**	**CA (HA)**	**CB**
ARG 229	119.8 (7.8)	55.9 (4.3)	31.2
SER 230	117.3 (8.3)	58.3 (4.4)	64.0
SER 231	122.8 (7.9)	60.4 (5.2)	65.6

The cryo-EM structure of the misfolded form of prion protein, PrP^{Sc}, is a relatively simple, β-sheet–rich amyloid that acts as a passive template, shifting focus to PrP^{C} as an active participant in conversion. The folded domain (FD) of PrP^{C} (2 β-strands and 3 α-helices) must adapt to $PrPS^{C}$. Variable-temperature NMR studies of bank vole PrP^{C} identified early unfolding of β1–β2, partial destabilization of α1, and their displacement from the FD. In contrast, α2 and α3 remained comparatively stable. NMR relaxation and MD simulations confirmed enhanced mobility of the β-regions and supported separation of the β1–β2–α1 unit from the FD, enabling β-sheet-compatible rearrangements with PrP^{SC}. Above 50 °C, PrP^{C} formed irreversible oligomers of ~12 subunits, retaining a folded core with exposed N-terminus and α2.